Photo-physical proprieties of new molecular materials for light-to-energy conversion

Li Liu

UNIVERSITÉ DE STRASBOURG

École Doctorale de Physique et Chimie Physique de Strasbourg

Institue de Physique et Chimie des Matériaux de Strasbourg

THÈSE

présentée par :

Li LIU

soutenue le : **14 juin 2017**

pour obtenir le grade de : **Docteur de l'université de Strasbourg**

Discipline/ Spécialité : Physique

Propriétés photo-physiques de nouveaux matériaux moléculaires pour la conversion de photon en énergie

THÈSE dirigée par :
Prof. Stefan HAACKE — Professor, Université de Strasbourg

RAPPORTEURS :
Prof. Villy SUNDSTRÖM — Professor, Lund University
Dr. Olivier POIZAT — Directeur de recherche, Université de Lille

EXAMINATEURS:
Prof. Luisa DE COLA — Professor, Université de Strasbourg
Dr. Fabrice ODOBEL — Directeur de recherche, Université de Nantes

Contents

Remerciements

Je tiens tout d'abord à Stefan Haacke, mon directeur de thèse, qui m'avoir permis de découvrir le travail de l'équipe BIODYN lors de mon stage de fin d'étude et de réaliser cette thèse. Je souhaite le remercier pour sa patience de nos discussions sur la physique et d'améliorer la façon de présenter mes résultats. C'est ma honneur de le rencontrer quand j'ai été la premier fois en france. Ca a été un grand plaisir de travailler avec lui.
Je voudrais également remercier Jérémie Léonard, pour tout ce qu'il a posé les bons questions et remarques à profondir la pensé et sa bonne humeur.
Un grand merci à Johanna Brazard pour ses super idées et ses corrections scientiques et surtout anglaises de ma thèse. Sans elle, il est au moins cinq fois plus difficile à finaliser cette travail.

Je remercie aux tous les doctorants et les post-docs dans l'équipe BioDyn, anciens comme nouveaux, qui ont participé à ce que ma thèse se passe dans de bonnes conditions. Sacha Maillot, Thomas Roland, Alexandre Cheminal et Moussa Gueye qui ont su nous donner leur savoir, discuter physiques et philosophiques, aider à ma vie qutodien et organiser les sorties et soirées. Merci à Juilien Nillon pour ses aides de NOPA et à Patricia Touron Touceda, Jamie Conyard, Youssef El Khoury et Vincent Kemlin pour ses conseils et discussions. Une pensé va aux doctorants qui finira ses thèses: Anastasia Ioanna Skilitsi, Damianos Agathangelou, Anthonin Huart et Edoardo Domenichini. Je souhaite bon courage pour la fin de leurs thèses.

Il me faut aussi remercier Olivier Crégut pour sa disponibilité et son excellent savoir faire en optique et en programmation, Jean Pierre Vola pour ses patience sur les outils électroniques.
Egalement merci à tous les amies que j'ai pu me faire durant cette thèse, pour les bons moments passés ensemble: Linlin, Thierry, Déborah, Xiaojie, Junhui, Arthur, Fatema et à tous du RUCK. En particulier mes amies qui m'a connu il y a plus de vingt ans, Gu.

Merci aussi à ceux que j'ai oublié de citer ici mais qui j'espère se reconnaitront.

Enfin, je souhaite remercier ma famille pour leur support tout au long de ma scolarité.

Résumé en français

I. Introduction

Pendant cette thèse, j'ai étudié les propriétés photo-physiques de nouveaux matériaux moléculaires, utilisés dans des dispositifs photovoltaïques, par spectroscopies résolues en temps. Les dispositifs photovoltaïques convertissent l'énergie solaire en électricité. C'est une source d'énergie renouvelable qui permet notamment de s'affranchir de la limitation en énergie fossile et ainsi de réduire le réchauffement problème climatique lié à l'effet de serre.

Actuellement, les dispositifs photovoltaïques présents sur le marché sont à base de silicium. A cause des processus de purification et de dopage, le silicium est cher et polluant. Le développement de nouveaux matériaux est donc intéressant pour réduire le coût de fabrication, ainsi que pour simplifier leur fabrication et les rendre moins polluants.

Une idée est de remplacer le silicium par un colorant synthétique. Cependant, le rendement de conversion de puissance des dispositifs à base de colorant (10,6% pour la cellule organique en tandem, et 11,9% pour la cellule à colorant dite cellule de Grätzel) est bien inférieur à celui des dispositifs à base de silicium (46% pour la cellule à multi-jonctions).[26]
La motivation de mon doctorat était de distinguer les processus physiques photo-induits, et de les relier à la structure chimique des systèmes étudiés, afin de désigner de nouveaux matériaux moléculaires en partenariat avec des chimistes.

Afin de suivre les processus photo-physiques ultrarapides (femtoseconde) des dispositifs photovoltaïques, les spectroscopies ultra-rapides résolues en temps sont appliquées. Ces-dernières sont combinées avec d'autres techniques, telles que l'absorption stationnaire, la fluorescence stationnaire et la spectroélectrochimie (les états et les espèces électroniques concernés sont identifiés par leur spectre). Ces techniques permettent de suivre les cinétiques et de déterminer les processus photophysiques, comme les transferts d'énergie ou de charge entre les différents états ou espèces du système.

Pendant la thèse, deux principaux projets ont été abordés. Le premier est sur une famille de molécules organiques avec comme spécificité de pouvoir s'auto-assembler en blocs donneur et accepteur.[56,57] Les molécules sont étudiées en changeant le bloc donneur (avec/sans le séparateurséparateur et nombre du groupe donneur), et en modifiant les solvants. Le deuxième est sur les complexes de fer[167,176] pour la cellule de Grätzel. L'idée est de remplacer le ruthénium, qui est plus commun, mais rare et toxique pour la cellule de Grätzel, par le fer en conservant le même rendement de conversion de puissance.

II. Méthodes

Les méthodes principales sont la spectroscopie d'absorption transitoire et de fluorescence résolue en temps. Les autres techniques (l'absorption et la fluorescence stationnaires UV-Vis et la spectro-électro-chimie) permettent de comprendre le scénario induit par le photon.

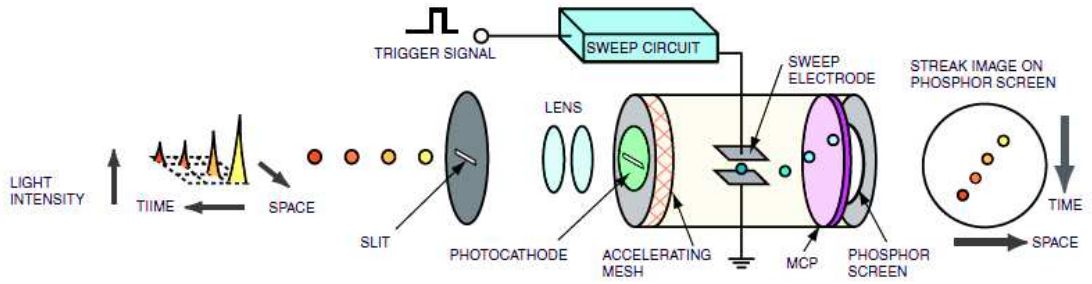

Figure F1. Schéma d'une caméra à balayage de fente.86 Les photons sont transformés en électrons et sont déviés par un champ électrique vertical généré par un balayage rapide. Selon leur temps d'arrivée, différentes tensions sont appliquées. Ainsi, la fluorescence générée se répand spectralement et temporellement sur les axes horizontaux et verticaux de la caméra CCD, respectivement.

Les mesures de fluorescence résolues en temps ont été enregistrées avec une caméra à balayage de fente avec une plage de temps de 1 ns à 500 µs. La résolution de temps est de 0,5% de la plage de temps choisie, sauf pour la plage de temps la plus courte (1 ns) où la résolution temporelle est de 10 ps. Après excitation d'un échantillon, sa fluorescence est imagée à l'entrée d'un spectromètre. Le spectromètre répand la fluorescence horizontalement en fonction des longueurs d'onde.
Les photons sont axés sur la photocathode. La photocathode très sensible pourrait convertir la majorité des photons en électrons. Les électrons accélérés passent un champ électrique vertical généré par un balayage de tension rapide. Le balayage de tension est déclenché par une source laser pour définir le temps zéro. Comme la force électrostatique dépend du moment où les électrons sont arrivés, ils sont déplacés le long de l'axe vertical. La plage de temps est réglable en modifiant la rampe de tension du champ électrique vertical. Les électrons résolus dans le temps sont amplifiés par la plaque de micro-canal (MCP) et transférés à des photons par un écran à phosphore. Par conséquent, la fluorescence générée est répartie spectralement et temporellement sur l'axe horizontal et vertical de la caméra CCD, respectivement.
La spectroscopie de fluorescence résolue dans le temps est une méthode efficace pour étudier les processus radiatifs, tels que la recombinaison d'excitons, le processus de transfert d'énergie et la recombinaison de porteurs libres.

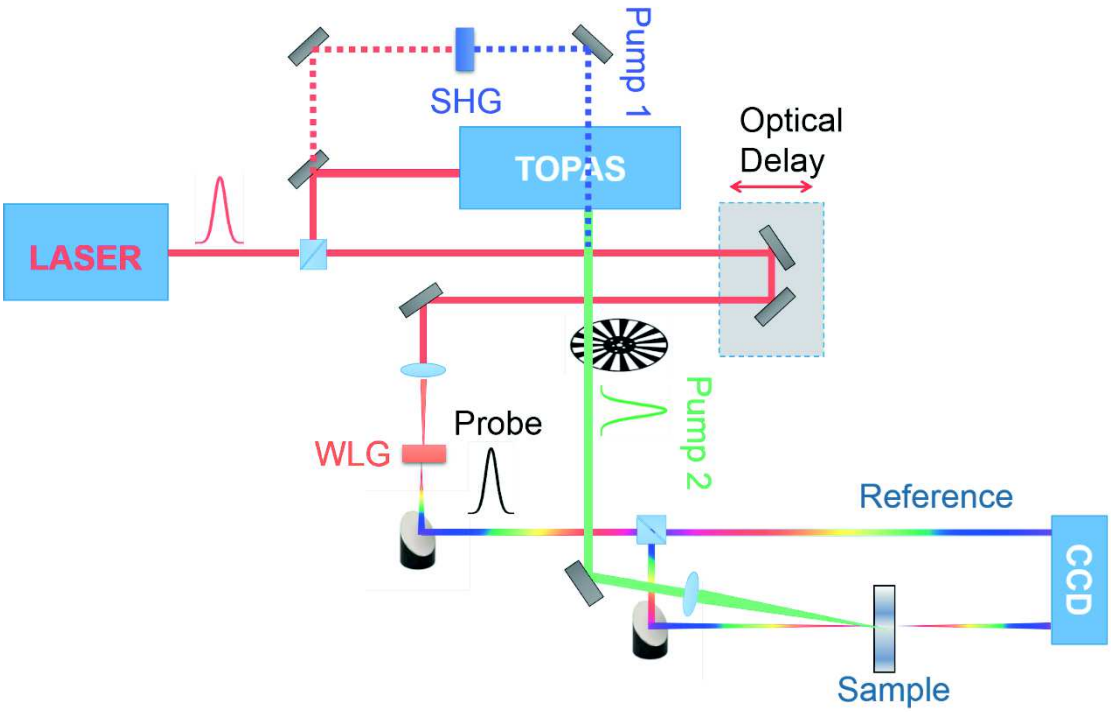

Figure F2. Schéma de principe d'un dispositif expérimental d'absorption transitoire.

La spectroscopie d'absorption transitoire consiste à suivre le changement d'absorption d'un échantillon après excitation. Il y a deux impulsions : l'une est intense, dite la pompe, centrée dans le maximum de la bande d'absorption de la molécule et déclenche la photophysique ; et l'autre est plus faible, dite la sonde, qui enregistre le spectre différentiel de l'échantillon. Une ligne à retard mécanique modifie le chemin optique de la sonde, et ainsi le retard de la sonde est modifié par rapport au moment où la pompe est arrivée. Ce retard permet de mesurer la cinétique de l'échantillon. Dans notre expérience, la précision aux temps courts est limitée par la résolution temporelle et le plus long retard mesurable est de 5 ns (limité par la longueur de la ligne à retard). Les modifications de l'échantillon correspondant à l'intensité optique sont acquises à différents retards après l'arrivée de la pompe par le spectromètre.

Les données se présentent sous la forme d'une matrice bidimensionnelle, en fonction du temps et des longueurs d'onde. Le changement de l'absorption est donné par la loi de Beer-Lambert:

$$\Delta A(\lambda, t) = \sum_i \varepsilon_{s_i}(\lambda) \Delta C_{s_i}(t) L$$

Où ε_{s_i} correspond au coefficient de l'extinction moléculaire de l'état S_i, ΔC_{s_i} est le changement de concentration de l'état S_i et L est la longueur de l'échantillon. Cette équation n'est valable que lorsque le coefficient d'extinction molaire de l'espèce ne dépend pas du temps.

Avant excitation par la pompe (t <0), les molécules sont dans leur état fondamental. Quand une partie des molécules absorbent des photons, elles sont excitées et vont dans un état excité. Cela conduit au blanchiment (*Ground State Bleaching* GSB), qui signifie que l'électron dans l'état fondamental est excité et se situe dans l'état excité . Après quelques temps, la molécule peut revenir à l'état fondamental et émettre un photon (*Stimulated Emission* SE) ou absorber un photon vers un état supérieur (*Excited State Absorption* ESA), ou subir une réaction, par exemple la formation de charge ou d'un état à transfert de charge. Le produit peut absorber un photon à un état d'énergie supérieur (*Photoproduct Absorption* PA) ou repeupler l'état fondamental (GSB). Le spectre différentiel est utilisé pour identifier les différents états dans le mécanisme moléculaire.

Les spectres d’absorption différentielle sont analysés par comparaison avec les données stationnaires, afin d’indiquer quel bloc et quel état sont impliqués. Les données cinétiques sont traitées de façon globale pour déterminer les constantes de temps associées aux spectres d’absorption différentielle. Le but de l'analyse des données est de distinguer ces spectres différentiels avec leurs constantes de temps comme le mécanisme moléculaire, et ainsi déterminer le schéma réactionnel.

III. Résultats

III. 1. Série de molécules pour des cellules photovoltaïques organiques

Dans la cellule photovoltaïque organique, la couche active absorbe la lumière solaire pour générer un courant électrique. En général, la couche active est composée de deux parties : un donneur électrique et un accepteur électrique. L'absorption de la lumière génère des excitons qui diffusent, se dissocient en paire de charges, et ces charges sont ensuite collectées aux électrodes. L'énergie de liaison de l'exciton est plus grande dans des matériaux organiques que l'énergie thermique. La dissociation se passe justement à l'interface entre le donneur et l'accepteur et l'électron diffuse dans l'accepteur. A cause de la mobilité des charges relativement faible dans les matériaux organiques, la durée de vie des charges doit être assez longue pour permettre aux charges d'aller jusqu'aux électrodes avant leur recombinaison. C'est la raison pour laquelle il est intéressant de prolonger leur durée de vie. Une deuxième possibilité est de maximiser le ratio interface/volume. Il peut diminuer la distance de diffusion à l'interface. Avec la durée de vie de transfert de charge plus longue, il est possible de générer plus de charges. [6]

L'état de transfert de charge joue un rôle important pour augmenter le rendement de la cellule photovoltaïque. Sa formation est limitée par la diffusion de l'exciton et sa durée de vie doit être assez longue pour former des charges séparées. La spectroscopie résolue en temps peut apporter une meilleure compréhension des propriétés photo-physiques et aider à désigner un nouveau matériel.

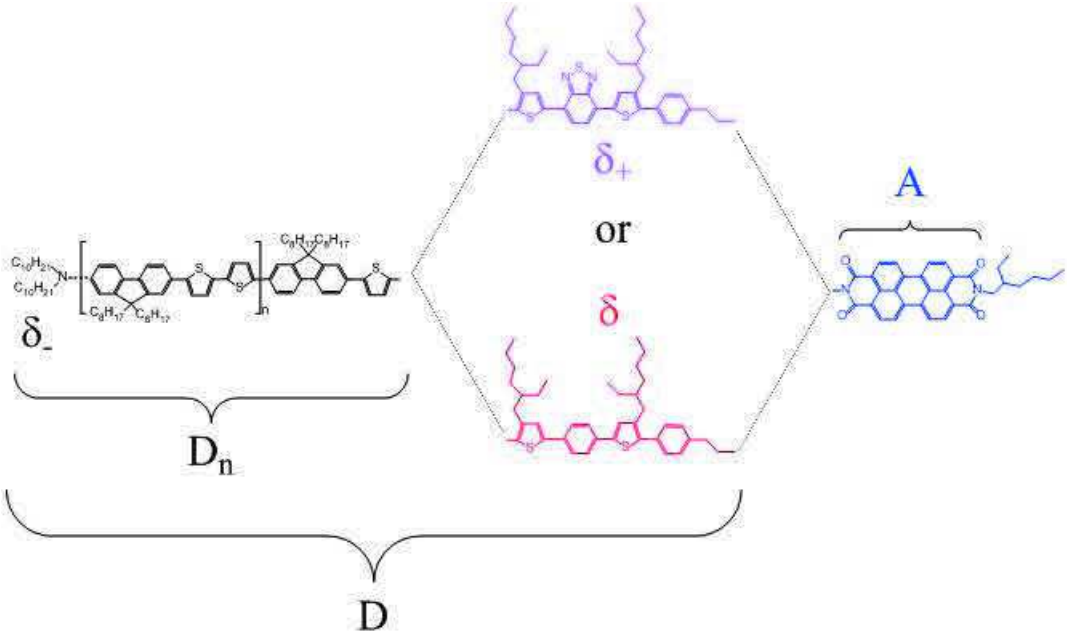

Figure F3. Les structures chimiques des molécules donneur-accepteur

Dans notre étude, la partie de l'accepteur (A) étudiée est le pérylène diimide (PDI), présentant la propriété d'auto-assemblage pour de structurer en film. La partie du donneur (D) est basée sur le bis-thiophène fluorène. Le bloc du donneur varie en fonction de la longueur du D (noté D_n, n: 0~3), du bloc séparateurle séparateur entre D et A (noté δ ou δ_+) et de l'amine terminale (notée δ_-).[2]

Le PDI n'est pas seulement largement utilisé comme pigment industriel, mais a également d'autres applications scientifiques, telles que la spectroscopie de fluorescence, les transistors organiques transparents, la structure fonctionnelle empilée π dans l'ADN et le photovoltaïque organique (OPV). Le PDI a deux caractéristiques importantes : 1) son image miroir de l'absorption et de la fluorescence, 2) un rendement quantique de fluorescence> 0,9. La stabilité remarquable de la PDI est également attribuée à l'absence d'électrons dans l'empilement π conjugué, ce qui le rend très résistant à la dégradation par oxydation et à d'autres voies de décomposition.
Ce groupement donneur est relié au groupement accepteur via une liaison constituée d'une chaîne flexible courte (éthylène) et d'un bloc moléculaire qui se présente sous deux électronégativités :basse et haute, respectivement, notées δ ou δ_+. Cette unité moléculaire de liaison est composée de thiophène-phényl-thiophène (pour δ) ou de thiophène-benzothiadiazole-thiophène (pour δ_+). En outre, une amine terminale peut être ajoutée à l'autre extrémité de la fraction donneuse en tant que «donneur d'électrons» et notée δ_-.

Au cours de cette thèse, j'ai effectué des mesures sur neuf molécules en solution (chloroforme). Quatre d'entre elles ont une longueur commune de donneurs (n = 1) pour étudier l'effet des différents donneurs, et deux séries de fragments de donneurs avec une augmentation de la longueur de donneurs (n = 0 ~ 2) pour étudier l'importance de la séparation des charges entre donneur et accepteur. À la fin, trois d'entre elles sont étudiées dans deux autres solvants (toluène et trichloréthylène) pour tester différentes polarités de solvant. Cette section se concentre sur les propriétés photo-physiques intramoléculaires, en particulier la durée de la vie de l'état de transfert de charge.

Une sélection de spectres d'absorption différentielle correspondante (ΔA) (20 fs, 2,5 ps 28 ps) est affichée dans la Figure F4 (A) ~ (C). Chaque spectre peut être décomposé en une somme de contributions d'espèces / états individuels, dont les signatures spectroscopiques sont identifiées par des expériences à l'état stationnaire (Section IV.2.1 dans la thèse).

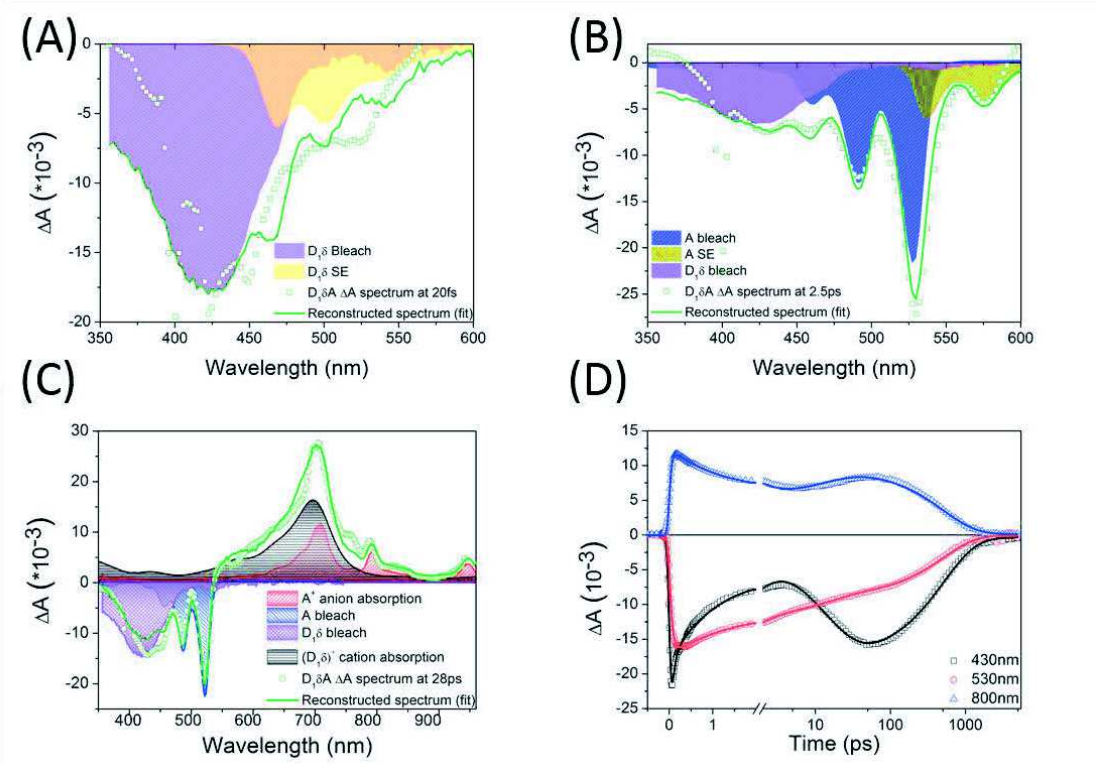

Figure F4 Identification des états photo-induits (A) Spectre d'absorption différentielle à 20 fs (rond vert) avec son ajustement (courbe solide verte) en tant que combinaison linéaire des spectres d'absorption de $D_1\delta$ (blanchiment, motif violet) et la fluorescence à l'état stationnaire de $D_1\delta$ (SE, motif

jaune). Le bon accord avec son ajustement est une preuve de $(D_1\delta)^*$. (B) Le spectre d'absorption différentielle à 2,5ps (rond vert) avec son ajustement (ligne continue verte) comme combinaison linéaire des spectres d'absorption à l'état stationnaire de A (agent de blanchiment, motif bleu), fluorescence à l'état stationnaire de A (SE, Motif jaune foncé) et les spectres d'absorption à l'état stationnaire de D (blanchiment, motif bleu). Le bon accord avec son ajustement est une preuve pour A*. (C) Le spectre d'absorption différentielle à 28ps (rond vert) avec son ajustement (courbe solide verte) en tant que combinaison linéaire des spectres d'absorption à l'état stationnaire de $D_1\delta$ (agent de blanchiment, motif rouge) A (agent de blanchiment, motif bleu) A^- (rouge Motif) et $(D_1\delta)^+$ (motif noir). Le bon accord avec son ajustement est une preuve de l'état CT. (D) Des traces cinétiques sélectionnées (symboles) et leur ajustement global (courbes solides) observés pour $D_1\delta A$ dans le chloroforme et correspondant au GSB donneur à 430 nm (noir), l'accepteur GSB à 490 nm (rouge) et la signature de l'anion à 800 nm (bleu)

Aux temps courts (figure F4 (A)), le spectre différentiel à 20 fs présente une large bande négative inférieure à 585 nm, contenant le blanchiment de $D_1\delta$ (GSB, motif violet) et son émission stimulée (SE, Motif jaune), et est donc attribué à l'état excité du donneur ($(D_1\delta)^*$). Le signal positif à une longueur d'onde plus longue (figure F4 (A)) est attribué à l'absorption de l'état excité plus élevé (ESA) de $D_1\delta^*$, conformément à l'identification précédente de la même signature sur des composés similaires[93]. Une inadéquation mineure est due à des artefacts expérimentaux, tels que le pic Raman et la modulation de phase croisée.

Après 2,5 ps (figure F4 (B)), les caractéristiques de $(D_1\delta)^*$ (large bande négative sans structure, motif violet) ont considérablement diminué et sont remplacées par quatre nouveaux pics négatifs à 460, 490, 530 et 575 nm, qui se distinguent facilement par l'absorption (motif bleu) et les bandes de fluorescence (motif jaune foncé) de A et le pic ESA positif à 700 nm[111], ainsi sous forme de GSB de A et SE de l'état excité A*. Ceci indique que la population de $(D_1\delta)^*$ s'est transformée en quelques picosecondes en raison d'un transfert d'énergie de $(D_1\delta)$ vers A et la forme A* est créée. Le transfert rapide d'énergie est attendu car le chevauchement spectral entre la bande de fluorescence de $(D_1\delta)$ et la bande d'absorption d'A (figure IV.2 (A) dans la thèse) est important.

Dans le spectre différentiel de 28 ps (figure F4 (C)), les pics négatifs à 490 et 530 nm (motif bleu) persistent alors que la bande à 410 nm (motif violet) associée au blanchiment du donneur indiquant que l'état fondamental de $D_1\delta$ et A sont dépeuplés. Simultanément, les caractéristiques spectrales de l'absorption induite (à une longueur d'onde> 550 nm) sont bien reproduites par la somme des spectres d'absorption des anions et de cations photo-induits (pics) à 710 et 800 nm pour A^- (motif rouge)et de 500 à 800 nm (motif noir) pour $(D_1\delta)^+$). Cela prouve qu'en quelques dizaines de picosecondes, un transfert de charge s'est produit, formant l'état CT composé des radicaux δ $(D_1\delta)^+$ et A^- ion. Sur les échelles de temps plus longues, les spectres différentiels ne changent pas en forme, mais seulement leurs amplitudes diminuent, montrant que l'état de transfert de charge (CT) se recombine, en réformant l'état fondamental.

En résumé, la dynamique de ces systèmes peut être décrite en trois étapes :

1. Dans les premières centaines de femtosecondes, le GSB de A est formé tandis que le GSB de $D_1\delta$ diminue, ce qui indique que le transfert d'énergie de $D_1\delta$ à A se produit.
2. Plus tard (dix premières picosecondes), le GSB du $D_1\delta$ augmente alors que le GSB de A reste, accompagné de la formation de la caractéristique spectrale des espèces chargées. Ce comportement cinétique et spectral indique la formation de l'état CT.
3. Ensuite, trois traces cinétiques remontent à zéro simultanément, en moins d'une nanoseconde. Ceci indique un retour vers l'état fondamental par recombinaison de charge.

Des constantes de fréquence plus précises avec leur spectre différentiel associé (*Decay-Associated differential spectrum*, DAS en anglais) sont réalisées dans le cadre de l'analyse globale (§ III.3.2 dans la thèse).

Cinq constantes de temps sont nécessaires pour atteindre un ajustement avec des résidus satisfaisants : 60 fs, 1,2 ps, 14 ps, 500 ps et 2,2 ns. Les spectres différentiels associés à ces constantes de temps (DAS) sont représentés sur la figure IV.7 dans la thèse et correspondent au schéma réactionnel suivant :

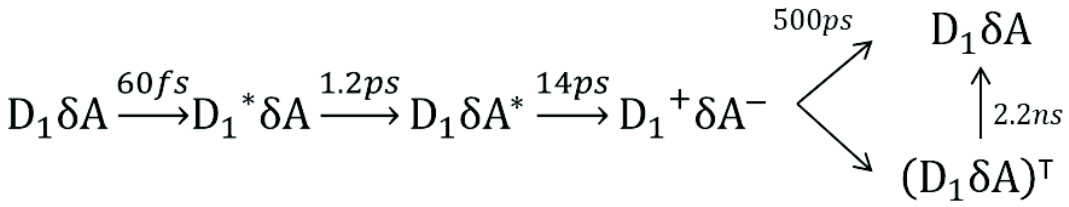

III. 3.1.1 Effet du donneur

Différents groupes donneurs sont étudiés pour surveiller l'influence des propriétés photo-induites sur la dynamique de l'état CT. L'addition de l'unité de benzothiadiazole (δ_+) montre un spectre de fluorescence largement décalé (de 500 nm pour $D_1\delta$ à 647 nm pour $D_1\delta_+$), ce qui diminue le recouvrement avec le spectre d'absorption de l'accepteur (figure IV.2 dans la thèse). Le transfert d'énergie, plus précisément Förster Resonance Energy Transfer (FRET, § I.3.2 dans la thèse), de ($D_1\delta_+$) à A n'est donc plus permis dans ce cas.

Sans FRET, la principale différence par rapport au $D_1\delta A$ est la formation directe des états CT à partir de l'état donneur excité $(D_1\delta_+)^*$. La figure F5 (A) illustre les spectres d'absorption différentielle à 80 fs (courbes noires) et 3,5 ps (courbes rouges) de $D_1\delta A$ (panneau supérieur) et $D_1\delta_+A$ (panneau inférieur). Dans le cas de $D_1\delta_+A$, les contributions de GSB et de SE de D sont observées, mais il n'y a pas de signature de l'état A* excité tel que SE à 575 nm ou l'ESA à 705 nm. L'absence de transfert d'énergie de $D\delta_+$ à A est ainsi confirmée. La seule différence observée est un changement d'ESA avec un pic plus intense à 950 nm, attribué à la relaxation vibrationnelle de la molécule.

Cependant, malgré le manque d'excitation de l'accepteur, on observe un signal apparenté au blanchiment de A vers 500 nm. Conformément à d'autres études[112,113,114], nous attribuons ce blanchiment à un changement Stark de l'absorption de A. Ceci est probablement dû au moment du dipôle intramoléculaire sur $(D_1\delta_+)^*$, avec l'électron localisé sur le séparateurle séparateur δ_+ ayant une affinité électronique élevée.

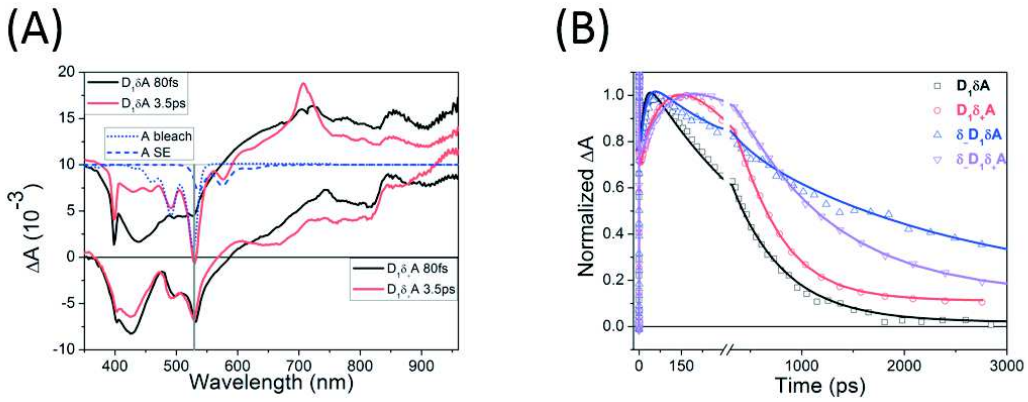

Figure F5(A) Spectres d'absorption différentielle sur $D_1\delta A$. La molécule est passée séquentiellement de l'état D excité, à l'état A excité et enfin à l'état de transfert de charge après excitation. (B) Les traces cinétiques à la longueur d'onde représentant l'état de transfert de charge pour quatre blocs donneur différents.

La figure F5 (B) souligne l'influence de la nature de la chaîne (soit δ ou δ_+) entre D_1 et A, et celle du groupe terminal δ_- sur D_1, à travers les traces cinétiques à 800 nm, i.e. en suivant la signature d'A^-. Le tableau IV.5 résume les constantes de temps associées à la formation de l'état CT et à la recombinaison de charges dans le chloroforme. L'addition de δ_+ ralentit le temps de formation de l'état CT. Deux molécules avec δ_+ ont des temps de formation d'état CT au moins cinq fois plus lents que les composés avec le séparateur le séparateur initial δ, car le temps de montée de la bande d'absorption d'anion est de 90 ps et 120 ps pour $D_1\delta_+A$ (rouge) et $\delta_-D_1\delta_+A$ (violet) par rapport à 14 ps pour $D_1\delta A$ (noir) et $\delta_-D_1\delta A$ (bleu). Cela peut être dû au manque de FRET en présence de δ_+ et au fait que l'état CT est formé de $(D_1\delta_+)^*$. En effet la délocalisation initiale joue un rôle majeur dans le taux de formation de l'état CT.[115] Inversement, δ_+ n'a pas d'impact significatif sur la cinétique de recombinaison de charge : cinétiques très similaires pour $D_1\delta A$ (noir) et $D_1\delta_+A$ (rouge) ou pour $\delta_-D_1\delta A$ (bleu) et $\delta_-D_1\delta_+A$ (pourpre).

La présence de l'amine terminale δ_- allonge le temps de recombinaison de charge, puisque les durées de vie des états CT sont augmentées d'un facteur 2,5 pour les molécules avec le séparateur δ_+ (1,2 ns pour $\delta_-D_1\delta_+A$ contre 0,48 ns pour $D_1\delta_+A$) et de 4,5 avec le séparateur δ (2,3 ns pour $\delta_-D_1\delta A$ contre 0,51 ns pour $D_1\delta A$). Cet effet devrait être dû à la plus grande distance de séparation entre les charges de l'état CT dans les molécules où δ- stabiliserait la charge positive sur l'extrémité de la fraction donneuse, i.e. plus loin de l'accepteur. Ces effets sont expliqués par une analyse quantitative de la théorie de Marcus-Jornter au § IV.2.3 dans la thèse.

III. 3.1.2 Effet de la longueur du donneur

D'après la théorie de Marcus, l'allongement de la distance de séparation de charge devrait conduire à une durée de vie plus longue de l'état CT, puisque le couplage électronique A et D est réduit. L'effet de la longueur du donneur est étudié dans le chloroforme et sur différentes molécules $D_n\delta_+A$ et $\delta_-D_n\delta A$ avec n = 0 ~ 3 et n = 0 ~ 2, respectivement. La même procédure d'identification des espèces que dans $D_1\delta A$ est effectuée et indique que les états CT sont formés dans tous les cas. L'analyse globale est appliquée pour déterminer les constantes de temps associées à la recombinaison de l'état CT dans chaque cas, et les résultats sont affichés dans le tableau IV.4.

Dans le cas de $D_n\delta_+A$ (Figure F6 (A) montrant des traces cinétiques à 800 nm, les symboles représentent des données expérimentales, et les courbes solides sont les ajustements paramétriques obtenus par analyse globale), la longueur du donneur n'a pas d'impact sur la formation de l'état CT, ni sur le temps de recombinaison, ce qui donne un temps de formation de 100 ps et un temps de recombinaison de 450 ps. Ce manque de changements pourrait être dû à l'effet de δ_+. Les états CT sont plus situés près de l'A, plutôt que du côté opposé du D.

En revanche, comme l'illustre la figure F6 (B), les molécules $\delta_-D_n\delta A$ se comportent complètement différemment : le groupe terminal δ_- stabilise l'état CT avec une longueur optimale du donneur n = 1 (courbes bleues), avec une augmentation de la durée de vie de l'état CT jusqu'à 2,3 ns. (0,4 ns et 1,1 ns pour n = 0 et n = 2, respectivement, en noir et en rouge). Cela pourrait être attribué également à un éloignement plus important des charges le long de la molécule, ce qui est cependant d'une efficacité optimale pour un fragment de donneur pas trop long.

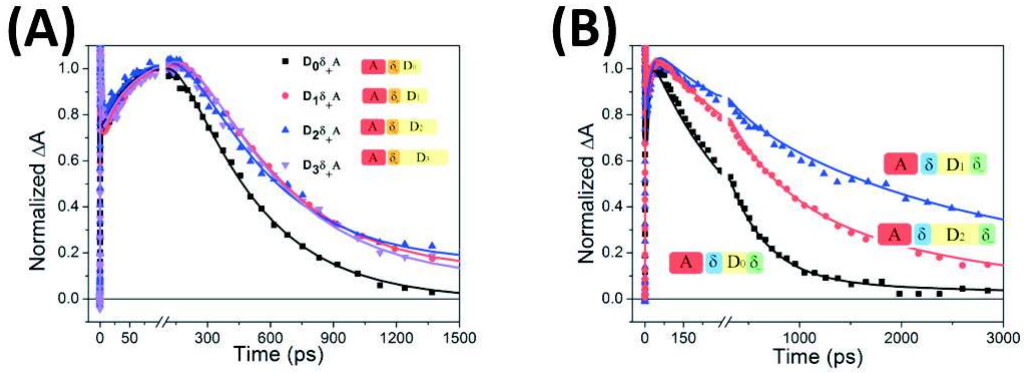

Figure F6. Traces cinétiques à 800nm : Effet de la longueur du donneur pour les molécules (A) Dnδ + A, avec n = 0 (noir), 1 (rouge), 2 (bleu) ou 3 (violet). La longueur du donneur n'a presque aucun effet sur la formation de l'état CT et sur les temps de recombinaison pour les molécules sans molécules δ- (B) δ-Dnδ + A, avec n = 0 (noir), 1 (rouge), 2 (bleu). (B) La durée de vie de l'état de CT est optimale pour n = 1.

III. 3.1.3 Effet du solvant

L'effet du solvant est testé en diminuant la polarité du solvant (chloroforme : 4.81, trichloréthylène : 3.42 et toluène : 2.38) afin d'étudier l'interaction avec l'environnement. En résumé, la durée de vie de l'état CT augmente lorsque la polarité diminue (tableau VI.5 dans la thèse). Une analyse numérique basée sur la théorie Marcus-Jortner explique que l'augmentation de la durée de vie de l'état CT est due à un couplage électronique plus faible.[108]

Pour chaque molécule, les états CT sont stabilisésdans des solvants moins polaires. Cependant, l'effet stabilisant de δ- précédemment observé dans le chloroforme n'est pas aussi important que l'effet de ces solvants. En raison des limitations expérimentales, une détermination précise de la durée de vie de l'état CT > 5 ns n'est pas possible. Cela nécessiterait de mesurer la cinétique sur une période plus longue que celle qui est accessible dans notre expérience d'absorption transitoire femtoseconde (6 ns).

III.3.1.4 Films à cristaux liquides

La figure F7 montre une sélection de spectres d'absorption différentielle (A) de $D_1\delta_+A$ excitée à 400 nm et les traces cinétiques sur la bande de l'ESA et du GSB pour quatre molécules ($D_1\delta A$, $D_1\delta_+A$, $\delta\_D_1\delta A$ et $\delta\_D_1\delta_+A$), après normalisation à 10 ps.

Pour les données d'absorption transitoire :
• Dans les premières picosecondes, une large bande d'ESA supérieure à 700 nm diminue et, pendant ce temps, une bande négative diminue de 450 à 600 nm. La bande spectrale négative du spectre d'absorption différentielle à 500 fs (courbe rouge de la figure F7 (A)) se caractérise par un pic à 470 nm (GSB, courbe pointillée) et un pic secondaire à 540 nm, que nous attribuons à SE. ESA et SE indiquent un état excité, qui est probablement $(D_1\delta_+)^*$, puisque le film est excité à 400 nm.
• De 1 ps jusqu'à 20 ps, le GSB inférieur à 450 nm reste alors que l'ESA au-dessus de 800 nm diminue considérablement et une nouvelle contribution positive compense le GSB entre 470 nm et 550 nm.
• Après 20 ps, un nouvel état, que nous appelons «photo-produit», est entièrement formé, en tant que large bande d'absorption de photo-produit (PA) centrée à 880 nm. La bande GSB autour de 460 nm est toujours présente et le spectre d'absorption différentielle diminue sans modifications spectrales majeures jusqu'à 5 ns.

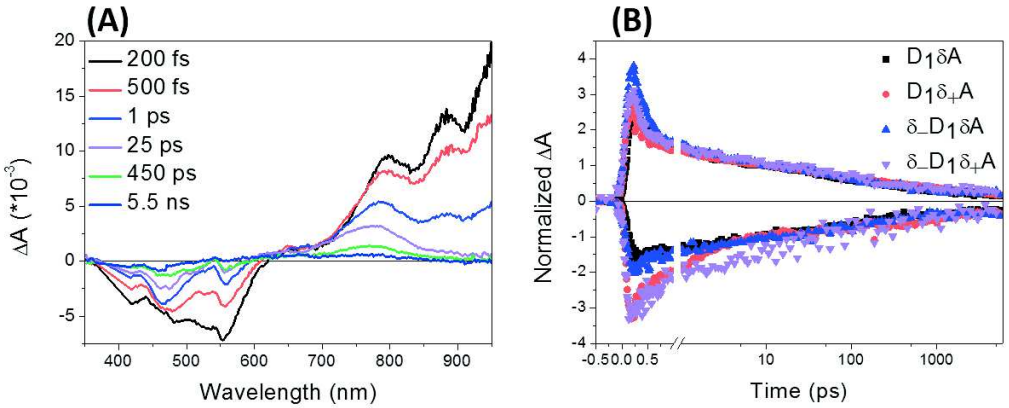

Figure F7. (A) Spectres d'absorption différentielle de D1δ + A excités à 400nm (B) Les traces cinétiques sont représentées aux longueurs d'ondes de PA et GSB, et normalisées à 10ps. Dans les films, les cinétiques des dyades D-A avec quatre groupes donneurs différents sont similaires après 10 ps, ce qui indique un état PA similaire de longue durée de vie et l'effet du donneur sur la recombinaison de charges n'est pas valide.

Parmi ces quatre molécules ($D_1\delta A$, $D_1\delta_+A$, $\delta\_ D_1\delta A$ et $\delta\_ D_1\delta_+A$), les traces cinétiques prises au maximum de la bande de PA (780, 880, 790 et 790 nm pour $D_1\delta A$, $D_1\delta_+A$, $\delta\_ D_1\delta A$ et $\delta\_ D_1\delta_+A$) et à celui de la bande de GSB (460, 560, 460 et 540 nm pour $D_1\delta A$, $D_1\delta_+A$, $\delta\_ D_1\delta A$ et $\delta\_ D_1\delta_+A$), sont représentés sur la Figure F7(b) après normalisation à 10 ps. Après 10 ps, les deux cinétiques sont similaires et montrent ainsi que les molécules retournent à l'état fondamental à partir de l'état PA, sans contribution d'aucun intermédiaire. Notez que, contrairement aux états CT en solution, le groupe donneur n'a presque aucun effet sur la durée de vie des photo produits dans le film avec une durée de vie de 2 ns. Notez aussi que le groupe de Geng a signalé un résultat similaire, de durée de vie constante des états CT.[127]

Les données sont ajustées paramétriquement par la somme de quatre fonctions exponentielleset de façon globale. Les caractéristiques spectrales et les durées de vie sont similaires pour les quatre molécules, indiquant le même mécanisme photo-induit : le premier état excité situé dans $(D_1\delta)$ ou $(D_1\delta_+)$ se relaxe en 0,2 à 0,5 ps dans un état intermédiaire, comme l'indique la bande d'ESA qui diminue rapidement à 800 nm et la bande SE de récupération autour de 450-

650 nm. Deux espèces de longue durée (> 100 ps et 4.4 ns) sont formées montrant une large bande d'absorption centrée à 780 nm (molécules avec $D_1\delta$) ou centrée à 880 nm (molécules avec $D_1\delta_+$). Les différentes durées de vie sont dues à une recombinaison de charge rapide et lente, très probablement liée à deux types de conformères moléculaires ou d'espèces de photo-produits. L'origine de l'espèce évoluant selon le temps intermédiaire, T2, n'est pas encore claire, mais peut être liée à la relaxation vibrationnelle du photo-produit, ou à une population d'état excité de faible amplitude.
Par conséquent, pour les molécules avec δ_+ ($D_1\delta_+A$ et $\delta_-D_1\delta_+A$), le schéma réactionnel est le suivant :

$$(D_1\delta_+)^*A \xrightarrow{T_1} \text{Intermediate state} \xrightarrow{T_2} PP \underset{T_4}{\overset{T_3}{\longrightarrow}} D_1\delta_+A$$

III.2 Complexes de fer pour des cellules de Grätzel

En 1991, Prof. Grätzel a réussi à atteindre un rendement de conversion de puissance jusqu'à 7,9% pour les cellules à colorant (*Dye-sensitized solar cells* en anglais) en utilisant le semi-conducteur (TiO_2) cristallin.[8] Le complexe à base de ruthénium est largement utilisé dans les cellules de Grätzel avec un haut rendement de conversion de puissance. [138] Cependant, le ruthénium est un métal qui est rare sur Terre et cher. L'objectif est donc de remplacer le ruthénium par le fer.

Par rapport à la cellule photovoltaïque organique, les processus photo-induits sont différents après excitation. L'exciton implique le centre métallique (orbital d) et le ligand autour (orbital π^*) et est localisé sur la liaison entre les deux, dites état MLCT (*Metal-to-Ligand Charge Transfer* en anglais). Puis, l'électron est injecté dans la bande de conduction du semi-conducteur et génère ainsi le photo-courant. Dans le cas du ruthénium, le processus d'injection se passe entre 100 fs et 50ps.[79]

C1 (Figure F8), le composé parent développé par le groupe Wärnmark, étend la durée de vie de l'état ^{3}MLCT jusqu'à 9 ps et est choisi comme composé de référence pour illustrer l'évolution spectrale caractéristique de la famille des composés de Fe (II).

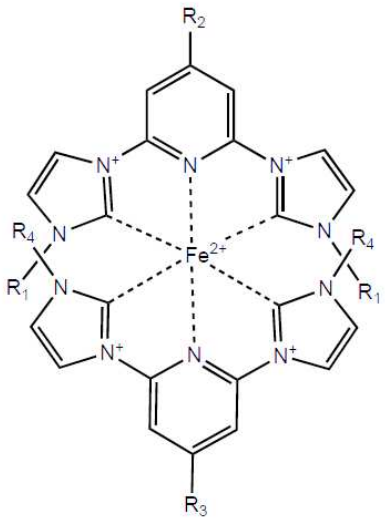

C1: R1=R4=Me, R2=R3=H
C2: R1=R4=Me, R2=R3=COOH

C5: R1=R4=Me, R2=H, R3=COOH
C6: R1=Me, R4=PhOMe, R2=H, R3=COOH
C7: R1=Me, R4=NPh_3, R2=H, R3=COOH

C8: R1= R4=Hex, R2=R3=H

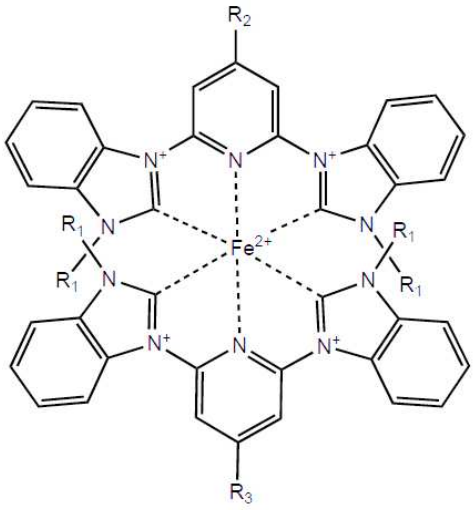

C3: R1=Me, R2=R3=H
C4: R1=Me, R2=R3=COOH

C9: R1=Hex, R2=R3=H

Figure F8 Structures chimiques des complexes de fer

Afin d'augmenter la durée de vie de l'état ^{3}MLCT de C1, plusieurs stratégies ont été étudiées (Figure F8) :

- Ajout d' un groupe d'ancrage : rend possible la fixation des complexes de Fe (II) sur une surface de TiO_2 pour obtenir une injection d'électrons efficace. Cela réduit lécart de bande optique, bloquant le retrait d'électrons.

- Modification du cycle NHC : augmente le caractère donneur d'électrons de NHC pour augmenter le niveau d'énergie de l'état MC.
- Modification de la substitution N : introduit de la rigidité stérique et / ou les distorsions de la géométrie octaédrique.

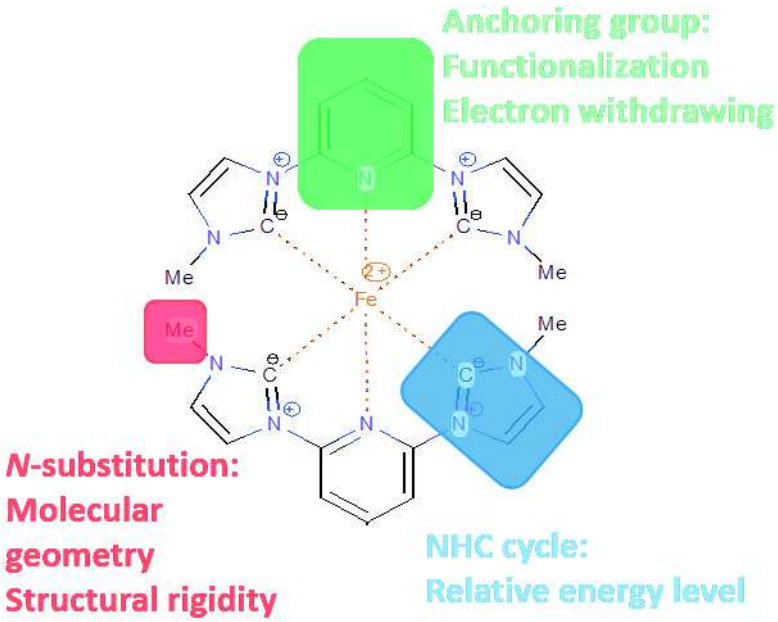

- Figure F9 Stratégies possibles pour prolonger la durée de vie de l'état ^{3}MLCT en ajoutant un groupe d'ancrage et les modifications sur le cycle NHC et la substitution N

À la suite de ces idées, neuf complexes de fer ont été synthétisés par nos collaborateurs chimistes et étudiés en solution (acétonitrile, MeCN) pour examiner :

- L'effet des groupes carboxyle (complexes C1, C2 et C5)
- L'effet des substitutions de ligands (complexes C1, C2, C3 et C4)
- L'effet de la rigidité (complexes C1, C3, C8 et C9).

Pour mieux comprendre les interactions entre les complexes et leur environnement, deux types d'effets du solvant ont été étudiés :

- L'effet du pH (complexe C2 dans MeCN, MeCN + acide chlorhydrique / HCl et MeCN + hydroxyde de sodium / NaOH)
- L'effet de la polarité (complexe C4 dans MeCN, MeCN + HCl, éthanol, diméthylsulfoxyde / DMSO, 2-butanol et diméthylformamide / DMF).

III.3.2.1 Effet d'un groupe carboxyle

Comme décrit précédemment, les complexes doivent être greffés sur la surface de TiO_2 afin d'obtenir une injection efficace d'électrons. Ainsi, C1 a besoin d'au-moins un groupe acide pour atteindre cet objectif. Le groupe carboxyle est un groupe classique d'ancrage, offrant une liaison carboxylique avec les oxygènes du TiO_2. En raison de son caractère attractif pour les électrons, le groupe carboxyle a un effet important sur le niveau d'énergie relatif de l'état ^{1}MLCT : la transition $t_{2g} \rightarrow \pi^*$ (pyridine) a un niveau d'énergie inférieur suggérant un décalage de l'état ^{1}MLCT et probablement de l'état ^{3}MLCT également. Tout d'abord, le complexe homoléptique C2 a été synthétisé et étudié (figure V.11).[154] Les études ATR-FTIR (rayonnement infrarouge de la réflectance totale atténuée) sur le N719- TiO_2 ont montré que le groupe carboxyle se lie au TiO_2 par un pont bidenté. Étant donné que la transition $t_{2g} \rightarrow \pi^*$ a la plus faible énergie pour la pyridine-COOH que pour la pyridine seulement, il était également intéressant d'étudier le complexe hétéoléptique C5 en solution et en film.

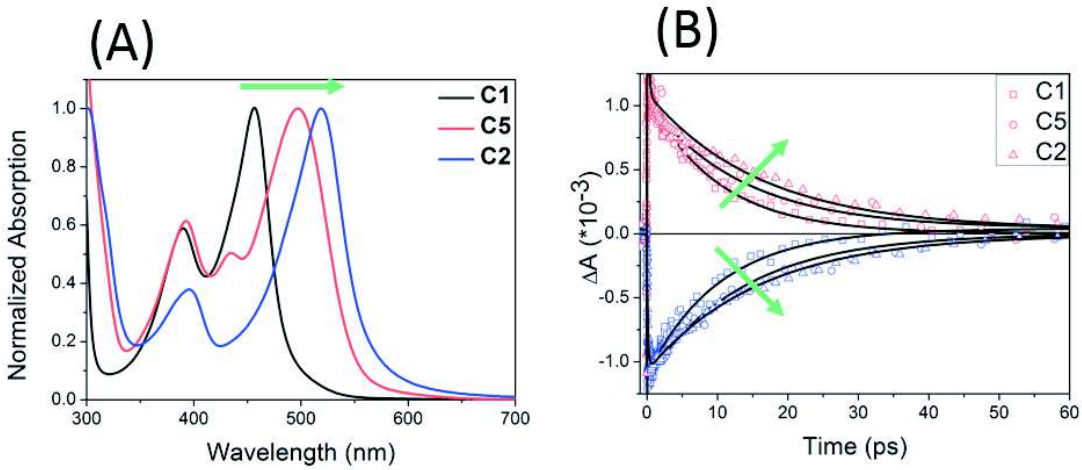

Figure F10 (A) Spectres d'absorption stationnaire normalisés de C1 (courbe noire), C5 (courbe rouge) et C2 (courbe bleue) dans MeCN. L'addition de groupe carboxyle décale les spectres d'absorption versle rouge. (B) Les traces cinétiques dans les bandes d'ESA (rouges) et de GSB (bleus) normalisées à 1 ps de C1 (carrés), C5 (ronds) et C2 (triangles) dans MeCN avec leurs ajustements paramétriques (courbes noires solides).

La figure F10 (A) illustre l'effet de l'addition de groupe carboxyle sur le complexe C1 (C1: zéro groupe carboxyle, courbe noire, C5: un groupe carboxyle, appelé complexe hétéroléptique, courbe rouge et C2: deux groupes carboxyle , appelé complexe homoléptique, courbe bleue). Après l'addition de deux groupes carboxyles des deux côtés de la partie centrale de pyridine (C2), un décalage batochromique de 60 nm de 460 nm à 520 nm (ΔE = 310 mV) se produit sur la transition $t_{2g} \rightarrow \pi^*$ (pyridine). Les groupes carboxyles diminuent le niveau d'énergie LUMO en attirant des électrons plus éloignés du centre métallique. Dans le cas hétéroléptique C5, la transition $t_{2g} \rightarrow \pi^*$ (pyridine) se divise en deux avec un décalage batochromique de 40 nm (de 460 nm à 500 nm) et un changement hypochromique de 25 nm (de 460 nm à 435 nm). Fait intéressant, le décalage hypochromique se traduit également par une diminution de la moitié du pic d'absorption principal (partage de la résonance, partage des forces de l'oscillateur).

La figure F10 (B) montre les traces cinétiques normalisées à 1 ps de C1 (courbes de symboles carrés), C5 (courbes de symboles circulaires) et C2 (courbes de symboles triangulaires supérieurs) prises dans l'ESA (courbes de symbole rouge) et le GSB (Courbes de symboles bleus) des bandes après excitation dans le visible (480 nm pour C1 et 515 nm pour C5 et C2) avec leurs ajustements paramétriques (courbes noires solides). Pour les deux complexes avec un groupe carboxyle, les signaux ESA et GSB affichent la même cinétique, ce qui indique une

récupération directe de l'état fondamental à partir de l'état excité, comme dans C1. En outre, les caractéristiques spectrales (deux grandes bandes ESA dans la région visible et UV) sont très semblables à celles observées en C1, ce qui indique que pour ces deux composés, l'ESA provient également de l'état ^{3}MLCT et retourne directement à l'état fondamental.

Les données ont été ajustées paramétriques par la somme d'une fonction gaussienne et bi-exponentielle par analyse globale (tableau V.1 dans la thèse). Comme le montre la figure F10, les durées de vie de l'état ^{3}MLCT augmentent à mesure que le nombre de groupes carboxyles augmente (10 ps pour C1, 14 ps pour C5 et 16,5 ps pour C2).
Comme C5 est asymétrique, un scénario possible est que deux voies de désactivation coexistent avec des durées de vie légèrement différentes. L'état ^{3}MLCT pourrait être une combinaison de l'état ^{3}MLCT de C1 et de celui de C2. D'autre part, il est également possible que tout le complexe ait un seul état ^{3}MLCT. Malheureusement, ces deux états ^{3}MLCT sont spectralement similaires et, trop proches temporellement pour pouvoir les distinguer. Un ajustement avec une composante mono-exponentielle pour l'état ^{3}MLCT a été effectué et également avec deux composantes. Les ajustements sont de la même qualité, et dans l'erreur expérimentale.

III.3.2.2 Effet du ligand

Afin d'améliorer le transfert d'électrons vers les ligands et l'effet NHC, les groupes benzimidazolylidène ont été introduits, en remplaçant les groupes imidazolylidène sur le cycle pyridine (C3). Pour permettre la coordination sur TiO_2, deux groupes carboxyles ont été ajoutés à C3 pour générer le complexe homoléptique C4.

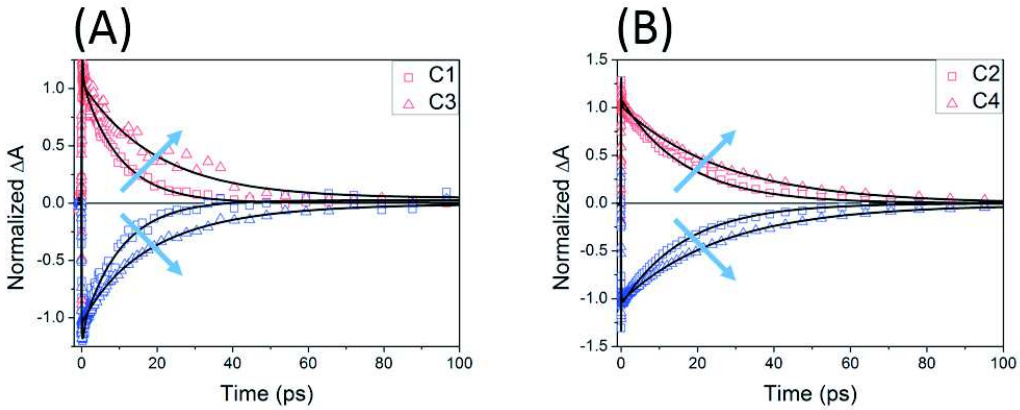

Figure F11 Les traces cinétiques dans l'ESA (rouges) et les bandes GSB (bleues) avec leurs ajustements paramétriques (lignes noires solides), normalisées à 1 ps pour l'effet ligand (A) sans C1 et C3 (B) et avec les groupes carboxyles C2 et C4.

La comparaison des traces cinétiques C1 et C3 montre une augmentation de la durée de vie de l'état ^{3}MLCT, comme le prévoyait une plus grande délocalisation des électrons (Figure F11 (A) et (B)). Les traces cinétiques de l'ESA (courbes de symboles rouges, symboles carrés pour C1 et C2 et courbes de symboles triangulaires pour C3 et C4) et les bandes GSB (courbes de symbole bleu) avec leurs ajustements paramétriques (lignes noires solides) sont normalisées à 1 ps.

En effet, après 1 ps, la relaxation vibrationnelle est terminée et il est donc plus facile de comparer les durées de vie de l'état ^{3}MLCT. Les durées de vie de chaque complexe déterminées par analyse globale sont données dans le tableau V.1. Apparemment, la modification des ligands, avec et sans groupe carboxyle, prolonge significativement la durée de vie de l'état ^{3}MLCT. La durée de vie de l'état ^{3}MLCT de C3 est considérablement augmentée (16,4 ps) par rapport à celle de C1 (10 ps). Le ligand benzimidazolylidène a un effet positif. C4, bénéficiant des groupes acides carboxylique, a la plus longue durée de vie d'état ^{3}MLCT (26 ps).

III.3.2.3 Effet de la substitution sur le ligand

Wärnmark et ses collègues ont suggéré que l'état ^{3}MLCT des complexes avec des ligands plus rigides pourrait durer plus longtemps en comparant C1 Fe(Carben-Met)$_2$ et Fe(Carben-tBu)$_2$.[167] La gêne stérique augmente d'un groupe méthyle à un groupe *tert*butyle, et diminue ainsi l'effet donneur d'électrons des ligands. La liaison ligand-métal est donc agrandie.
Selon ces résultats, nous avons décidé de substituer le groupe méthyle par un groupe hexyle, ce qui est une substitution commune dans les colorants organiques pour augmenter la rigidité des ligands.[173] Cette modification a été effectuée sur deux ligands : C1 et C3 pour devenir C8 et C9, respectivement. Le groupe hexyle présente deux autres avantages : i) protection du centre métallique, ii) et augmentation de la solubilité dans les solvants apolaires.

Puisque deux ligands tridentés sont orthogonaux, les chaînes sur les deux côtés pourraient avoir une influence sur la gêne stérique. Pour identifier cet effet, deux groupes méthyle sur le côté de l'imidazolylidène (C1, courbe noire) et du benzimidazolylidène (C3, courbe rouge) sont

remplacés par deux groupes hexyles en C8 (courbe noire pointillée) et C9 (courbe pointillée rouge). Les spectres d'absorption stationnaires et normalisés sont présentés sur la figure V.17 dans la thèse. Les chaînes allongées n'ont aucune influence sur la transition $t_{2g} \rightarrow \pi^*$ (pyridine), car aucun changement spectral n'est observé. L'origine de l'élargissement du spectre de C9 nécessite des éclaircissements supplémentaires.

Les figures F12 (A) et (B) montrent que l'augmentation de la rigidité de C1 et C3 prolonge la durée de vie de l'état ^{3}MLCT : de 10 à 14 ps et de 16,4 à 19,5 ps dans le cas de l'imidazolylidène (C1 À C8) et les ligands benzimidazolylidène (C3 à C9), respectivement. Selon les PES calculés et les PEC (Figure V.9 dans la thèse), l'étirement de la longueur de liaison Fe-C est nécessaire pour désactiver l'état ^{3}MLCT. En effet, la rigidité du ligand empêche la relaxation et prolonge la durée de vie de l'état ^{3}MLCT. Cette hypothèse reste à être confirmée par des calculs quantiques, qui sont en préparation.

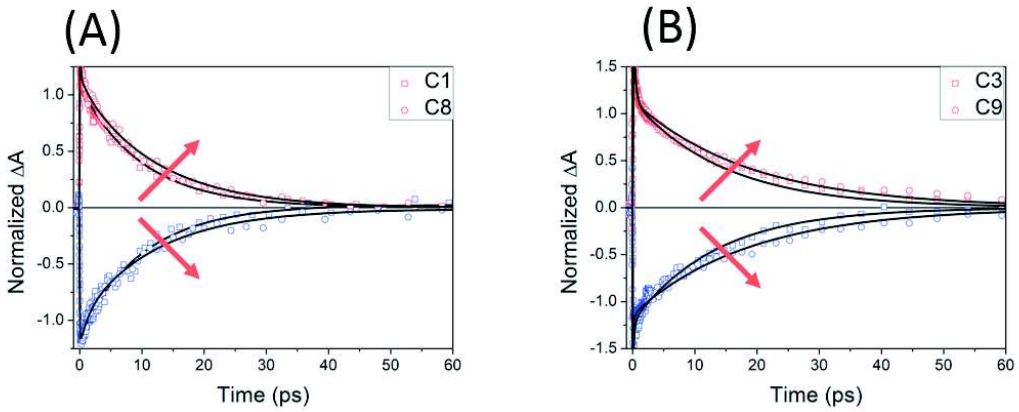

Figure F12 Traces cinétiques dans les bandes ESA (bleu) et GSB (rouge) avec leurs ajustements paramétriques, normalisés à 1 ps pour l'effet de la rigidité basé sur (A) ligand d'imidazolylidène (C1 : Met et C8: Hex) et (B) ligand de benzimidazolylidène (C3 : Met et C9: Hex).

III.3.2.4 Effet de l'environnement

Comme décrit précédemment, l'addition de groupe carboxyle prolonge la durée de vie d'état ^{3}MLCT de C2. Cet effet pourrait être corrélé à une amélioration du caractère de transfert de charge dans les complexes. Pour répondre à cette hypothèse plus clairement, C2 a été étudié à différents pH : neutre (MeCN), acide (MeCN-HCl) et basique (MeCN-NaOH).

Afin de faire varier le pH, le pH de l'acétonitrile pur est ajusté avec une goutte de HCl à 37% ou une goutte de NaOH 2 mol*L^{-1} dans H_2O dans 50 ml de MeCN, appelé MeCN-HCl et MeCN-NaOH, respectivement. C2 est dissous à différents pH : MeCN-HCl (courbe noire), MeCN (courbe rouge) et MeCN-NaOH (courbe bleue). Les spectres d'absorption stationnaires sont représentés sur la figure F13 (A). A pH faible (MeCN-HCl et MeCN), C2 est protoné, l'état MLCT le plus bas étant centré à 520 nm. En solution basique (MeCN-NaOH), C2 est déprotoné et le groupe carboxyle est chargé négativement. La forme déprotonée entraîne un déplacement hypsochromique de 40 nm du spectre d'absorption. Cela indique que les groupes carboxyles négativement chargés augmentent l'énergie des états ^{1}MLCT les plus bas.

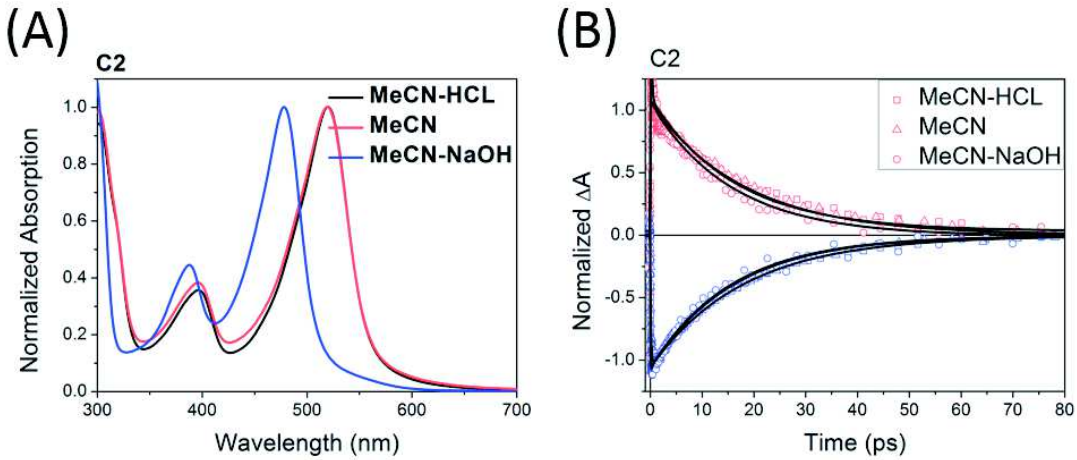

Figure F13 (A) Spectres d'absorption stationnaires normalisés à l'état d'équilibre de C2 dans des solutions de différents pH (complexe C2 dans MeCN pur (courbe noire), MeCN + HCl (courbe rouge) et MeCN + NaOH (courbe bleue)) et (B) Traces cinétiques de C2 dans les bandes ESA (rouge) et GSB (bleu) dans MeCN (carré), MeCN-HCl (cercle) et MeCN-NaOH (triangle) normalisées à 1ps avec leurs ajustements paramétriques (courbes noires).

Les expériences d'absorption transitoire ont été effectuées dans les mêmes conditions, sauf que C2 dans MeCN-NaOH a été excité à 480 nm au lieu de 515 nm pour C2 dans MeCN et MeCN-HCl.
La dynamique de C2 dans des conditions neutres et acides est identique (la durée de vie de l'état ^{3}MLCT est de 16,5 ps) tandis que celle dans des conditions basiques est légèrement plus rapide (14,5 ps). La charge négative des ligands empêche le transfert de charge vers les ligands et donc les états MLCT deviennent plus faibles en énergie. Les études théoriques ont montré que le groupe carboxyle neutre diminue de 10% le couplage électronique, le moment dipolaire représenté sur la figure V.22 qui réduit la durée de vie de l'état ^{3}MLCT.

III.3.2.5 Films sur une couche de semi-conducteur

Les durées de vie de l'état ^{3}MLCT des nouveaux complexes de Fe(II) sont comparables à celles des DSSC de complexes de Ru(II) (plus de 10 ps), mais leurs performances PCE sont encore faibles et ne sont pas significativement améliorées par rapport à celles précédemment rapportés par Gregg et al.[155] Par conséquent, il est essentiel d'aborder la question de l'efficacité d'injection d'électrons à partir de l'état ^{3}MLCT à partir des nouveaux complexes de Fe (II).
Récemment, Wärnmark et ses collègues ont affirmé que C2 a une injection d'électrons proche de l'unité à travers l'état ^{3}MLCT, après avoir étudié C2 par résonance paramagnétique électronique, spectroscopie d'absorption transitoire, spectroscopie terahertz et calcul quantique.[176]
Une telle efficacité d'injection d'électrons semble suspecte, car une fois que C2 est greffé sur une surface nanoporeuse de TiO_2/Al_2O_3, un groupe carboxyle est attaché à la surface et le complexe devient hétéroleptique comme C5. Dans un complexe hétéroleptique, deux états ^{3}MLCT sont attendus avec des niveaux d'énergie similaires : i) la partie inférieure greffée sur TiO_2/Al_2O_3, ii) et la partie supérieure avec un groupe carboxyle libre. Ainsi, lors de l'excitation, la population de l'état ^{1}MLCT est divisée en deux états ^{3}MLCT avec un rapport de près de 50/50%. Ensuite, il semble difficile d'atteindre une efficacité d'injection d'électrons proche de l'unité grâce à l'état ^{3}MLCT.

Pour soutenir notre hypothèse d'une faible efficacité d'injection d'électrons grâce à l'état ^{3}MLCT, des expériences d'absorption transitoire et de fluorescence résolues dans le temps ont été effectuées sur C2, C4, C5 et C7 en film.

Les temps de vie des films Fe (II) -TiO_2 étudiés par spectroscopie d'absorption transitoire et analysés globalement sont résumés dans le tableau V.3 dans la thèse. Tous ces composés présentent des signatures spectrales et des dynamiques similaires. Ces résultats confirment notre hypothèse initiale où les électrons de l'état ^{3}MLCT peuvent prendre deux voies différentes : i) injection sur TiO_2 (τ_2) ii) et relaxation à l'état fondamental (τ_3).

Les complexes hétéroleptiques (C5 et C7) montrent une injection d'électrons plus rapide et la substitution accélère l'injection d'électrons en 1 ps. Dans la structure sandwich, l'environnement a également un effet sur l'injection d'électrons. Ainsi, le pH peut jouer un rôle sur le PCE, et il est nécessaire d'optimiser tous les paramètres de fabrication des DSSC à base de Fe (II) afin d'améliorer leur efficacité.

IV. Conclusions

La compréhension de la formation de porteur libre photo-induite et de la dynamique de recombinaison de charge est essentielle pour améliorer les performances photovoltaïques des cellules solaires. Étant donné que ces processus se produisent à des échelles de temps de la picoseconde à la nanoseconde, les spectroscopies résolues en temps sont des méthodes expérimentales polyvalentes pour accéder à une telle dynamique spectro-temporelle ultra-rapide. Comme le montrent de nombreux groupes et dans de nombreuses publications, l'information spectro-temporelle permet, en principe : 1) d'identifier les espèces photo-induites (états excités, excitons, états CT, polarons, etc.) et comment elles sont liées les unes aux autres par un schéma réactionnel, et 2) déchiffrer les taux de transition ou les durées de vie de ces espèces, ainsi que les rendements quantiques des transitions correspondantes.

Dans ce travail, la spectroscopie d'absorption transitoire femtoseconde a été utilisée avec une région spectrale de 300 à 950 nm, une gamme temporelle allant jusqu'à 6 ns et avec une résolution de temps de moins de 60 fs. Cependant, la superposition temporelle et spectrale des différentes contributions rend difficile l'interprétation des réactions photo-induites. Ainsi, des mesures de fluorescence résolues en temps ont été effectuées pour étudier la dynamique de l'état excité. L'identification des espèces nouvellement formées, telles que l'espèce chargée, nécessite la combinaison de spectroscopies transitoires avec d'autres techniques, telles que la spectro-électrochimie et la spectroscopie THz (non utilisées dans ce travail) pour déterminer leur signature spectrale et caractériser leur dynamique, respectivement.
Cependant, les spectroscopies classiques ont leurs limites : 1) détection spectrale étroite et 2) manque d'informations spatiales. Pour observer et déterminer les espèces impliquées dans les processus photo-induits, la détection spectrale doit être dans la gamme spectrale des espèces produites, par exemple il sera utile d'identifier l'injection d'électrons dans la gamme IR moyen. En outre, la morphologie contribue de manière significative aux études en couche active. La taille typique du faisceau de sonde (100 μm de diamètre) permet seulement une résolution globale moyenne sur plusieurs domaines cristallins. Cependant, la morphologie des films a été sondée par d'autres techniques, telles que TEM et la diffraction d'électrons, l'hétérogénéité des conformations moléculaires, comme discuté pour le système d'oligomères D-A, complique la compréhension de l'ensemble du scénario photo-induit.

L'étude de l'oligomère D-A en solution montre un impact sur les interactions intramoléculaires. Les différents séparateurs (δ ou δ_+) modifient le mécanisme de formation de l'état à transfert de charge (par FRET ou non, respectivement) et sa constante de temps. En outre, la conception chimique sur l'amine terminale (δ_-) prolonge la durée de vie de la recombinaison de l'état à transfert de charge (2 à 3 fois). En réduisant la polarité du solvant, la recombinaison de l'état à transfert de charge diminue jusqu'à un ordre de grandeur, ce qui indique que l'environnement a une influence plus forte.
Dans les films, on observe également que l'environnement a un effet important sur la dynamique des états à transfert de charge. Malgré la modification de la fraction D, les états photo-produits ont une durée de vie de l'ordre de la nanoseconde. Des expériences sont nécessaires pour identifier quel état est formé. L'hypothèse la plus probable est la formation d'une paire de polaron qui est un état non radiatif.

En perspective, le point clé est de déterminer l'état du photoproduit dans les films. Étant donné que le champ électrique externe ne peut affecter que la paire de polaron sans excimère, la spectroscopie de modulation de charge est une autre alternative possible. Elle permettrait d'étudier l'effet d'un biais appliqué sur les OSC et observer les spectres des espèces chargées. Des recherches supplémentaires sur l'information spatiale sont particulièrement intéressantes, en combinant la spectroscopie résolue en temps avec la microscopie, comme la référence 177.

Il est essentiel de mentionner que la meilleure PCE basée sur les OSC (11,5% dans la Figure II.1) est encore beaucoup plus faible que celle basée sur des cellules solaires inorganiques (46%, non montrées). En outre, la durée de vie relative plus faible des OSC limite également ses applications dans des projets à long terme et difficiles à remplacer, comme les panneaux solaires pour les satellites ou les chambres à flotteur en mer. Cependant, en raison de sa fabrication facile sur de grandes surfaces flexibles, faible poids et faible prix, les OSC peuvent encore trouver leur propre part de marché.
Le travail sur les complexes de Fe (II) a permis d'obtenir un complexe ayant la durée de vie de l'état ^{3}MLCT la plus longue à température ambiante en solution, à ce jour. La compréhension de leurs propriétés photophysiques est renforcée par des calculs de chimique quantique. Grâce à l'effet de la structure électronique, l'état ^{3}MC a un niveau d'énergie supérieur à celui de l'état ^{3}MLCT. La substitution N pourrait contribuer davantage à prolonger la durée de vie de l'état ^{3}MLCT de ces complexes.

Bien que la durée de vie de l'état de fonctionnement de 26 ps de l'état ^{3}MLCT soit atteinte en solution, la PCE du dispositif photovoltaïque correspondant[154,175] n'a pas été amélioré significativement par rapport à d'autres complexes classiques de Fe (II).[155] Ainsi, deux possibilités pourraient conduire à cet effet : 1) une mauvaise efficacité d'injection d'électrons à partir des états ^{1,3}MLCT ou / et 2) une recombinaison rapide d'électrons-trous à l'interface. Wärnmark et al. ont proposé que l'efficacité de l'injection d'électrons soit proche de l'unité.[176] Dans notre option, deux ligands (la partie inférieure est greffée sur TiO_2 et la partie supérieure est libre) ont des niveaux électroniques similaires. Une fois que l'état ^{3}MLCT est situé en haut, l'injection d'électrons est interdite en raison de la géométrie, et la relaxation vers l'état fondamental se produit. Par conséquent, l'injection d'électrons est en compétition avec la relaxation vers l'état fondamental. Ainsi, l'estimation de l'efficacité d'injection d'électrons en fonction de la durée de vie est douteuse.

En perspective, des preuves directes sont nécessaires pour prouver notre hypothèse. Outre la spectroscopie de fluorescence résolue en temps et la spectroscopie terahertz, la spectroscopie de rayons X résolue en temps pourrait fournir plus de preuves de l'injection d'électrons et de la recombinaison de charge à l'interface. En tant que photosensibilisateur bon marché, les complexes de Fe (II) avec d'autres modifications, telles que l'ajout de séparateur ou d'unité complexe secondaire, peuvent également être utilisés non seulement pour les DSSC, mais aussi pour d'autres applications, comme la dissociation de l'eau.

I. Introduction

Light is color. Light is energy. It fuels life, and it feeds the spirits. It inspires art, religion, and science. Light holds the secrets of the universe. For thousands of years, human beings have tried to resolve the nature of light and manipulate it.

The most common way to produce energy in nature is photosynthesis by plants. Even though the photosynthesis process depends on the species, the basic principle is still same. The sunlight is absorbed and creates electrons. Through multiple processes, the light energy is converted into chemical energy such as sugars.
Based on this old and efficient idea to produce energy by absorbing the sunlight, chemists could synthetize different types of molecules with versatile properties to enhance the efficiency of the light-to-energy conversion.
In this PhD thesis, finalized at Institut de Physique et Chimie de Matériaux de Strasbourg, we study different types of solar cells (donor-acceptor molecules for organic solar cells in §II.3 and § IV, Iron(II) complexes for dye-sensitized solar cells in §II.4 and §V) and focus on photophysical mechanisms, especially the energy/electron transfer processes by using ultrafast spectroscopies. Our purpose is to understand how the molecular structure of artificial compound and its interaction with environment effect photo induced processes, then the conversion efficiency and to provide our advice to synthetize efficient photo conversion systems throught the photophyscial point of view.

I.1 Solar Light

The light can be considered as black-body radiation which emits a characteristic spectrum at a certain temperature from a body. And the most common thermal light source is the Sun. The Sun emits light in a broad range from ultraviolet (UV) to infrared (IR). The solar spectrum, when measured above the Earth atmosphere can be well approximated by an ideal emission spectrum of a black body at 5900 K.

Due to the Earth atmosphere and its position from the Sun, the standard solar spectrum receives on Earth is called AM 1.5G (global) with an integrated power density 1000 W*m^{-2}. The name stands for sunlight traveled through 1.5 times the path length of the equator air mass (AM). Those spectra are shown in Figure I.1.

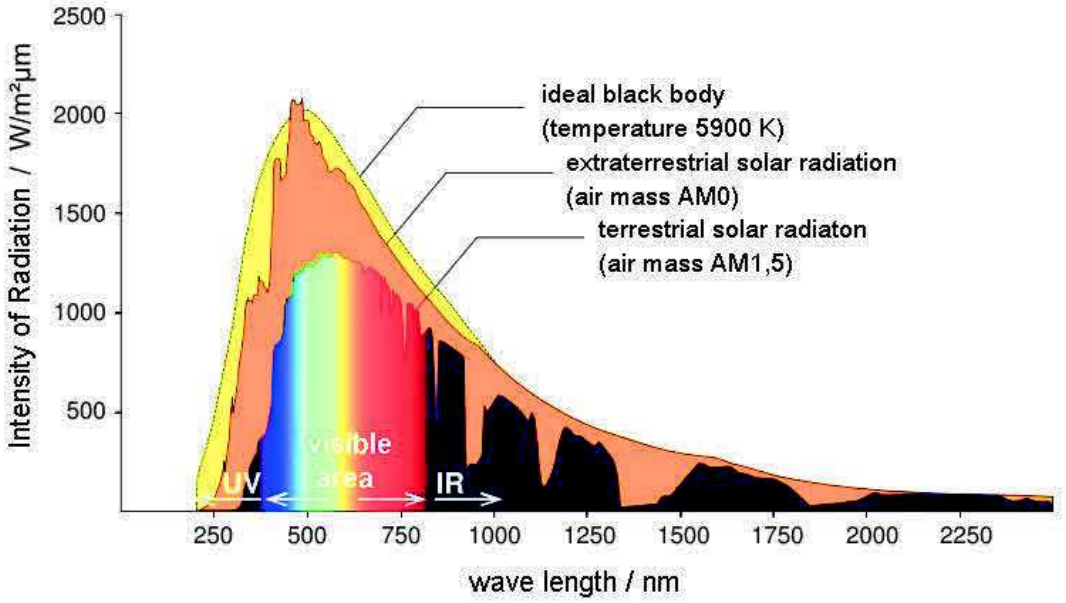

Figure I.1 5900 K ideal black body spectrum (yellow), solar spectrum in space (orange) and AM 1.5G solar spectrum (colored) on Earth.[1] The AM 1.5G solar spectrum is the standard spectrum on the Earth surface, especially taking account of the air sphere absorption.

I.2 Light-Matter Interactions

Light is an electromagnetic wave composed of an electric field and a magnetic field. The interaction between light and matter involves mainly the conversion of the energy at characteristic frequencies. According to quantum mechanics, light can also be considered as an ensemble of particles: Photons, which have a quantified energy according to the Planck-Einstein relation:

$$E = h\nu = \frac{hc}{\lambda} \quad \text{(Eq.I.1)}$$

where h, v and λ are Planck constant, frequency and wavelength in the vacuum, respectively.

I.2.1 Absorption

According to the quantum mechanics point of view, any microscopic object, elementary particles, atoms, molecules have an energy spectrum characterized by discrete energy levels. In molecules, the energy gap between the electronic states is much larger than that between the vibrational states. The former corresponds to the energy of a UV or visible(Vis) photon, and the latter is typical in the energy range of an IR photon.

The presence of discrete energy levels signifies that the absorption only takes places if the photon energy is equal to the energy gap between the initial state (i) and the final state (j):

$$h\nu = E_j - E_i \quad \text{(Eq.I.2)}$$

Absorption occurs only when the electric field of the light is resonant with the transition dipole moment between the initial and final states:

$$\overrightarrow{\mu_{Ji}} = \langle \Psi_j | \hat{\mu} | \Psi_i \rangle = \langle \theta_j | \theta_i \rangle \langle \phi_j | \hat{\mu} | \phi_i \rangle \quad \text{(Eq.I.3)}$$

where Ψ_i and Ψ_j are the wavefunctions of the initial and final states and $\hat{\mu}$ is the transition dipole moment operator. According to the Born-Oppenheimer approximation, the vibrational part of the wavefunction, θ, can be separated from the electronic one, ϕ. $|\overrightarrow{\mu_{Ji}}|^2$ is proportional to the transition probability and $|\langle \theta_j | \theta_i \rangle|^2$ represents the overlap of vibrational wavefunctions of the initial and final states, known as the Franck-Condon factor. The Franck-Condon principle implies that electronic transition takes place vertically in energy diagram without any geometry modification (nuclei are fixed).

The transition dipole moment is related to molar absorption or extinction coefficient ε through the oscillator strength:

$$f = \frac{8\pi^2 m_e \varepsilon_0}{3he^2} |\overrightarrow{\mu_{Ji}}|^2 = \frac{4m_e c \varepsilon_0}{N_A e^2} In10 * \int \varepsilon(\nu) d\nu = 4.319 * 10^{-9} \int \varepsilon(\nu) d\nu \quad \text{(Eq.I.4)}$$

where m_e, ε_0, e and N_A are the mass of an electron, the vacuum permittivity, its charge, and the Avogadro constant.

Experimentally, the absorbance A(λ) of a sample is defined as following:

$$A(\lambda) = -\log\left(\frac{I_0(\lambda)}{I_{trans}(\lambda)}\right) = -\log(T(\lambda)) \quad \text{(Eq.I.5)}$$

where $I_0(\lambda)$ and $I_{trans}(\lambda)$ are the incident and transmitted spectral intensities and $T(\lambda)=I_0/I_{trans}$ is the internal transmittance at a given wavelength λ.

For molecules in solution, the Beer-Lambert law is the relation between molar extinction coefficient and absorbance (assuming isolated, fully solvated molecules):

$$A(\lambda) = \varepsilon cl = l\sum_i \varepsilon_i(\lambda)c_i \quad \text{(Eq.I.6)}$$

where c is the concentration and l is the optical path through the sample. If the sample is a mixture of multiple species, the absorption is the sum of each contribution.

Under low concentration conditions, molecules in solution are considered as isolated, *i.e.* monomeric species, and characterized by the above discussion. Under high concentrations condition or in the solid state, the monomers can interact with each other and form dimers, trimers, or aggregates of N molecules. The electronic resonance coupling in dimers is described by two extreme cases, the so-called H- and J-aggregates.[2,3] Figure I.2 shows these aggregates and their corresponding electronic state levels. In a dimer aggregate with simplified conditions, the energy gap of the ground state and the excited state is reduced due to the higher dielectric constant in the solid state than that in the solution.

As a consequence of excitonic coupling, the S_1 state splits into two excitonic states. The magnitude of this splitting depends on the extent of the transition dipole moment delocalization, thus on the distance between the monomers, and their mutual arrangement.

For the dimer, two identical monomers with their dipole moments ($\overrightarrow{\mu_1}$ and $\overrightarrow{\mu_2}$) aggregate and separate by a distance vector ($\vec{R}$) as shown in Figure I.2, the excited state resonance interaction V is approximated by the electrostatic interaction between dipole moments:

$$V = \left(\frac{1}{4\pi\varepsilon_0 R^3}\right)\left[\overrightarrow{\mu_1} * \overrightarrow{\mu_2} - \frac{3(\overrightarrow{\mu_1}*\vec{R})(\overrightarrow{\mu_2}*\vec{R})}{R^2}\right] \quad \text{(Eq.I.7)}$$

When the transition dipole moments are parallel and "side-by-side" ($\overrightarrow{\mu_1} * \vec{R} = 0$), the dimer forms a H-aggregate, resulting in a positive coupling:

$$V = \left(\frac{1}{4\pi\varepsilon_0 R^3}\right)\overrightarrow{\mu_1} * \overrightarrow{\mu_2} > 0 \quad \text{(Eq.I.8)}$$

Therefore, H-aggregate predicts the transition strength: the high-lying state is allowed, and the low-lying state is forbidden. Thus, the steady-state absorption spectrum shows a blue-shift. According to the Kasha rule, the high-lying state is not emissive due to the fast relaxation to the low-lying state and the low-lying state is forbidden. So, the fluorescence is quenched.[4,5]

When the transition dipole moments are in-line and "head-to-tail" ($\overrightarrow{\mu_1} * \vec{R} = \mu_1 \cdot R$), the dimer forms a J-aggregate, resulting a negative coupling:

$$V = -\left(\frac{1}{4\pi\varepsilon_0 R^3}\right) * 2\overrightarrow{\mu_1} * \overrightarrow{\mu_2} < 0 \quad \text{(Eq.I.9)}$$

Here the situation is reversed: the low-lying state is an active and high-lying state is dark. Thus, the J-aggregate predicts a red spectral shift on the steady-state absorption and fluorescence spectra.

In a more general case, the transition dipole moments are coplanar with a distortion angle θ, the coupling is:

$$V = \left(\frac{1}{4\pi\varepsilon_0 R^3}\right)\overrightarrow{\mu_1} * \overrightarrow{\mu_2} * (1 - cos^2\theta) \quad \text{(Eq.I.10)}$$

In Figure I.2, two cases are highlighted: i) the transition dipole moments are in-line (slip angle θ = 0°, J-aggregate) ii) or side-by-side (θ = 90°, H-aggregate). While for the general case of coplanar monomers, both excitonic states are populated. This trend is represented by sigmoidal curves in Figure I.2.
At the magic angle (θ = 54.7°), both sigmoidal curves have an intersection point, and the two states are equal in energy. Thus, their absorption spectra are not anymore distinguished from those of their monomers.
The transitions from S_0 to S_1 states on the solid sigmoidal curve are strongly allowed (high oscillator strengths), whereas the ones to the energy levels on the dashed line are forbidden (zero oscillator strength). Consequently, the aggregates absorption maxima are shifted to lower energies or to higher energies, respectively.

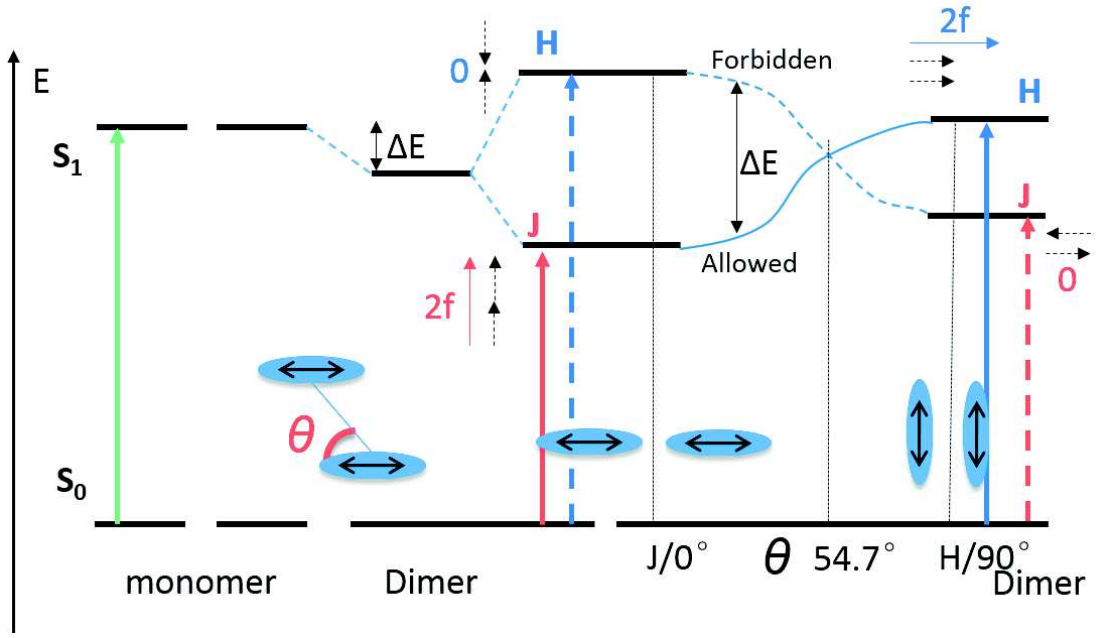

Figure I.2 Schematic Jablonski diagram for the excitonic coupling in a dimer with the collinear orientation of their transition dipole moments. The interconnecting axis is tilted by the slip angle θ, with respect to the dipole axis. Adapted from Ref.6

For H-aggregate, no emission is expected. In practice, some weak emission can be observers low-lying state due to the vibronic excitation from high vibrational levels (0-1, 0-2, etc.) in several H-aggregate case, such as poly(3-hexylthiophene) (P3HT)[7,8] and perylene bisimides.[9,10]

I.2.2 Radiative and Nonradiative Processes

Upon photon absorption, the molecule is in its excited state. Then several photophysical processes lead the molecule back to its lowest electronic state (the ground state S_0). The different relaxation pathways are illustrated in the Jablonski diagram (Figure I.3). These processes are classified in: i) radiative process with the emission of a photon (dotted arrows), ii) or non-radiative process without any photon emission (solid arrows). The states with a spin multiplicity of one and three are noted S_n (singlet) and T_n (triplet), respectively. The number n increases as the energy of electronic states.

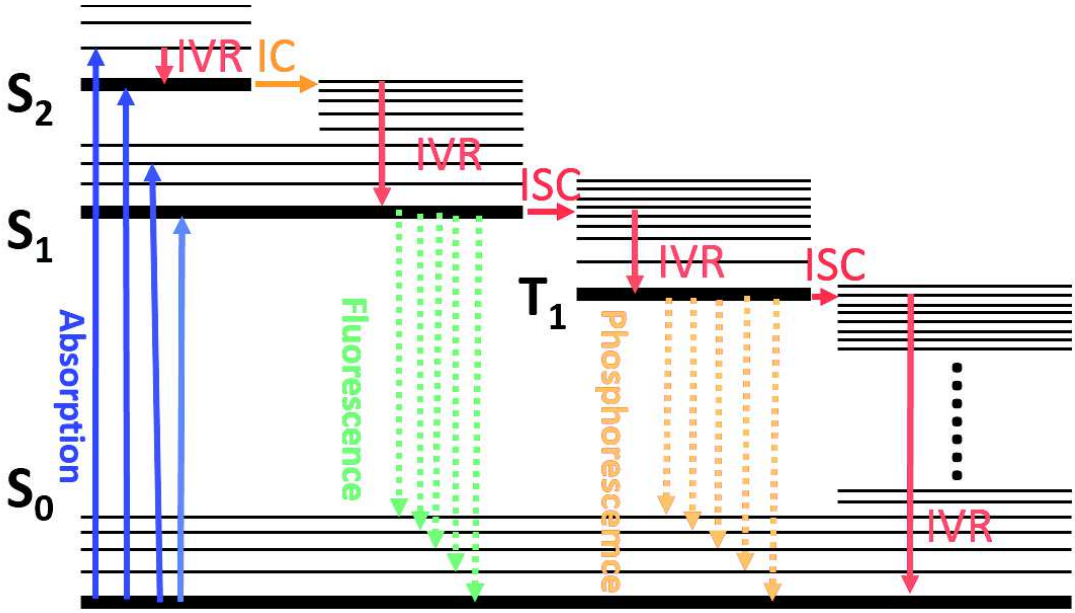

Figure I.3 Jablonski diagram for processes that excited molecules can undergo after excitation to their second singlet excited state S_2. The bold and thin black lines represent the electronic and vibrational levels, respectively. IC: internal conversion, IVR: intramolecular vibrational energy relaxation, ISC: intersystem crossing. Absorption (blue), fluorescence (green) and phosphorescence (yellow) corresponds to the photon absorption from the ground state to some excited state, the photon emission from same spin states and the photon emission from different spin states, respectively.

I.2.2.1 Nonradiative Processes

Internal conversion and intersystem crossing. Internal conversion (IC) and Intersystem crossing (ISC) indicate two different processes of energy relaxation. IC takes place between two states of identical spin whereas the spin changes in ISC. As shown by the horizontal arrows in Figure I.3, the energy is transferred from the fundamental vibrational states of the upper excited electronic state to a high vibrational state of the lower excited state.
In principle, the ISC is a spin-forbidden process in organic molecules due to the weak spin-orbital coupling. Thus, its rate is much smaller than the IC rate. However, if a heavy atom or paramagnetic species exists in the system, an angular orbital momentum is introduced and couples with the change of spin. Thus, the ISC rate can be significantly increased and compete with other processes, known as the El-Sayed's rule.[11, 12]

Intramolecular vibrational energy relaxation. A molecule in a higher vibrational state will relax to the lowest vibrational state. During this process, the energy is redistributed among normal modes of the molecule (Intramolecular vibrational energy redistribution, IVR). This process is also called vibrational cooling (VC) when the energy is dissipated into the

environment. The relaxation rate of those two processes depends on excess energy and they take place from sub-picosecond to several picoseconds.

I.2.2.2 Radiative Processes

Luminescence implies the emission of a photon. It is categorized as fluorescence or phosphorescence depending if the emission occurs between two states with the same spin: $S_1 \rightarrow S_0$, or between two different spin multiplicities: $T_1 \rightarrow S_0$, respectively. Due to weak spin-orbital coupling in organic molecules, the transient from T_1 to S_0 is spin forbidden, phosphorescence is much slower than fluorescence. For molecules containing heavy atoms, phosphorescence is more frequently observed as strong spin-orbital coupling enhances phosphorescence quantum yield. As phosphorescence has a much lower radiative rate, the photoluminescence intensity is smaller than that of fluorescence at the same time and generally, the phosphorescence doesn't contribute to the stimulated emission in transient absorption spectroscopy dataset (more details in § III).

Two basic rules describe the luminescence: Kasha and Vavilov rules. Kasha rule implies that the radiative process takes place only from the lowest excited electronic state of a given spin state, S_1 or T_1.[13] The Vavilov rule is a direct consequence of Kasha rule, as it states that the luminescence quantum yield is independent of the excitation wavelength.[14]

The emission to high vibrational ground state results in an interesting observation; the emission spectrum is typically a mirror image of the absorption spectrum. It happens when the excitation does not change the nuclear geometry (Frank-Condon factors are the same). Then, the vibrational state spacing is similar in S_1 and S_0; a similar vibronic structure can be observed in the absorption and emission spectra of rigid molecules, leading to a mirror-like image.
The energy difference between the band maximum of steady-state absorption in the lowest energy and the maximum of fluorescence in the highest energy is known as the Stokes shift due to solvent effect or vibrational relaxation.[15]

The relaxation of the molecule in the excited electronic state involves a competition between the radiative and non-radiative processes. The overall emission efficiency is defined as the ratio of the radiative rate constant and the sum of all the rate constants, expressed as quantum yield:

$$\phi = \frac{k_r}{k_r + k_{nr}} \quad \text{(Eq.I.11)}$$

where k_r and $k_{nr} = k_{IC} + k_{ISC}$ are the radiative and non-radiative rate constants. The excited-state lifetime is equal to the inverse of the sum of the rates of all relaxation pathways:

$$\tau_{excited-state} = \frac{1}{k_r + k_{nr}} \quad \text{(Eq.I.12)}$$

I.3 Photoinduced Processes

Besides the basic processes described above, several additional notions and mechanisms are necessary to understand the light-to-energy conversion in condensed matter or materials made for such applications.

I.3.1 Excitons and Polarons

Exciton. In the typical semiconductor such as TiO_2, the photoexcitation has an energy exceeding its band gap (the energy difference between the conduction band and the valence band). The excitation results in an electron transfer from the valence band to the conduction band. Thus, an electron forms in the conduction band and a positive charge/hole is in the valence band. This electron is highly attracted by the localized hole through Coulombic interaction. This bound electron-hole pair is a neutral particle also called exciton and formed within femtosecond.[16, 17]
The Coulombic interaction V introduces a stabilizing energy balance. Thus, the exciton has less energy than unbound electron-hole pair. The difference is called the binding energy and is related to the Coulombic interaction by the relation:

$$V = \frac{e^2}{4\pi\varepsilon_0\varepsilon_r r} \quad \text{(Eq.I.13)}$$

where e is the elementary charge, ε_0 the vacuum permittivity, ε_r the dielectric constant and r the distance between electron and hole.

On the one hand, in inorganic semiconductors, the radius of the exciton is 40-100 Å which is one order of magnitude larger than the lattice distance (Wannier-Mott exciton). And the binding energy is lower than 40 meV because the dielectric constant is large. Thus, the Wannier-Mott exciton can separate into free carriers at room temperature. The Figure I.4 illustrates these two different types of exciton.
On the other hand, for organic semiconductors, due to the low dielectric constant ($\varepsilon_r < 3$), the binding energy is more than 300 meV. The radius of the exciton is smaller and typically less than 5 Å (Frenkel exciton). It indicates that the exciton is located on the same lattice and diffuses as the same particle. Thus, Frenkel excitons are stable at room temperature. Besides along the polymer chain or in the crystal, the exciton can be transferred by energy transfer, such as Förster resonance energy transfer.

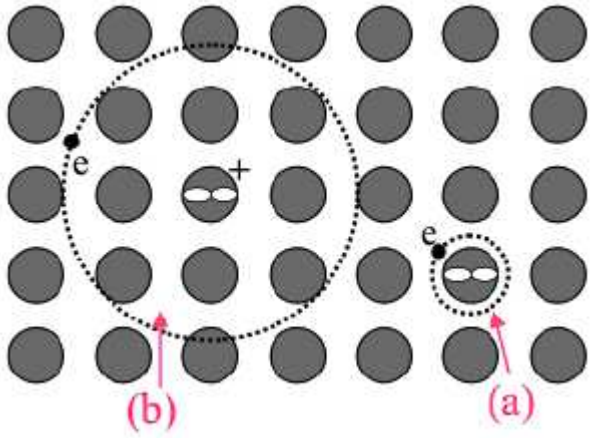

Figure I.4 Different types of the exciton. (a) Frenkel exciton with small radius < 5 Å, typically in organic materials and (b) Wannier-Mott exciton with large radius 40-100 Å, typically in inorganic materials. From ref. [18]

Polarons and charge-transfer states. In an inorganic semiconductor, at room temperature, free carriers are generated from thermally activated or dissociated Wannier-Mott excitons. In organic materials, the separated charges are more localized due to the poor screening of the electric field, and the electron-hole pair is still weakly bound by Coulombic interaction. When a transition dipole to the molecular ground state is still observed, the state is a charge-transfer state. If the charged species can diffuse in the lattice, they are named polarons. Once the electron-hole escape the Coulombic capture radius, they form free carriers or called as charge separated state.

I.3.2 Förster Resonance Energy Transfer (FRET)

A molecule can transfer its excitation energy to another molecule via coupling of the respective transition dipoles. The energy transfer takes place from the excited state of the donor (D) to the ground state of the acceptor (A).

$$D^* + A \rightarrow D + A^*$$

The energy transfer process is non-radiative and can take place between two separate moieties, linked donor and acceptor or along stacking chromophores.

For the Förster theory, the energy transfer happens at a shorter distance (much shorter than the visible light wavelength) by Coulomb interaction without the prerequisite of the donor and acceptor molecular orbitals overlapping (Dexter type energy transfer).
Due to dipole-dipole interaction, the coupling strength between donor and acceptor is expressed by the energy:

$$V = \frac{{f_L}^2}{4\pi\varepsilon_0 n^2}\frac{|\overrightarrow{\mu_D}||\overrightarrow{\mu_A}|}{{r_{DA}}^3}\kappa \quad \text{(Eq.I.14)}$$

where $f_L=(n^2+2)/3$ is the Lorentz correction factor, accounting for the refractive index n of the dipole's environment, $\overrightarrow{\mu_D}$ and $\overrightarrow{\mu_A}$ are the transition dipole moments for $D^* \rightarrow D$ and $A \rightarrow A^*$, r_{DA} is the distance between donor and acceptor and, κ depends on two dipoles orientation. If the relative orientation of the dipoles is random the average of κ is $\sqrt{2/3}$.

The energy transfer rate constant depends on the overlap of the donor fluorescence spectrum and the acceptor absorption spectrum:

$$k_{ET} \sim \frac{4\pi^2}{h}|V|^2 \sim \frac{1}{\tau_D}\left(\frac{R_0}{r_{DA}}\right)^6 \quad \text{(Eq.I.15)}$$

where τ_D is the fluorescence lifetime of the donor without the acceptor and R_0 is the Förster radius. The Förster radius can be determined by:

$${R_0}^6 = \frac{9000 * In(10)\kappa^2\phi_{f,D}}{128\pi^5 N_A n^4}J(\lambda) \quad \text{(Eq.I.16)}$$

$$J(\lambda) = \frac{\int_0^\infty F_D(\lambda)\varepsilon_A(\lambda)\lambda^4 d\lambda}{\int_0^\infty F_D(\lambda)d\lambda} \quad \text{(Eq.I.17)}$$

where $\phi_{f,D}$ is the quantum yield of the donor, N_A is the Avogadro constant, J(λ) is the overlapped integral, $F_D(\lambda)$ is the donor fluorescence spectrum, and $\varepsilon_A(\lambda)$ is the molar absorption coefficient. The typical R_0 is from 30 to 60 Å, which is similar to the biological macromolecules sizes.

As the rate constant of FRET highly depends on the distance between donor and acceptor, FRET also has been widely used to measure the distance and detect molecular interaction in biology. Thus, FRET has been used as a spectroscopic ruler for distance measurement between two molecules/moieties of the molecule.[15]

I.3.3 Marcus Theory

Besides the intrinsic relaxation pathways IVR, IC and ISC and energy transfer, electron transfer is also a common photochemical reaction. The electron can be transferred from the excited state of a donor to the ground state of an acceptor molecule or the hole from the ground state of an excited acceptor to the ground state of a donor in order to form the following charged species:

$$D^* + A \rightarrow D^+ + A^-$$
$$D + A^* \rightarrow D^+ + A^-$$

The electron transfer can occur when the energy of the product state is lower than the one of the reactant states. Then the free energy of this reaction is given by the Rehm-Weller equation: [15,19]

$$\Delta E^0 = e[E_{ox}(D) - E_{red}(A)] - E_{00} \quad \text{(Eq.I.18)}$$

where E_{ox}(D) and E_{red}(A) are the oxidation and reduction potential energies of the donor and acceptor, respectively, and E_{00} is the energy gap of the reactant.

The electron transfer process has been successfully explained by Marcus theory, based on the transition state theory.[20] In the classical Marcus theory, the reactant and the product are described as free energy surfaces with two identical parabolas. The barrier that the reactant has to overcome is represented by the activation energy:

$$\Delta G^+ = \frac{(\Delta G^0 + \lambda)^2}{\lambda} \quad \text{(Eq.I.19)}$$

where ΔG^0 is the free Gibbs energy, and λ is the reorganization energy, accounting for the intramolecular reorganization energy (λ_i, structural changes in the reactant) and solvent reorganization energy (λ_{sol}, rearrangement of the solvent). By the Born-Hush approach, the latter is expressed as:

$$\lambda_{sol} = \frac{e^2}{4\pi\varepsilon_0}\left(\frac{1}{2r^+} + \frac{1}{2r^-} - \frac{1}{R_{cc}}\right)\left(\frac{1}{n^2} - \frac{1}{\varepsilon}\right) \quad \text{(Eq.I.20)}$$

where n and ε are the refractive indexes and dielectric constant of the solvent. r^+ and r^- are as the radii of hole and electron densities, and R_{cc} is the electron-hole centroid distance.

The rate constant of electron transfer is derived as:

$$k = \frac{4\pi^2}{h}|V|^2 \frac{1}{\sqrt{4\pi\lambda k_B T}} \exp\left[-\frac{(\Delta G^0 + \lambda)^2}{4\lambda k_B T}\right] \quad \text{(Eq.I.21)}$$

where V refers to the electronic coupling between the reactant and product states and depends on the overlap of their electronic wavefunctions, k_B is the Boltzmann constant and T is the temperature.
Strong coupling denotes the adiabatic limit when the two potential energy surfaces effectively split into two and the electron transfer proceeds along the lower potential energy surface as shown in Figure I.5. However once the coupling is small relative to k_BT, the electron transfer occurs non-adiabatically. [21]

The equation indicates that the electron transfer rate constant at first increases as ΔG^0, until reaching a maximum, then decreases. The plot of $\ln(k_{ET})$ as the function of ΔG^0 exhibits the famous bell shape in Figure I.5. Three regions are discerned:

1. Normal region: $-\Delta G^0 < \lambda$
2. Optimal region: $-\Delta G^0 \approx \lambda$
3. Inverted region: $-\Delta G^0 > \lambda$

In the normal region, the rate constant increases with ΔG^0 and the opposite behavior is predicted in the inverted region. The solid curve in the bottom panel in Figure I.5 shows the expected behavior.

A semi-quantum mechanical model introduced by Jortner[22] takes into account the vibrational modes. The coupling between the vibrational modes of the reactants and the products shows new pathways that increase the ET rate constant in the inverted region as shown by the dotted curve in the bottom panel in Figure I.5. [23, 24, 25]

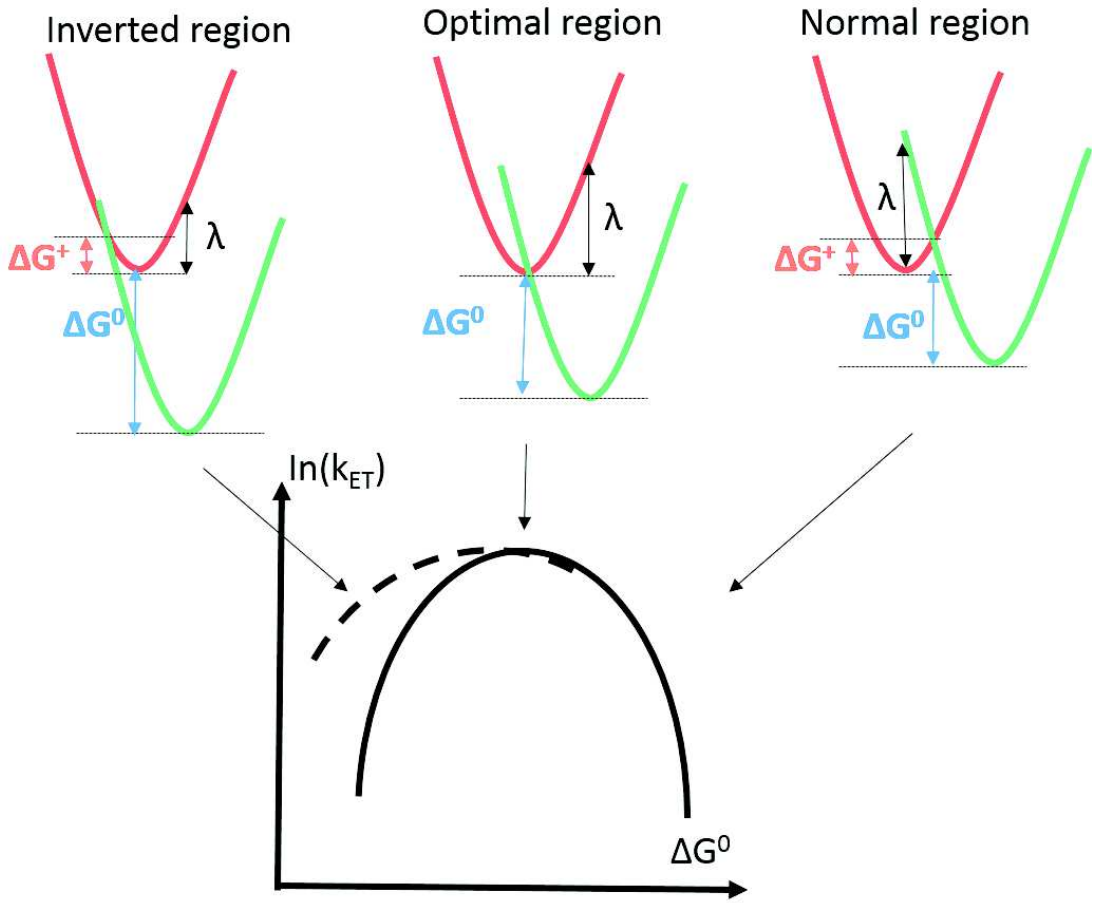

Figure I.5 Position of two free energy surfaces according to the three regions of the Marcus theory (top panel) and the corresponding electron transfer rate constant as the function of free Gibbs energy (solid curve in the bottom panel) with the semi-quantum Jortner modified model (dotted curve in the bottom panel)

II. Photovoltaic Processes in Solar Cells

II.1 The Photovoltaic effect

Due to the global economic development and increasing living standards, the needs for energy have experienced rapid growth during the past few decades. It can be foreseen that the world's electricity consumption will rise by 50% until 2050. Our daily lives are supported by fossil fuels such as oil, natural gas, and coal. However, they bring two main problems, the limited availability of fossil energy sources, especially oil and climate problems, such as global warming. Therefore, scientists have a great interest in the development of renewable energies such as green biological energy resources, geothermal power, and solar energy.

As a member of the solar system, the earth gets about $6.3*10^{16}$ W solar energy each year, which is a thousand times more than the total energy required for the whole world ($1.5*10^{13}$ W in 2009). Besides the natural photosynthesis, the solar energy can generate thermal energy by heating high thermal materials, such as a cooker or a water heater or split water into hydrogen and oxygen and store them away or be directly converted into electrical energy. Compared with other renewable resources, the solar cells can be used anywhere without geographic limitation.

The light-to-electricity conversion, due to the so-called photovoltaic effect, was firstly observed by Alexandre-Edmond Becquerel in 1839 and was explained by Albert Einstein in 1905, which brought the latter a Nobel Prize. Even though the photovoltaic effect was observed in semiconductors (Se and Pt) since 1877, photovoltaics were not well investigated until silicon has been taken into account in the 1940s by Gerald Pearson. Later the power conversion efficiency of the silicon solar cells has been improved to 6% by Darryl Chapin and Calvin Fuller.[3]

Since then, multiple technologies have been developed in order to improve the power conversion efficiency, including the modification of device structure (bilayer, bulk heterojunction, multi-junction), the development of new semiconductor material families (GaAs, III-V groups, CIGS: Copper Indium Gallium Selenide) and new concepts (organic solar cells, dye-sensitized solar cells and perovskite solar cells). Figure II.1 displays different types of solar cells invention and their record power conversion efficiency in last 20 years.

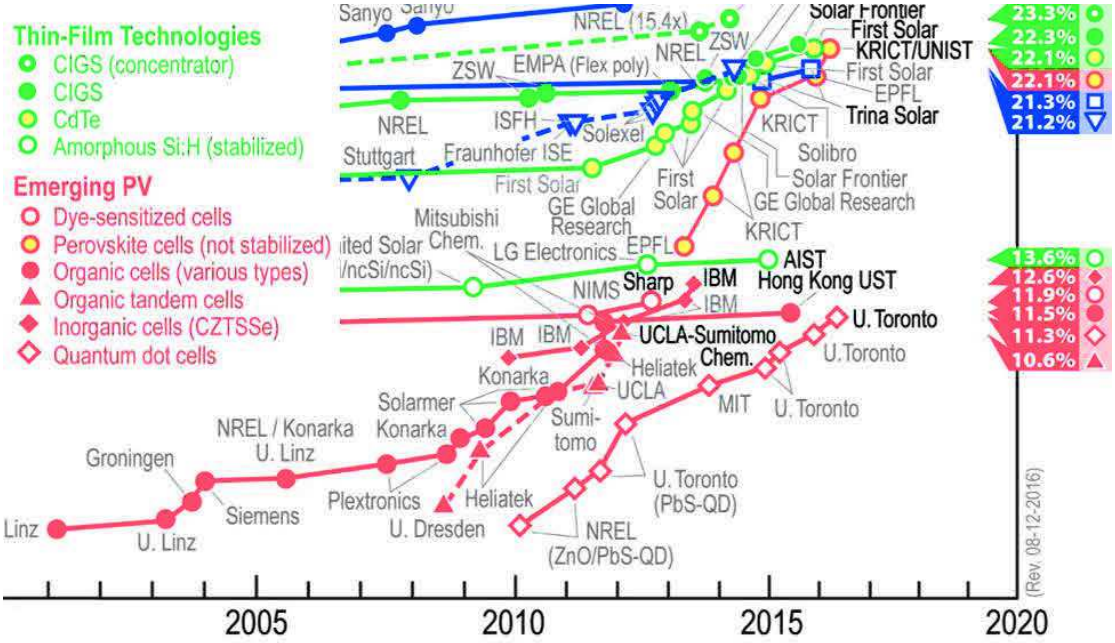

Figure II.1 Record power conversion efficiencies achieved with different types of solar cells in the lab scale. [26] Blue square: multi-crystalline Si solar cells and blue triangle: thin film crystal Si solar cells. For organic solar cells (solid circle curve) and dye-sensitized solar cells (circle curve), the PCE is still below 12 % which is much smaller than Si solar cells (around 21 %).

In order to fully understand the solar cells and interactions between different components, it's essential to study complete solar cells and separate components. Therefore, several techniques are developed to analyze the solar cells. The principal goals are to: 1) measure the internal device working properties on complete solar cells under solar light conditions to characterize the PCE, 2) study different energy and/or charge transfer process and 3) optimize new materials.

The key characterization of complete solar cells is the power conversion efficiency η, determined by the current-voltage (I-V) measurement. For the efficiency measurement, the white light from a solar simulator is used as the light source. And the AM 1.5G spectrum is taken as the standard irradiative spectrum, as shown in Figure I.1.
An ideal I-V curve is illustrated in Figure II.2.[27] The short circuit current Jsc is determined at V = 0 V and the open-circuit voltage V_{oc} is found at I = 0 A. As shown in the top panel of Figure II.2, the maximum output P_{max} is obtained when working at a bias V_{max} such that product $|I_{max} * V_{max}|$ is maximum.

The power conversion efficiency is given by:

$$\eta = \frac{J_{max} * V_{max}}{P_{in}} = FF * \frac{J_{sc} * V_{oc}}{P_{in}} \quad \text{(Eq. II.1)}$$

where P_{in} is the incident power density, J_{sc} is the short-circuit current density, V_{oc} is the open-circuit voltage, and FF denotes the fill factor.

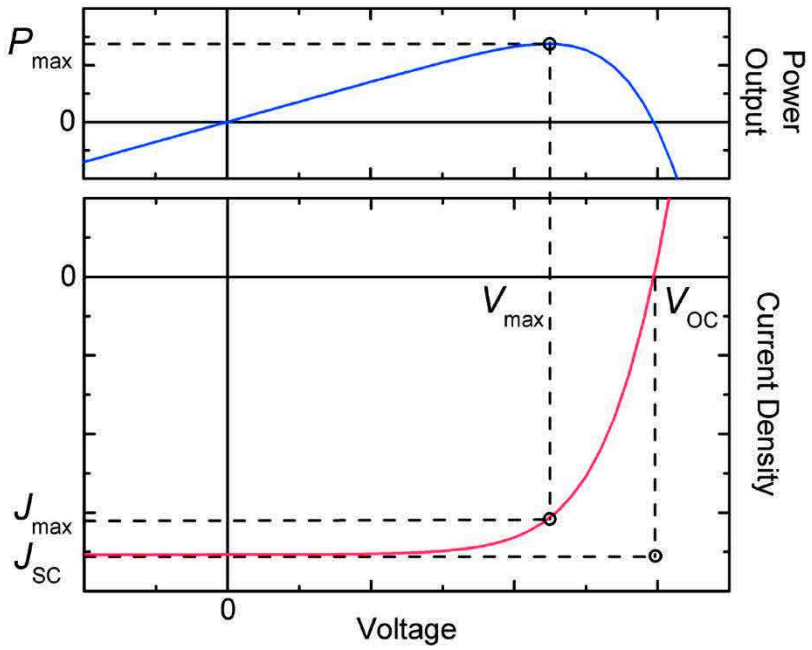

Figure. II.2 Bottom panel: Illustration of the current-voltage characteristic of a solar cell. Top panel: cell output power (blue line) as a function of voltage. Jsc: Short-circuit current. Voc: Open-circuit voltage. Pmax: Maximum power. Jmax: Maximum current. Vmax: Maximum voltage.[27]

Short-circuit Current. The short-circuit current is the photocurrent through the solar cell when the voltage applied on the device is zero. The photocurrent results from the generation and collection of free carriers upon light absorption. Alternatively, J_{sc} can be evaluated by measuring the monochromatic incident photon-to-current conversion efficiency (IPCE), in which a careful spectral mismatch correction between the molar absorption and solar spectrum can be taken account as the ideal AM 1.5G spectrum is not regular in this measurement. J_{sc} is given by

$$J_{sc} = \int IPCE(\lambda) * e * \phi_{AM\ 1.5G}(\lambda) d\lambda \quad \text{(Eq.II.2)}$$

where e is the elementary charge, and $\phi_{AM\ 1.5G}$ is the flux of AM 1.5G.

J_{sc} is shown to be determined by a series of parameters, including absorption coefficient, optical band gap, exciton binding energy, exciton dissociation rate, free carriers mobilities, and recombination rate. As compared to inorganic semiconductors and hybrid perovskites, the photovoltaic performance of organic semiconductors are significantly limited by the large exciton binding energy, small carrier mobility (in silicon $\mu_e \approx 1000$ cm^2/(Vs) and in organic solar cells, $\mu_e \leq 1$ cm^2/(Vs)) and fast recombination rate. Most importantly, the charge-transfer state, as a unique feature for OSCs, monitoring charge transfer state formation and recombination both in kinetics and quantum yield is important, as this state is involved in the most of energy loss mechanisms (exciton dissociation, charge transfer dissociation into free carriers).

Open-circuit Voltage. The open-circuit voltage corresponds to the forward bias on the solar cell at zero current flow. Theoretically, V_{oc} is given by

$$V_{OC} = \frac{nk_BT}{q} In(\frac{I_{Ph}}{I_0} + 1) \quad \text{(Eq. II.3)}$$

where n is the ideality factor, k_B is the Boltzmann constant, T is the temperature, q is the elementary charge, I_{Ph} is the photocurrent or the short-circuit current and I_0 is the dark saturation current.

Typically, the I_{ph}/I_0 term has a small variation while the saturation current could change by

orders of magnitude. According to Eq. II.3, the most critical parameter is the saturation current I_0, reflecting the density of defects or trap states in the materials systems.
The maximal V_{oc} is determined by many parameters. For OSCs, the maximal V_{oc} is the energy difference between the Highest Occupied Molecular Orbital (HOMO) of the acceptor to Lowest Unoccupied Molecular Orbital (LUMO) of the donor. More details are given in § II.4

Fill-Factor. The fill-factor represents the ratio of the maximum output power from the product of Jsc and Voc. In the figure, the fill-factor is the largest rectangle on the I-V curve. In general, a significant serial resistance and a small parallel resistance tend to reduce the fill-factor.

Besides the I-V characterization, the steady-state and time-resolved spectroscopies are useful tools to analyze the solar cells and their components, especially to achieve the last two goals: to study different energy and/or charge transfer process and to optimize new materials.
In this work, we combined the means of spectroscopy measurements to investigate energy/charge transfer processes and to aim at designing new molecular materials in two types of solar cells.

II.2 Photovoltaic semiconductors

In the commercial photovoltaic market, doped silicon is still the most used material. The solar cells based on silicon works as a p-n junction. The principle of the p-n junction can be found easily in many handbooks of solid state physics. As mentioned in the §. I.3.1, Wannier-Mott excitons are generated with large radii typically in inorganic semiconductors or in the newly emerging organic-inorganic hybrid perovskites. Thus, the binding energy due to the Coulomb potential energy is easy to overcome and exciton dissociates at room temperature.[28]
Besides home-based applications, the aircraft Solar Impulse 2 finished a few months ago its first world round trip without any fuels. The silicon solar cells were mounted on the wings, fuselage and horizontal tail plane. Energy gained from the solar cells is stored in lithium polymer batteries to allow the aircraft to fly during nights.
However, the cost of generating power by using silicon solar cell is much more expensive than that of commercial power generation. Since pure silicon is manufactured by high temperature and vacuum processes and has a large number of associated parts, the pay-back time is still very long (typically 1-2 years). Furthermore, since the silicon modules are massive, dissemination to homes has a limitation because of the high installation costs and legal requirements for installation.

Since the 1990s, new technologies have been developed to obtain low-cost and high efficient solar cells, such as dye-sensitized solar cells (DSSCs in § II.4 and § V), organic solar cells (OSCs in § II.3 and § IV) and more recently perovskite solar cells. The first two types of solar cells will be discussed in details in the following sections.
Organic-inorganic hybrid perovskites have demonstrated incredibly promising photovoltaic performance (PCE ~ 20%) after less than five years development[29] due to the broad light harvesting property (visible to near infrared), ultrafast charge dissociation (~1 ps), long charge carrier lifetimes (~1 μs), and excellent charge mobilities (10-100. $cm^2/(Vs)$). With the flexibility of materials design by modifications of organic cation or halide anion, hybrid methyl halogen perovskites can exhibit high photoluminescence quantum efficiency and tunable optical bandgap. However, the understanding of the fundamental photophysics is still in progress, and photo-degradation severely limits today the operation lifetime of the corresponding solar cells.

II.3 The photovoltaic effect in organic solar cell materials

II.3.1 Principle of OSCs

The working principle of OSCs is composed of four steps: 1.light absorption and exciton generation within the active layer, 2.exciton diffusion towards D/A interfaces, 3.exciton dissociation at D/A interfaces and 4.charge collection at electrode interfaces. A simplified scheme of the photo-induced processes and their relative energy level diagram[30] is shown in Figure II.3 neglecting recombination processes.

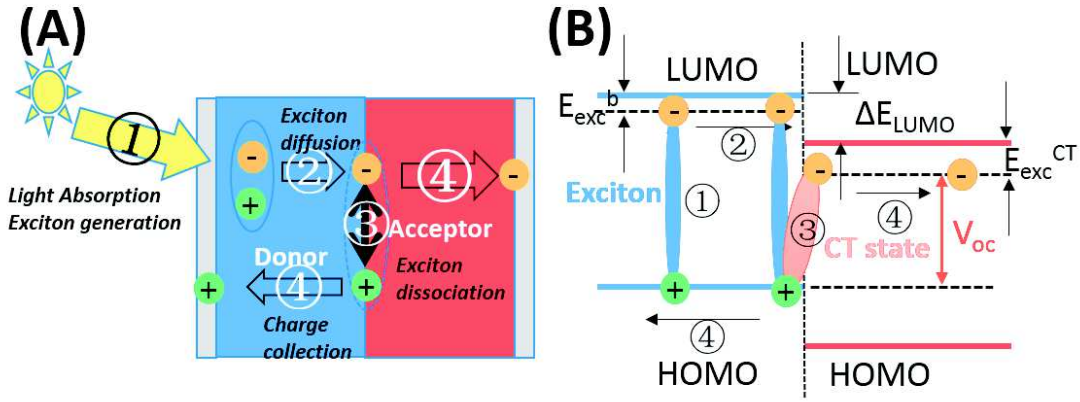

Figure II.3 (A) Simplified photo-induced process in OSCs with its four essential steps: 1) Light absorption and exciton generation 2) exciton diffusion 3) exciton dissociation and 4) charge collection and (B) Energy level diagram of the donor-acceptor interface showing the principle steps. The maximal Voc is determined by the energy gap between LUMO(A) and HOMO(D).[30]

Light absorption and exciton generation. Photovoltaic conversion first requires the absorption of photons emitted by the sun. The absorption of incident waves causes excitation in the transition of an electron from HOMO to LUMO. In close-packed molecules, HOMO and LUMO may extend over several molecules (H-/J- aggregate).
After the absorption, the electron-hole pair localizes and binds, forming a Frenkel exciton. The characteristic absorption strength is dependent on its molecular extinction coefficient in the range of incident wavelengths. Once in the excited state, the molecule would decay radiatively (fluorescence or phosphorescence) or non-radiatively (vibration on rotation of molecules).
In OSCs, the origin of the photovoltaic effect requires the dissociation of the exciton, rather than free charges. Exciton (Frenkel type) is the localized electronic excited state because of strong electron-hole coupling (electrostatic interaction) induced by structural deformation (electron-lattice interactions) and low dielectric constants (ε_r=3 ~ 4) with a typical high binding energy about 300 meV, which is much larger than thermal energy (26 meV in room temperature). So the electron-hole pair can't break up spontaneously. The Frenkel exciton needs a potential energy sink that separates the electron from the hole, which occurs at the interface between the two components, the donor and acceptor, as shown in Figure II.3.B.

Exciton diffusion. The photogenerated excitons can diffuse through the material, carrying the excitation energy towards the break sites which provide sufficient energy offset for exciton dissociation. Particularly, exciton diffusion can happen through either intra-chain diffusion or inter-chain diffusion. Essentially, exciton diffusion can be described as an incoherent energy transfer process, such as the FRET in § I.3.2. The energy transfer process will lower the energy and could be intramolecular or intermolecular. Meanwhile, once the initially generated exciton

in the Franck-Condon state as the 'hot' exciton, the exciton diffusion could also occur as well as the "cold" action after the intramolecular vibrational relaxation.

Exciton dissociation and charge separation. Exciton dissociation is one of the key issues for improving the photovoltaic performance, particularly for OSCs. At the D/A interface, an energy offset (ΔE_{LUMO} in Figure II.3 (B)) is created due to the difference in the potential energies between donor and acceptor. Once an exciton reaches the D/A interface, it can be dissociated into an electron into the acceptor's LUMO and a hole in the donor's HOMO, forming charge transfer (CT) states. Essentially, exciton dissociation requires that exciton's energy is greater than the energy of A's LUMO level minus the charge transfer state binding energy.
CT states can be viewed as weakly bound electron-hole pairs at the D/A interface. Marcus theory[31] has successfully explained this electron transfer process in amounts of chemical reaction as mentioned in § I.3.3. The CT state population is a precursor to a formation of free carriers, because charge transfer state dissociation leads to unbound charge separation state. Their dynamic evolution is of importance to escape Coulombic attraction. The longer lifetime of CT states brings more possibilities to generate free carriers.

Onsager proposed a quantitative model to explain the charge separation process.[32] For a located and weakly bound electron-hole pair/CT state by Coulomb interaction, the mobile electron needs a far enough distance to escape the potential energy generated by the located hole and to create free carriers through Brownian random motion. Onsager defines a Coulomb capture radius r_c where the Coulomb interaction is equal to the thermal energy k_BT:

$$r_c = \frac{e^2}{4\pi\varepsilon_r\varepsilon_0 k_B T} \quad \text{(Eq. II.4)}$$

where e is the electron charge, ε_r is the local dielectric constant, ε_0 is the permittivity of vacuum, k_B is Boltzmann constant and T is temperature. Later, Braun proposed a more accurate model by including the CT state lifetime.[33]

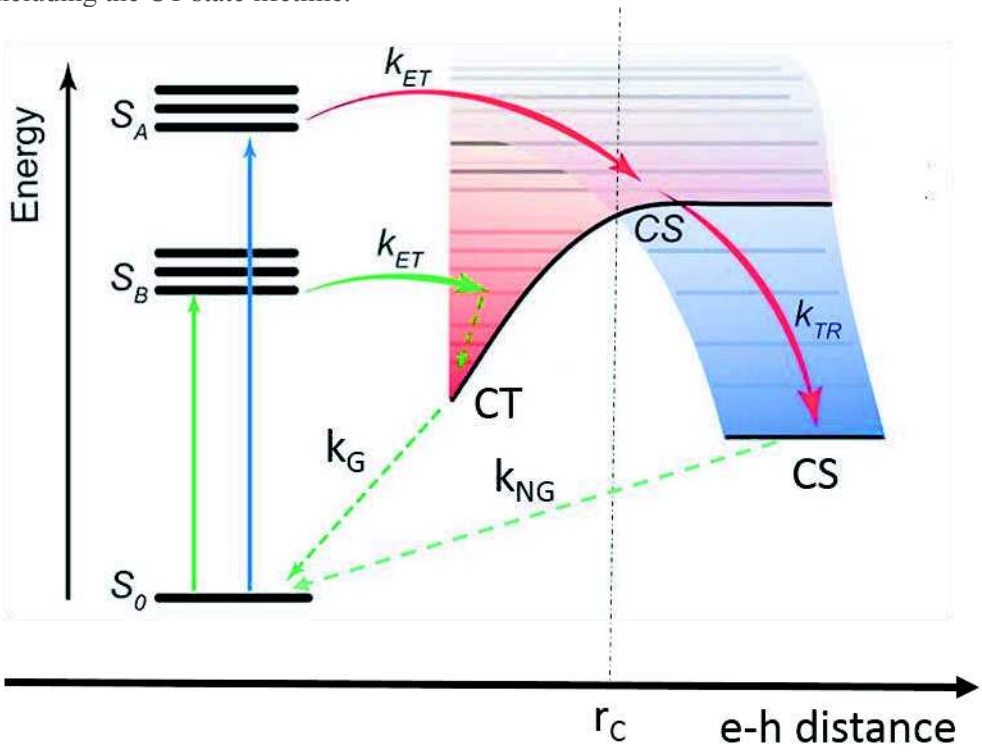

Figure II.4 Energy level diagram showing a model of charge generation and recombination at organic D/A heterojunctions. The exciton containing higher energy (S_A) results in electron transfer to the acceptor with enough excess energy to directly form the charge separated state (CS state). The lower energy exciton (S_B) does not have sufficient excess energy to escape the coulomb interaction and form the CT state.[21]

Figure II.4 shows a model with different competition mechanisms originally from CT state, proposed by Ohkita *et al.*[34] and included recent ultrafast spectroscopy and theoretical results.[35,36,37,38,39,40] For the Onsager theory, the formation of free carriers needs that the electron escapes the Coulomb capture radius. In recent cases, there is a second pathway to form charge separation state through "hot" excitons.

Charge collection. Charge transport is another key process right after exciton dissociation. Ideally, the separated electrons and holes should move towards respective electrodes to form an electrical current. This step is primarily determined by the interface between active layer and electrode. If the electrode interface is not carefully optimized, it can cause a dissipative sink of the transported charges. Organic materials have a low value of mobility, which increases the rate of charge carrier recombination on their pathways to the electrodes. This low value may be compensated either by improving the crystallinity of the active layer or by the use of intermediate layers. In a simplified point view without electron and hole transport layers, these layers are sandwiched between the active layer and the electrodes. In addition, electrical charge transport is highly dependent upon the purity of the materials as impurities act as traps that significantly reduce the mobility.

Charge recombination. Simultaneously with those four steps, energy loss is potentially present in many instances and through detrimental processes, such as exciton relaxation or radiative recombination, geminate and non-geminate carrier recombination. *Exciton relaxation* usually occurs when the distance between the local sites (where the exciton is generated) and the D/A interface is longer than the diffusion length. Once excitons diffuse to the D/A interface, forming CT states, these CT states must overcome the Coulomb interaction to generate the free carriers. However, this charge separation process is difficult due to low charge mobilities and poor charge screening effect in OSCs. Thus, when the separation doesn't happen, *geminate (or monomolecular) recombination* will take place. After the dissociation of CT states, the free carriers need to escape from Coulombic capture. During the diffusion of free carriers, the electron could recombine with the hole generated from another exciton, namely *non-geminate (or bimolecular) recombination*.
These two recombination processes can be distinguished kinetically as the geminate recombination usually happens within 100 ns in OSCs and the non-geminate recombination takes place after the diffusion process.[21] Most importantly, geminate recombination is independent of excitation density as an exponential decay, while the non-geminate recombination has a second order kinetic showing a power dependence kinetics.[41]

In the above discussion, we only consider that excitons are generated in the donor domain. In general, excitons generated in the acceptor domain have similar behaviors as the previous discussion except the hole transfer replaces the electron transfer.

II.3.2 Solar cells designs

Organic solar cells are photovoltaic devices using the organic semiconductors as the active (or light absorber) layer. OSCs started to attract people's attentions since 1986. Tang first improved the PCE over 1 % by vapor-depositing donor/acceptor (D/A) bilayer to create an energy offset[42], since Frenkel excitons need the donor-acceptor interface to split into free carriers, and form an interfacial charge transfer (CT) state. Therefore the thickness of the active layer must be shorter than the diffusion length, which is the main limitation of OSCs.
The exciton can migrate for a certain distance, namely the exciton diffusion length L_D, before relaxing back to the ground state. As the exciton is electrically neutral, the motion of exciton is not affected by an electrical field, it rather diffuses randomly, with an average value of L_D of not more than 10 nm in the case of polymers.[43] If the thickness of the active layer is larger than L_D, most of the excitons recombine before reaching the interface. To remedy this problem, the

interface area within an exciton diffusion distance of L_D from the exciton location needs to optimize. For this aim, several solutions have been proposed such as the optimization of the diffusion length by improving the structure of the polymer or increasing the contact area between the donor and the acceptor.

Later on, the bulk heterojunction was designed in 1995, in order to increase the interface areas.[44,45,46] Furthermore, the donor and acceptor domains must be connected to the cathode and anode, respectively, and short circuits avoided, in order to collect a maximum of free carriers and generate the highest photon current possible.
For the BHJ solar cells, the P3HT-PCBM is a "traditional" blend with less than 5% PCE.[47]. In the past few years, the amount of new donors were designed, synthesized and reported with the fullerene acceptors.[48,49,50] In 2013, Chen *et al*. used a polymer showing a strong interchain aggregation as a donor and achieved a PCE of 7.6%.[51] Later, by modifying the polymer chain length and optimizing the device conditions, a record PCE of 11.5% is reached.[52] However, the fullerene acceptors (PCBM/$PC_{70}BM$) still have some shortcomings, such as weak molar absorption, limited tunability on the absorption spectrum and high synthetic costs, especially C_{70}.[53] In the Ref [53] Nielson *et al.* reviewed three typical non-fullerene acceptors: perylene diimide, rotationally symmetric molecules and calamitic molecules. Recently, the PCE reached 9.5% for the non-fullerene OSCs.[54]
But, without any morphology control, due to the random organization of the D and A domains, the bulk heterojunction suffers from two main drawbacks: 1) uncontrollable diffusion length and 2) discontinuous areas.

Therefore, the ideal structure is the interdigitated heterojunction as shown in Figure II. 5 to optimize morphology. To reach this ambition, the molecules with the self-assembling properties are of interest. The preferable phase separation can be controlled by the chemical methods (specific solvent mixture[55] or annealing[56,57]). However, up to now, the self-assembling molecules forming the interdigitated heterojunction have not reached a better PCE than the conventional bulk heterojunction. § IV shows our investigations on a family of self-assemblage molecules.

Figure II.5 Evolution of the active layer structure to maximize the PCE of OSCs. The first OSC obtained above 1 % PCE is based on the bi-layer structure. Nowadays, the BHJ is most common and successful OSC structure. The interdigitated heterojunction is an attractive candidate for the next structural generation.

II.3.3 Guidelines to design new molecules

The above discussion allows us to propose some directions for designing new molecules to improve the overall efficiency. From Eq.II.1, the power conversion efficiency is determined by three parameters: J_{sc}, V_{oc} and FF.

Generally, FF is determined by the free carrier mobilities and the contact between the active layer and electrodes. J_{sc} can be increased by enlarging the absorption spectrum with regard to absorbing IR photons. The absorption spectrum extending to 800 nm is optimal for a single junction cell. This is a balance between the photons harvesting and the maximum electronic energy drawn out.

In addition, the open-circuit voltage can be considered as the energy difference between the Fermi level of donor and Fermi level of acceptor (in a simple approximate LUMO(A) and HOMO(D)). Lowering the donor HOMO to achieve a higher V_{oc} should be treated with caution as it could raise the energy of the charge separated state. Therefore, the thermodynamic dissociation pathway is in competition with ISC into low energy triplet state of acceptor may be activated instead of the charge separated state.[58]

Nowadays, the diffusion efficiency is typically taken as unity as the domain size of donor and acceptor is less than the diffusion length. Charge collection depends on the free carrier mobilities and the contact with two electrodes. It then appears that the CT state plays a more critical role, since dissociation and recombination of the CT decide on the generation of the free carriers to be collected. CT state is the weakly bound electron-hole pair as the origin of free carriers. Thus its population and lifetime lie at the core of charge generation to the yield of free carrier generation.[21,40]

In conclusion, transient absorption spectroscopy has been widely proven to be an indicator to observe the formation and recombination of CT states in both isolated solution and thin film. It is a straightforward way to follow the photo-induced processes and give the direct evidence of the population loss in each process.

II.4 Photovoltaic effect in DSSCs

II.4.1 Principle of DSSCs

A simplified schematic representation of an operational DSSCs device is illustrated in Figure.II.6(A).[59] The typical DSSC contains five components: a substrate coated with transparent conductive oxides, the semiconductor layer (usually TiO_2), sensitizers adsorbed onto the surface of the semiconductor, an electrolyte containing a redox mediator, and a counter electrode.

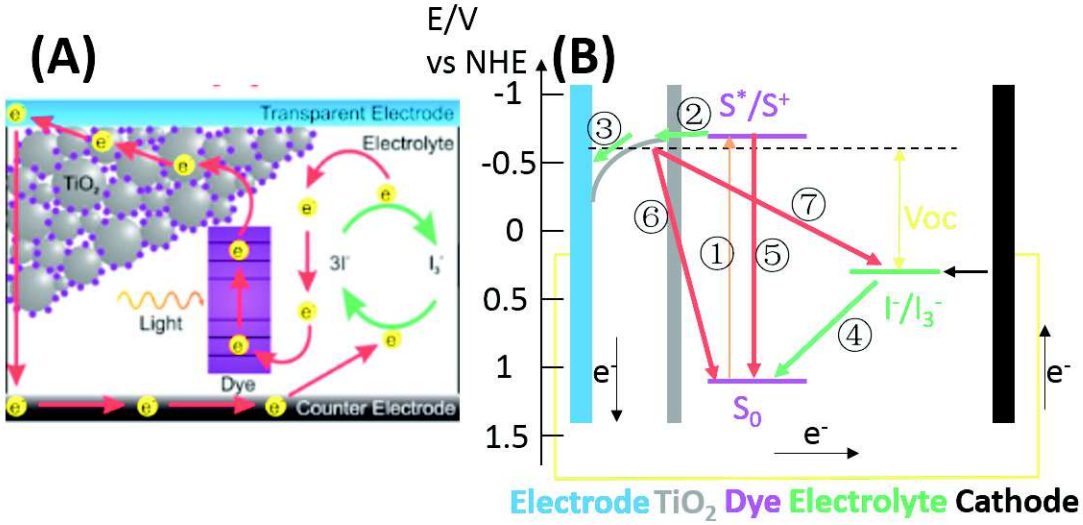

Figure II.6 (A) Simplified operation devices with its components of DSSCs [59](B) Simplified energy diagram of an operational DSSCs device to display the electron transfer processes. The basic electron transfer processes are indicated by numbers. The energy levels refer to a DSSC based on the dye N3, TiO_2 and I^-/I_3^- redox couple. The voltage output of the device is approximately given by the splitting between the TiO_2 Fermi level (dashed line) and the chemical potential of the redox electrolyte.[60]

The basic energy transfer processes in an operational DSSC device with the potential energy levels of N3 dye on TiO_2 and redox electrolyte I^-/I_3^- couple is illustrated in Figure II. 6(B).[60]

The first step is the absorption of a photon by the sensitizer (S), resulting in an electron to be promoted in the excited state. (**1.Absorption**.) As the sensitizers are grafted on the surface of the semiconductor, then, the electron in the excited state can be injected into the conduction band of semiconductor (**2. Electron injection**). The electrons are transported through the Oxide Film until the electrode to generate the photocurrent. (**3. Electron transport**). The oxidized dyes are regenerated in their neutral state by electron transfer from the redox electrolyte I^-. (**4.Regeneration of oxidized dyes**). Besides these desired processes, the detrimental processes are the excited state relaxation of the sensitizer (**5**) and recombination of an electron in the TiO_2 film with oxidized dyes (**6**) or electrolyte (I_3^-,**7**).

All these processes are or were extensively studied by time-resolved spectroscopies. § II.4.2.2 gives an account of results from femtosecond spectroscopy that monitors the details of excited state relaxation of the sensitizers and ultrafast CT to the semiconductor.

Due to the low free carriers mobilities, the thickness of device must be shorter than the diffusion length of free carriers. However, in order to absorb as much photon as possible, the thickness of device should be larger than the typical absorption length (~ 100 nm). Thus, designing the OSCs with both good light harvesting properties and good carrier transporting properties is a difficult task to achieve.
On the other hand, Dye-Sensitized Solar Cells (DSSCs) separate these two concerns into two individual parameters: the light harvesting property is optimized by matching the dye's extinction coefficient to the solar emissive spectrum; while the charge separation occurs at the interface of dye/semiconductor and charge collection takes place in the semiconductor and electrolyte. Since dyes are grafted into the semiconductor by chemical bonding, the exciton diffusion process is neglected. The high dielectric constant of the semiconductor (TiO_2, $\varepsilon_r = 80$) gives rise to much lower Coulomb attraction and binding energies of the CT states than those in OSCs. The high free carriers mobilities only depend on TiO_2 and electrolyte.[61]

Several attempts to inject electrons from photo-excited dyes into the conduction band of semiconductors were made in the 1960s.[62,63] However, only semiconductors with smooth interfaces, were used. The real breakthrough happened in 1991, when O'Regan and Grätzel first proposed to use the mesoporous nanocrystalline TiO_2 as the electrode, thereby significantly increasing the dye-covered surface area, leading to a power conversion efficiency of 7.2%.[64] With the advent of the famous ruthenium N3 complex, the efficiency was improved to up to 10%.[65] However, the record efficiencies reached a plateau at 10~11%, and the most efficient devices have remained essentially unchanged from its original design. Nowadays, the record power conversion efficiency of a DSSC based on a porphyrin sensitizer is 13%.[66]

Even though the power conversion efficiency of DSSCs is still less than that of standard silicon solar cells, the high long-term stability[67] and short pay-back time (less than one year) make that DSSCs are widely applied over all the world in the last two decades.[60]

II.4.2 Key parameters in DSSCs

In the conventional DSSCs, several hundreds of alternatives have been investigated. Until recently, for the sensitizer, transition metal complexes have provided the best results, including Ru(II) complexes[68], Os(II) complexes[69], Co(II) complexes[70,71], Zn(II) complexes[66,72,]. Organic dyes also are of interest due to their tunable absorption spectrum[73]. The favorable oxide films are made of TiO_2, ZnO, SnO_2 and Nb_2O_3.[74] But the different morphologies such as a nanoparticle, nanofiber, and core-shell structure have been developed.

Several parameters affect the efficiency. From the photophysical concern, the following two points require attention while optimizing the device or designing new sensitizers.

II.4.2.1 Energy level

The energy level of the semiconductor conduction band. As shown in Figure II.5, the maximal open-circuit voltage V_{oc} is the energy difference between the Fermi level of TiO_2 and potential redox level of I^-/I_3^-. For a typical DSSC based on Ru(II)-TiO_2, V_{oc} is around 700 meV. The position of conduction band edge depends on two parameters: surface charges and the dipole moment induced by the absorbed dye.[75] Due to protonation/deprotonation on the TiO_2 surface, the band edge has a 59 meV/pH shift for the TiO_2 film in aqueous solutions.[76] And the additives of electrolyte (Li^+ and/or tBP$^+$, 4-*tert*-butylpyridine) have a powerful influence on V_{oc}. Hagfeldt *et al.*[77] reported a total V_{oc} increase of 260 meV. The addition of tBP$^+$ contributes 160meV by promoting the conduction band edge towards higher energy level. Similar energy shifts due to tBP$^+$ were also observed by Durrant *et al.*[78]

The energy level of the sensitizer excited state. The conduction band edge should be as high as possible to obtain high V_{oc}. In contrast, in order to achieve high electron injection from excited sensitizer, the conduction band edge should be lower than the excited state of the sensitizer. Furthermore, we also want to decrease the band gap of the sensitizer in order to match the solar spectrum, especially in the near-IR regime to obtain high short-circuit current Jsc.

In conclusion, a compromise of conduction band edge and excited state of the sensitizer should be taken to reach high V_{oc} with an efficient electron injection.

II.4.2.2 Injection efficiency: Electron injection *vs.* excited state relaxation

In DSSCs, the charge separation of electron-hole pair occurs through the ultrafast electron injection from the excited state of the sensitizer to the semiconductor. Generally, the electron injection kinetics into TiO_2 are found multi-exponential by components in the femto- and picosecond timescale. Several experimental reports on Ru(II) complexes show the electron injection could take place from both nonthermalized and thermalized excited state.[79,80,81]

For an efficient DSSC, the electron injection efficiency is more important. In general, the injection efficiency is defined as:

$$\phi_{inj} = \frac{n_{inj}}{n_{inj}+n_{rel}} = \frac{k_{inj}}{k_{inj}+k_{rel}} \quad \text{(Eq .II.5)}$$

where n_{inj} and n_{rel} are the populations of electrons injected or subject to excited state relaxation and k_{inj} and k_{rel} are the rate constants of those two processes. For an efficient DSSC ($\Phi_{inj} \approx 99\%$), it suffices to have k_{inj} two orders of magnitude larger than k_{rel}.

We can consider the excited-state relaxation as an intrinsic property of the dye molecules (ISC, IC and radiative recombination). The transient absorption spectroscopy reveals the electron injection process by measuring the absorption changes associated with oxidized dyes' cation formation and recombination. Therefore, the electron injection can be determined by Eq. II.5. The intrinsic radiative recombination rate constant can be estimated by the replacement TiO_2 by a larger band gap Al_2O_3.[82]
Besides the overlapping of the excited state of the sensitizer and the conduction band edge of TiO_2 as mentioned before, the electron injection lifetime, as well as the efficiency, also depends on dye aggregation[83] and solvent pH.[84]
The time-resolved experiments should give a direct indication of the electron injection efficiency by measuring the k_{rel} and $k_{inj}+k_{rel}$.

III. Experimental Setups and Data Analysis

III.1 Introduction

Time-resolved spectroscopies allow probing spectral features as a function of time. They are mainly used to study the photochemical or photophysical properties of various compounds. Depending on the type of phenomena and their timescales, different spectroscopies are suitable. Figure III.1 shows a typical timescale for different processes.[17]

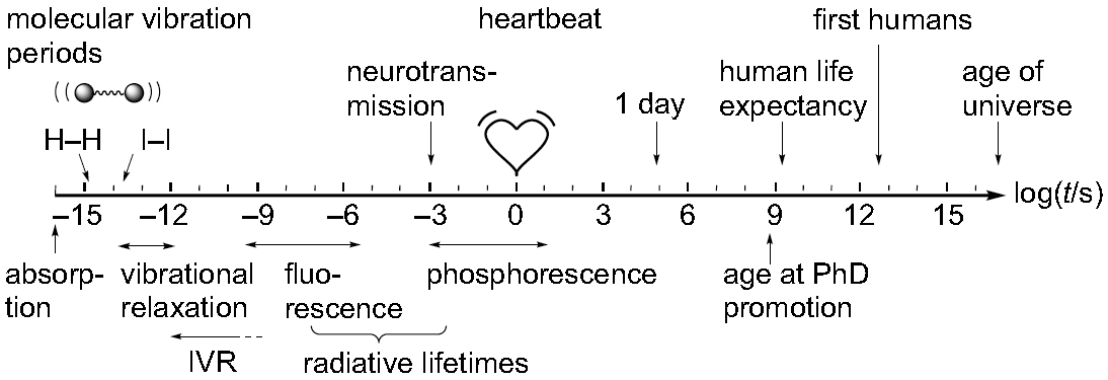

Figure III.1 Timescale of different processes.[17] The photon is absorbed within sub-fs. The molecular vibration periods and IVR normally happen within sub-ps. The radiative processes take place in the ns to μs timescale.

Since the photophysical phenomena that we are investigating - electron transfer processes and charge transfer state formation in OSCs, electron injection and excited state relaxation in DSSCs - occur on the femtosecond to the nanosecond timescale, the experimental setups need to have femtosecond time resolution and reach the nanosecond time delay.
The femtosecond time resolution requires femtosecond laser pulses as the source and femtosecond sampling over the full-time delay. The fastest photodiodes have a time resolution of ~10 ps. Therefore, over past 30 years, a variety of techniques were developed relying on nonlinear optics in order to resolve molecular processes with femtosecond or sub-femtosecond resolution.

In this thesis, UV-NIR femtosecond transient absorption spectroscopy setups were used with a combination of picosecond time-resolved fluorescence measurement (streak camera) to determine the photophysical properties of two types of solar cell materials.

III.2 Experimental setups

Femtosecond transient absorption and time-resolved fluorescence spectroscopy involve several nonlinear optical phenomena.

III.2.1 Nonlinear Optics

The light is an electromagnetic wave composed of an electric field and a magnetic field. In a femtosecond laser pulse, the electric field is intense enough to generate polarization terms as follows:

$$\vec{P} = \varepsilon_0(\chi^{(1)}\vec{E} + \chi^{(2)}\vec{E}^2 + \chi^{(3)}\vec{E}^3 + \cdots) \quad \text{(Eq.III.1)}$$

where the $\chi^{(n)}$ term is n^{th}-order electric susceptibility due to the material properties.

Second-order Polarization. The second order polarization is proportional to $\chi^{(2)}$ and the square of the electric field. A frequent use of the second order polarization is the sum- and difference frequency generation. The second order polarization for an electric field with two frequencies is given by:

$$\overrightarrow{P^{(2)}}(t) = 2\varepsilon_0\chi^{(2)}(A_1{A_1}^* + A_2{A_2}^*) + \varepsilon_0\chi^{(2)}\{{A_1}^2\exp(-i2\omega_1 t) + {A_2}^2\exp(-i2\omega_2 t)\} + 2A_1A_2\exp[-i(\omega_1+\omega_2)t] + 2A_1{A_2}^*\exp[-i(\omega_1-\omega_2)t] \quad \text{(Eq.III.2)}$$

It contains the zero frequency, double frequency ($2\omega_1$ and $2\omega_2$),sum ($\omega_1+\omega_2$) and difference ($\omega_1-\omega_2$) terms. The last two terms represent the *sum-frequency generation* (SFG) and *difference-frequency generation* (DFG). And the double frequencies terms are responsible for the *second harmonic generation* (SHG).

These different radiations exist at the same time, but in general one particular will be selected and enhanced by specific conditions (*e.g.* phase matching condition).
One common application of second order polarization is *optical parametric amplification* (OPA). It is the same idea as DFG where an intense beam (pump) and a weak beam (idler) interact in a nonlinear crystal to generate an output beam (signal) under the phase matching condition. The energy of the pump is transferred to the idler to get the signal. Normally, the idler is a broadband beam. By selecting a specific phase matching condition, the wavelength of the signal is tunable.

Third order polarization. Under high electric field, the refractive index of the medium becomes a function of the electric field intensity, known as optical Kerr effect. The refractive index modification is given approximatively by:

$$\Delta n \approx \frac{3\chi^{(3)}}{4c\varepsilon_0 n^2} I \quad \text{(Eq.III.3)}$$

It results in a nonlinear phase delay of the wave itself (self-phase modulation SPM) or of another wave (cross-phase modulation, XPM). The broadening of femtosecond laser pulses, *i.e. white light generation*, is due to SPM.

III.2.2 Time-resolved fluorescence

Time-resolved fluorescence measurements reported here were recorded with a streak camera system (Hamamatsu C10627) with different time ranges from 1 ns to 500 µs. The time resolution is 0.5 % of the chosen time range except for the shortest time range (1 ns) where the time resolution is 10 ps.

The tunable excitation is the output of a home-built noncollinear optical parametric amplifier (NOPA) [85], seeded by the second harmonic of a Yb-doped fiber laser (TANGERINE, Amplitude System). The excitation wavelength is adjusted to the absorption maximum of the sample.
The principle of a streak camera is illustrated in Figure III.2. After excitation of a sample, its fluorescence is imaged on the entrance of a spectrometer in front of the streak scope. The spectrometer spreads the fluorescence horizontally depending on the wavelengths.

The spectrally spread photons are focused on the photocathode. The highly sensitive photocathode converts a portion (10-20 %) of photons to electrons. The accelerated electrons pass a vertical electric field generated by a fast tension sweep. The tension sweep is triggered by the laser source to define the time zero. As the electrostatic force depends on the time the electrons arrive, they are displaced along the vertical axis. The time range is tunable with the different slope of the vertical electric field. The time-resolved electrons are amplified by the Micro-Channel Plate (MCP) and transferred back to photons by a phosphor screen. Therefore, the generated fluorescence is spread spectrally and temporally on the horizontal and vertical axes of the CCD camera, respectively.

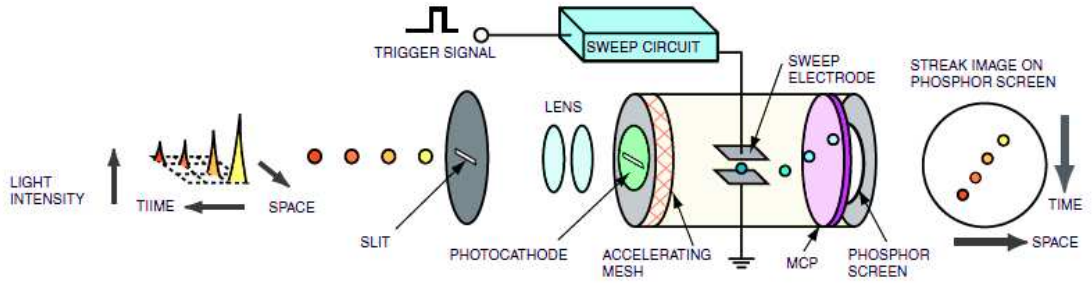

Figure III.2 Schematic of a streak camera.[86] The spectrally spread photons are converted into electrons and pass a vertical electric field generated by a fast tension sweep. Depending on the arrival time, different tensions are applied. Thus, the generated fluorescence is spread spectrally and temporally on the horizontal and vertical axes of the CCD camera.

Time-resolved fluorescence spectroscopy is an efficient method to study the excited state lifetimes of molecules and solid state materials. These can be limited by radiative processes, such as exciton or free carriers recombination, or non-radiative processes: energy and charge transfer processes, or intersystem crossing.

III.2.3 Transient absorption spectroscopy

Transient absorption spectroscopy is a useful technique to investigate photo-induced processes. Depending on the excitation wavelength, probe range and delay time, a wide variety of experimental setups could be used.

In this work, we want to unravel the photophysical properties of two types of solar cell materials absorbing UV and Vis photons. We probe photophysical mechanisms such as energy transfer, charge transfer, and electron injection. Thus, the probing spectral range spans from UV to NIR with femtosecond time resolution. Figure III.3 displays the experimental setup scheme.

A Chirp Pulse Amplifier (Pulsar, Amplitude Technology) delivers 0.5 mJ femtosecond pulses centered at 800 nm with 40 fs time resolution, at 5 kHz repetition rate. The laser beam is split into two parts: one intense to generate the pump, and one weak to generate the probe. Depending on the desired excitation wavelength, the pump beam passes either: i) a nonlinear crystal (BBO) to produce a 400 nm pump (60 fs) by SHG, ii) or an OPA (TOPAS, Light conversion) to generate a visible pump (480 or 515 nm, 40 fs).

The pump-probe delay until 6 ns is controlled by a mechanical delay line on the probe beam. The latter is then focused on a 2 mm calcium fluoride crystal to produce the white light continuum from 290 to 950 nm. Afterward, the probe beam is split into two: probe and reference. The reference is used to measure and thus to correct for the white light fluctuations. And since pump and probe beams overlap spatially in the sample, the probe monitors the sample's absorption and how it is changed by the pump-induced photochemistry.

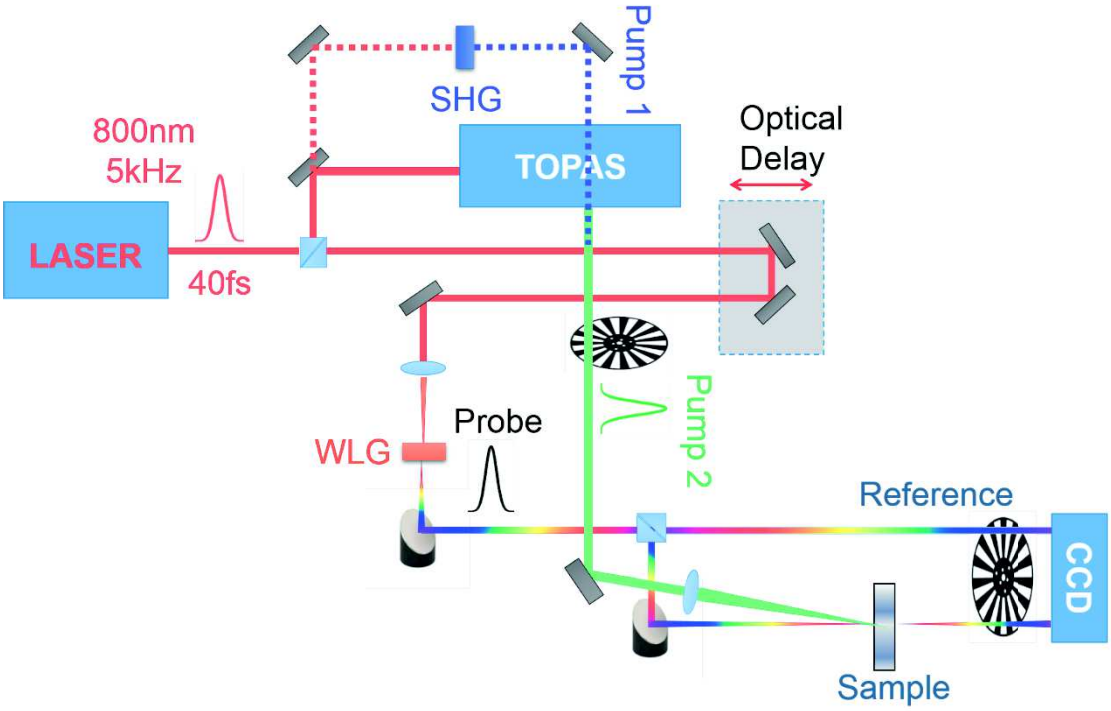

Figure III.3 Scheme of the experimental setup of transient absorption spectroscopy.

The pump beam is chopped by a mechanical chopper. A series of the probe and reference spectra with and without pump are recorded by the CCD camera after passing the spectrometer. The corresponding spectra differential absorbance ΔA are acquired at different delay times t and are given by:

$$\Delta A(\lambda, t) = \log\left(\frac{I_{wo.\ pump}(\lambda,t)}{I_{w,pump}(\lambda,t)}\right) = \sum_i \varepsilon_{s_i}(\lambda)\Delta C_{s_i}(t)L \quad \text{(Eq III.4)}$$

where $I_{w,pump}$ and $I_{wo,pump}$ are the transmitted light intensities with and without the pump, ε_{Si} the extinction coefficient in the state S_i, ΔC_{Si} the concentration change in state S_i after excitation and L is the sample's path length.

Figure III.4 illustrates a promoted electron in the excited state triggered by the pump (Figure III.4 (A)) at time T=0 and monitored by the pump at time T= t_1 or t_2 (Figure III.4 (B)). The respective differential absorption spectra are depicted in Figures III.4 (C) and (D). There are four phenomena induced by the pump and contained in the differential absorption spectrum: ground state bleaching (GSB), stimulated emission (SE), excited state absorption (ESA) and photoproduct absorption (PA).

In the absence of pump (t < 0), molecules are in their fundamental state (ground state). Upon photon absorption, some molecules are excited and populate an excited state. This leads to *Ground State Bleaching* (GSB), which means that the electron population is reduced to the ground state by the pump pulse (delta C_{S0} <0)). After some delays (T=t_1), the molecule may: return to the ground state and emit a photon (*Stimulated Emission*, SE) or absorb a photon to a higher energy state (*Excited State Absorption* ESA), as shown in Figure III.4 (C), or undergo a reaction, *e.g.* charge formation and charge transfer state. The product may absorb a photon to a higher energy state (*Photoproduct Absorption* PA) or relax to the ground state (GSB), as shown in Figure III.4 (D).

At a specific delay time, the differential absorption spectrum allows distinguishing which state and species, and in the case of the D-A dyads (§IV), which moieties are involved in the photoinduced processes. The GSB has the signature of ground state absorption spectrum with a negative sign, because it indicates a number of molecules lacking in the ground state population. Since stimulated emission is due to excited state electrons relaxing back to the ground state via photon emission (Fig. III.4 (B)), the SE spectrum is similar to the steady-state fluorescence spectrum. While the photoproduct is formed, such as a charge-transfer state, the PA will show the spectral features of charged species, which can be directly measured by spectro-electro-chemistry as illustrated in Figure III.4 (D).

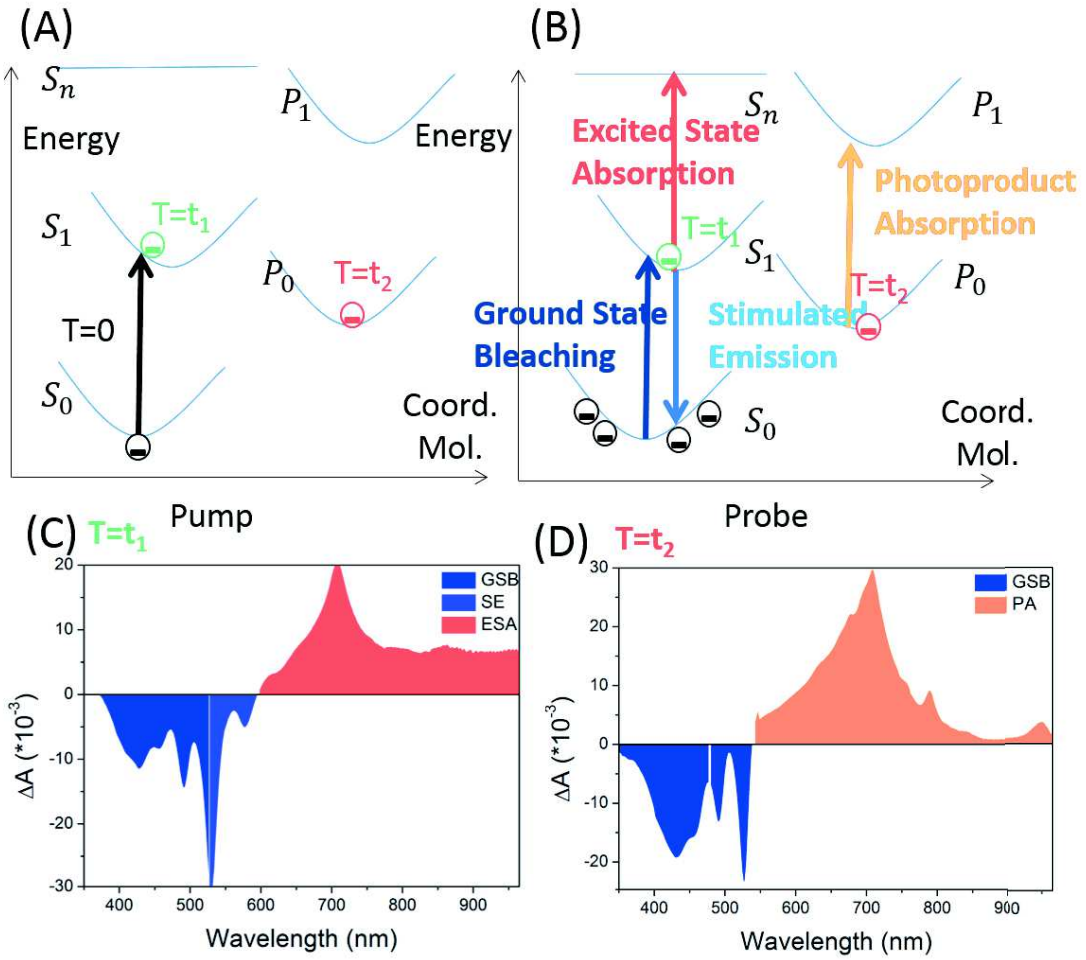

Figure III.4 Schematic diagram of a simplified system. (A) Promoted electron in the excited state or photoproduct state only with the pump (B) different phenomena observed by the probe at various time delay T=t_1 or t_2 and (C) the differential absorption spectrum at T=t_1 and (D) the differential absorption spectrum at T=t_2

III.3 Data correction and analysis

The transient absorption data are a collection of measurements in two dimensions: along the spectral and temporal axes. For pump-probe pulse coincidence (zero delay time), the recorded data have some artifacts such as cross-phase modulation, and Raman scattering. Furthermore, the probe is a broadband white light continuum, and the refraction index depends on the wavelength. Thus, the absolute zero delay between the pump and the probe relays on the wavelength and needs to be accurately defined before analyzing the data (chirp correction).
After data correction, the data are analyzed by global analysis and/or target analysis. The spectral information could determinate which moieties or which states are involved in the photo-induced processes and the temporal information provides the corresponding reaction dynamics.

III.3.1 Data correction

III.3.1.1 The solvent response

Even though solvents and substrates are usually transparent in the visible region, pump pulse can induce Raman scattering (RS) and two-photon absorption if the intensity is high enough. In transient absorption spectroscopy, the interaction of the pump and the probe in the medium can generate some non-linear signals as the cross-phase modulation (XPM, Eq. II.3) and stimulated Raman scattering (SRS) and pump-probe two-photon absorption. For the solvents used here, two-photon absorption can be neglected.
XPM induces spectral modifications with probe's temporal chirp, and the interaction of pump and probe leads to SRS through solvent vibrational energy level.[87]
When pump and probe are coincident, it gives rise to an apparent optical density change at a solvent specific wavelength. This time signal is called RS signal. Even so, for the pump-probe experiment, it's an unwanted signal.
Those contributions are measured in similar conditions as the ones of the samples by performing the measurements on the solvent/substrate immediately after the ones performed in the sample solution. The solvent/substrate data are subtracted from the sample data to isolate the transient absorption contribution of the investigated molecules.

III.3.1.2 Group Velocity Dispersion

Group velocity dispersion is a phenomenon related to the group velocity (Eq. III.5) dependency on the frequency. In a pump-probe experiment, the probe is used to register the transient absorption changes and has a broadband spectrum. So, it will make all wavelengths arrive at different time zero.[88]

$$v_g = \left(\frac{dk}{d\omega}\right)^{-1} = \left(\frac{c}{n}\right) / \left(1 - \frac{\lambda_0}{n}\frac{dn}{d\lambda_0}\right) \quad \text{(Eq III.5)}$$

$$\mathrm{D} = \frac{\mathrm{d}}{\mathrm{d}\omega}\left(\frac{1}{v_g}\right) \quad \text{(Eq III.6)}$$

Although we use parabolic mirrors to reduce GVD, the probe has to pass through white light continuum generation crystal, quartz capillary, and solvent where the pulse is dispersed. In the experiment, we consider a broadband pulse (300-950 nm for OSCs and 300-700 nm for DSSCs) and observe that the UV part arrives about 500 fs later than the near-IR part. To make sure all wavelengths arrived at the same time zero, GVD is corrected by a polynomial fitting procedure.

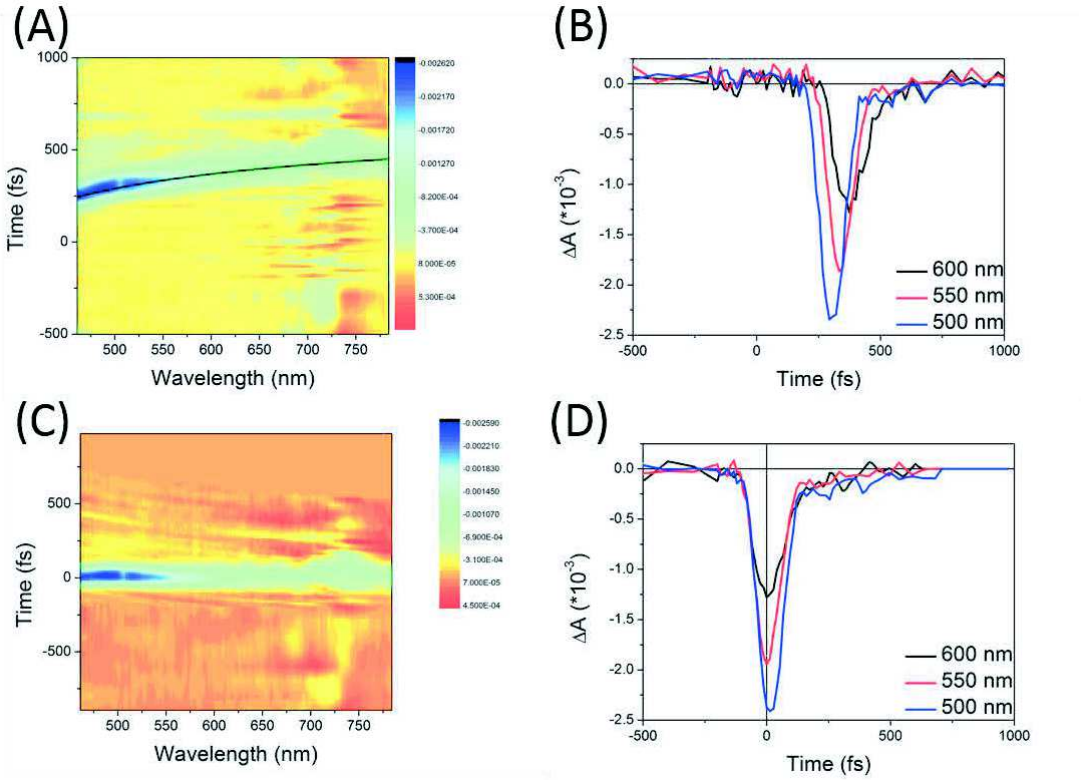

Figure III.5 (A) Transient absorption data of chloroform excited at 400 nm with the polynomial fit (black solid curve) defining the GVD curve (B).kinetic traces at 340, 400 nm and 450 nm, showing prominent XPM processes and temporal shifts. (C) and (D) same as (A) and (B), respectively after GVD correction.

A typical example is introduced in Figure III.5 to illustrate GVD compensation in chloroform excited at 400 nm. A home-implemented Scilab routine time-shifts the data for the different wavelengths according to the determined GVD polynomial fit correction. Figure III.5 (C) and (D) show the signal after GVD correction.

In general, the global time zero is determined manually by the center of the SRS signal. Due to the GVD correction by a polynomial fitting, the time zero has a typical accuracy of 20 fs.
Since the spectral range of the spectrometer is only of 350 nm, and we are interested in a much wider spectral range (300-950 nm for OSCs and 300-700 nm for DSSCs), we measured the data in two or three spectral regions. After the data correction described above, the two or three data sets are assembled together. The wavelength ranges measured are significantly overlapping to do this data treatment. Finally, the broadband transient absorption data are obtained.

III.3.2 Data Analysis

In this work, the photo-induced processes investigated are within nanosecond timescale and without any bimolecular processes. Thus, the kinetics obey to the 1st order rate equation as:

$$\frac{dN_j(t)}{dt} = k_{i,j}N_j(t) \quad \text{(Eq. III.7)}$$

where $N_j(t)$, and $k_{i,j}$ are the concentration in the state j and rate constant from the state i to j, respectively.

Therefore, the transient absorption data correspond to exponential decay or rise of each species (different moieties or different states) involved in the photoinduced processes.

The temporal accuracy of transient absorption data is limited by the instrumental response function (IRF). During the global analysis, the IRF is taken into account as a Gaussian function with a full width half maximum σ. The experimental kinetics are the convolution of the IRF and the sum of exponential functions:

$$\Delta A(\lambda, t) = (\sum_i A_i \exp(-k_i(t - t_0))) \otimes \mathrm{IRF}\ (\sigma, t_0) \quad \text{(Eq.III.8)}$$

$$\mathrm{IRF}(\sigma, t_0) = Gaussian\ (\sigma, t_0) = \frac{1}{\sigma\sqrt{2\pi}} \exp((\frac{t-t_0}{\sigma})^2) \quad \text{(Eq.III.9)}$$

If the rate constant is close to or faster than the time resolution σ, the convolution yields to the shape of a Gaussian. Thus, instead of the exponential function, a Gaussian adjustment function is added to represent the unresolved component.

It is worth to notice that this approximation considers that the transient data are bilinear and independent temporally and spectrally. This approximation is true when only electronic state populations are involved. In some particular cases such as the vibrational relaxation in the excited state, the kinetic is a non-exponential delay and correlates with the spectral evolution.

III.3.2.1 Singular Value Decomposition (SVD)

The singular value decomposition is a mathematical process to diagonalize a m*n matrix as:

$$\Delta A_{m,n}(\lambda, t) = U_{m,m}(\lambda) S_{m,n} V^T_{n,n}(t) \quad \text{(Eq.III.10)}$$

where $U_{m,m}$ and $V_{n,n}$ are orthonormal matrices and $S_{m,n}$ is a diagonal matrix, named as singular values. These matrices are placed in the descending order according to $S_{m,n}$.

The singular value $S_{m,n}$ is the indication of the weight of the vector pair of $U_{m,m}$ m^{th} row, and $V_{n,n}$ n^{th} column in the whole ΔA matrix. The ΔA matrix can be reconstructed by the dominant singular values (typically, the first four or five) with their vector pairs, and the rests are considered as noise. This discrimination is often difficult to make, but the standard noise floor of data at negative delay times is a good reference. By plotting the singular values and their respective spectra and dynamics, the most significant contributions of ΔA can be determined to form a noise-filtered data set.

III.3.2.2 Global analysis

After SVD analysis (N pairs of vectors are chosen), the temporal $K(t)=SV^T(t)$ matrix is used to characterize the dynamics in the data since it contains all the temporal evolution of the whole data. In a so-called "global analysis" approach, each vector in the K matrix is fitted by the function described in Eq. III.8 simultaneously with shared exponential rate constants.

$$K(t) = S * V^T = \begin{bmatrix} S_1 * V_1^T \\ \vdots \\ S_N * V_N^T \end{bmatrix} = \begin{bmatrix} A_{1,1} & \cdots & A_{1,j} \\ \vdots & \ddots & \vdots \\ A_{N,1} & \cdots & A_{N,j} \end{bmatrix} * \begin{bmatrix} \exp(-k_1 t) \\ \vdots \\ \exp(-k_j t) \end{bmatrix} \otimes IRF \quad \text{(Eq.III.11)}$$

with $\Delta A(\lambda,t)=U(\lambda)*K(t)$

The fit gives the different rate constants with the associated amplitudes for the vectors in K matrix. The product of the fitted amplitudes $A_{i,j}$ with the spectral matrix U gives the differential spectra associated to the fitted decays, called DAS for decay-associated differential spectra.

$$DAS(\lambda) = \begin{bmatrix} DAS_1 \\ \vdots \\ DAS_j \end{bmatrix} = \begin{bmatrix} U_1 \\ \vdots \\ U_N \end{bmatrix} * \begin{bmatrix} A_{1,1} & \cdots & A_{1,j} \\ \vdots & \ddots & \vdots \\ A_{N,1} & \cdots & A_{N,j} \end{bmatrix} \quad \text{(Eq. III.12)}$$

with $\Delta A(\lambda, t) = \sum_j DAS_j(\lambda) * \exp(-k_j t)$

These DAS contain the spectral information occurring at the particular rate constant k_i. In many cases, a close inspection of the DAS allows us to identify which moiety or which state evolves with the rate k_i.

A typical example of this analysis procedure is applied on a Donor-Acceptor molecule presented in § IV. The 2D plot of TA data obtained after excitation at 400 nm is displayed in Figure III.4 (A).

In the present case, the first five vectors of the K matrix are fitted globally, meaning that the same function is used to fit the five vectors simultaneously. The global fitting, using the function introduced in Eq. III.5 is illustrated in Figure III.4 (B). Most of the fitting parameters (t_0, σ, the five finite time constants k_i) are shared and only the amplitudes A_i are optimized independently.

The associated decay spectra are reconstructed from the set of A_i obtained as a result of the fitting routine. These DAS are displayed in Figure III.6 (C). They represent the wavelength dependent weight of each decaying component k_i throughout the data set. Further explanation can be found in § IV.

Figure III.6 (D) displays the five residuals obtained by this global fitting with a minimum number of fit components and shows that they all have amplitudes smaller than the first neglected singular transient (TR6). The satisfied fitting results have two criteria: 1) the residuals are statistically distributed around zero, meaning all relevant time scales are captured by the fit and 2) the standard deviation of the residuals is smaller than the experimental noise level, represented by the first neglected singular transient.

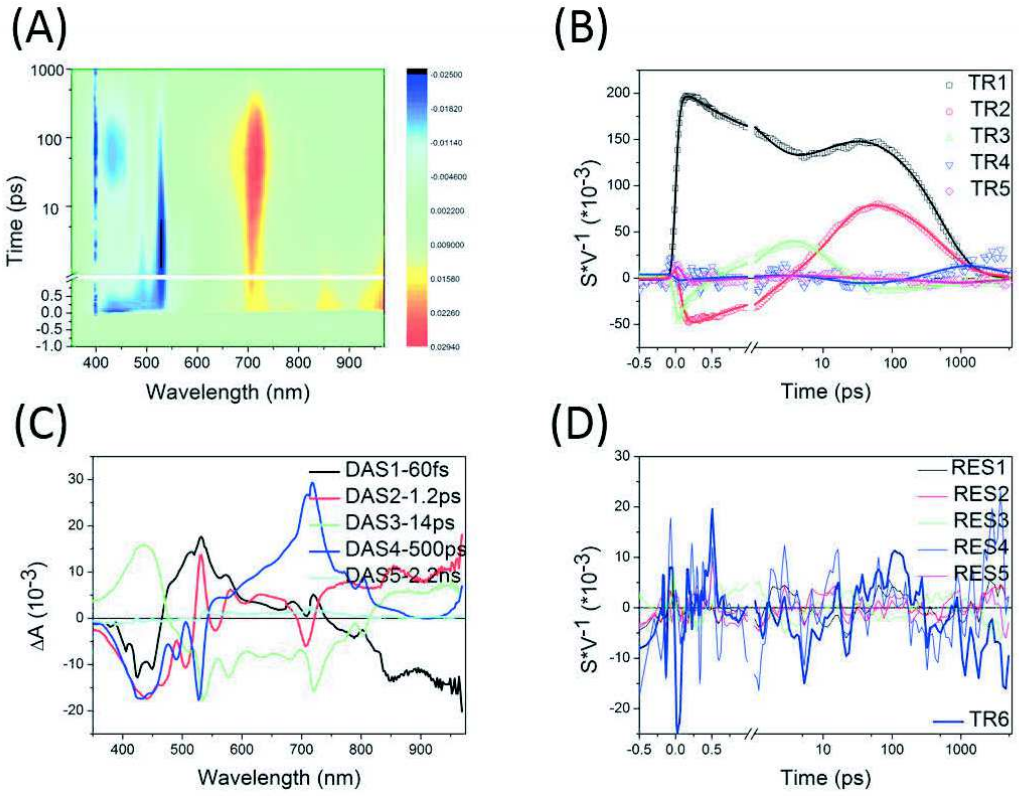

Figure III.6 Global analysis of the entire 2D plot. (A) Transient absorption data (in color code) as a function of wavelength (nm) and time delay (ps). (B) The five dominant singular transients (K matrix) and their corresponding fits by the fitting function introduced above. (C) Decay-Associated Spectra obtained by global analysis. (D) The residuals are corresponding to the simultaneous fitting of the five singular kinetics of panel B, compared to the first neglected singular transient (TR6).

IV. Donor-Acceptor Molecules for Organic Photovoltaics

IV.1 Donor-Acceptor Molecules

The principle of organic solar cells (OSCs) is described in § II.3. In order to harvest photons and generate free carriers, one of the key parameters is the active layer. The active layer usually consists of a Donor and an Acceptor.
As mentioned previously,[53] perylene diimide (PDI) is a good alternative acceptor material to replace fullerene acceptor for OPV. Furthermore, with its self-assembly propriety, PDI could form the interdigitated heterojunction. However, the PDI still have some drawbacks, such as the lower solubility making it harder to use in the ''roll-to-roll'' technique with the soluble polymer.[89] Recently, Geng and co-workers showed that PDI-based **D-A** dyads form well defined lamellar mesophases with a perfect phase separation at a sub-10 nm length scale and power conversion efficiency reached up to 2.7% based on single PDI acceptors.[90] Later, the power conversion efficiency achieved 6% based on a helical PDI acceptor.[91] Nowadays, the highest PCE reached 8.4% based on a helical PDI acceptor containing selenophene.[92]

A Donor-Acceptor dyad (**D-A**) oligomer based on a phenyl-bisthiophene-phenyl moiety as donor and a PDI moiety as acceptor was designed and studied by transient absorption spectroscopy in solution and film[93,94] by our group. It shows an excellent self-assembling structure alternating donor and acceptor.[95] Nevertheless, the CT state lifetime is rather short (50 ps) in solution and the majority of CT states recombines in less than 100 ps in a film. In order to improve the photophysical properties, then the PCE, the second generation of **D-A** molecules with variable parameters has been designed and synthesized by our collaborators (Dr. Pierre-Olivier Schwartz and Dr. Stéphane Méry at *IPCMS*). The chemical structure of these **D-A's** is shown in Figure IV.1.[56,57]

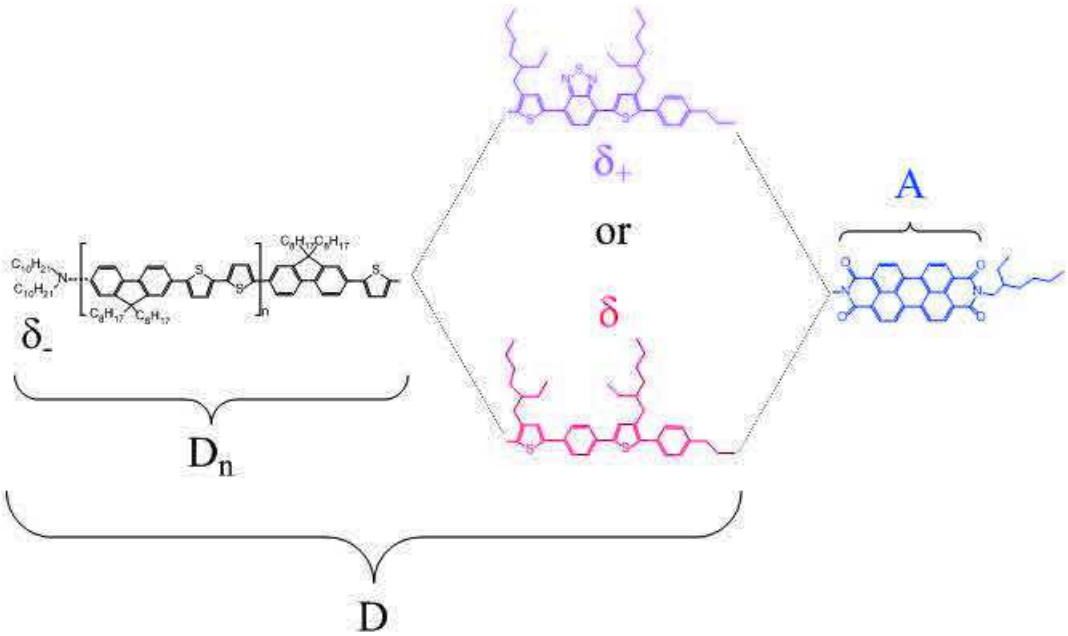

Figure IV.1 Chemical structures of Donor-Acceptor molecules. The donor (**D**) consists of one 9,9-dioctylfluorene-thiophene unit and repeated units ($\mathbf{D_n}$, n=0 to 3) of 9,9-dioctylfluorene and bithiophene and The acceptor (**A**) is perylene diimide. A short flexible spacer (ethylene) with a linking molecular unit is composed of thiophene–phenyl–thiophene (for **δ**) or thiophene–benzothiadiazole–thiophene (for **δ+**) is used to connect the donor and the acceptor. Furthermore, a terminal amine can be added at the other end of the donor moiety as ''electron-donating'' unit and is denoted **δ-**.

The donor (**D**) consists of one 9,9-dioctylfluorene-thiophene unit and repeated units ($\mathbf{D_n}$, n=0 to 3) of 9,9-dioctylfluorene and bithiophene (F8T2) to vary the donor length. F8T2 is applied in p-type Field Effect Transistors (FETs)[96] and as Organic Light Emitting Diodes (OLEDs)[97]. The high hole mobility, up to $\mu_h=5*10^{-3}$ $cm^2V^{-1}S^{-1}$ [98] makes F8T2 a good potential donor for organic photovoltaic solar cells. A power conversion efficiency of 2.7% was achieved based on F8T2-PCBM blends.[99] Thus, the F8T2 is a good candidate as a donor. The repeated units are expected to extend the distance between electron and hole. According to the Marcus theory,[20] the elongation of electron-hole distance could lead to a longer CT state lifetime.

The acceptor (**A**), perylene diimide (PDI, as perylene-3,4:9,10-teracarboxylic acid diimide) is also abbreviated as PBI (perylene-3,4:9,10-bis(dicarboximide)). PDI is not only widely used as an industrially suitable color pigment[100], but also has other scientific applications, such as in single molecule fluorescence spectroscopy[101], organic transparent transistors[102], metal-to-supramolecular structures[103], π-stacked functional structures in DNA[104] and organic photovoltaics (OPV)[56,105]. Figure IV.2(A) illustrated an important feature: the mirror image relation of absorption and fluorescence, and a fluorescence quantum yield >0.9[106]. These properties are attributed to the rigid and planar scaffold and a small non-radiative rate as S_1 to T_1 intersystem crossing (ISC) is much slower than the radiative lifetime.[107] The outstanding stability of PDI is also attributed to the electron-lacked of the π-conjugated scaffold, which makes it very resistive to oxidative degradation and other decomposition pathways.[6]

In the **D-A** dyads, the donor moiety is connected to the acceptor group via a linking moiety made of a short flexible spacer (ethylene) and a molecular unit that comes in two varieties of low and high electronegativity, respectively, denoted **δ** or $\boldsymbol{\delta_+}$. This linking molecular unit is composed of thiophene–phenyl–thiophene (for **δ**) or thiophene–benzothiadiazole–thiophene (for $\boldsymbol{\delta_+}$). Furthermore, a terminal amine can be added at the other end of the donor moiety as ‘‘electron-donating’’ unit and is denoted $\boldsymbol{\delta_-}$.

IV.2 Isolated molecules in solution

Nine molecules (in Table IV.1) have been investigated in solution (chloroform). 1) Four of them have a common donor length (n=1) to study the different donor moieties and 2) two series of donor moieties with increasing donor length (n=0~2 for **$D_1\delta_+A$** and n=0~3 for**δ-$D_1\delta A$**) to investigate the importance of charge separation between donor and acceptor. In the end, three of them are studied in two more solvents (toluene and trichloroethylene) as a function of solvent polarities. This section focuses on intramolecular photophysical properties, especially how charge transfer state dynamics is tuned. The results are published in ref 108, and built on the PhD thesis of T. Roland[94].

Table IV.1 Studied molecules as different donor moiety (column) and different donor length (raw).

		Donor length			
		0	1	2	3
Donor moiety	$D_n\delta$		**$D_1\delta A$**		
	$D_n\delta_+$	**$D_0\delta_+A$**	**$D_1\delta_+A$**	**$D_2\delta_+A$**	**$D_3\delta_+A$**
	δ-$D_n\delta$	**δ-$D_0\delta A$**	**δ-$D_1\delta A$**	**δ-$D_2\delta A$**	
	δ-$D_n\delta_+$		**δ-$D_1\delta_+A$**		

IV.2.1 Steady-state spectroscopies

The steady-state absorption and fluorescence measurements were performed on **D_n-A** in chloroform in order to provide useful spectral characterizations of the species expected to contribute to the transient absorption signals.
In addition, spectro-electro-chemistry was used to obtain the spectra of the radical ions. These spectral features will allow an identification of the molecular species involved in the photochemical cascade, as well as the role of energy and charge transfer.

IV.2.1.1 Steady-state absorption and fluorescence

Figure IV.2(A) illustrates the steady-state absorption spectra (solid curves) and emission spectra (dotted curves) of individual compositions moieties (**$D_1\delta$** (black curves), **δ** (red curves), **$D_1\delta_+$** (green curves) and **A** (blue curves)) of the **D-A** in chloroform.

$D_1\delta$ shows only one absorption band centered at 425 nm without any vibrational structure. Surprisingly, the **$D_1\delta$** fluorescence spectrum shows vibrational structure as two peaks at 468 and 499 nm and a shoulder at 550 nm. **δ_+** consists of two absorption bands. The main band, centered at 323 nm (not shown), represents the transition to high-lying excited state ($S_0 \rightarrow S_2$) and a second band, centered at 478 nm, corresponds to the transition to the first excited state ($S_0 \rightarrow S_1$).

δ_+ fluorescence appears around 598 nm. Two bands and a small shoulder are observed in the absorption spectrum of **$D_1\delta_+$**. The highest absorption band, centered at 323 nm (not shown), indicates the π-π^* transition in **D_1**[109] and second absorption band at 420 nm and the shoulder around 510 nm correspond the internal charge transfer between **D_1** and **δ_+**.[110]

While the spectral features of **$D_1\delta$** and **δ_+** can be recognized in the absorption spectrum of **$D_1\delta_+$**, their spectral shifts (from 425 to 421 nm for **D_1** and from 480 to 504 nm for **δ_+**) reveal the electronic coupling between the **D_1** and **δ_+** moieties. The lowest excited state of **$D_1\delta_+$** is located

on δ_+ and displays a fluorescence spectrum similar to that of δ_+ but with a 49 nm red shift from 598 to 647 nm. And the existence of δ_- ($\mathbf{D_1\delta A}$ *vs.* $\delta_-\mathbf{D_1\delta A}$ and $\mathbf{D_1\delta_+A}$ *vs.* $\delta_-\mathbf{D_1\delta_+A}$) does not change the absorption spectral feature as shown in Figure IV.2(B)

The absorption spectrum of **A** indicates that the lowest energy transition exhibits a strong vibrational structure as three individual peaks at 460, 490 and 527 nm. The peak separation of vibronic progression is 1400 cm^{-1}, whose vibrational mode frequency is associated with an out-of-phase C-C stretch of PDI core. The fluorescence of **A** obeys Kasha's rule and stands as a Stokes-shifted mirror image of the $S_0 \rightarrow S_1$ transition band with identical vibrational structure (at 536, 575 and 625 nm), indicating fast relaxation from the Franck-Condon (FC) region to the vibrationally relaxed excited state.

It is critical to confirm if the electronic coupling exists between donor moieties and acceptor moiety in the ground state. Figure IV.2(B) displays normalized absorption spectra at 527 nm of $\mathbf{D_1\delta A}$ (black curve), $\delta_-\mathbf{D_1\delta A}$ (blue curve) $\mathbf{D_1\delta_+A}$ (red curve) and $\delta_-\mathbf{D_1\delta_+A}$ (purple curve) with comparison of individual moiety ($\mathbf{D_1\delta}$ (black dot line) $\mathbf{D_1\delta_+}$ (yellow dot line) and **A** (blue dot line)) in chloroform. The absorption spectra of four dyads could be decomposed as a linear spectral combination of their donor moieties and acceptor moiety, indicating that coupling between donor and acceptor is negligible. Thus, molecules will be considered as two individual parts.

Increasing the repeated unit number n for $\mathbf{D_n\delta_+A}$ in chloroform, the donor length has a significant influence on the absorption spectrum, as shown in Figure IV.2(C) since the HOMO (Highest Occupied Molecular Orbital) of $\mathbf{D_n\delta_+}$ is localized on the D_n unit. Thus the absorption spectrum has a red shift with increasing donor length (62 nm, 10 nm, and 8 nm respectively) and its amplitude is roughly proportional to the donor length. The red shift is due to increase the length of $\mathbf{D_n}$.

In order to investigate the interaction between molecules and environment, $\mathbf{D_1\delta A}$, $\mathbf{D_1\delta_+A}$ and $\delta_-\mathbf{D_1\delta A}$ are dissolved in three solvents of increasing polarity: toluene (ε=2.38), trichloroethylene (TCE, ε=3.42) and chloroform (ε=4.89). Figure IV.2(D) shows $\mathbf{D_1\delta_+A}$ absorption spectra in these three solvents normalized at 529 nm. No significant spectral feature change is observed, besides a 3 nm blue shift for TCE.

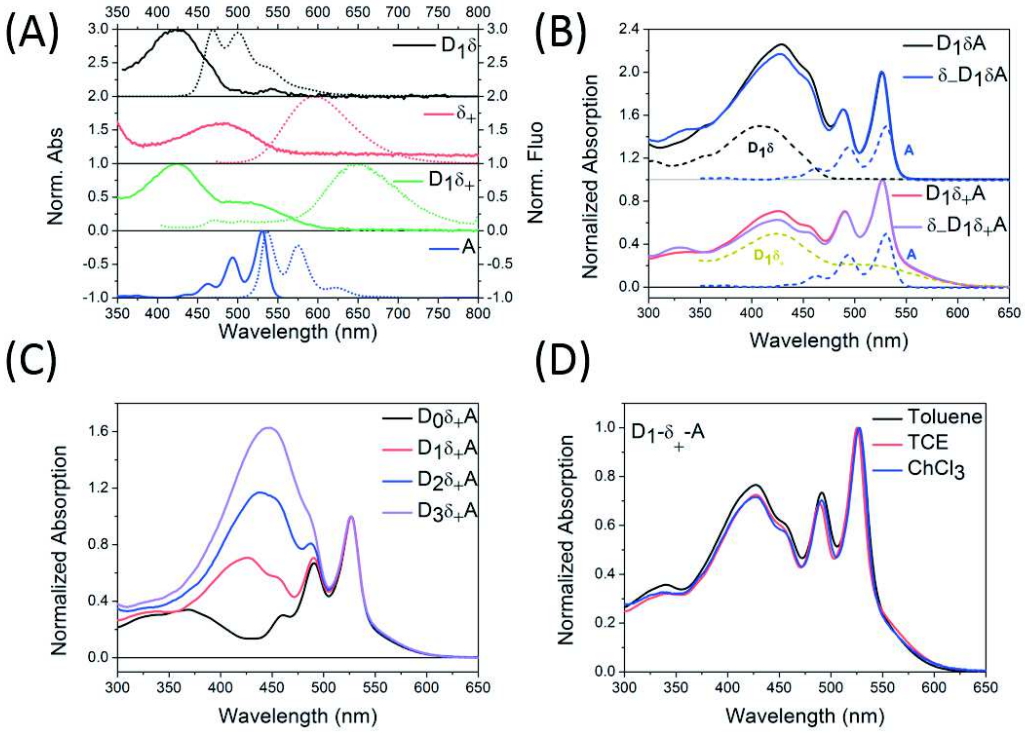

Figure IV.2 Steady-state absorption and fluorescence measurements (A) Normalized absorption (solid lines) and fluorescence spectra (dotted lines) of **D₁δ** (black curves), **δ₊** (red curves), **D₁δ₊** (green curves) and **A** (blue curves) in chloroform (B) Absorption spectra normalized at 527 nm of **D₁δA** (black curve), **δ-D₁δA** (blue curve) **D₁δ₊A** (red curve) and **δ-D₁δ₊A** (purple curve) with comparison of individual moieties (**D₁δ** (black dotted line), **D₁δ₊** (yellow dotted line) and **A** (blue dotted line)) in chloroform (C) Absorption spectra normalized at 527 nm of **Dₙδ₊A** (n=0: black curve, 1: red curve, 2:blue curve and 3: purple curve) in chloroform (D) Absorption spectra normalized at 527 nm of **D₁δ₊A** in toluene (black curve), trichloroethylene (TCE, red curve) and chloroform (blue curve)

IV.2.1.2 Spectro-electro-chemistry

As said in § III.2.3, it is important to have as much spectral information as possible about the expected species involved in a given system studied by transient absorption spectroscopy. Since in OSCs, one expects to create charges, characterizing the spectra of charged species is of prime interest. Spectro-electro-chemistry was used to obtain those spectra. The experiments were performed by Kirsten Bruchlos at the *Institut für Polymerchemie* in Stuttgart in S. Ludwigs' team. The experimental setup is described in ref.108.

The molecules are dissolved in 1mg/ml in DCM. The energy potentials are shown in Table IV.2 and energy levels of HOMO (Highest Occupied Molecular Orbital), and LUMO (Lowest Unoccupied Molecular Orbital) are presented in Figure IV.3(A). The Figure IV.3(B) shows normalized absorption spectra of charged species: cation $(\mathbf{D_1\delta})^+$ (black curve), cation $(\delta_+)^+$ (red curve), cation $(D_1\delta_+)^+$ (green curve) and anion A^- (blue curve).

The main spectral feature of $(\mathbf{D_1\delta})^+$ is the absorption band around 707 nm. $(\delta_+)^+$ has the similar spectral feature with a 51 nm red shift at 758 nm. And $(D_1\delta_+)^+$ has a broader band centered at 700nm. The 7 nm blue shift compared with $(D_1\delta)^+$ indicates that the cation is located on $\mathbf{D_1}$ rather than on δ_+. A^- is easily recognized by three characteristic distinct peaks at 719, 803 and 970 nm.

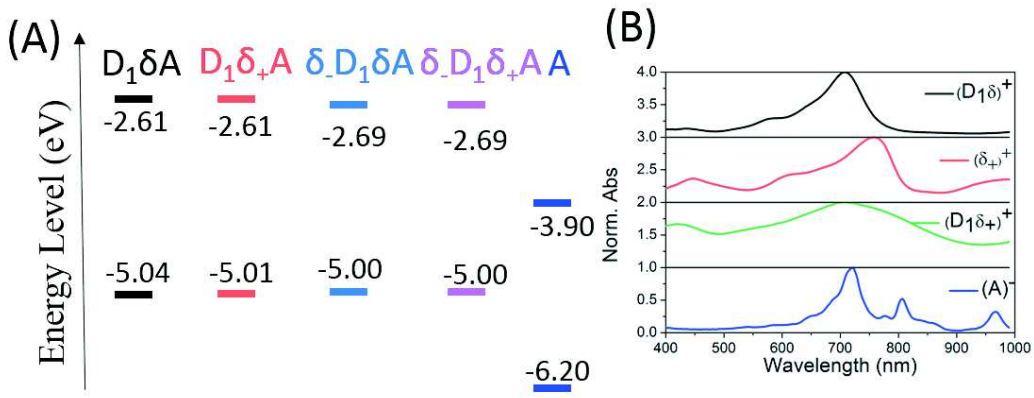

Figure IV.3 (A) Diagram energy levels of **D₁δA**, **D₁δ₊A**, **δ₋D₁δA**, **δ₋D₁δ₊A** and **A** in DCM by spectro-electro-chemistry (B) Absorption spectra normalized of **D₁δ** (black curve), **δ₊** (red curve), **D₁δ₊** (green curve) and **A** (blue curve) in DCM

Table IV.2 Oxidation and reduction energy of four molecules in DCM and respective HOMO/LMUO energy, showing in Figure IV.3(A).

	E^{ox} (eV)	E^{red} (eV)	E_{HOMO}(D) (eV)*	E_{LUMO}(A) (eV)*
D₁δA	-0.06	-1.32	-5.04	-3.78
D₁δ₊A	-0.09	-1.27	-5.01	-3.83
δ₋D₁δA	-0.10	-1.27	-5.00	-3.83
δ₋D₁δ₊A	-0.10	-1.24	-5.00	-3.86

*$E_{HOMO}(D) = -(E^{ox}+5.1)$ and $E_{LUMO}(A) = -(E^{red}+5.1)$, noted in Figure IV.3(A)

Table IV.3 summarizes the steady-state spectral properties useful for the analysis of time-resolved results.

Table IV.3 Characteristic wavelengths of the ground state, charged state and excited state, as well as the fluorescence of individual moieties of the **D₁δA** and **D₁δ₊A** dyads in solution.

	Absorption	Fluorescence	Radical ions	ESA*
D₁δ	425 nm	468 and 499 nm	707 nm	697 nm
δ₊	323 and 478 nm	598 nm	758 nm	-
D₁δ₊	343, 421 and 504 nm	647 nm	700 nm	-
A	460, 490 and 527 nm	536, 575 and 625 nm	719, 803 and 970 nm	709 nm

* Individuals transient absorption experiments data[111]

IV.2.2 Time-resolved spectroscopy

In order to study intramolecular properties, **D-A**s are dissolved in chloroform, except when studying the solvent effect (in which case toluene or trichloroethylene was used.). The concentration of **D-A**s is around 0.25m mol/L to achieve an optical density of 0.4 in a 1-mm cuvette at 400 nm. For the time-resolved experiments, the sample is circulated in a 0.5 mm flow cell with a peristaltic pump and appropriate tubing (resistant in the used solvent) to avoid photodegradation. The excitation wavelength is 400 nm in the $S_0 \rightarrow S_1$ absorption band of **D** with an intensity of 20 nJ/pulse in the linear response regime with 40 fs pulse duration. The previous study by Dr. Roland shows no dynamic difference of excitation of D or A.[112] The relative polarization of pump and probe is setted as 54.7°, the magic angle. More information on the experimental setup and data processing are given in § III. The photophysical properties of **D_1δA** in chloroform are treated here as a case study illustration. A typical 2D plot of a transient absorption data set after data processing is illustrated as Figure IV.4 with the horizontal axis representing wavelength, the vertical axis representing delay time between the pump and the probe and the color representing the absorption changes.

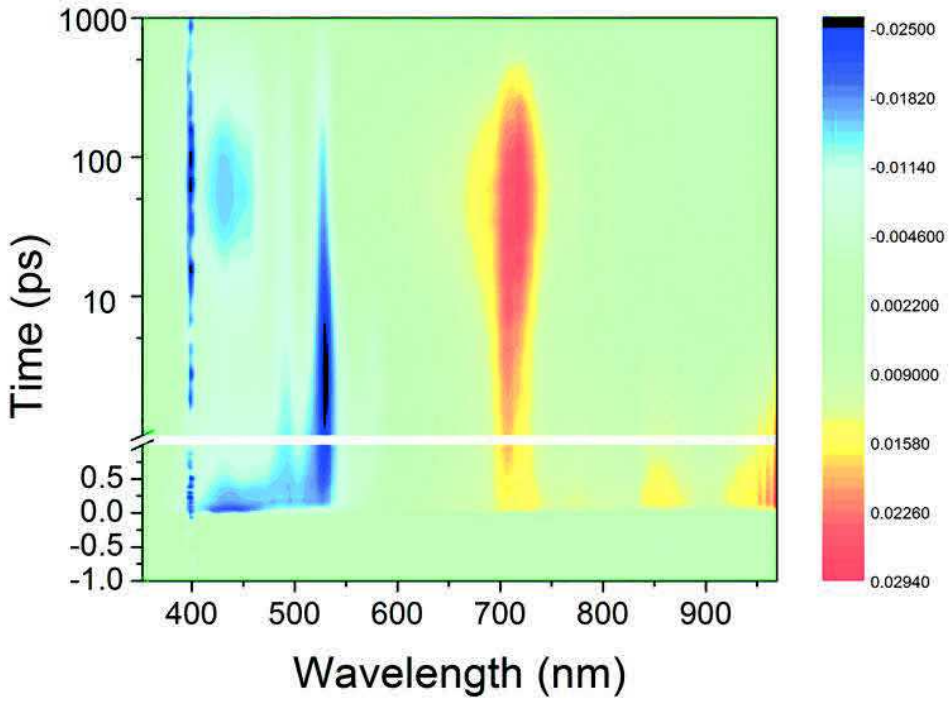

Figure IV.4 2D plot of transient absorption data set of **D_1δA** in chloroform excited at 400nm, the horizontal axis representing wavelength, the vertical axis representing delay time between the pump and the probe and the color representing the absorption changes.

The spectral evolution of the transient absorption (TA) signals, namely differential absorption spectra (ΔA), is presented in Figure IV.5. The first hundred femtoseconds exhibit changes in the absorption spectra with a broad negative band below 585 nm and three positive peaks at 700, 850 and 960nm, as the ΔA at t=100 fs (black curve). Within the first picosecond, a second characteristic differential absorption spectrum (t=1.2 ps, purple curve) with four individual negative peaks at 460, 490, 525 and 575 nm and a pronounced positive band centered at 710nm is formed.

After the first tens of picoseconds (Figure IV.5(B)), the differential spectral feature (t= 30 ps, blue curve) changes as the negative band around 410 nm reforms, the negative peak at 575

disappears, and the positive band at 710 nm broadens with an additional positive peak at 800 nm. This signal decays without any spectral change until several nanoseconds.

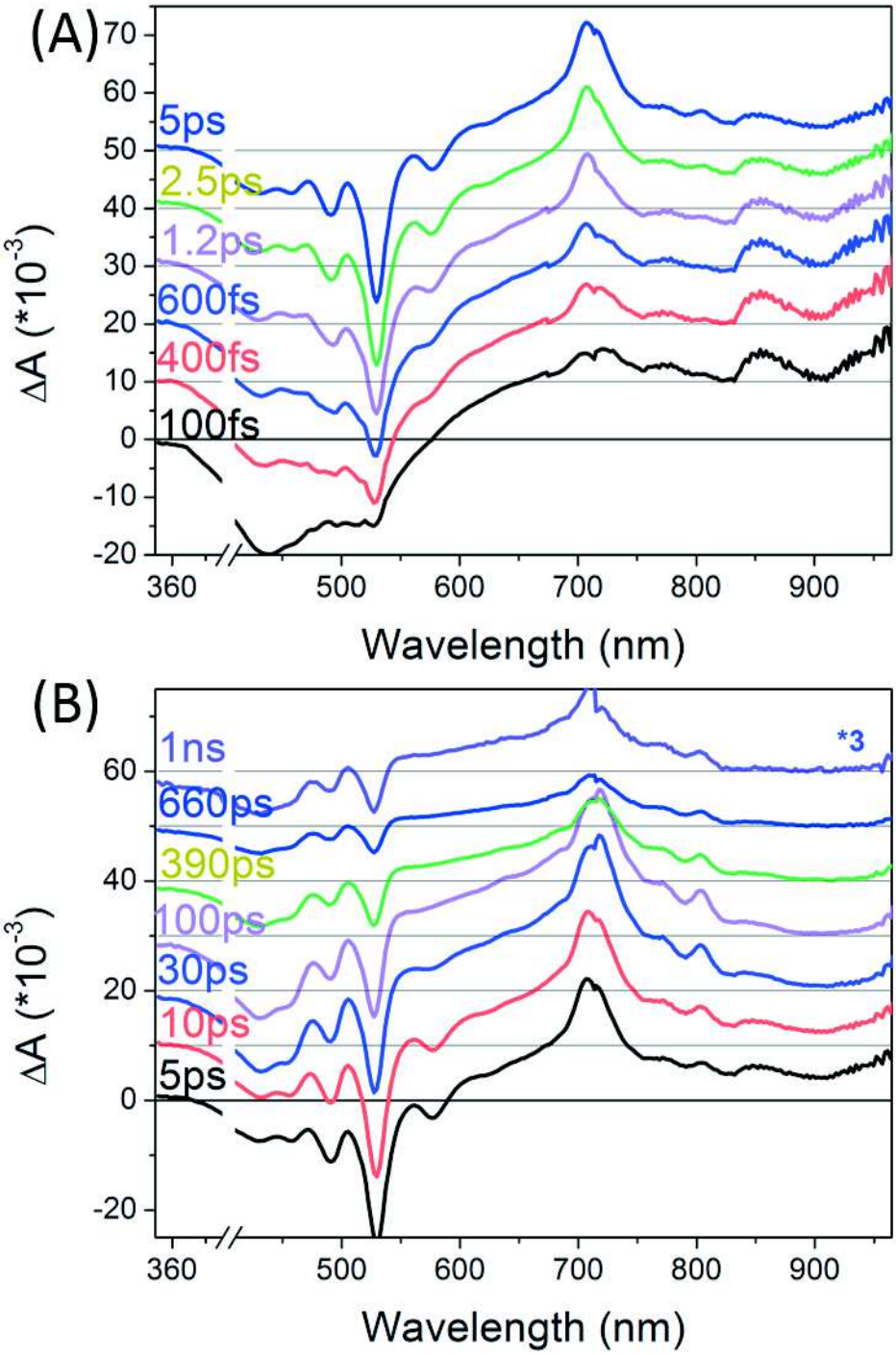

Figure IV.5 Selection of differential absorption spectra of **$D_1\delta A$** in chloroform (A) within the first 5ps, showing the formation of **D** excited state and energy transfer from **D** excited state to **A** excited state (B) until 1ns, illustrating the formation of CT state from **A** excited state and CT state recombination. The differential absorption spectrum at 1ns is magnified by 3 to show the spectral feature.

A selection of the corresponding differential absorption (ΔA) spectra (20 fs, 2.5 ps 28 ps) is displayed in Figure IV. 6(A) to (C). Each spectrum can be decomposed into a sum of contributions of individual species/states, the spectroscopic signatures of which are identified by steady-state experiments (§ IV.2.1).

At early times (Figure. IV.6(A)) the differential spectrum at 20 fs (green symbols curve) features a broad negative band below 585 nm, containing **$D_1\delta$** Ground State Bleach (GSB, purple pattern) and Stimulated Emission (SE, yellow pattern), and is thus attributed to the excited state of the donor (**$(D_1\delta)^*$**). The positive signal at a longer wavelength (Figure IV.5(A)) is assigned to the Excited State Absorption (ESA) of **$D_1\delta^*$**, in line with previous identification of the same signature on similar compounds.[93] The minor mismatch is due to experimental artifacts, such as Raman peak and cross-phase modulation, but also, most probably, due to an ESA at < 400nm reducing the GSB.

After 2.5 ps (Figure IV.6(B)), the features of **$(D_1\delta)^*$** (broad structureless negative band, purple pattern) have reduced significantly and are replaced by four new negative peaks at 460, 490, 530 and 575 nm, which are easily distinguished as the absorption (blue pattern) and fluorescence bands (dark yellow pattern) of **A**, and the positive ESA peak at 700 nm (not shown here, see Figure. IV.5[111]. Hence, these signals are GSB of A and SE from the excited state **A***. This and the reduced bleach of **$(D_1\delta)$** indicate that the population of **$(D_1\delta)^*$** has decayed within a few picoseconds due to an energy transfer from **$(D_1\delta)$** to **A** and forms **A***. The fast energy transfer is expected as the spectral overlap between the fluorescence band of **$(D_1\delta)$** and the absorption band of **A** (Figure IV.2(A)) is substantial.

In the 28 ps differential spectrum (Figure IV.6(C)), the negative peaks at 490 and 530 nm (blue pattern) persist while the band at 410 nm (purple pattern) associated with the donor's bleach reforms, indicating that the ground states of both **$D_1\delta$** and **A** are depopulated. Simultaneously, the spectral features of the induced absorption (at wavelength > 550 nm) are reproduced well by the sum of the anion and cation photo-product absorption (PA) spectra (peaks at 710 and 800 nm for **A^-** (red pattern), and a broad induced absorption from 500 to 800 nm (black pattern) for **$(D_1\delta)^+$**). It proves that within a few tens of picoseconds, a charge transfer has occurred, forming the CT state composed of the **$(D_1\delta)^+$** and **A^-** ion radicals. On longer time scales, the differential spectra do not change in shape, but only their amplitudes decrease, showing that the charge-transfer (CT) state recombines, reforming the ground state.

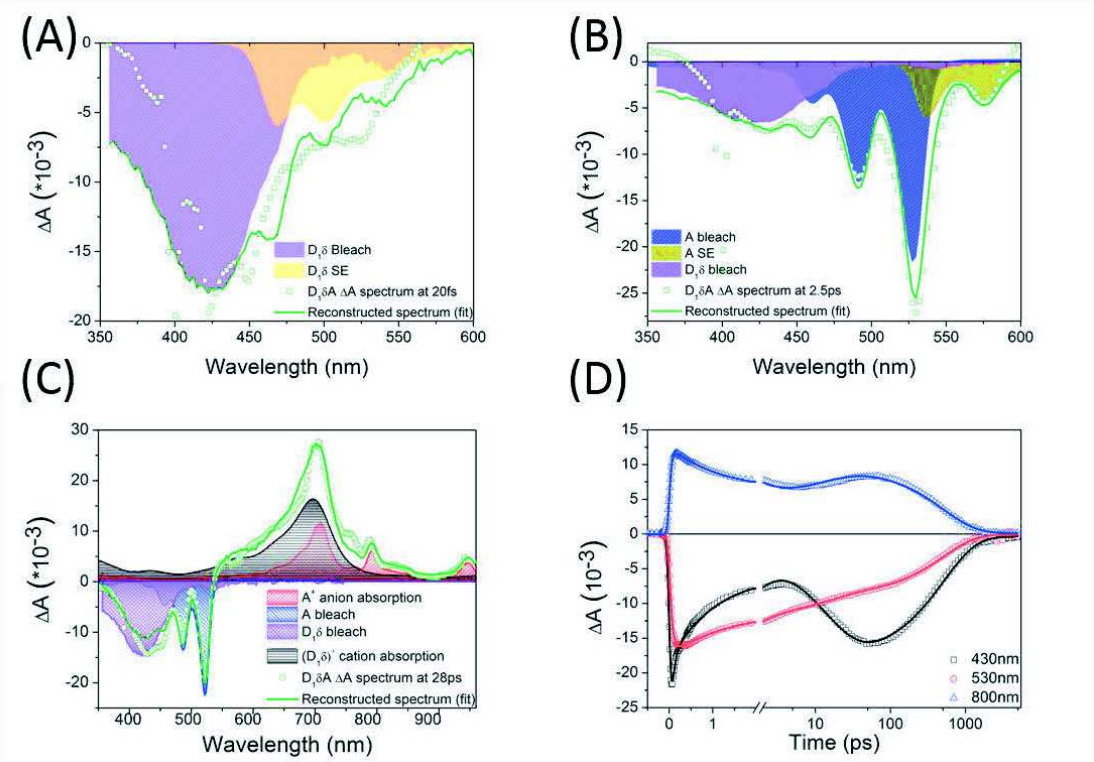

Figure IV.6 Identification of photo-induced states (A) Differential absorption spectrum at 20 fs (green symbol curve) with its fit (green solid curve) as a linear construction of steady-state absorption spectra of $\mathbf{D_1\delta}$(bleach, purple pattern) and steady-state fluorescence of $\mathbf{D_1\delta}$(SE, yellow pattern). The good agreement with its fit is evidence for $(\mathbf{D_1\delta})^*$. (B) Differential absorption spectrum at 2.5ps (green symbol curve) with its fit (green solid line) as a linear combination of steady-state absorption spectra of **A** (bleach, blue pattern), steady-state fluorescence of **A** (SE, dark yellow pattern) and steady-state absorption spectra of D (bleach, blue pattern). The good agreement with the fit is evidence for **A***. (C) Differential absorption spectrum at 28ps (green symbols curve) with its fit (green solid curve) as a linear construction of steady-state absorption spectra of $\mathbf{D_1\delta}$(bleach, red pattern) **A** (bleach, blue pattern) $\mathbf{A}^-$ (red pattern) and $(\mathbf{D_1\delta})^+$ (black pattern). The good agreement with its fit is evidence for CT state. (D) Selected kinetic traces (symbol curves) and global fit (solid curves) observed for $\mathbf{D_1\delta A}$ in chloroform and corresponding to the donor GSB at 430 nm (black), the acceptor GSB at 490 nm (red) and the anion signature at 800 nm (blue).

The TA kinetics measured at different characteristic wavelengths allow characterizing the time evolution of the various absorption bands. These kinetics (symbol curves) and their respective fits are presented in Figure IV.6(D) (solid curves with same colors, temporal parameters are the same as obtained by global analysis on the whole spectral range). The 430 (black symbol curve) and 530 nm (red symbol curve) monitor the GSB of $\mathbf{D_1\delta}$ and **A** respectively. The 800 nm kinetic trace (blue symbol curve) is the signature of ESA(A) at the early time and of anion species at a long time.

In summary,

- Within the first few hundred femtoseconds, **A**'s GSB is formed while and $\mathbf{D_1\delta}$'s GSB decreases, indicating that energy transfer from $\mathbf{D_1\delta}$ to **A** occurs.
- At a later time (first ten picoseconds), the $\mathbf{D_1\delta}$'s GSB rises while **A**'s GSB remains, accompanied by the formation of the charged species spectral feature. This kinetic and spectral behavior points out the formation of CT state.
- Then, three kinetic traces go back to zero simultaneously in less than one nanosecond.

More precise rate constants with their associated differential spectrum (Decay Associated differential Spectrum, DAS) are carried out through the global analysis (§ III.3.2).
Five time constants are needed to achieve a fit with satisfying residuals: 60 fs, 1.2 ps, 14 ps, 500 ps and 2.2 ns, as their Decay Associated differential Spectra (DAS) shown in Figure IV.7 and corresponding to the following reaction scheme.

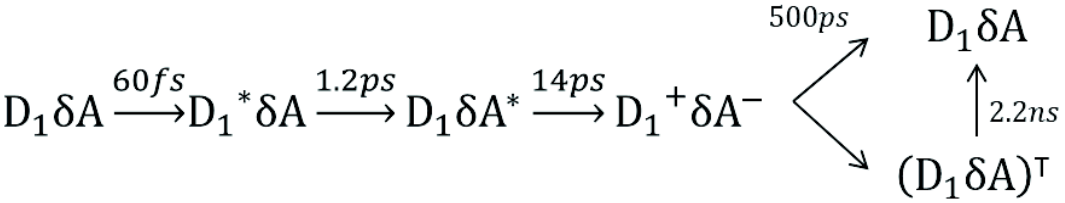

- The first very short time constant (60 fs, black curve) is close to the experimental time resolution, the spectral features are a mixture of artifacts, due to pump and probe cross-phase modulation, thermalization of the GSB spectrum of **D₁δ**, and the rise of the ESA of (**D₁δ**)* (>700 nm). Consequently, the 60 fs spectral evolution is due to (**D₁δ**)* excited state equilibration.
- DADS2 (1.2 ps, red curve) shows the energy transfer from **D₁δ** to **A**, as the GSB of **D₁δ** decays in the 400 to 500 nm range and the GSB, SE, and ESA of the **A** are formed (peaks at 490, 535, 575 and 705 nm).
- The formation of the CT state is then associated with the 14 ps time constant through hole transfer. In DADS3 (14 ps, blue curve), the positive band from 400 to 500 nm along with negative peaks at 719 and 806 nm mean the reformation of **D₁δ**'s GSB and the formation of the CT state. The negative peaks at 535 and 575 nm due to the decay of the SE also confirm this process.
- DADS4 (500 ps purple curve) matches with spectro-electro-chemistry measurement as shown in Figure IV.6(C) and represent the CT state recombination in 0.50 ns.
- The long-lived DADS5 (2.2 ns green curve) has the similar spectral form as DADS4 with ten times less amplitude and is probably due to a minority of longer-lived molecular conformation of the same CT state or a triplet state.

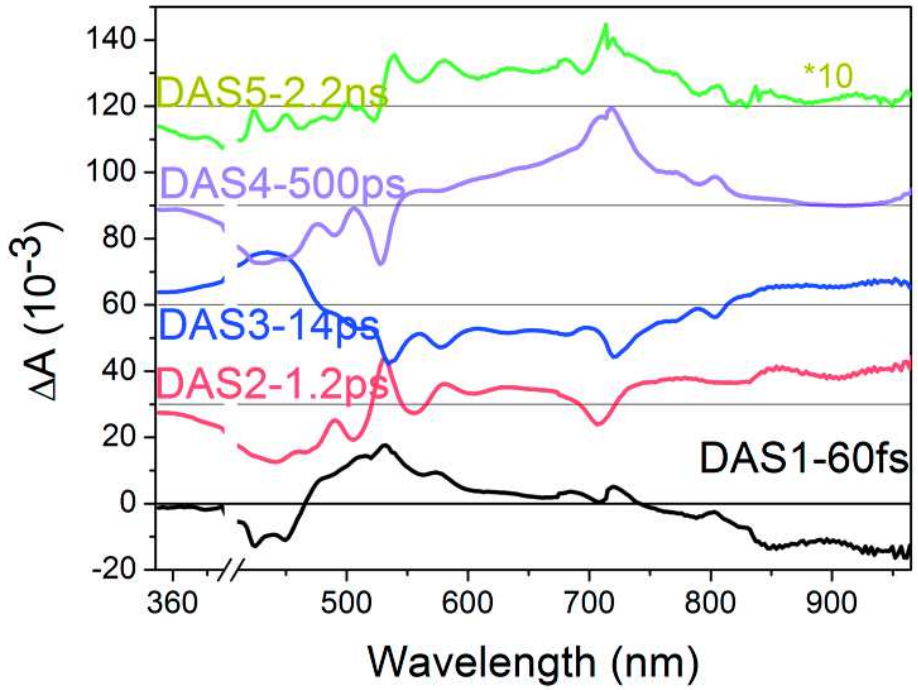

Figure IV.7 Decay-Associated Differential Spectra of **D₁δA** excited at 400nm obtained by global analysis.

IV.2.2.1 Effect of donor moiety

Different donor moieties are studied to monitor the influence of the chemical design on photoinduced properties, especially CT state dynamics. Adding the benzothiadiazole unit (δ_+) shows a strongly red-shifted (from 500 nm for **$D_1\delta$** to 647 nm for $D_1\delta_+$) fluorescence spectrum, resulting in a mismatch with the acceptor absorption (Figure IV.2). The energy transfer, more specifically Förster Resonance Energy Transfer (FRET, § I.3.2), from ($D_1\delta_+$) to **A** is thus not expected in this case.

With the absence of FRET, the main difference compared to the above **$D_1\delta A$** is the direct formation of the CT states from the excited donor state ($D_1\delta_+$)*. The Figure IV.8(A) illustrates the differential absorption spectra at 80 fs (black curves) and 3.5 ps (red curves) of **$D_1\delta A$** (Top panel) and **$D_1\delta_+A$** (Bottom panel). In the case of **$D_1\delta_+A$**, contributions of $D_1\delta_+$ bleach and SE are observed, but there is no signature of the excited **A*** state such as SE at 575 nm or the ESA at 705 nm. The absence of energy transfer from $D\delta_+$ to **A** is confirmed. The only difference observed is an ESA change with an increased peak at 950 nm, attributed to the vibrational relaxation of the molecule.

However, despite the lack of excitation of **A**, a signal akin to the bleach of **A** is observed in the 500 nm region. In line with other reports,[113,114,115] we attribute it to a Stark shift of **A**'s absorption. This is most likely due to the intramolecular dipole moment on ($D_1\delta_+$)*, with the electron localized on the δ_+ spacer with high electron affinity.

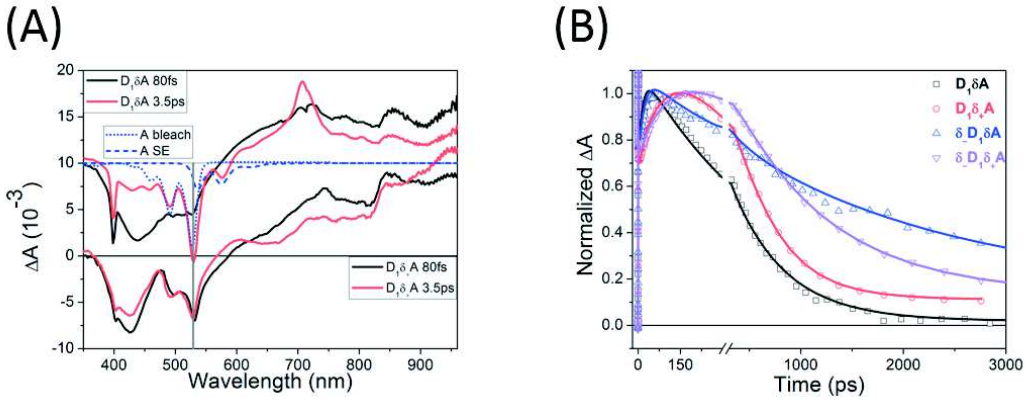

Figure IV.8 (A) Influence of δ_+ in chloroform. Top: In **$D_1\delta A$**, the 80 fs spectrum contains the contributions of the **$D_1\delta$**'s GSB and SE, while the 3.5 ps one displays the excited state of **A**, through its bleach, SE (blue curves), and ESA (peak at around 700 nm), indicating the energy transfer from **$D_1\delta$** to **A** on the few ps time scale. The negative peak at 400nm is due to pump light scatter. Bottom: in **$D_1\delta_+A$**, both differential spectra show similar features, involving $D_1\delta_+$'s GSB and SE, but also a shape akin to that of **A**'s GSB. Yet, no SE nor ESA from **A*** nor induced absorption from A^- can be seen: this is explained by the localization of the excitation on the δ_+ group, that Stark-shifts the absorption band of **A**. (B) Kinetics at 800 nm, where the anion A^- absorbs preferentially, normalized at their second maximum, corresponding to the maximum CT state population.

Figure IV.8(B) highlights the influence of the nature of the spacer (either **δ** or δ_+) between **D_1** and **A**, and that of the terminal **δ**- on **D_1**, through the kinetic traces at 800 nm, the signature of A^-. Table IV.5 summarizes the time constants associated with the CT formation and recombination in chloroform. The addition of δ_+ slows down the CT formation time as the rise time of the CT state. Two molecules with δ_+ have CT state formation times at least 5 times slower than the compounds with the regular **δ** spacer, since the rise time of the anion absorption band is 90 ps and 120 ps for **$D_1\delta_+A$** (red) and δ-$D_1\delta_+A$ (purple) *vs.* 14 ps for **$D_1\delta A$** (black) and δ-$D_1\delta A$ (blue). It may be due to the lack of FRET in the presence of δ_+ and to the fact that CT

state is formed from ($D_1\delta_+$)* as the initial delocalization plays a major role in charge transfer formation rate.[116] Conversely, δ_+ does not have a significant impact on charge recombination kinetics, as very similar decay kinetics for **$D_1\delta A$** (black) and **$D_1\delta_+A$** (red) or for **$\delta_-D_1\delta A$** (blue) and **$\delta_-D_1\delta_+A$** (purple).

The presence of the terminal amine **δ_-** lengthens the CT state recombination time, since the lifetimes of the CT states are increased by a factor of about 2.5 for molecules with the **δ_+** spacer (**1.2** ns for **$\delta_-D_1\delta_+A$** *vs.* **0.48** ns for **$D_1\delta_+A$**) and of 4.5 with the **δ** spacer (**2.3** ns for **$\delta_-D_1\delta A$** *vs.* 0.51 ns for **$D_1\delta A$**). This effect is expected to be due to the larger separation distance between the charges of the CT state in molecules where **δ_-** would stabilize the positive charge on the extremity of the donor moiety, further away from the acceptor. A quantitative analysis by Marcus-Jornter theory is presented in § IV.2.3.

V.2.2.2 Effect of donor length

Based on the classical Marcus theory, the elongation of charge separation distance should lead to a longer CT state recombination lifetime, since the electronic coupling A and D is reduced. The different donor length of **$D_n\delta_+A$** and **$\delta_-D_n\delta A$** molecules with n=0 ~ 3 and n=0 ~ 2 are synthesized and studied in chloroform. The same species identification procedure as in **$D_1\delta A$** is carried out and indicates that CT states are formed in all cases. The global analysis is applied to determine the time constants associated with the CT state recombination in each case, and the results are displayed in Table IV.4.

In the case of **$D_n\delta_+A$** (Figure IV.9(A) showing traces at 800 nm, symbols represent experimental data, and solid curves are fitted with same temporal parameters as global analysis), the donor length has no impact on CT state formation and recombination time, resulting in the range of a 100 ps formation time and a 450 ps recombination time. This lack of changes could be due to the effect of **δ_+**. The CT states are more located near to the **A**, rather than on the opposite side of **D**.

As illustrated in Figure IV.9(B), an entirely different observation is made with the **$\delta_-D_n\delta A$** molecules: the terminal δ_- stabilizes the CT state as the optimal donor length n=1 (blue curves) , with an increase of the CT state lifetime up to 2.3 ns. (0.4 ns and 1.1 ns for n=0 and n=2, respectively, in black and red) This could be understood as previously as an effect of spreading further apart the charges along the molecule, which is however optimally efficient for a not-too-long donor moiety.

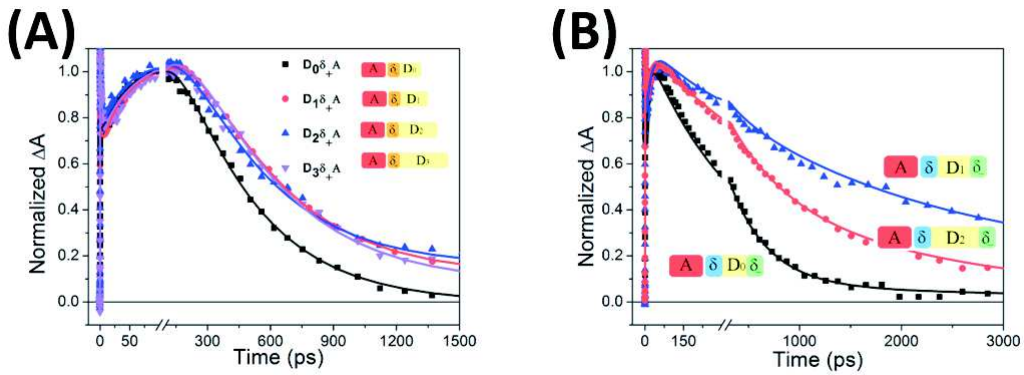

Figure IV.9 Kinetic traces at 800nm: Effect of donor length for the (A) **$D_n\delta_+A$** molecules, with n = 0 (black), 1 (red), 2 (blue) or 3 (purple). The donor length almost has no effect on the CT formation and recombination times for molecules without **δ_-**. (B) **$\delta_-D_n\delta_+A$** molecules, with n = 0 (black), 1 (red), 2 (blue). The CT state lifetime is optimal for n=1.

Table IV.4 Charge transfer state formation and recombination time constants for $D_n\delta^+A$ and $\delta^-D_n\delta A$ with increasing donor length.

n	$D_n\delta^+A$		$\delta^-D_n\delta A$	
	Formation	Recombination	Formation	Recombination
0	90ps	410ps	20ps	0.4ns
1	90ps	480ps	14ps	2.3ns
2	150ps	440ps	14ps	1.1ns
3	140ps	430ps		

IV.2.2.3 Effect of solvent

To investigate the influence of the interaction with the environment, and in particular of the solvent polarity, we compare the results obtained in chloroform to toluene and TCE for the **$D_1\delta A$**, **$D_1\delta^+A$,** and **$\delta^-D_1\delta A$** molecules. The kinetic traces at 800 nm are depicted in Figure IV.10. Table IV.5 displays the CT state formation and recombination time constants obtained by global analysis.

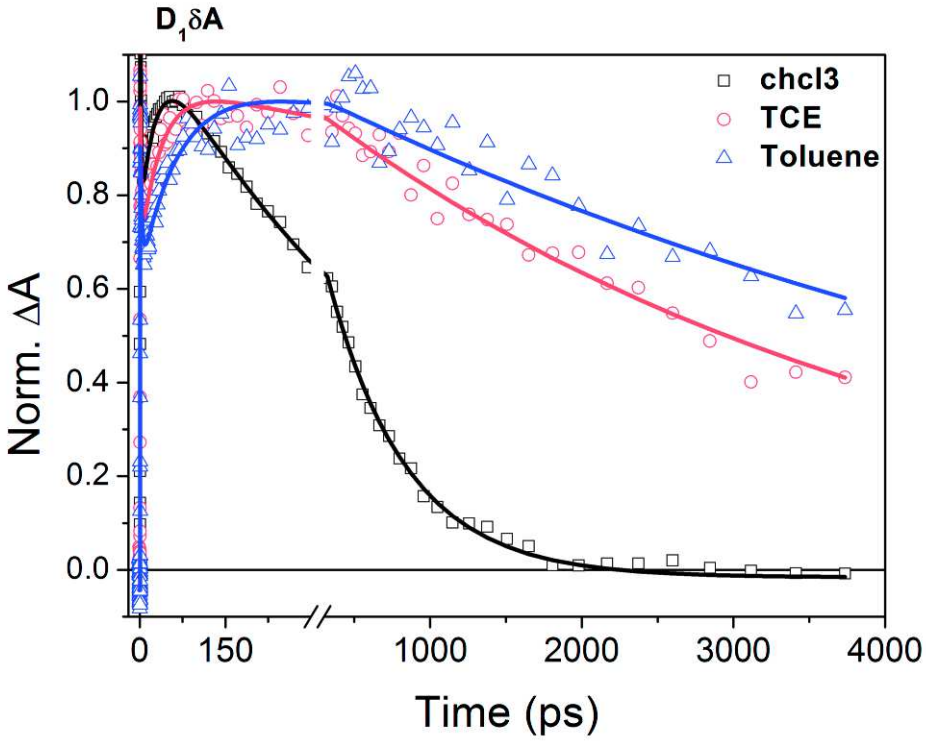

Figure IV.10 Kinetic traces at 800 nm of **$D_1\delta A$** in different solvents (symbol curves) with their fits (solid curves): $chcl_3$ (black curves), TCE (red curves) and toluene (blue curves).By decreasing solvent polarity, the CT state lifetime is significantly extended.

For each molecule, the CT states are stabilized, as their lifetimes increase, in less polar solvents. However, the stabilizing effect of **δ^-** previously observed in chloroform is not as large as the effect of these solvents. Due to experimental limitations, a precise determination of the > 5 ns CT lifetimes is not possible. This would require measuring the kinetics over a time span longer than accessible in our femtosecond pump-probe experiment (6 ns).

Table IV.5: Effect of the solvent polarity: CT state formation and recombination time constants (in ns) of **$D_1\delta A$**, **$D_1\delta_+A$** and **$\delta_-D_1\delta A$** in toluene, trichloroethylene (TCE) and chloroform. The bulk dielectric constants are from[117].

Solvents Dielectric constants ε		Toluene ε=2.38 (3.5*)	TCE ε=3.42	Chloroform ε=4.81
$D_1\delta A$	Formation (ns)	0.026	0.014	0.014
	Recombination (ns)	5.7	4	0.50
$\delta_-D_1\delta A$	Formation (ns)	0.030	0.019	0.014
	Recombination (ns)	6.7	6	2.3
$D_1\delta_+A$	Formation (ns)	0.26	0.15	0.090
	Recombination (ns)	6.2	2.8	0.48
$\delta_-D_1\delta_+A$	Formation (ns)			0.12
	Recombination (ns)			1.2

*An effective dielectric constant of 3.5 is found in literature for toluene, to account for the effect of its strong electric quadrupole moment.[118]

IV.2.3 Marcus-Jortner Analysis

In order to clarify the observed influence of the molecular structure and solvent polarity on the CT state formation and recombination, Marcus theory (in § I.3.3) is not sufficient and the data were analyzed according to Marcus-Jornter theory[20], which doesn't assume the high-temperature limit T>150K[119] and includes the vibrational states.

Within that theory, the rate constant k for the electron transfer occurring upon CT state formation or recombination can be written as:[114,115]

$$k = \left(\frac{4\pi^3}{h^2 \lambda_{sol} k_B T}\right)^{1/2} V^2 \exp\left(-\frac{\lambda_{mol}}{E_{vib}}\right) \sum_{n=0}^{\infty} \frac{\left(\frac{\lambda_{mol}}{E_{vib}}\right)^n}{n!} \exp\left(-\frac{(\Delta G^o + \lambda_{sol} + nE_{vib})^2}{4\lambda_{sol} k_B T}\right) \quad \text{Eq.IV.1}$$

where V is the electronic coupling between initial and final states, k_B the Boltzmann constant and T the temperature (room temperature in our case: 298K). λ_{mol} is the intramolecular reorganization energy, which is computed by geometry optimization in the relevant states (coll. I. Burghardt) and displayed in Table IV.6. E_{vib} is the energy of an effective, high-frequency vibrational mode and is set here to 1500 cm^{-1} (0.186 eV), the characteristic frequency of C=C bond stretching, λ_{sol} is the solvent reorganization energy, which is estimated in different solvents by the Born-Hush approach:[117]

$$\lambda_{sol} = \frac{e^2}{4\pi\varepsilon_0}\left(\frac{1}{2r^+} + \frac{1}{2r^-} - \frac{1}{R_{cc}}\right)\left(\frac{1}{n^2} - \frac{1}{\varepsilon}\right) \quad \text{Eq.IV.2}$$

In this equation, n and ε are the refractive indexes and dielectric constant of the solvent. r^+ and r^- are as the radii of hole and electron densities, and R_{cc} is the computed electron-hole centroid distance.
The Gibbs free energies for charge recombination (ΔG_{CR}^0) and charge separation (ΔG_{CS}^0) in different solvents are calculated from continuum dielectric theory:[120]

$$\Delta G_{CR}{}^0 = -[E_{ox}(D) - E_{red}(A)] + \frac{e^2}{4\pi\varepsilon_0\varepsilon R_{CC}} + \frac{e^2}{8\pi\varepsilon_0}\left(\frac{1}{r^+} + \frac{1}{r^-}\right)\left(\frac{1}{\varepsilon_{ref}} - \frac{1}{\varepsilon}\right) \quad \text{Eq.IV.3}$$

$$\Delta G_{CS}{}^0 = [E_{ox}(D) - E_{red}(A)] - \frac{e^2}{4\pi\varepsilon_0\varepsilon R_{CC}} - \frac{e^2}{8\pi\varepsilon_0}\left(\frac{1}{r^+} + \frac{1}{r^-}\right)\left(\frac{1}{\varepsilon_{ref}} - \frac{1}{\varepsilon}\right) - E_{00} \quad \text{Eq.IV.4}$$

E_{ox} and E_{red} are oxidation and reduction potential energies, respectively. ε_{ref} is the dielectric constant of dichloromethane (ε_{ref}=8.93)[113], in which oxidation and reduction potentials were measured. E_{00} is the energy of the excited state from which the CT state is formed, namely ($\mathbf{D_n\delta_+}$)* for molecules containing $\boldsymbol{\delta_+}$ or **A*** for molecules containing **δ** when resonant energy transfer precedes electron transfer. A Jablonski diagram is shown in Figure V.10(A) illustrating the calculation of Eq. IV. 2 ~ 4. The solvation effect is taken account on the E_{red}(A). The purple ΔG_{CS}^0 implies the CT state formation from ($\mathbf{D_n\delta_+}$)* and the yellow ΔG_{CS}^0 stands for the charge separation from **A*** through the hole transfer after the FRET from $\mathbf{D_1\delta}$ or $\boldsymbol{\delta}$-$\mathbf{D_1\delta}$ to **A** .

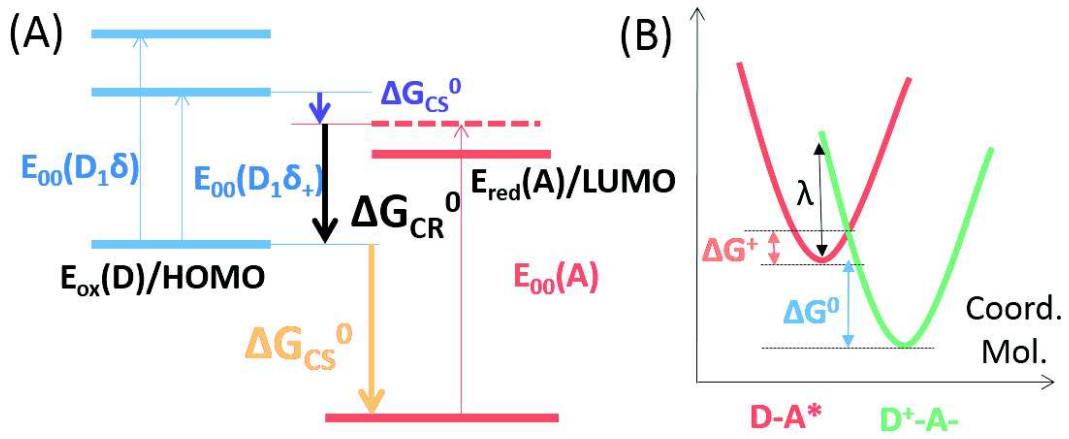

Figure IV.11 (A) Jablonski diagram for the calculation of charge separation and charge recombination, including different pathways to form CT state due to the spacer (**δ** or **δ**$_+$) and (B) Free energy surface of the reactant (**D**$_1$**δ**-**A***) and product ((**D**$_1$**δ**)$^+$-**A**$^-$) as a function of the generalized reaction coordination for electron transfer.

We now apply the Marcus-Jortner formalism to both CT formation and recombination. Tables IV.6 and IV.7 summarize the values of all parameters appearing in Eq. IV.1 to 4 for various solvents and molecules, as well as the computed solvent reorganization energies and Gibbs free energies.

Table IV.6. Parameters and molecular reorganization energies used in the Marcus-Jortner model. r^+ , r^- and R_{CC} are taken as the hole, electron density radii and the distance between electron and hole density centers as calculated from electronic structure modeling (I. Burghardt's team). E_{red} and E_{ox} are the oxidation and reduction potential energies determined experimentally (N. Leclerc, ICPEES). E_{00} is the energy gap between the lowest excited state and the ground state, from which the CT states are formed. λ_{mol}, are the computed molecular reorganization energy for charge recombination and charge formation.

	D$_1$δA	**D$_1$δ$_+$A**	**δ$^-$D$_1$δ$_+$A**
r_+ (nm)	0.8	0.7	0.9
r_- (nm)	0.4	0.4	0.4
R_{cc} (nm)	2.3	2.2	2.5
E_{red} (eV)	-0.40	-0.40	-0.40
E_{ox} (eV)	0.89	0.89	0.81
E_{00} (eV)	2.32	1.92	1.92
λ_{mol} (eV) Formation	0.33	0.30	0.28
λ_{mol} (eV) Recombination	0.57	0.68	0.69

First, we note that CT state recombination takes place in the *Marcus inverted regime* as $-\Delta G^0 > \lambda = \lambda_{sol}+\lambda_{mol}$. CT state formation from (**D**$_1$**δ**$_+$)* and (**δ**$^-$**D**$_1$**δ**$_+$)* occurs in the normal Marcus regime while CT state formation from **A*** happens in the (nearly) optimal Marcus regime, as the difference between $-\Delta G_{CS}^0$ and λ is less than 0.06meV.

Hence, we conclude that changing the solvent polarity would have a stronger influence on the charge recombination than on charge formation. This is confirmed when using the right-hand side of Eq. IV.1 to predict the expected solvent influence on the various ET steps of interest. Since all solvents have a similar refractive index, one can verify that the main solvent influence comes from the change in dielectric constant, by plotting k/V^2 as a function of ε (eq. IV.1 to 4) for different types of ET reactions for **D**$_1$**δ**$_+$**A** and **D**$_1$**δA** characterized by various Gibbs energies (ET from (**D**$_1$**δ**$_+$)*, **A*** or CT states) and different λ_{mol}, r^+, r^-, R_{cc}. An effective dielectric constant of 3.5 for toluene is expected to account for the effect of its strong electric quadrupole moment.[121]

Table IV.7. Estimated solvent reorganization energies λ_{sol} (Eq. IV.2) and Gibbs free energies for charge recombination ΔG^0_{CR} (Eq. IV.3) and charge separation ΔG^0_{CS} (Eq.IV.4)

		Toluene	TCE	Chloroform
ε		3.5	3.42	4.89
n		1.496	1.477	1.446
$D_1\delta A$	λ_{sol} (eV)	0.333	0.344	0.568
	$-\Delta G^0_{CS}$ (eV)	0.739	0.725	0.907
	$\lambda_{CS}=\lambda_{mol}+\lambda_{sol}$ (eV)	0.663	0.674	0.898
	$-\Delta G^0_{CR}$ (eV)	*1.580*	*1.594*	*1.412*
	$\lambda_{CR}=\lambda_{mol}+\lambda_{sol}$ (eV)	*0.903*	*0.914*	*1.138*
$D_1\delta_+A$	λ_{sol} (eV)	0.349	0.360	0.595
	$-\Delta G^0_{CS}$ (eV)	0.323	0.309	0.500
	$\lambda_{CS}=\lambda_{mol}+\lambda_{sol}$ (eV)	0.649	0.660	0.895
	$-\Delta G^0_{CR}$ (eV)	*1.594*	*1.609*	*1.418*
	$\lambda_{CR}=\lambda_{mol}+\lambda_{sol}$ (eV)	*1.029*	*1.040*	*1.275*
$\delta_- D_1\delta_+A$	λ_{sol} (eV)			0.554
	$-\Delta G^0_{CS}$ (eV)			0.585
	$\lambda_{CS}=\lambda_{mol}+\lambda_{sol}$ (eV)			0.834
	$-\Delta G^0_{CR}$ (eV)			*1.333*
	$\lambda_{CR}=\lambda_{mol}+\lambda_{sol}$ (eV)			*1.244*

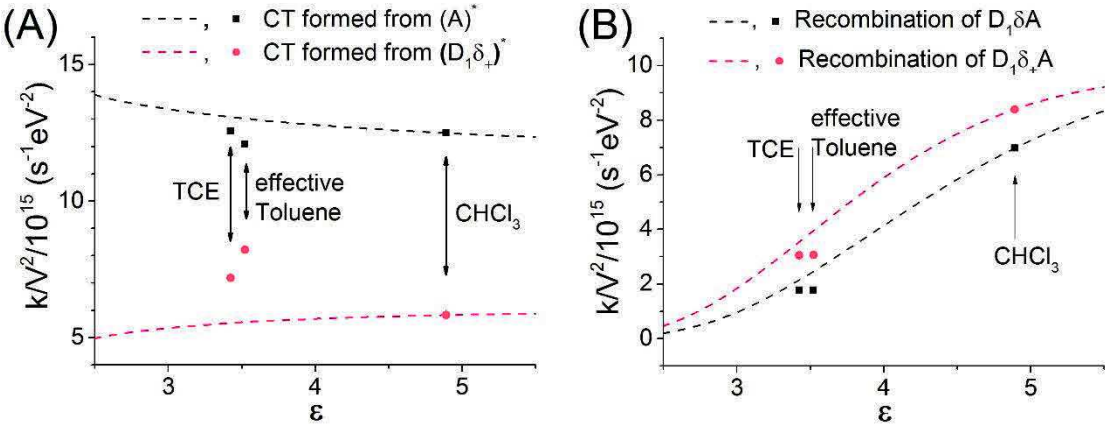

Figure IV.12 Influence of the solvent on k/V^2 as predicted from Eq.IV.1 to 5 for (A) CT state formation from ($D_1\delta_+$)* (red) or A* (black), and (B) CT state recombination in $D_1\delta_+A$ (red) and $D_1\delta A$ (black). Dashed lines illustrate the dependence on ε assuming a fixed value of n (here n = 1.446 corresponding to chloroform), squares and dots give the values computed with the correct values of n and ε (Table IV.5) for each solvent.

Figure IV.12 shows that the change of solvent is expected to affect the CT formation kinetics comparatively weakly (by less than 50%), but the recombination by a factor of ~3, mostly due to the change in ε. These opposite trends can be traced back to the different Marcus regimes (inverted *vs.* quasi-optimal) of CT formation and recombination for the present molecules. Given the very crude level of description of the solvent influence by Eq. IV.2 (which assumes a dielectric sphere kind of model,[119] while the hole and electron density distributions are very much elongated in the present systems), these trends remarkably reproduce the observations, since the solvent influence is indeed significantly stronger for CT recombination than for CT formation (Table IV.5). In addition, by using the observed ET rates for k, we can further exploit Eq.IV.1 and infer the magnitude of the electronic coupling terms V given in Table IV.8. Since

the observed solvent influence on the CT formation and recombination is larger than that predicted by Figure IV. 12, Eq.IV.1 leads to a residual solvent dependence of the electronic coupling term k/V^2. Although a solvent-dependent coupling may be expected due to *e.g.* solvent-induced electrostatic interaction shielding.[22,121] the accuracy of this prediction is uncertain given the very crude approximation made for the solvent reorganization energy (Eq. IV.2). A more accurate modeling of the solvent influence would require a molecular-based (rather than continuous) modeling of the solvent,[19] which goes beyond the scope of the present work.

Table IV.8 shows that the electronic coupling terms V are small, in the range of 0.3 to 2 meV. This is in line with the electronic couplings already computed for very similar dyad compounds[122] or deduced by a similar approach for other large organic donor and acceptor compounds[121] connected by saturated bonds. Interestingly, the faster CT state formation in the compounds containing δ rather than δ_+ as a donor-acceptor spacer clearly appears, resulting from a 2- to 3- fold stronger "hole" coupling between **A*** and CT state than between (**$D_1\delta_+$**)* and CT state.[122]
Importantly, regarding the molecular design strategy, it is most relevant to compare the results obtained for **$D_1\delta A$** / **$\delta\text{-}D_1\delta A$** and **$D_1\delta_+A$** / **$\delta\text{-}D_1\delta_+A$** in chloroform. We note that upon adding the terminal amine **δ-** on **$D_1\delta_+A$** a nearly 3-fold increase in CT state lifetime is observed in chloroform, which, by Eq.IV.1 relates back to a reduction by a factor of 1.7 in the estimated electronic coupling V (Table IV.8). The latter is commonly assumed to be proportional to the overlap between both wavefunctions and to decay exponentially with the electron-hole separation distance in the CT state, according to $V^2=V_0^2\exp(-\beta R_{CC})$.[57] Typical values for the decay length scale have been reported to be in the range of $\beta \sim 0.3\text{-}0.7 Å^{-1}$ for ET through covalent bonds or involving carrier tunneling (superexchange) in organic molecules[57,123-125]. The quantum calculation finds actually two CT states with R_{CC} = 23 Å (CT1) and R_{CC} = 42 Å (CT2), respectively. In the present case, electronic structure modeling predicts that adding the terminal **δ-** moiety on **$D_1\delta_+A$** should increase the electron-hole distance R_{CC} by 3 Å in the CT1 state and as much as 18 Å if the relevant CT state would rather be of CT2 character. With a 1.75-fold decrease of V, these changes in R_{CC} would correspond to a rather small β value of 0.34 $Å^{-1}$ (considering only CT1) or an unrealistically small value of 0.06 $Å^{-1}$ when considering the CT2 state. We conclude that the observed CT state is essential to the CT1 character, possibly slightly mixed with CT2, due to the near-degeneracy with that second state.[108]

Table IV.8. Electronic couplings for charge formation and charge recombination, calculated by Eq. IV.1 taking into account the experimental reaction rates (in Table IV.5)

V(meV)		Toluene (ε=3.5)	TCE	Chloroform
$D_1\delta A$	Formation	1.783	2.385	2.392
	Recombination	0.313	0.376	0.535
$D_1\delta_+A$	Formation	0.682	0.975	1.381
	Recombination	0.236	0.343	0.495
$\delta\text{-}D_1\delta_+A$	Formation			0.886
	Recombination			0.306

IV.3 DAD's in liquid crystal films

Four molecules with different donor moieties (**$D_1\delta A$**, **$D_1\delta_+A$**, **$\delta\_D_1\delta A$** and **$\delta\_D_1\delta_+A$**) were studied in the film phase in order to observe the photo-physical properties in similar condition as in the organic solar cells. It allows investigating the influence of intermolecular interactions on photo-induced processes.
The films are prepared by Laure Biniek at the *Institut de Charles Sadron*, Strasbourg. They are prepared through the doctor-blading technique from solution at 45°C on a quartz substrate and then post-annealed at 200ºC to form a long range π-π* stacking on PDI.
Through electron diffraction and X-ray scattering methods, a zipper-like arrangement of DA has been revealed due to strong π stacking of PDIs.[56,57]

IV.3.1 Steady-state properties

IV.3.1.1 Steady-state absorption and Spectro-electro-chemistry

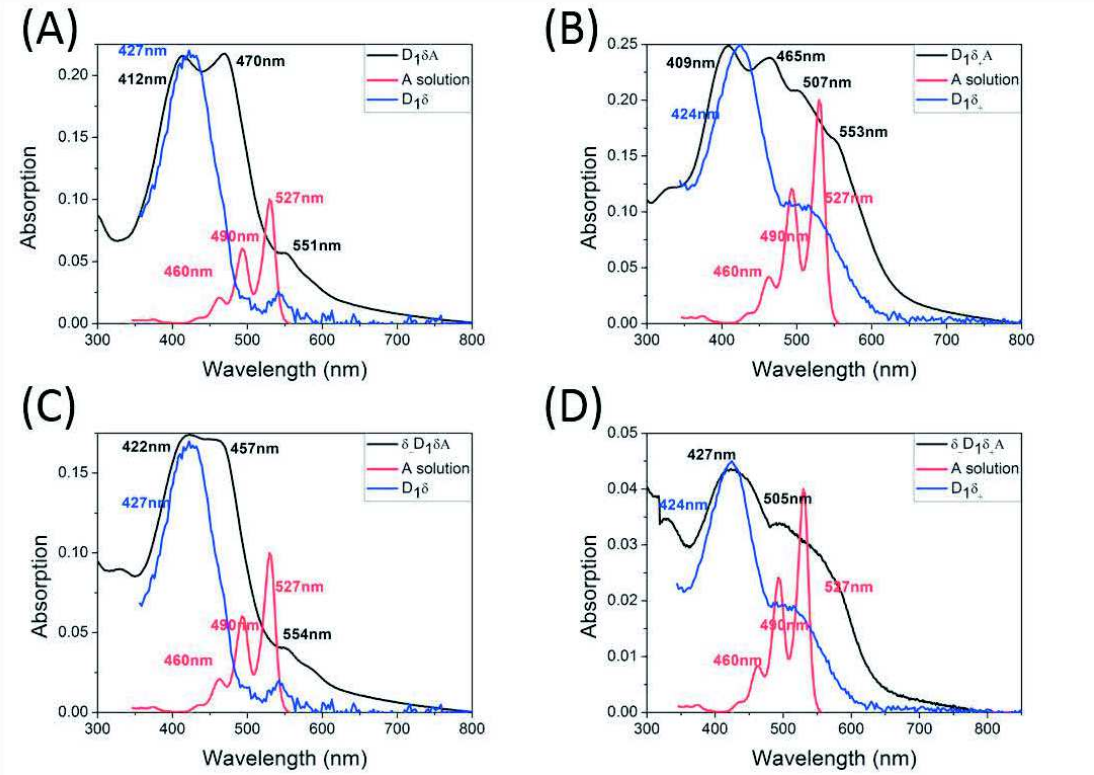

Figure IV.13 Absorption spectra of (A) **$D_1\delta A$** (B) **$D_1\delta_+A$** (C) **$\delta\_D_1\delta A$** and (D) **$\delta\_D_1\delta_+A$** in the film (black curves in all panels), respective Donor moiety (blue curves) and Acceptor (red curves) in chloroform. You should make a spectral shape analysis decomposing the peaks. This allows for a better determination of the peak wavelengths.

The steady-state absorption spectra (black curves) of four molecules are displayed in the Figure IV.13 with respective donor moiety (blue curves) and acceptor (red curves) in chloroform. The molecules with normal **δ** spacer ((A): **$D_1\delta A$** and (C): **$\delta\_D_1\delta A$**) have two intense peaks around 410 and 460 nm and a weak shoulder at 550 nm. Compared with the characteristic absorption spectrum in solution, the highest energy absorption band around 410 nm belongs primarily to **$D_1\delta$**. For the molecules with high electron affinity **δ_+** ((B): **$D_1\delta_+A$** and (D): **$\delta\_D_1\delta_+A$**), the shoulder between 480 nm and 600 nm is due to the contribution of δ_+ as in the solution. The >

55 nm blue shift (from 527 to 470 and 457 nm) of the absorption peak of PDI indicates H-aggregation of PDI, as commonly observed[9,10,126] and revealed by different structure analysis methods (see next section).

Spectro-electro-chemistry was also performed in the film to identify the charged species spectra, and the results are depicted in Figure IV.14. The films are prepared following the same protocol as the film for transient absorption experiments, except for the fact that the substrates used have an ITO electrode in order to adapt to the experimental setup. The replacement of substrate from quartz to ITO electrode does not significantly affect the molecules' organization. The steady-state absorption spectra of the same molecule on different substrates are similar.

In Figure IV.14, the differential absorption spectra ($\Delta A(\lambda) = A_{red/ox}(\lambda) - A_0(\lambda)$, $A_{red/ox}(\lambda)$: steady-state absorption measured at reduction or oxidation voltages and $A_0(\lambda)$: steady-state absorption measured at zero voltage) of cations and anions normalized at a maximum of GSB are illustrated in order to highlight the individual GSB contributions of donor and acceptor moieties in films. Oxidation $(\mathbf{D_1\delta})^+$ (**$D_1\delta A$**: black curve and **$\delta_-D_1\delta A$**: blue curve) mainly produces a negative peak at 412 nm with a broad positive band between 500 nm and 800nm. $(\mathbf{D_1\delta_+})^+$ (**$D_1\delta_+A$**: red curve and **$\delta_-D_1\delta_+A$**: purple curve) have an extra negative contribution at 550 nm due to **δ_+** and positive band shifted to the near-IR regime (700 nm for **$D_1\delta_+A$** and >1000 nm for **$\delta_-D_1\delta_+A$**). For A^-, the differential absorption spectral feature is similar to all four molecules as a negative peak at 460nm and three characteristic positive peaks at 714, 800 and 965 nm.

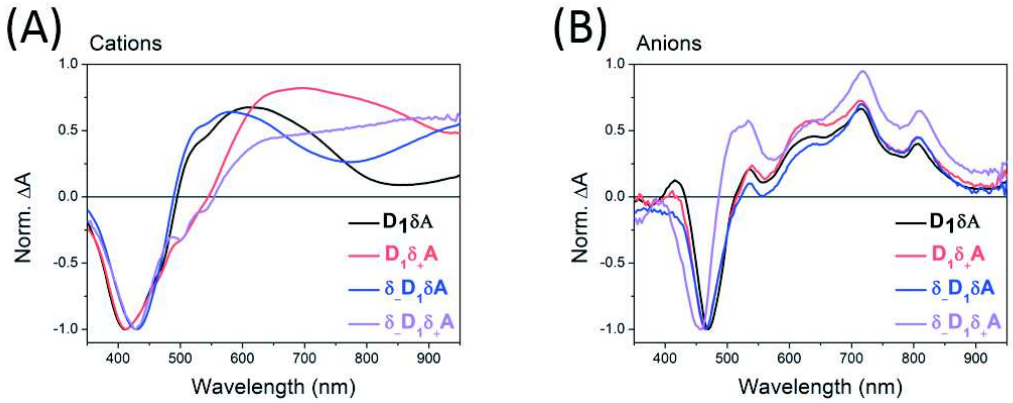

Figure IV.14 Normalized differential spectra of **$D_1\delta A$** (black curves), **$D_1\delta_+A$** (red curves), **$\delta_-D_1\delta A$** (blue curves) and **$\delta_-D_1\delta_+A$** (purple curves) (A) cation and (B) anion at maximal bleach in the film obtained by spectro-electro-chemistry.

IV.3.1.2 Morphology

Laure Biniek *et al.* have established **D-A** thin film structures by a combination of electron diffraction, grazing incidence X-ray diffraction and high-resolution transmission electron microscope (HR-TEM) as shown in Figure IV.15(A).[57] The major feature is a zipper-like arrangement.

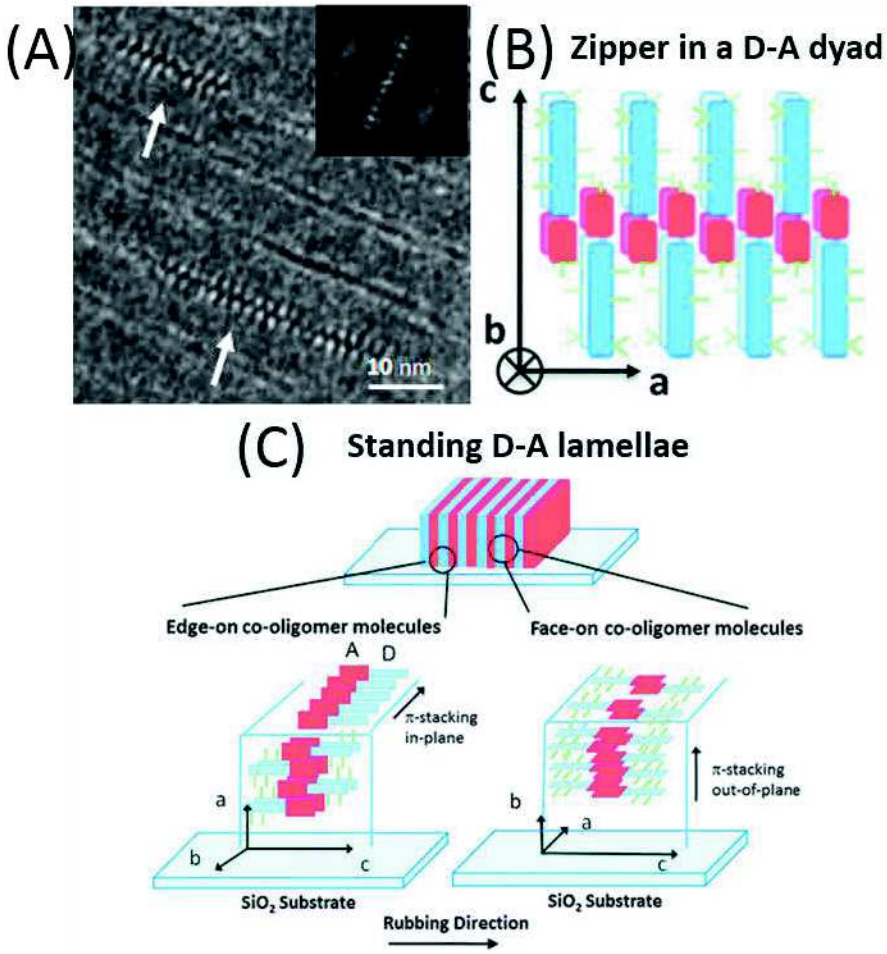

Figure. IV.15 (A) HR-TEM images of **$D_1\delta A$** showing the characteristic zipper-like molecular packing. The white arrows point at the zipper-like arrangement of co-oligomers in the HR-TEM images. In these zones, the electron beam is parallel to the stacking direction of the PDI blocks (b axis). The insets show the fast Fourier transforms. (B) a schematic illustration of the zipper packing of the **$D_1\delta A$** is shown. It is a top-view of the zip along the normal to the substrate plane and corresponds to the zones indicated by white arrows in the TEM images and (C) schematic representations of the standing and flat-on orientations of the crystalline lamellae. The acceptor PDI group is shown in red, the donor moiety in blue. [57]

In Figure IV.15 (A), the HR-TEM image of the rubbed and annealed films of **$D_1\delta A$** shows some areas with a zipper-like self-organization. The films consist essentially of standing **D-A** lamellae. However, the electron-diffraction patterns indicate that within the edge-on lamellae (left panel in Figure IV.15(C)), the stacking of the molecules can occur with the π-stacking either in-plane or out-of-plane (right panel in Figure IV.15(C)).

IV.3.2 Time-resolved spectroscopies

Figure IV.16 displays a selection of differential absorption spectra ((A) and (B)) and time-resolved fluorescence results ((C) and(D)) of **$D_1\delta_+A$** excited at 400 nm.

For the transient absorption data:

- Within the first 1 ps, a broad ESA band above 700 nm decreases and meanwhile a negative spectral band decreases from 450-600 nm. The negative spectral band of the differential absorption spectrum at 400 fs (red curve in Figure IV.16(A)) is characterized by a peak around 470 nm (GSB, dotted curve) and a secondary peak at 540 nm, which we attribute to SE as a negative contribution. ESA and SE indicate an excited state, which is probably $(D_1\delta_+)^*$, since the film is excited at 400 nm.
- From 1 ps until 20 ps, the GSB below 450 nm remains while the ESA above 800 nm decreases greatly and a new formed positive contribution compensates the GSB between 470 nm and 550 nm.
- After 20 ps, a long-lived state, that we refer to as "photo-product" is fully formed, as a broad photoproduct absorption (PA) band centered at 880 nm. The GSB band around 460 nm is still present and the differential absorption spectrum decreases without major spectral changes until 5 ns.

For time-resolved fluorescence results in Figure IV.16(C):

- The photoluminescence (PL) spectrum at 10 ps contains an intense peak at 640 nm and a secondary peak at 530 nm. Its spectral feature is similar to the steady-state fluorescence spectrum of $D_1\delta_+$ (dotted green curve in Figure IV.2(A)).
- From 10 to 20 ps, the PL spectrum broadens and has a 10 nm red shift and the secondary peak at 530 nm totally recovers.
- The PL spectrum significantly decays until 300 ps without any spectral changes.

The normalized PL kinetic traces illustrated in Figure IV.16(D) are consistent with the PL spectral evolution, showing three components decays: unresolved Gaussian decay at 520 nm and a fast and major exponential decay within 30 ps and a slow and weak decay within 100 ps at 640 and 700 nm.

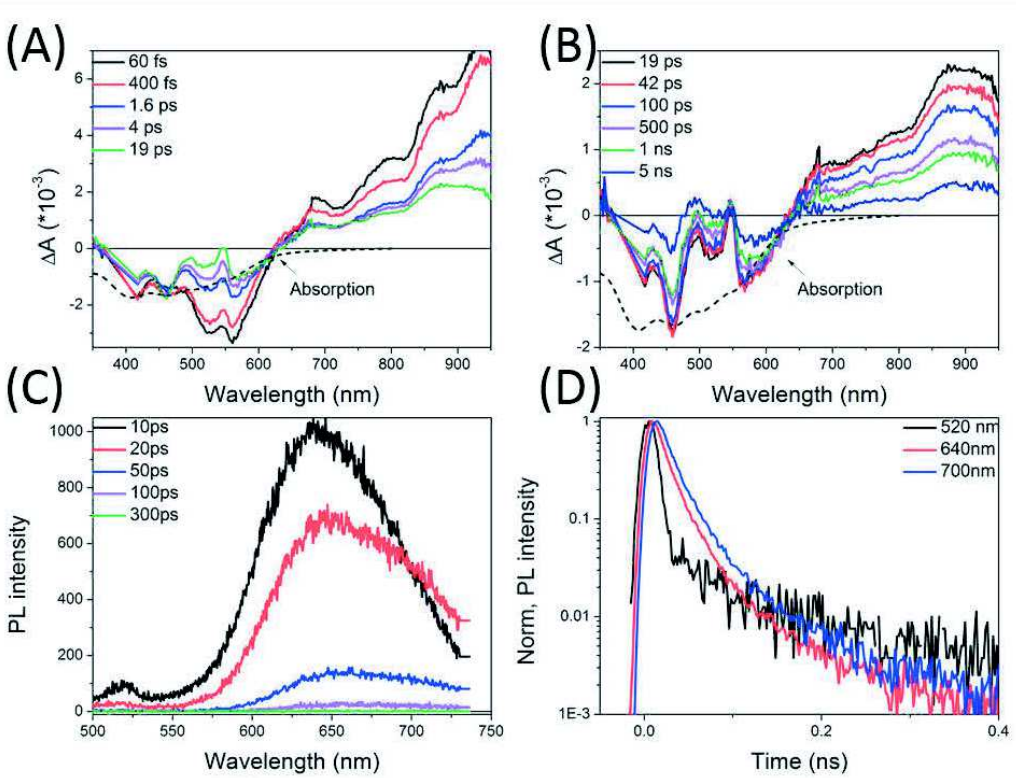

Figure IV.16 Selected differential absorption spectra of **$D_1\delta_+A$** excited at 400nm (A) within the first 20 ps (B) until 5 ns, (C) time-resolved PL spectra within 300 ps and (D) normalized PL kinetic traces at 520 nm, 640 nm and 700 nm.

Among those four molecules (**$D_1\delta A$**, **$D_1\delta_+A$**, **$\delta\_D_1\delta A$** and **$\delta\_D_1\delta_+A$**), the kinetic traces taken at the peak of the PA (780, 880, 790 and 790 nm for **$D_1\delta A$**, **$D_1\delta_+A$**, **$\delta\_D_1\delta A$** and **$\delta\_D_1\delta_+A$**) and the GSB peak (460, 560, 460 and 540 nm for **$D_1\delta A$**, **$D_1\delta_+A$**, **$\delta\_D_1\delta A$** and **$\delta\_D_1\delta_+A$**), normalized at 10 ps, are shown in the Figure IV.17. After 10 ps, the mirror-like recovery property indicates that the molecules relax to the ground state from the PA state, without the contribution from any intermediate. Note that, unlike the CT states in solution, the chemical design of donor moiety nearly has no effect on the photoproduct state lifetimes in the film with ~2 ns lifetime. Note that Geng's group reported a similar result, of constant photo-product lifetimes.[127]

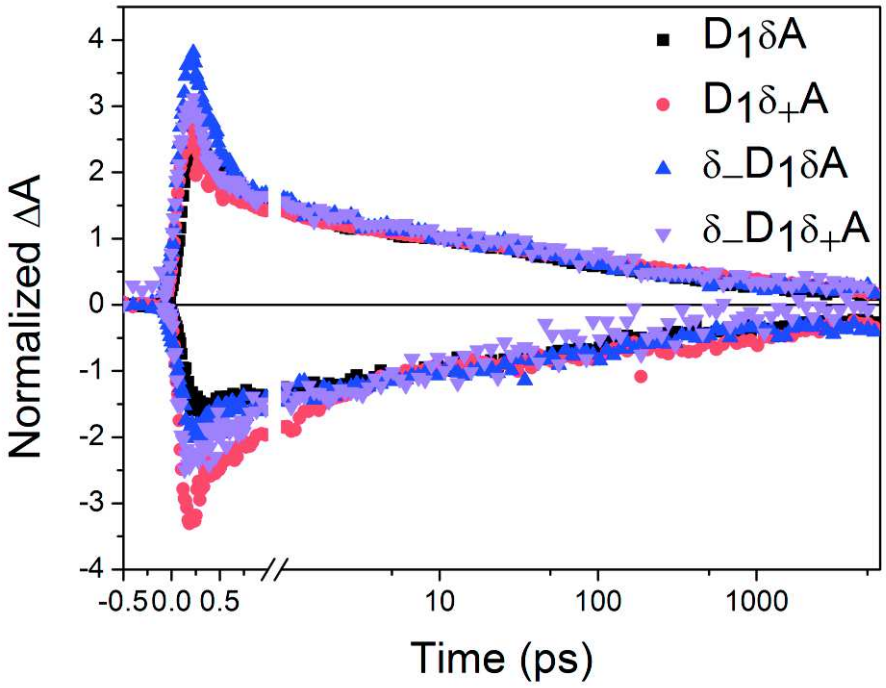

Figure IV.17 Kinetic traces are taken at the PA and GSB peak wavelengths, normalized at 10ps. In films, **D-A** dyads with four different donor moieties have the similar kinetic behavior after 10 ps, indicating the similar long-lived PA state formed and the effect of donor on CT state recombination is invalid.

Figure IV.18 illustrates the differential absorption spectrum at 100 ps in the film of **$D_1\delta_+A$** (black curve) with a comparison of the differential absorption spectra of charged species, as presented in Figure IV.13 (Cation spectrum: red curve and anion spectrum: blue curve). In solution, we have identified that the differential absorption spectrum at 28 ps of **$D_1\delta A$** is the CT state spectrum, since it corresponds to the linear combination of the amplitude of **$D_1\delta$**'s GSB spectrum **A** GSB spectrum and charged species spectra as shown in Figure IV.6 (C). Now, we want to analyze the TA spectrum in the same way for the films. In the GSB parts, the intense negative peaks at 460 nm and 560 nm indicate the photoproduct state involves **A**, and maybe **$D_1\delta_+$**, but due to excessive pump beam scattering, the region around 400 nm is not observable. The photoproduct absorption (a broad band centered at 880 nm) has an entirely different spectral feature than the differential spectra of charged species. (**$(D_1\delta_+)^+$**: centered at 700 nm and **A^-** two peaks at 710 nm and 820 nm). It is obviously impossible to reconstruct the ΔA spectrum by a linear combination of the radical ion spectra. Thus, it's difficult to directly conclude that the photoproduct state is the CT state by compared the differential spectra obtained by the transient absorption spectroscopy and spectro-electro-chemistry. The same situation occurs in the other three films, as displayed in Appendix.I.

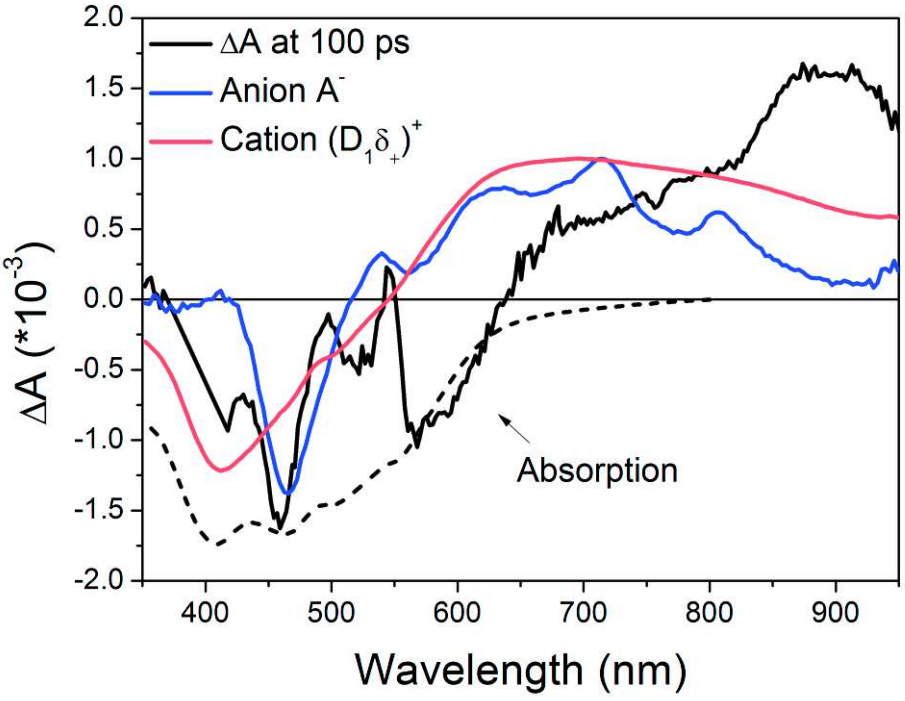

Figure IV. 18 Comparison of TA spectrum at 100 ps of **$D_1\delta A$** excited at 400 nm with differential spectra of cation species (red curve) and anion species (blue curve) measured by spectro-electro-chemistry. No direct spectral evidence shows the existence of CT state.

Global analysis of four exponential functions is applied to reveal different states or species along the course of the reaction with their lifetimes. The similar spectral features and lifetimes among four molecules indicate the same photoinduced scenario: The first excited state located in (**$D_1\delta$**) or ($D_1\delta_+$) relaxes within 0.2-0.5 ps lifetime to an intermediate state, as indicated by the rapidly decreasing ESA band above 800 nm and recovering SE band around 450-650 nm. Two spectrally similar long-lived species (>100 ps and 4.4 ns) are formed showing a broad absorption band centered at 780 nm (molecules with **$D_1\delta$**) or centered at 880 nm (molecules with $D_1\delta_+$). The different lifetimes are both due to fast and slow recombination, most probably related to two classes of molecular conformations or photoproduct species. The nature of the intermediate T_2 time scale is not clear yet, but may be related to vibrational relaxation of the photoproduct, or small amplitude excited state population.
Therefore, for the molecules with δ_+ (**$D_1\delta_+A$** and δ-**$D_1\delta_+A$**), the reaction scheme is:

$$(D_1\delta_+)^*A \xrightarrow{T_1} \text{Intermediate state} \xrightarrow{T_2} PP \underset{T_4}{\overset{T_3}{\longrightarrow}} D_1\delta_+A$$

The similar reaction scheme is excepted for the molecules with **δ** (**$D_1\delta A$** and δ-**$D_1\delta A$**) besides the photoproduct state may form from the **A** after FRET as in the solution. The same time-resolved fluorescence experiments were performed. However, PL spectrum and kinetic traces depend on the pump location. The origin of the problem is unclear, and it may be due to the inhomogeneity in films. It seems to indicate that the excitation spot size (100 μm) is not enough to average over the statistical distribution of local D-A intermolecular conformations (Figure IV.15). In those cases, the time-resolved fluorescence experiments can not be direct evidence.

Table IV.9. Rate constants of four D-A molecules in the film analyzed globally.

	T_1 (fs)	T_2 (ps)	T_3 (ps)	T_4 (ns)
$D_1\delta A$	450	8.8	200	4.4
$D_1\delta_+ A$	330	2.8	88	4.4
$\delta_- D_1\delta A$	370	4.2	100	4.4
$\delta_- D_1\delta_+ A$	200	3	78	4.4

IV.3.3 Discussion

As a prerequisite to obtaining free carriers, then photocurrent, it is crucial to identify whether the CT state is formed or not in the **D-A** films. A several ns long-lived photo-product state is formed in all studied **D-A** films. The direct evidence by spectro-electro-chemistry is not validated. Importantly, the PA spectra show clearly that the **A** moiety is involved since the GSB observed is dominated by **A**. However since optical excitation created pairs of charges and combined with the self-assembly properties of **A** to form ~100 nm chain, we propose two possibilities for the nature of the photoproduct state: the **A** excimer[128] or delocalized charges/polaron pairs[129], which will be spectroscopically different from the single charged anion or cation spectra. Both interpretations are consistent with the observation of the same decay times for all four donor compositions.

Since excimers decay radiatively, time-resolved fluorescence experiment should be a useful approach to identify the existence of excimers in the ns range. Unfortunately, due to the inhomogeneity of films, results of time-resolved fluorescence have high variability, especially for the molecules containing **δ**. Thus, different fluorescence spectra and different decay dynamics were observed. Therefore, at the present stage, time-resolved fluorescence results cannot be directly compared to the TAS data, even though indications for weakly emissive species with longer lifetimes were found. Repeating these experiments is in progress.

Indeed, the missing agreement with the spectro-electro-chemistry data may be due to the strong intermolecular interaction. According to the steady-state absorption spectra (Figure V.12), the absorbance of **D-A** films cannot be treated as the sum of **D**'s absorption and **A**'s absorption, indicating significant electronic interaction in the ground state, as expected from the tight molecular packing (§IV.3.1.2). Clearly, intermolecular interactions between the dipole moments of neighboring A's are stronger than intra-molecular ones. Hence, it is possible that the CT state absorption may be different from a linear combination of the spectro-electro-chemistry spectra, wherein only one type of charge is accumulated.
To clarify our hypothesis, transient THz spectroscopy could be an alternative to study possible conductivity changes due to the CT state or delocalized charges.

IV.4 Conclusions

By using transient absorption spectroscopy and time-revolved fluorescence measurements, we investigated a novel family of **D-A** molecules in solution and in thin films.

The study of **D-A** molecules in solution allowed to evidencing the influence of intra-molecular interactions and the role of the donor subunits **δ-** or **δ+**. With the benzene-containing **δ** spacer, an ultrafast (~1 ps) energy transfer to the acceptor precedes CT formation such that electron transfer (ET) occurs from the **A*** state on a ~10 ps time scale. Introducing such a spacer increases the CT lifetime more than 10-fold with respect to the first generation of DAD's lacking such a spacer [93].
Instead, the benzothiadiazole **δ+** spacer precludes the initial energy transfer, and a significantly slower (~100 ps) ET occurs from the originally photoexcited donor (**D_nδ+**)* state. Irrespective of the nature of the spacer (**δ** or **δ+**), the CT state lifetime increases upon adding the terminal amine **δ-** on the donor block, up to 5 fold with the optimum donor length n=1 in chloroform, and possibly also in other solvents, but lifetimes >3 ns are not accurately measured here. Reducing the solvent polarity (from chloroform to toluene) slows down the CT state recombination by up to 1 order of magnitude and to a lesser extent the CT state formation (by a factor 2 or 3 at most). We note that in the slightly more polar chlorobenzene (ε=5.62) the CT lifetime of similar

In films, despite the modification of the **D** moiety, photo-product states are observed in all four studied **D-A** films, with different differential spectra but similar lifetimes. More experimental proofs are needed to identify which state it is. Excimers or delocalized charges are the most plausible candidates, because of the A π-stacking chains.
However, and as an unexpected result and response to the initial motivation of synthesizing DA's with varying donor groups, the chemical design of molecular structure does not have a significant impact on the lifetime of this state.

As much as intermolecular interactions clearly dominate the photochemistry in the films, we showed that the solvent polarity had a larger impact on enhancing the CT lifetimes than the chemical design of the Donor moiety. This is in agreement with a previous study of the first generation DAD in films where the inter-molecular interactions and couplings were shown to play a more important role in the charge generation processes.[93,130] This indicates that the molecular arrangement in films must be part of the oligomer design, and that it is more important to address these aspects and their effect on CT lifetimes than to stabilize the CT on a single oligomer. Thus, as for organic materials used for bulk heterojunctions, the molecular design challenge involves multi-scale considerations, here in particular for the simulation of the molecular packing of the oligomers.

In the term of outlook, other non-fullerene acceptors have reached impressive high PCE by building 2D conjugated polymers.[54] The perspective of the 2D-conductive channel could be bright. The interdigital structure shows transverse dimensions leading to the fast and efficient formation of interfacial CT state within the exciton lifetime and high carrier mobility allowing for high intermolecular hopping rates. The TEM image of PDI (Figure IV.16) illustrates the evidence of the zipper-like conductive structure of PDI. Therefore, we expect the OSCs based on the PDI could be improved moreover. Furthermore, the morphology plays an important role in photo-induced processes (exciton diffusion, charge collection etc.) and optimizing the device PV performance. The combination of typical ultrafast time-resolved spectroscopies with electron microscopy will be a powerful tool to investigate the solar cells.

The work on isolated Donor-Acceptor molecules in solution (§ IV.2) led to an article:

L. Liu, P. Eisenbrandt, T. Roland, M. Polkehn, P.-O. Schwartz, K. Bruchlos, B. Omiecienski, S. Ludwigs, N. Leclerc, E. Zaborova, J. Léonard, S. Méry, I. Burghardt, S. Haacke ‘‘Controlling Charge Separation and Recombination by Chemical Design in Donor-Acceptor Dyads’’*Phys. Chem. Chem. Phys., 2016, 18, 18536*

PCCP

PAPER

View Article Online
View Journal | View Issue

Cite this: *Phys. Chem. Chem. Phys.*, 2016, **18**, 18536

Controlling charge separation and recombination by chemical design in donor–acceptor dyads†

Li Liu,‡[a] Pierre Eisenbrandt,‡[b] Thomas Roland,[a] Matthias Polkehn,[b] Pierre-Olivier Schwartz,[a] Kirsten Bruchlos,[c] Beatrice Omiecienski,[c] Sabine Ludwigs,[c] Nicolas Leclerc,[d] Elena Zaborova,§[d] Jérémie Léonard,[a] Stéphane Méry,[a] Irene Burghardt*[b] and Stefan Haacke*[a]

Received 29th January 2016,
Accepted 15th May 2016

DOI: 10.1039/c6cp00644b

www.rsc.org/pccp

Conjugated donor–acceptor block co-oligomers that self-organize into D–A mesomorphic arrays have raised increasing interest due to their potential applications in organic solar cells. We report here a combined experimental and computational study of charge transfer (CT) state formation and recombination in isolated donor–spacer–acceptor oligomers based on bisthiophene–fluorene (D) and perylene diimide (A), which have recently shown to self-organize to give a mesomorphic lamellar structure at room temperature. Using femtosecond transient absorption spectroscopy and Time-Dependent Density Functional Theory in combination with the Marcus–Jortner formalism, the observed increase of the CT lifetimes is rationalized in terms of a reduced electronic coupling between D and A brought about by the chemical design of the donor moiety. A marked dependence of the CT lifetime on solvent polarity is observed, underscoring the importance of electrostatic effects and those of the environment at large. The present investigation therefore calls for a more comprehensive design approach including the effects of molecular packing.

1 Introduction

The important progress made in recent years in organic electronics relies among others on the ability of controlling the structure of the active organic material constituents on the scale of a few nanometers.[1–5] In the context of organic photovoltaics, the most prominent examples are bulk heterojunctions (BHJ) made of p-type donor and n-type acceptor materials, the physics of which has been rationalized in a large number of review articles.[6,7] BHJ organic solar cells are composed of a blend of two materials (a polymer[8,9] or small molecule[10,11]) with, in most cases, a fullerene derivative as an acceptor, but efficient solar cells with non-fullerene acceptors were also reported.[12–14] The main requirement, which poses serious constraints on the microphase separation capabilities, is to control the intermixing and the size of grains, while preserving a good percolative conductivity through the D and A blocks (film morphology).[15] Different approaches were published to tackle the challenge of achieving D and A block sizes, if possible by self-organization, at dimensions smaller than the exciton diffusion lengths.[5] Here, monodisperse conjugated oligomers have the advantage of their uniform and/or monodisperse chemical structures,[16–18] and their molecular lengths can be well controlled at will on the 2–10 nm scale.

Many groups have synthesized D–A dyads, made up of these monodisperse oligomers, towards organic solar cells; but PCEs were however limited to the 1% range.[19–22] If the D–A co-oligomers are chemically designed to form smectic liquid-crystalline (LC) or other types of mesomorphic phases at room temperature,[23–25] it could be possible to obtain separate D and A 2D-conductive channels with (a) transverse dimensions such that the interfacial CT state would form readily on time scales much shorter than the exciton lifetime and (b) high carrier mobility if the electronic coupling within the A and D planes allows for high inter-molecular hopping rates. It is worth noting that the use of block co-polymers is a similar approach, which has proven to be another interesting route for achieving phase separation and remarkable device performances,[26] and the importance of the choice of the chemistry of the linker group introduced between the D and A blocks was recently highlighted.[27]

Significant progress was recently made by designing a D–A block co-oligomer based on a fluorene donor with adequate

[a] *Institut de Physique et Chimie des Matériaux de Strasbourg & Labex NIE, Université de Strasbourg, CNRS UMR 7504, 23 rue du Loess, Strasbourg 67034, France. E-mail: stefan.haacke@ipcms.unistra.fr*
[b] *Institute for Physical and Theoretical Chemistry, Goethe University Frankfurt, Max-von-Laue-Str. 7, 60438 Frankfurt/Main, Germany. E-mail: burghardt@chemie.uni-frankfurt.de*
[c] *Institut für Polymerchemie, Universität Stuttgart, 70569 Stuttgart, Germany*
[d] *ICPEES, Université de Strasbourg, CNRS UMR 7515, ECPM, 25 rue Becquerel, 67087 Strasbourg Cedex2, France*
† Electronic supplementary information (ESI) available. See DOI: 10.1039/c6cp00644b
‡ These authors contributed equally to this work.
§ Current address: CiNaM, Aix Marseille Université, CNRS UMR 7325, Campus de Luminy, 13288 Marseille, France.

side chains, and perylene diimide (PDI) as an acceptor, reaching PCEs above 2%.[28,29] PDI or derivatives thereof are indeed good alternative acceptor materials featuring higher extinction coefficients than PCBM, and comparably high PCEs were recently reported in BHJs.[13,14] A combined investigation of the ultrafast CT dynamics and the conduction properties led the authors to conclude that the CT generation/recombination dynamics and efficiencies are determined by separate material properties.[30] The chemical composition (in particular the presence of a spacer between D and A[29]) would be decisive in controlling the CT lifetime of a single oligomer in solution, but in the film the question remains largely open due to the uncertain spectroscopic signature of charged species. Instead, the carrier mobilities and thus their collection yield would be linked to the film morphology, which determines how the oligomers align so as to form conductive channels of high persistence length.[30] Even though Geng and collaborators reported the highest PCE for a self-assembled organic solar cell (2.7%),[29] it is clear that there is still a lot of room for improvement on both hindering geminate CT recombination and optimizing the charge transport with high and balanced electron and hole mobilities.

A DAD oligomer based on PDI and a phenyl–bisthiophene–phenyl donor moiety was designed by our team in 2009 and then studied by pump–probe spectroscopy[31,32] both isolated in solution and in a smectic LC film at room temperature. In the isolated molecules, a 120 fs resonance energy transfer from the selectively excited D to the central acceptor was observed, followed by the formation of a CT or biradical $D^{\bullet+}A^{\bullet}$ state within 2.5 ps. This state proved to be very short-lived, recombining within 50 ps to the ground state, and partially to the D triplet state. In the film, CT states were formed much more rapidly – within 0.4 ps – due to a highly efficient intermolecular charge transfer pathway in conjunction with exciton delocalization.[33,34] These CT states exhibit a somewhat longer 1.2 ns recombination time. These relatively short lifetimes mean that unrealistically high electrical fields or carrier mobilities would be required for efficient charge separation.

In line with the conclusions of Geng *et al.*,[30] a second generation of oligomers was devised with the aim of increasing the intra-molecular CT lifetime to well above 1 ns, while preserving the close to 100% CT formation efficiency. Several variants of this new D–A system were designed in order to study the effect of D–A electronic coupling and intra-molecular reorganization on the CT state formation and lifetime (Fig. 1). To the PDI acceptor moiety, a donor block of variable length (D_n) is attached, composed of bisthiophene–fluorene units (n = 0 to 3). This donor block is connected to the acceptor group *via* a linking moiety made of a short flexible spacer (ethylene) and a molecular unit that comes in two varieties of low and high electronegativity, respectively, denoted δ_+ or δ. This linking molecular unit is composed of the sequence thiophene–benzothiadiazole–thiophene (for δ_+) or thiophene–phenyl–thiophene (for δ). Furthermore, a terminal amine can be added at the other end of the donor block that is regarded as "electron-donating" and denoted δ^-. Alkyl chains laterally attached to the D block are required for the solubility and the formation of mesophases[35]

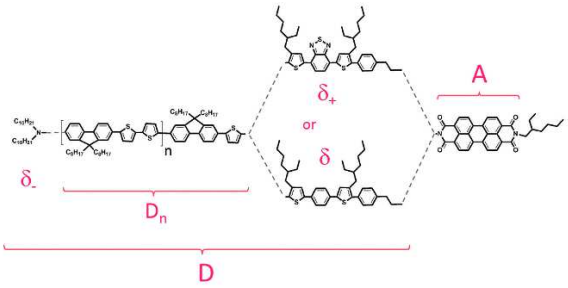

Fig. 1 Chemical structure of the D–A dyads studied in this paper. The donor core D_n (n = 0 to 3) is connected to the PDI acceptor by a linking moiety δ or δ_+ in order to reduce electronic coupling and thus prolong the CT lifetime. To amplify this effect, the δ_- end group is meant to shift the donor HOMO further away from A. D denotes the entire donor block.

as well, in addition to the stacking propensity of PDIs.[36] Those donor–acceptor species were produced both with the molecular architecture of dyads (D–A) and triads (D–A–D or A–D–A).

The synthesis of these oligomers as well as detailed structural characterization of the films obtained by varying substrate preparation and annealing conditions were already reported.[35,36] In particular, it was found that the D_nA's (n = 0 and 1) can lie flat on the substrate and adopt a zipper-like structure[36] through π-stacking. This is consistent with the absorption spectra, which display excitonic coupling with an almost ideal H-type aggregate configuration.

The present study focuses on the photophysics of isolated D_nA's in solvents of different polarity. In various types of donor species as depicted in Fig. 1, the spatial location and extension as well as the energy of the donor frontier orbitals are expected to change independently of the acceptor. To a first approximation, we expect the electronic coupling energy to decay exponentially as a function of the centroid distance R_{CC} between the frontier orbitals,[37] so as to reduce the CT recombination rate and increase the CT lifetimes.[38,39] In the following, we will employ ultrafast spectroscopy to study the behavior of these different donor–acceptor molecules, to identify how exactly the charge transfer dynamics is tuned by the chemical modification of the donor species, and the solvent polarity. The relevant donor and acceptor excitations and charge transfer states, as well as the intramolecular reorganization energies, were calculated using Time-Dependent Density Functional Theory (TDDFT) methods. Using the Marcus–Jortner formalism[40,41] for the calculation of charge transfer rates, this combined approach allows rationalizing the effect of the design parameters of the donor block on the CT formation and recombination kinetics at the individual oligomer level, as well as the major role of the interaction with the environment *via* the solvent influence.

2 Methods

Transient absorption spectroscopy

The experimental pump–probe setup was already described in previous papers:[32,42] the femtosecond laser source is a Ti:Sapphire regenerative amplifier laser system (Pulsar, Amplitude Technology)

delivering 40 fs-long pulses, at 5 kHz, centered at 800 nm. The beam is split into two. One beam is used to produce a 400 nm pump beam by second harmonic generation in a β-barium borate (BBO) crystal. The second beam goes to a delay line before being focused on a CaF_2 or sapphire crystal to generate a broad white-light continuum (300–1000 nm). The latter is split into two again: the probe that is sent through the sample and the reference. Both are detected using a spectrometer and a CCD camera in order to measure the sample absorbance and the white-light power fluctuations respectively. Relative linear polarization between pump and probe beams is set at the magic angle (54.7°) to measure population kinetics independently from the effect of rotational diffusion in solution. By chopping the pump beam, the camera records alternatively the absorption spectrum of the unexcited and excited molecules at 220 Hz, and the differential absorption (ΔA) spectra are calculated. The FWHM of the instrument response function (IRF) is 80 fs.[42,43] The pump pulse intensity was set so as to ensure a linear dependence of the ground state bleach signals in all experiments reported below. Data are processed to correct the effects of group velocity dispersion (chirp) in the white light continuum and to subtract the non-linear signal from the solvent and the presence of any delay-independent background.[42,43] All transient spectra presented in this work are obtained by appending three datasets covering three adjacent spectral windows, from 320 to 990 nm. After chirp correction, the zero time-delay is defined with an error bar of 20 fs over the entire observation spectral window.[43]

The oligomers are diluted in chloroform ($CHCl_3$), trichloroethylene (TCE) or toluene at $\sim$0.25 mmol L^{-1} and flown through a 0.5 mm quartz cuvette, using a peristaltic pump. Their absorption spectrum is independent of concentration indicating no aggregation at $\sim$0.25 mmol L^{-1}. The sample absorbance is 0.4 in the 1 mm cuvette at 400 nm.

Differential spectra are interpreted as the spectroscopic signature of the time-dependent populations $c_i(t)$ of molecular states or species involved in the photoreaction:

$$\Delta A(\lambda, t) = \sum_i \varepsilon_i(\lambda)(c_i(t) - c_{i0})d, \quad (1)$$

where $\varepsilon_i(\lambda)$ and c_{i0} are respectively the extinction coefficient and initial concentration of species i, and d the sample thickness. Assuming that the populations $c_i(t)$ obey a rate equation model, the 2-dimensional datasets are analyzed quantitatively by fitting with a sum of exponential functions: $\Delta A(\lambda, t) = \sum_i A_i(\lambda)e^{-t/\tau_i}$. This fit can be done separately for each wavelength, in particular at wavelengths where the spectroscopic signature of a particular species dominates. The fitting may also be performed globally over the entire 2D dataset. This is performed after singular value decomposition (SVD) is used for data reduction and simultaneous fitting of the few dominant singular transients (see details in the ESI†).

Cyclic voltammetry

The oxidation and reduction potentials of the donor and acceptor moieties, respectively, were measured within ±0.03 V by cyclic voltammetry, carried out using a BioLogic VSP potentiostat using platinum electrodes at a scan rate of 20 to 50 mV s^{-1}.[35] A Pt wire was used as a counter electrode and Ag/Ag^+ as a reference electrode in a 0.1 M dichloromethane solution of tetrabutylammonium tetrafluoroborate. Ferrocene was used as internal standard to convert the values obtained in reference to Ag/Ag^+ to the saturated calomel electrode (SCE) scale.

Spectroelectrochemistry

In order to identify the spectroscopic signature of transient CT states the absorption spectra of the radical anion ($A^{\bullet-}$) and cations ($\{D_1\delta\}^{\bullet+}$, $\{D_1\delta_+\}^{\bullet+}$, and $\{\delta_+\}^{\bullet+}$) of acceptor and donors are recorded using a spectro-electro-chemical setup described in ref. 44, during the electrochemical charging of the sample solution (10^{-3} M in dichloromethane/0.1 M tetra-*n*-butylammonium hexafluorophosphate solution). The electrochemical charging was carried out in a thin layer cell using a three-electrode arrangement. *In situ* UV/Vis spectra were recorded on a Zeiss modular spectrometer system with MCS 621-components in reflection mode using the Pt disc electrode as mirror.

Computational methods

Since all of the above donor–acceptor combinations represent very large molecular species, the application of high-level *ab initio* methods was possible only to a limited extent, such that TDDFT is employed throughout. Similarly to our previous work,[45] long-range corrected functionals, *i.e.* the CAM-B3LYP functional[46] and the ωB97XD functional[24] which includes dispersion corrections, were used to properly describe the energetic position of the CT state(s), which is crucial for the interpretation of the spectroscopic results. In addition, the CIS method[47] was used for comparison. TDDFT and CIS results were validated against selected benchmarks by the Second-Order Approximate Coupled Cluster Singles and Doubles (CC2) method[48–50] as well as by the Second-Order Algebraic Diagrammatic Construction (ADC(2)) method.[51,52] The def2-SVP and def2-TZVP basis sets were employed.[53,54] In all calculations, alkyl chains are replaced by methyl groups to reduce the computational cost.

Solvent effects were included using the conductor-like screening model (COSMO).[55,56] As in our previous work,[45] calculations were performed with a solvent cavity equilibrated to the ground state charge distribution.

As a measure of charge separation in the charge transfer states belonging to various donor–acceptor combinations, electron–hole centroid distances (R_{CC}) were calculated from the corresponding orbital transitions of the excitation, using as weights the amplitudes given for each transition. To this purpose, we used the procedure as implemented in the Multiwfn-package.[57]

Calculations were performed using the Turbomole 6.4 package,[58] the Orca 3.0 package,[59] and the Gaussian09 package.[60]

3 Experimental & computational results

Here, we first report on steady-state spectra of various dyads depicted in Fig. 1, giving first indications of the role of energy and charge transfer in these species (Section 3a). We then

deduce the photophysical pathways of the $D_1\delta A$ species from transient absorption spectra, showing that energy transfer precedes charge transfer in this system (Section 3b). The effect of introducing the more electro-negative benzothiadiazole δ_+ spacer precludes energy transfer, in full agreement with the relaxation pathway as indicated by the computed state ordering (Section 3c). Next, we explore the effect of adding a terminal δ moiety and increasing the number of donor (D_n) units. This analysis highlights the key role of the δ units in the substantial lengthening of the CT lifetimes (Section 3d). Finally, the role of solvent polarity is explored in Section 3e.

(a) Steady-state properties

Fig. 2 displays the steady state absorption and emission spectra of the $D_1\delta_+A$ dyad, its constituting moieties, and the corresponding charged species. Table 1 summarizes their absorption and emission maximum wavelengths. While the spectral features of D_1 and δ_+ can be recognized in the absorption spectrum of $D_1\delta_+$, their red-shifts (by 12 and 30 nm, respectively, see Table 1) reveal the electronic coupling between the D_1 and δ_+ moieties. The lowest excited state of $D_1\delta_+$ is located on δ_+ and displays a fluorescence spectrum similar to that of δ_+ but with a 49 nm red shift. Upon linking donor and acceptor moieties, no further spectral shifts of the donor and acceptor absorption bands are observed, indicating negligible electronic coupling between them in the $D_1\delta_+A$ dyad. Besides, we note that the absorption spectrum of A overlaps well with the fluorescence spectrum of $D_1\delta$ in the 450 to 540 nm range but not with that of $D_1\delta_+$. This indicates that direct energy transfer may occur from $D_1\delta$ to A but not from $D_1\delta_+$ (see below). As for the charged species (see Methods), the $(D_1\delta)^{\bullet+}$ cation has a main peak at around 707 nm and a shoulder at 580 nm. The $(D_1\delta_+)^{\bullet+}$ cation is characterized by a similar though broader band centered at 700 nm, rather than at 750 nm as for the $(\delta_+)^{\bullet+}$ cation, indicating that the hole is rather located on D_1 than on δ_+. The $A^{\bullet-}$ anion spectrum shows three characteristic narrow peaks at 719, 806 and 963 nm, as already reported.[32,61]

To rationalize the experimental findings, an accompanying electronic structure analysis is carried out for various systems depicted in Fig. 1. TDDFT calculations are combined with selected CC2 and ADC(2) benchmark calculations as described in Section 2.

Fig. 3 shows the relevant excitations which are here illustrated for the smallest representative system, *i.e.*, the $D_0\delta_+A$ dyad. The lowest transitions correspond to two donor excitations (denoted DS_1 and DS_2), one acceptor excitation (AS_1), and the lowest charge transfer (CT_1) transition. A comparison with the $D_0\delta A$ dyad shows that only one donor transition (*i.e.*, DS_2) is relevant in the latter case, since the DS_1 excitation localized on the δ_+ moiety is absent. This is fully consistent with the observation of the low-energy absorption shoulder at 510 nm and the red-shifted emission at 647 nm (Table 1) related to δ_+. Apart from this, the DS_2, AS_1, and CT_1 transitions are entirely analogous in the two systems, even though the energetics differ slightly.

A detailed comparison of the energetics for the $D_n\delta_+A$ *vs.* $D_n\delta A$ species (n = 0, 1), as well as for the related δ $D_n\delta_+A$ *vs.* δ $D_n\delta A$ species that include a terminal amine group (δ), is given in Fig. 4. The computed energy difference between the DS_2 and AS_1 states is about 0.6 eV in the $D_0\delta_+A$ dyad, and slightly reduced to about 0.5 eV in $D_0\delta A$. In the $D_1\delta_+A$ system, a significant mixing of the DS_2 and DS_1 transitions occurs, whereas the $D_1\delta A$ system exhibits mixing of the DS_2 and AS_1 transitions

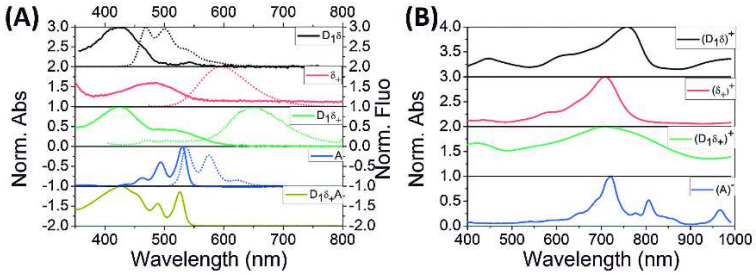

Fig. 2 Absorption (solid lines) and emission (dashed lines) spectral signatures of a selection of neutral (panel A, in chloroform) and charged (panel B, in dichloromethane, see Methods) species that will be relevant for the interpretation of transient absorption spectroscopy data.

Table 1 Characteristic wavelengths of absorption and emission spectra of the optically excited or generated species in the $D_1\delta A$ and $D_1\delta_+A$ dyads

$D_1\delta$	Bleach	408 nm
	Fluorescence	469 and 499 nm
	Radical cation	707 nm and a shoulder at 580 nm
$D_1\delta_+$	Bleach	424 nm and a shoulder at 510 nm
	Fluorescence	647 nm
	Radical cation	A broad band centered at 700 nm, a shoulder at 770 nm, and a smaller band at 420 nm
A	Bleach	460, 490 and 525 nm
	Fluorescence	535, 575 nm and a shoulder at 620 nm
	Radical anion	719, 806 and 963 nm

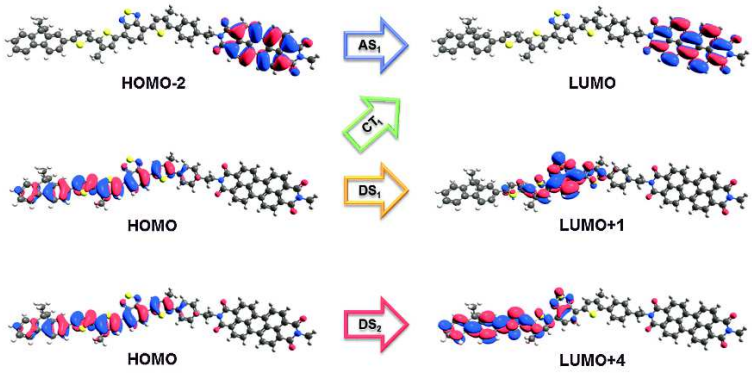

Fig. 3 Relevant excitations in the $D_0\delta_+A$ dyad. AS_1 denotes the acceptor singlet excitation and CT_1 denotes the principal charge transfer transition, while DS_1 and DS_2 denote two donor excitations, with the DS_1 excitation localized on the δ_+ moiety.

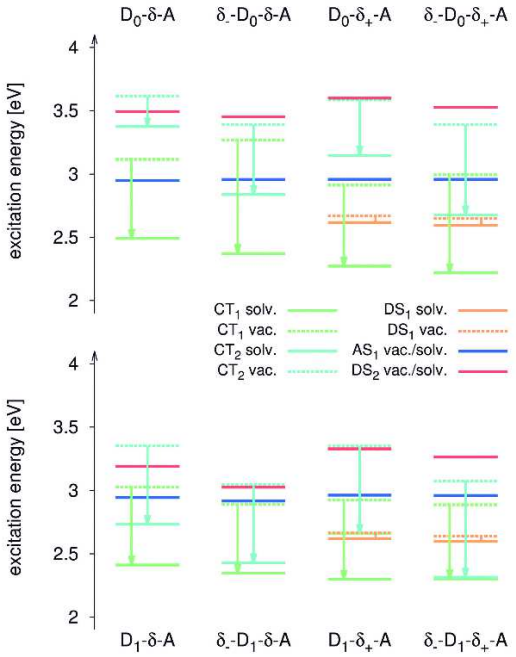

Fig. 4 Excitation energies in vacuum and chloroform, obtained using the COSMO solvent model in conjunction with TDDFT using the CAM-B3LYP functional (as implemented in ORCA[59]). For each of the five relevant electronic states (DS_1, DS_2, AS_1, CT_1, and CT_2) and all dyad species indicated along the abscissa, vacuum energies (vac) are indicated along with the corresponding shifted energies for the solvated species (solv) immersed in a solvent cavity equilibrated to the ground state charge distribution. Note that the shift is negligible for AS_1 and DS_2 (< 0.1 eV), such that a single entry is given for these states.

(with a 80 : 20% mixture in both cases). Depending on the choice of the density functional, the CT_1 state lies between DS_2 and AS_1 in vacuum (CAM-B3LYP) – as shown in Fig. 4 – or higher than the DS_2 state (ωB97XD). A detailed comparison of the results obtained with different density functionals is shown in the ESI.†

As also illustrated in Fig. 4, an additional charge transfer state (denoted CT_2) appears at higher energies, slightly below the DS_2 excitation. Addition of the terminal amine group (δ) tends to stabilize this state. The CT_2 state potentially has some impact upon the charge transfer, by mixing with the CT_1 state. However, given that the CT_2 state by itself exhibits a significantly larger electron–hole distance than the CT_1 state, and thus strongly reduced electronic coupling between D and A, its direct contribution to the charge transfer rate turns out to be minor (see the discussion below).

The modified energetics in solution (chloroform) are assessed by using a continuum solvation model (COSMO), with a solvent cavity equilibrated to the ground state charge distribution. Fig. 4 illustrates that both CT states are considerably stabilized. In systems containing the terminal amine (δ) moiety, the CT_2 state is lowered to the range of the donor excitations, and even becomes nearly degenerate with CT_1 in δ $D_1\delta_+A$. These effects are likely further emphasized if equilibration with respect to the CT states is considered. From the experimental point of view, given the long CT lifetimes, solvation of the CT states is expected to proceed until full equilibration.

(b) Photophysics of $D_1\delta A$ in chloroform

As a case-study illustrative of the dyads investigated here, we first focus on the photophysics of the $D_1\delta A$ compound in chloroform. Fig. 5 displays a selection of the corresponding differential absorption (Δ*A*) spectra (120 fs, 2.5 ps 28 ps and 1.0 ns). Each spectrum can be decomposed into a sum of contributions of individual species/states, the spectroscopic signatures of which are identified in complementary experiments (see "steady-state properties"). In the following, we will refer only to their maximum wavelengths compiled in Table 1.

At early times (Fig. 5: 120 fs, black) the differential spectrum features a broad negative band below 585 nm, which matches well with the shape of the sum of $D_1\delta$ ground state bleach and fluorescence bands (*cf.* Fig. 2 and Table 1), and is thus attributed to the excited state ($(D_1\delta)^*$) of the donor. The positive signal at a longer wavelength is attributed to the excited state absorption (ESA) of $D_1\delta^*$, in line with previous identification of

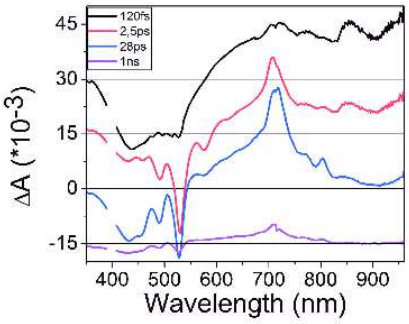

Fig. 5 Selected differential absorption spectra of $D_1\delta A$ in chloroform, at 120 fs (black), 2.5 ps (red), 28 ps (blue) and 1.0 ns (pink). The spectra are shifted vertically for easier reading.

the same signature on similar compounds.[32] Hence, the early spectrum illustrates selective excitation of D_1 as expected with the 400 nm pump wavelength, since the acceptor's absorption is almost zero at this wavelength.

After 2.5 ps, the features of $(D_1\delta)^*$ have disappeared and are replaced by four new negative peaks at 460, 490, 530 and 575 nm, which perfectly match the absorption and fluorescence bands of the acceptor A and are therefore interpreted as ground state bleach of A and stimulated emission from the excited A* state. This and the reduced bleach of $(D_1\delta)$ indicate that the population of $(D_1\delta)^*$ has decayed within a few picoseconds due to an energy transfer from $(D_1\delta)^*$ to A*, as expected due to the large spectral overlap of the fluorescence band of $(D_1\delta)$ and the absorption band of D.

In the 28 ps differential spectrum, the negative peaks at 530 and 575 nm persist while the band at 420 nm associated with the donor's bleach reforms, indicating that the ground states of both $D_1\delta$ and A are depopulated. Simultaneously, as illustrated in Fig. 6, the spectral features of the induced absorption (>550 nm) are reproduced well by the sum of the anion and cation absorption spectra (peaks at ~713 and 800 nm for $A^{\bullet-}$, broad induced absorption from 500 to 800 nm for $(D_1\delta)^{\bullet+}$).

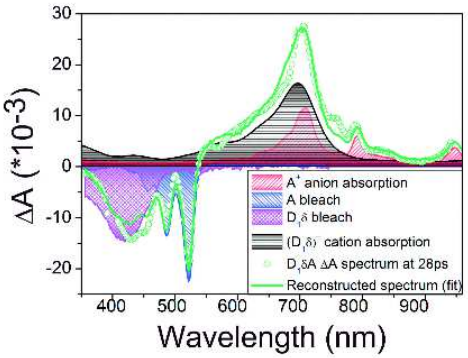

Fig. 6 Differential spectrum of $D_1\delta A$ in chloroform at 28 ps (green circles), and its fit (green line) by a linear superposition of the steady-state absorption spectra of $D_1\delta$ (bleach, pink), A (bleach, blue), $(D_1\delta)^+$ (black) and A (red). The good agreement with the fit is evidence for the CT state.

This proves that within a few tens of picoseconds, a charge transfer has occurred, forming the CT state composed of the $(D_1\delta)^{\bullet+}$ and $A^{\bullet-}$ ion radicals.

On longer time scales, the differential spectra do not change in shape, but only their amplitudes decrease, showing that the CT state recombines, reforming the ground state.

In summary, these observations support the following reaction scheme for the $D_1\delta A$ photoreaction in chloroform:

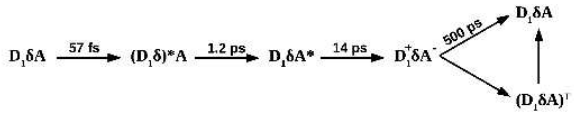

Time constants associated with each of these transitions are obtained by global fitting (see Methods and ESI†) of the 2D differential dataset. As shown in the ESI,† five time constants are needed to achieve a fit with satisfying residuals: 57 fs, 1.2 ps, 14 ps, 0.50 ns and 2.2 ns. As discussed in the ESI,† the spectral shape of the decay-associated difference spectra indicates the relevant processes: the first very short time constant (57 fs) is close to the experimental time-resolution, but, in accordance with previous work, reflects vibrational relaxation within the donor.[62] As shown above, energy transfer between $(D_1\delta)^*$ and A is complete within 2.5 ps, with an energy transfer rate of $(1.2\ ps)^{-1}$. The formation of the CT state, fully observed after 28 ps (Fig. 6) is then associated with the 14 ps time constant. Note that electron transfer (ET) occurs here between the HOMOs, since the excitation is on A* and not on D*. This is followed by its recombination in 0.50 ns. Finally, a longer-lived, minor species is tentatively attributed to triplet states, which decay on a 2.2 ns time scale.

As illustrated in Fig. 7, this transfer pathway is compatible with the calculated energetics of the δ-substituted system. Here, we consider the $D_0\delta A$ species, for which state-specific geometry optimizations were performed. From Fig. 7, we can infer that excitonic mixing between the DS_1 and AS_1 states occurs near

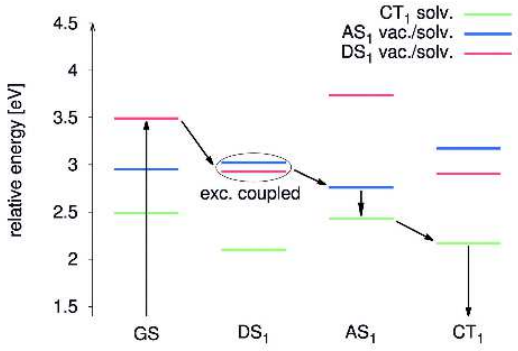

Fig. 7 Illustration of a possible photochemical pathway for the $D_0\delta A$ species, obtained from geometry optimizations for the respective electronic states. Relative energies are reported for a series of equilibrium structures for the respective states, shown along the *x* axis (where GS refers to the ground state equilibrium structure). Excitonic coupling between the DS_1 and AS_1 states ("exc. coupled") is observed at the DS_1 equilibrated geometry. All energies refer to chloroform solvent.

the optimized geometry of the DS_1 state, followed by a transition from the AS_1 state to the CT_1 state.

(c) Molecular design: effect of the spacer composition, δ *versus* δ_+

A first analysis of the influence of the molecular structure design on the photophysics of the dyads is made by comparing $D_1\delta_+A$ in chloroform to $D_1\delta A$ documented above: adding the benzothiadiazole unit strongly red-shifts the fluorescence spectrum of the $D_1\delta_+$ moiety, compared to $D_1\delta$, resulting in a lack of overlap with the acceptor absorption (see Fig. 2). The suppression of energy transfer from $(D_1\delta_+)^*$ to A is thus expected in this case.

This is confirmed by the transient absorption data obtained for $D_1\delta_+A$. By analyzing the results in a similar fashion as done previously, we can obtain the following reaction scheme:

$$D_1\delta_+A \xrightarrow{<100\ fs} (D_1\delta_+)^*A \xrightarrow{90\ ps} (D_1\delta_+)^{+}A^{-} \xrightarrow{480\ ps} D_1\delta_+A$$

The main difference here as compared to the above $D_1\delta A$ molecule is that energy transfer from $(D_1\delta_+)^*$ to A* is absent, resulting in the direct formation of the CT states from the excited donor state $(D_1\delta_+)^*$. This is highlighted in Fig. 8, where differential spectra at 80 fs and 3.5 ps are shown for both molecules in chloroform. In the case of $D_1\delta_+A$, contributions of $D_1\delta_+$ bleach and SE are observed, but there is no signature of the excited A* state such as SE at 575 nm or the ESA at 705 nm, confirming the absence of energy transfer from D* to A*. However, despite the excitation of A, a signal akin to the bleach of A is observed in the 500 nm region. In line with other reports,[63–65] we attribute it to a Stark shift of A's absorption. This is most likely due to the intra-molecular dipole moment on $(D_1\delta_+)^*$, with the electron localized on the δ_+ spacer with high electron affinity.

Together with the available experimental results, our calculations lead to a possible pathway for CT formation as illustrated in Fig. 9 for the $D_0\delta_+A$ system. Here, state-specific geometry optimizations were performed and the resulting energetic ordering is shown for different equilibrium geometries pertaining to the respective electronic states. In full agreement with the reaction scenario derived from the experiments (see above), initial excitation to the DS_2 state entails subsequent transfer to the DS_1 state, followed by CT_1 formation. Note, though, that the sketches of Fig. 7 and 9 do not give information about actual state crossings. The present calculations also yield values for intramolecular reorganization energies that are used in the Marcus–Jortner analysis reported below.

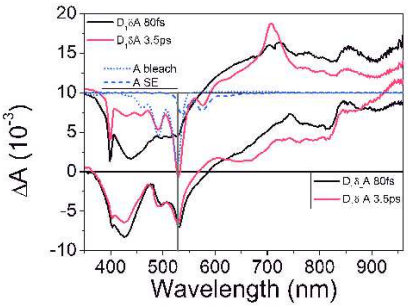

Fig. 8 Influence of δ_+ in chloroform. Top: In $D_1\delta A$, the 80 fs spectrum contains the contributions of the donor's bleach and stimulated emission, while the 3.5 ps one displays the excited state of A, through its bleach, SE (blue curves), and excited state absorption (peak at around 700 nm), indicating the energy transfer from donor to acceptor on the few ps time scale. Bottom: in $D_1\delta_+A$, both differential spectra show similar features, involving D's bleach and SE, but also a shape similar to that of bleach of A. Yet, no SE nor ESA from A* nor induced absorption from A – can be seen: this is explained by the localization of the excitation on the δ_+ group, that Stark-shifts the absorption band of A.

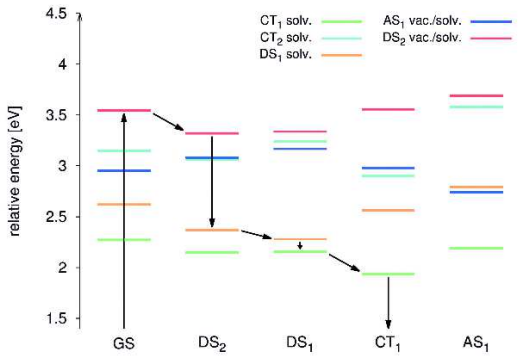

Fig. 9 Illustration of a possible photochemical pathway for $D_0\delta_+A$, suitable to describe the experimental results. Relative energies are reported for a series of equilibrium structures for the respective states, shown along the *x* axis (where GS refers to the ground state equilibrium structure). As in Fig. 7, all state energies refer to chloroform solvent.

(d) Molecular design of long-lived CT states: the effect of δ and the length of the donor moieties

Besides the nature of the spacer (either δ or δ_+) we also studied the influence of (i) the terminal amine δ and (ii) the length *n* of the donor block. Fig. 10 compares the kinetic traces recorded in chloroform at 800 nm, where the signature of the anion $A^{\bullet}$ is the strongest, in a selection of compounds. First Fig. 10A illustrates the influence of the nature of the spacer (either δ or δ_+) between D_1 and A, and that of the terminal δ on D_1. Table 2 summarizes the time constants associated with the CT formation and recombination. Interestingly, molecules with δ_+ have CT state formation times at least 5 times slower than the compounds with the regular δ spacer, since the rise time of the anion absorption band is 90 ps and 120 ps for $D_1\delta_+A$ (red) and δ $D_1\delta_+A$ (pink), respectively, *versus* 14 ps for $D_1\delta_+A$ and δ $D_1\delta_+A$. This may be linked to the lack of prior energy transfer in the presence of δ+ as compared to the compounds with the δ spacer, and to the fact that ET occurs from D* in the former case (see the Discussion section). Conversely, δ_+ does not have a significant impact on charge recombination kinetics, since Fig. 10A also displays very similar decay kinetics for $D_1\delta A$ (black) and $D_1\delta_+A$ (red) on the one hand or for δ $D_1\delta A$ (blue) and δ $D_1\delta_+A$ (pink) on the other.

More interesting is the effect of functionalizing the D_1 moiety with the terminal δ substituent, since the lifetimes of the

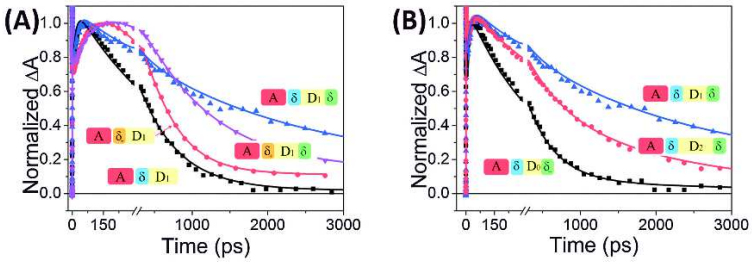

Fig. 10 Kinetics at 800 nm, where the anion $A^{\bullet-}$ absorbs preferentially, normalized at their second maximum, corresponding to the maximum CT state population. (A) Influence of δ_+ and δ_- for a fixed (n = 1) donor length: $D_1\delta A$ (black), $D_1\delta_+A$ (red), $\delta\_D_1\delta A$ (blue) and $\delta\_D_1\delta_+A$ (pink). The effect of δ_+ is to slow down the CT state formation, while δ_- slows down its recombination. (B) Influence of the donor length on the CT state lifetime on the $\delta\_D_n\delta A$ molecules, with n = 0 (black), 1 (blue) and 2 (red). The CT state lifetime is optimum for n = 1.

Table 2 Charge transfer state formation and recombination time constants for $D_n\delta_+A$ and $\delta\_D_n\delta A$ with increasing donor length

	$D_n\delta_+A$		$\delta\_D_n\delta A$	
n	Formation (ps)	Recombination (ps)	Formation (ps)	Recombination (ns)
0	90	410	20	0.4
1	90	480	14	2.3
2	150	440	14	1.1
3	140	430		

CT states are increased by a factor of about 2.5 for molecules with the δ_+ spacer (1.2 ns for δ $D_1\delta_+A$ *versus* 0.48 ns for $D_1\delta_+A$) and of 4.5 for compounds with the δ_- spacer (2.3 ns for δ $D_1\delta A$ *versus* 0.51 ns for $D_1\delta A$). This effect is expected to be due to the larger separation distance between the charges of the CT state in molecules where δ would stabilize the positive charge on the extremity of the donor moiety, farther away from the acceptor. A quantitative analysis is presented in Section 5.

Finally, we explore the effect of lengthening the donor moiety by investigating the photophysics of the $D_n\delta_+A$ and δ $D_n\delta_+A$ molecules, with n = 0 to n = 3 (see Fig. 1 and 10B). The same global fitting analysis as above is applied to determine the time constants associated with the CT state recombination in each case and the results are displayed in Table 2.

All the $D_n\delta_+A$ compounds display the same CT state formation and recombination time (see Fig. S4, ESI†), in the range of 450 ps, showing that the donor length has no impact on the kinetics of the photophysics in these compounds, in line with previous conclusions reported by ref. 30. However, a quite different observation is made with the δ $D_n\delta A$ molecules as illustrated in Fig. 10B: in this case, the stabilizing effect of the terminal δ substituent is optimal for n = 1, with an increase of the CT state lifetime of up to 2.3 ns. This could be understood as previously as an effect of spreading further apart the charges along the molecule. For n = 2 or larger, the more distant δ would not be able to shift the D electronic density further away from $A^{\bullet}$, as it does for n = 1.

(e) Effect of the solvent

To investigate the influence of the interaction with the environment, in particular the solvent polarity, we compare the results obtained in chloroform with those in toluene and trichloroethylene (TCE) for the $D_1\delta_+A$, $D_1\delta A$ and δ $D_1\delta A$ compounds. Table 3 displays the CT state formation and recombination time constants obtained by the same global fitting procedure as above.

For each molecule, the CT states are stabilized, *i.e.* their lifetime is increased, in less polar solvents. However, the stabilizing effect of δ previously observed in chloroform is not as large in these solvents. This may however be due to experimental limitations since a precise determination of the multi-ns CT lifetimes would require measuring the kinetics over a time span longer than accessible in our femtosecond pump–probe experiment (6 ns).

Table 3 Effect of the solvent polarity: CT state formation and recombination time constants (in ns) of $D_1\delta_+A$, $D_1\delta A$ and $\delta\_D_1\delta A$ in toluene, trichloroethylene (TCE) and chloroform. The bulk dielectric constants are taken from ref. 66

Solvent dielectric constants ε		Toluene ε = 2.38 (3.5[a])	TCE ε = 3.42	Chloroform ε = 4.81
$D_1\delta A$	Formation (ns)	0.026	0.014	0.014
	Recombination (ns)	5.7	4	0.50
$\delta\_D_1\delta A$	Formation (ns)	0.030	0.019	0.014
	Recombination (ns)	6.7	6	2.3
$D_1\delta_+A$	Formation (ns)	0.26	0.15	0.090
	Recombination (ns)	6.2	2.8	0.48
$\delta\_D_1\delta_+A$	Formation (ns)			0.12
	Recombination (ns)			1.2

[a] An effective dielectric constant of 3.5 is found in the literature for toluene, to account for the effect of its strong electric quadrupole moment.[38]

4 Analysis and discussion

(a) Effect of molecular design on CT formation and recombination

We summarize the above results as follows:

(i) With the benzene-containing δ spacer, an ultrafast (~1 ps) energy transfer to the acceptor precedes the CT formation such that electron transfer (ET) occurs from the A* state on a ~10 ps time scale.

(ii) Instead, the benzothiadiazole-containing δ_+ spacer precludes the initial energy transfer, and a significantly slower (~100 ps) ET occurs from the originally photoexcited donor $(D_n\delta_+)^*$ state.

(iii) Irrespective of the nature of the spacer (δ or δ_+), the CT state lifetime increases upon adding the terminal amine δ on the donor block, up to 5-fold with the optimum donor length $n = 1$ in chloroform, and possibly also in other solvents, but lifetimes >3 ns are not accurately measured here.

(iv) Reducing the solvent polarity (from chloroform to toluene) slows down the CT state recombination by up to one order of magnitude, and to a lesser extent the CT state formation (by a factor 2 or 3 at most). We note that in the slightly more polar chlorobenzene ($\varepsilon = 5.62$) the CT lifetime of similar D–A compounds (with no spacer and no δ moiety) was even shorter (on the 0.1 ns time scale),[30] in line with the trend observed here as a function of dielectric constant.

(v) Electronic structure modeling gives evidence for a stabilizing effect by the δ terminal group of the second, higher-lying CT_2 state, characterized by much larger charge separation distance. An even stronger influence of the solvent is expected when allowing for solvent equilibration with respect to the CT states. As a result of both effects, both CT states may become nearly degenerate in particular for $n = 1$, suggesting an effective larger charge separation for the compounds incorporating $D_1\delta$.

(b) Marcus–Jortner analysis

In order to rationalize the observed influence of the molecular structure and solvent polarity on the CT state formation and recombination kinetics, it is instructive to recast the above results within Marcus theory for electron transfer (ET),[41] particularly the Jortner-modified version of the latter, which is not restricted to the high-temperature regime[40] and permits the inclusion of internal vibrations. In the following, we will consider both CT formation and recombination rates.

Within that theory, the rate k for the electron transfer occurring upon CT state formation or recombination can be written as:[67,68]

$$k = \left(\frac{4\pi^3}{h^2\lambda_{sol}k_BT}\right)^{1/2} V^2 \exp\left(-\frac{\lambda_{mol}}{E_{vib}}\right) \sum_{n=0}^{\infty} \frac{\left(\frac{\lambda_{mol}}{E_{vib}}\right)^n}{n!} \times \exp\left(-\frac{(\Delta G^0 + \lambda_{sol} + nE_{vib})^2}{4\lambda_{sol}k_BT}\right) \quad (2)$$

where V is the electronic coupling between initial and final states, k_B is the Boltzmann constant and T is the temperature (here, 298 K). λ_{mol} is the intramolecular reorganization energy, which is computed by geometry optimization in the relevant states (see above) and displayed in Table S2 (ESI†). E_{vib} is the energy of an effective, high-frequency vibrational mode and is set here to 1500 cm^{-1} (0.186 eV), the characteristic frequency of C=C bond stretching. λ_{sol} is the solvent reorganization energy, which is estimated in different solvents using the Born–Hush approach:[69]

$$\lambda_{sol} = \frac{e^2}{4\pi\varepsilon_0}\left(\frac{1}{2r^+} + \frac{1}{2r^-} - \frac{1}{R_{CC}}\right)\left(\frac{1}{n^2} - \frac{1}{\varepsilon}\right) \quad (3)$$

In this equation, n and ε are the refractive index and the dielectric constant of solvent. r^+ and r^- are the radii of hole and electron densities, and R_{CC} is the electron–hole centroid distance, as computed above (see Table 4).

The Gibbs free energies for charge recombination (ΔG^0_{CR}) and charge separation (ΔG^0_{CS}) in different solvents are calculated from continuum dielectric theory:[70]

$$\Delta G^0_{CR} = -[E_{ox}(D) - E_{red}(A)] + \frac{e^2}{4\pi\varepsilon_0\varepsilon R_{CC}} + \frac{e^2}{8\pi\varepsilon_0}\left(\frac{1}{r^+} + \frac{1}{r^-}\right)\left(\frac{1}{\varepsilon_{ref}} - \frac{1}{\varepsilon}\right) \quad (4)$$

$$\Delta G^0_{CS} = [E_{ox}(D) - E_{red}(A)] - \frac{e^2}{4\pi\varepsilon_0\varepsilon R_{CC}} - \frac{e^2}{8\pi\varepsilon_0}\left(\frac{1}{r^+} + \frac{1}{r^-}\right)\left(\frac{1}{\varepsilon_{ref}} - \frac{1}{\varepsilon}\right) - E_{00} \quad (5)$$

where E_{ox} and E_{red} are oxidation and reduction potential energies (see Methods). ε_{ref} is the dielectric constant of dichloromethane ($\varepsilon_{ref} = 8.93$),[66] in which oxidation and reduction potentials were measured. E_{00} is the energy of the excited state from which the CT state is formed, namely $(D_n\delta_+)^*$ for molecules containing δ_+ or A* for molecules containing δ, when resonant energy transfer precedes ET (see above).

A measure of the charge separation (*i.e.*, electron–hole separation) in different dyad systems is provided in terms of the computed electron–hole centroid distances (R_{CC}), as shown in Table 4. The method to calculate the distance R_{CC} refers to the corresponding orbital transitions of the excitation and uses the amplitudes given for each transition as weights (as implemented in the Multiwfn-Package).[57] The results reported in Table 4 show that the addition of δ results in an increase of

Table 4 For the various combinations of donor/acceptor moieties, (i) electron–hole centroid distance R_{CC}, in the lowest energy CT_1 state, along with (ii) radii of electron (r^-) and hole (r^+) densities are shown

Structure	Distance R_{CC} [nm]	r^+	r^-
$D_0\delta A$	2.0	0.6	0.4
$D_1\delta A$	2.3	0.8	0.4
$D_0\delta_+A$	2.0	0.6	0.4
$D_1\delta_+A$	2.2	0.7	0.4
$\delta\_D_0\delta A$	2.3	0.7	0.4
$\delta\_D_1\delta A$	2.9	1.0	0.4
$\delta\_D_0\delta_+A$	2.3	0.7	0.4
$\delta\_D_1\delta_+A$	2.5	0.9	0.4

R_{CC} in the CT_1 states of at least 3.0 Å for D_0 and D_1. This means that the effect is larger for the shorter donor. Furthermore, the CT_2 state shows a very large increase of R_{CC} of about 20 Å as compared with $D_1\delta_+A$ (with respect to the CT_1).

We now apply the Marcus–Jortner formalism to both CT formation and recombination. Tables S2 and S3 (see ESI†) summarize the values of all parameters appearing in eqn (2) to (5) for various solvents and molecules, as well as the computed solvent reorganization energies and Gibbs free energies.

First we note that CT state recombination takes place in the so-called Marcus inverted regime as $-\Delta G^0 > \lambda = \lambda_{sol} + \lambda_{mol}$. CT state formation from $(D_1\delta_+)^*$ and $(\delta\ D_1\delta_+)^*$ takes place in the normal Marcus regime while CT state formation from A* occurs in the (nearly) optimal Marcus regime, as the difference between $-\Delta G^0_{CS}$ and λ is less than 0.06 meV.

Hence, we conclude that changing the solvent polarity would have a stronger influence on the charge recombination than on charge formation. This is confirmed when using the right-hand side of eqn (2) to predict the expected solvent influence on various ET steps of interest. Since all solvents have a similar refractive index, one can verify that the main solvent influence comes from the change in the dielectric constant, by plotting k/V^2 as a function of ε (eqn (2) to (5)) in Fig. 11 for different types of ET reactions for $D_1\delta_+A$ and $D_1\delta A$ characterized by different Gibbs energies (ET from $(D_1\delta_+)^*$, A* or CT states), for different λ_{mol}, r^+, r^-, and R_{cc} (see Table S2 in ESI†). Here, following previous reports, we introduce an effective dielectric constant of 3.5 for toluene, as expected to account for the effect of its strong electric quadrupole moment.[38]

Fig. 11 shows that the change in the solvent is expected to affect the CT formation kinetics comparatively weakly (by less than 50%), but the recombination by a factor of ~3 is mostly due to the change in ε. These opposite trends can be traced back to the different Marcus regimes (inverted *vs.* quasi-optimal) of CT formation and recombination for the present molecules. Given the very crude level of description of the solvent influence by eqn (3) (which assumes a dielectric-sphere kind of model,[41] while the hole and electron density distributions are very much elongated in the present systems), these trends remarkably reproduce the observations, since the solvent influence is indeed significantly stronger for CT recombination than for CT formation (see Table 3). In addition, by using the observed ET rates for k, we can further exploit eqn (2) and infer the magnitude of the electronic coupling term V given in Table 5. Since the observed solvent influence on the CT formation and recombination is larger than that predicted by Fig. 11, eqn (2) actually predicts a residual solvent dependence of the electronic coupling term. Although a solvent-dependent coupling may be expected due to *e.g.* solvent-induced electrostatic interaction shielding,[71,72] the accuracy of this prediction is uncertain given the very crude approximation made for the solvent reorganization energy (eqn (3)). A more accurate modeling of the solvent influence would require a molecular-based (rather than continuum) modeling of the solvent,[73] which goes beyond the scope of the present work.

All the electronic coupling energies V are very small, in the range of 0.3 to 2 meV. This is in line with the electronic couplings already computed for very similar dyad compounds[33,34] or deduced by a similar approach for other large organic donor and acceptor compounds[38] connected by saturated bonds. Interestingly, the faster CT state formation in the compounds containing δ rather than δ_+ as a donor–acceptor spacer clearly appears as a result of a 2- to 3-fold stronger "hole" coupling between A* and CT states than between $(D_1\delta_+)^*$ and CT states.[33,34]

Importantly, in view of assessing the molecular design strategy, it is most relevant to compare the results obtained for $D_1\delta A/\delta\ D_1\delta A$ and $D_1\delta_+A/\delta\ D_1\delta_+A$ in chloroform. We note that upon adding the terminal amine δ on $D_1\delta_+A$ a nearly 3-fold increase in the CT state lifetime is observed in chloroform, which, on the basis of eqn (2), relates back to a reduction by a factor of 1.7 in the estimated electronic coupling V (see Table 5).

Table 5 Electronic couplings for charge recombination and charge formation, calculated using eqn (2) taking into account the experimental reaction rates (in Table 3)

V (meV)		Toluene (ε = 3.5)	TCE	Chloroform
$D_1\delta A$	Formation	1.783	2.385	2.392
	Recombination	0.313	0.376	0.535
$D_1\delta_+A$	Formation	0.682	0.975	1.381
	Recombination	0.236	0.343	0.495
$\delta\_D_1\delta_+A$	Formation			0.886
	Recombination			0.306

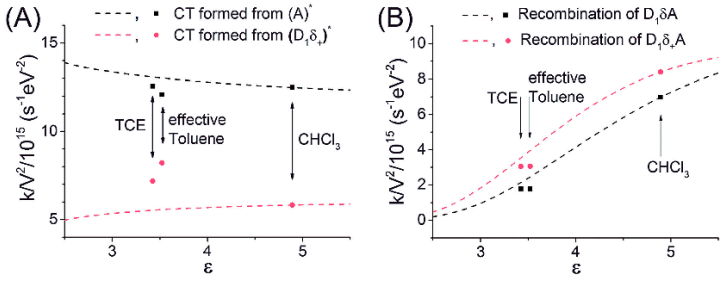

Fig. 11 Influence of the solvent on k/V^2 as predicted from eqn (2) to (5) for (A) CT state formation from $(D_1\delta_+)^*$ (red) or A* (black), and (B) CT state recombination in $D_1\delta_+A$ (red) and $D_1\delta A$ (black). Dashed lines illustrate the dependence on ε assuming a fixed value of n (here n = 1.446 corresponding to chloroform), squares and dots give the values computed with the correct values of n and ε (Table S4, ESI†) for each solvent.

The latter is commonly assumed to be proportional to the overlap between both wavefunctions, and to decay exponentially with the electron–hole separation distance in the CT state, according to $V^2 = V_0^2 \exp(-\beta R_{CC})$.[37] Typical values for the decay length scale have been reported to be in the range of $\beta \sim 0.3$–0.7 Å^{-1} for ET through covalent bonds or involving carrier tunneling (super-exchange) in organic molecules.[37,74–76] In the present case, electronic structure modeling predicts that adding the terminal δ moiety on $D_1\delta_+A$ should increase the electron–hole distance R_{CC} by 3 Å in the CT_1 state and as much as 18 Å if the relevant CT state would rather be of CT_2 character. With a 1.75-fold decrease of V, these changes in R_{CC} would correspond to a rather small β value of 0.34 Å^{-1} (considering only CT_1) or an unrealistically small value of 0.06 Å^{-1} when considering the CT_2 state. We therefore conclude that the observed CT state is essentially of CT_1 character, possibly slightly mixed with CT_2 character, due to the near-degeneracy with that second state.

5 Conclusion

The present work is in line with a large body of recent literature showing that the chemical design of donor–bridge–acceptor species has a pronounced impact on photo-induced processes and their lifetimes in solution. The D–A compounds presented here bear the additional beneficial property of forming mesomorphic phases at room temperature,[35,36] which is of potential interest for solar cell applications.[28,29] As compared to the first generation DAD designed in our lab,[32] the CT state lifetime has been increased by up to 10-fold. The small electronic coupling is the main reason for the relatively slow CT formation time and long lifetime. This conclusion was already supported by previous experiments on a family of similar compounds with the donor and acceptor moieties connected by an alkyl spacer of increasing length.[29] Here, the terminal δ amine is shown to further reduce the electronic coupling and thus further enlarge the CT lifetime by a factor of 2 to 5 when the donor length is optimal ($n = 1$), most likely due to the enhancement of the electron–hole distance in the CT state. The latter distance is slightly increased upon modification of the lower-lying CT state (CT_1) by the δ addition, but possibly also by the mixing with a very different CT state (CT_2 with much larger electron–hole separation), which may become nearly degenerate with CT_1 upon adding δ. Interestingly, changing the donor length in the absence of the terminal δ moiety does not influence the CT state formation or recombination kinetics, in agreement with other reports.[30]

Besides, the influence of the solvent polarity is even more pronounced in affecting the CT lifetime, evidencing the role of the interactions with the environment. From the strong influence of the environment on the CT lifetime observed here upon changing the solvent polarity, we may expect that in a self-assembled film of these compounds the intermolecular interaction may strongly modify the conclusions drawn here after studying the intramolecular charge transfer and recombination processes. This was observed *e.g.* in the previous generation of DAD compounds[32] and rationalized by the onset of more efficient intermolecular charge transfer processes[5] and of a ns-lived CT lifetime component, favored in the film structure. Subsequent investigations of similar DA compounds in films also revealed ns-lived CT signatures.[30] This suggests that tailoring the intrinsic molecular property should be seen only as one of the relevant building blocks within the overall design strategy for optimizing the CT state lifetime in functional films.

More generally in the context of solar cells, this relates to the important question as to which extent the CT dynamics of isolated D–A oligomers is relevant for the D–A when incorporated in smectic LC films and how the OPV device performances are affected. It was recently conjectured that the film morphologies determine the charge transport properties, while the intramolecular D–A properties controlled by their chemical composition and determined from solution phase experiments (*e.g.* ultrafast spectroscopy) would independently govern the CT recombination rate and thus the availability of separated charges.[29,30] The combination of both effects rationalizes high external quantum efficiencies (EQE), fill factors (FF) and thus PCE. Our present work challenges the above viewpoint, as the solvent dependence of the CT recombination rates indicates that the dielectric properties and thus reorganization energy of the D–A oligomer environment has to be accounted for. In addition, our previous work on D–A oligomer films highlights that the formation of charge separated states or weakly bound CT states was favored and strongly dependent on the D–A inter-oligomer arrangement (nano-morphology) and the delocalized character of the excitonic absorption.[32–34]

Acknowledgements

This work was supported by the ANR PICASSO project (ANR 2011-BS08-0009), the joint DFG/ANR MolNanoMat project (DFG BU1032/3-1; ANR 2011-INTB-1012-01), and the European Community *via* the Interreg IV-A program (C25, Rhin Solar Project). L. L. acknowledges support from the Université de Strasbourg, and T. R. from the Région Alsace and CNRS.

References

1 F. J. M. Hoeben, P. Jonkheijm, E. W. Meijer and A. P. H. J. Schenning, *Chem. Rev.*, 2005, **105**, 1491–1546.
2 H. Liu, J. Xu, Y. Li and Y. Li, *Acc. Chem. Res.*, 2010, **43**, 1496–1508.
3 J.-T. Chen and C.-S. Hsu, *Polym. Chem.*, 2011, **2**, 2707–2722.
4 S. D. Dimitrov and J. R. Durrant, *Chem. Mater.*, 2014, **26**, 616–630.
5 L. Lu, T. Zheng, Q. Wu, A. M. Schneider, D. Zhao and L. Yu, *Chem. Rev.*, 2015, **115**, 12666–12731.
6 T. M. Clarke and J. R. Durrant, *Chem. Rev.*, 2010, **110**, 6736–6767.
7 C. Deibel, T. Strobel and V. Dyakonov, *Adv. Mater.*, 2010, **22**, 4097–4111.
8 J. Subbiah, B. Purushothaman, M. Chen, T. Qin, M. Gao, D. Vak, F. H. Scholes, X. Chen, S. E. Watkins, G. J. Wilson,

A. B. Holmes, W. W. H. Wong and D. J. Jones, *Adv. Mater.*, 2015, **27**, 702–705.
9 L. Huo, T. Liu, X. Sun, Y. Cai, A. J. Heeger and Y. Sun, *Adv. Mater.*, 2015, **27**, 2938–2944.
10 T. Bura, N. Leclerc, S. Fall, P. Lévèque, T. Heiser, P. Retailleau, S. Rihn, A. Mirloup and R. Ziessel, *J. Am. Chem. Soc.*, 2012, **134**, 17404–17407.
11 Q. Zhang, B. Kan, F. Liu, G. Long, X. Wan, X. Chen, Y. Zuo, W. Ni, H. Zhang, M. Li, Z. Hu, F. Huang, Y. Cao, Z. Liang, M. Zhang, T. P. Russell and Y. Chen, *Nat. Photonics*, 2015, **9**, 35–41.
12 O. K. Kwon, M. A. Uddin, J. H. Park, S. K. Park, T. L. Nguyen, H. Y. Woo and S. Y. Park, *Adv. Mater.*, 2016, **28**, 910–916.
13 D. Meng, D. Sun, C. Zhong, T. Liu, B. Fan, L. Huo, Y. Li, W. Jiang, H. Choi, T. Kim, J. Y. Kim, Y. Sun, Z. Wang and A. J. Heeger, *J. Am. Chem. Soc.*, 2016, **138**, 375–380.
14 D. Sun, D. Meng, Y. Cai, B. Fan, Y. Li, W. Jiang, L. Huo, Y. Sun and Z. Wang, *J. Am. Chem. Soc.*, 2015, **137**, 11156–11162.
15 S. Günes, H. Neugebauer and N. S. Sariciftci, *Chem. Rev.*, 2007, **107**, 1324–1338.
16 R. E. Martin and F. Diederich, *Angew. Chem., Int. Ed.*, 1999, **38**, 1350–1377.
17 P. F. H. Schwab, J. R. Smith and J. Michl, *Chem. Rev.*, 2005, **105**, 1197–1280.
18 J. L. Segura, N. Martin and D. M. Guldi, *Chem. Soc. Rev.*, 2005, **34**, 31–47.
19 J. Roncali, *Chem. Soc. Rev.*, 2005, **34**, 483–495.
20 T. M. Figueira-Duarte, A. Gegout and J.-F. Nierengarten, *Chem. Commun.*, 2007, 109–119, DOI: 10.1039/B609383C.
21 T. Nishizawa, H. K. Lim, K. Tajima and K. Hashimoto, *Chem. Commun.*, 2009, 2469–2471, DOI: 10.1039/B902060H.
22 J. Cremer, E. Mena-Osteritz, N. G. Pschierer, K. Mullen and P. Bauerle, *Org. Biomol. Chem.*, 2005, **3**, 985–995.
23 E. Peeters, P. A. van Hal, S. C. J. Meskers, R. A. J. Janssen and E. W. Meijer, *Chem. – Eur. J.*, 2002, **8**, 4470–4474.
24 J. D. Chai and M. Head-Gordon, *Phys. Chem. Chem. Phys.*, 2008, **10**, 6615–6620.
25 K. J. Lee, J. H. Woo, E. Kim, Y. Xiao, X. Su, L. M. Mazur, A. J. Attias, F. Fages, O. Cregut, A. Barsella, F. Mathevet, L. Mager, J. W. Wu, A. D'Aleo and J. C. Ribierre, *Phys. Chem. Chem. Phys.*, 2016, **18**, 7875–7887.
26 C. Guo, Y.-H. Lin, M. D. Witman, K. A. Smith, C. Wang, A. Hexemer, J. Strzalka, E. D. Gomez and R. Verduzco, *Nano Lett.*, 2013, **13**, 2957–2963.
27 J. W. Mok, Y.-H. Lin, K. G. Yager, A. D. Mohite, W. Nie, S. B. Darling, Y. Lee, E. Gomez, D. Gosztola, R. D. Schaller and R. Verduzco, *Adv. Funct. Mater.*, 2015, **25**, 5569.
28 L. Bu, X. Guo, B. Yu, Y. Qu, Z. Xie, D. Yan, Y. Geng and F. Wang, *J. Am. Chem. Soc.*, 2009, **131**, 13242–13243.
29 J. Qu, B. Gao, H. Tian, X. Zhang, Y. Wang, Z. Xie, H. Wang, Y. Geng and F. Wang, *J. Mater. Chem. A*, 2014, **2**, 3632.
30 B.-R. Gao, J.-F. Qu, Y. Wang, Y.-Y. Fu, L. Wang, Q.-D. Chen, H.-B. Sun, Y.-H. Geng, H.-Y. Wang and Z.-Y. Xie, *J. Phys. Chem. C*, 2013, **117**, 4836–4843.
31 T. Roland, G. H. Ramirez, J. Leonard, S. Mery and S. Haacke, *J. Phys.: Conf. Ser.*, 2011, **276**, 012006.
32 T. Roland, J. Léonard, G. Hernandez Ramirez, S. Mery, O. Yurchenko, S. Ludwigs and S. Haacke, *Phys. Chem. Chem. Phys.*, 2012, **14**, 273–279.
33 M. Polkehn, P. Eisenbrandt, H. Tamura, S. Haacke, S. Mery and I. Burghardt, Proc. SPIE **9884**, Nanophotonics VI, Brussels, Belgium, 2016.
34 M. Polkehn, H. Tamura, P. Eisenbrandt, S. Haacke, S. Méry and I. Burghardt, *J. Phys. Chem. Lett.*, 2016, **7**, 1327–1334.
35 P. O. Schwartz, L. Biniek, E. Zaborova, B. Heinrich, M. Brinkmann, N. Leclerc and S. Mery, *J. Am. Chem. Soc.*, 2014, **136**, 5981–5992.
36 L. Biniek, P.-O. Schwartz, E. Zaborova, B. Heinrich, N. Leclerc, S. Mery and M. Brinkmann, *J. Mater. Chem. C*, 2015, **3**, 3342–3349.
37 C. C. Moser, J. M. Keske, K. Warncke, R. S. Farid and P. L. Dutton, *Nature*, 1992, **355**, 796–802.
38 B. P. Karsten, R. K. M. Bouwer, J. C. Hummelen, R. M. Williams and R. A. J. Janssen, *J. Phys. Chem. B*, 2010, **114**, 14149–14156.
39 F. Kanal, F. Ruetzel, H. Lu, M. Moos, M. Holzapfel, T. Brixner and C. Lambert, *J. Phys. Chem. C*, 2014, **118**, 23586–23598.
40 D. A. Copeland, N. R. Kestner and J. Jortner, *J. Chem. Phys.*, 1970, **53**, 1189–1216.
41 R. A. Marcus and N. Sutin, *Biochim. Biophys. Acta, Rev. Bioenerg.*, 1985, **811**, 265–322.
42 J. Briand, O. Bram, J. Rehault, J. Léonard, A. Cannizzo, M. Chergui, V. Zanirato, M. Olivucci, J. Helbing and S. Haacke, *Phys. Chem. Chem. Phys.*, 2010, **12**, 3178–3187.
43 T. Roland, PhD thesis, University of Strasbourg, 2014.
44 A. Ruff, E. Heyer, T. Roland, S. Haacke, R. Ziessel and S. Ludwigs, *Electrochim. Acta*, 2015, **173**, 847–859.
45 J. Wenzel, A. Dreuw and I. Burghardt, *Phys. Chem. Chem. Phys.*, 2013, **15**, 11704.
46 T. Yanai, D. P. Tew and N. C. Handy, *Chem. Phys. Lett.*, 2004, **393**, 51–57.
47 J. B. Foresman, M. Head-Gordon, J. A. Pople and M. J. Frisch, *J. Phys. Chem.*, 1992, **96**, 135–149.
48 O. Christiansen, H. Koch and P. Jorgensen, *Chem. Phys. Lett.*, 1995, **243**, 409–418.
49 C. Hättig, *J. Chem. Phys.*, 2003, **118**, 7751–7761.
50 C. Hättig and F. Weigend, *J. Chem. Phys.*, 2000, **113**, 5154–5161.
51 C. Hättig, in *Advances in Quantum Chemistry, Vol 50: A Tribute to Jan Linderberg and Poul Jorgensen*, ed. J. R. Sabin and E. Brandas, Elsevier Academic Press Inc., San Diego, 2005, vol. 50, pp. 37–60.
52 A. B. Trofimov and J. Schirmer, *J. Phys. B: At., Mol. Opt. Phys.*, 1995, **28**, 2299–2324.
53 F. Weigend, *Phys. Chem. Chem. Phys.*, 2006, **8**, 1057–1065.
54 F. Weigend and R. Ahlrichs, *Phys. Chem. Chem. Phys.*, 2005, **7**, 3297–3305.
55 A. Klamt and G. Schürmann, *J. Chem. Soc., Perkin Trans. 2*, 1993, 799–805, DOI: 10.1039/p29930000799.
56 S. Sinnecker, A. Rajendran, A. Klamt, M. Diedenhofen and F. Neese, *J. Phys. Chem. A*, 2006, **110**, 2235–2245.
57 T. Lu and F. Chen, *J. Comput. Chem.*, 2012, **33**, 580–592.

58 University, of, Karlsruhe, and, Forschungszentrum, Karlsruhe and GmbH, Journal, 1989–2016.
59 F. Neese, *Wiley Interdiscip. Rev.: Comput. Mol. Sci.*, 2012, **2**, 73–78.
60 M. J. Frisch, G. W. Trucks, H. B. Schlegel, G. E. Scuseria, M. A. Robb, J. R. Cheeseman, G. Scalmani, V. Barone, B. Mennucci, G. A. Petersson, H. Nakatsuji, M. Caricato, X. Li, H. P. Hratchian, A. F. Izmaylov, J. Bloino, G. Zheng, J. L. Sonnenberg, M. Hada, M. Ehara, K. Toyota, R. Fukuda, J. Hasegawa, M. Ishida, T. Nakajima, Y. Honda, O. Kitao, H. Nakai, T. Vreven, J. A. Montgomery Jr., J. E. Peralta, F. Ogliaro, M. J. Bearpark, J. Heyd, E. N. Brothers, K. N. Kudin, V. N. Staroverov, R. Kobayashi, J. Normand, K. Raghavachari, A. P. Rendell, J. C. Burant, S. S. Iyengar, J. Tomasi, M. Cossi, N. Rega, N. J. Millam, M. Klene, J. E. Knox, J. B. Cross, V. Bakken, C. Adamo, J. Jaramillo, R. Gomperts, R. E. Stratmann, O. Yazyev, A. J. Austin, R. Cammi, C. Pomelli, J. W. Ochterski, R. L. Martin, K. Morokuma, V. G. Zakrzewski, G. A. Voth, P. Salvador, J. J. Dannenberg, S. Dapprich, A. D. Daniels, Ö. Farkas, J. B. Foresman, J. V. Ortiz, J. Cioslowski and D. J. Fox, 2009.
61 D. Gosztola, M. P. Niemczyk, W. Svec, A. S. Lukas and M. R. Wasielewski, *J. Phys. Chem. A*, 2000, **104**, 6545–6551.
62 T. Roland, E. Heyer, L. Liu, A. Ruff, S. Ludwigs, R. Ziessel and S. Haacke, *J. Phys. Chem. C*, 2014, **118**, 24290–24301.
63 V. Gulbinas, Y. Zaushitsyn, H. Bässler, A. Yartsev and V. Sundström, *Phys. Rev. B*, 2004, **70**, 035215.
64 J. Leonard, E. Portuondo-Campa, A. Cannizzo, F. van Mourik, G. van der Zwan, J. Tittor, S. Haacke and M. Chergui, *Proc. Natl. Acad. Sci. U. S. A.*, 2009, **106**, 7718–7723.
65 M. Scarongella, A. A. Paraecattil, E. Buchaca-Domingo, J. D. Douglas, S. Beaupré, T. McCarthy-Ward, M. Heeney, J. E. Moser, M. Leclerc, J. M. J. Fréchet, N. Stingelin and N. Banerji, *J. Mater. Chem. A*, 2014, **2**, 6218–6230.
66 D. R. Lide, *CRC Handbook of Chemistry and Physics*, CRC Press, 1997.
67 N. R. Kestner, J. Logan and J. Jortner, *J. Phys. Chem.*, 1974, **78**, 2148–2166.
68 J. Ulstrup and J. Jortner, *J. Chem. Phys.*, 1975, **63**, 4358–4368.
69 H. Oevering, M. N. Paddon-Row, M. Heppener, A. M. Oliver, E. Cotsaris, J. W. Verhoeven and N. S. Hush, *J. Am. Chem. Soc.*, 1987, **109**, 3258–3269.
70 A. Weller, *Z. Phys. Chem.*, 1982, **133**, 93–98.
71 K. Ando, *J. Chem. Phys.*, 1997, **107**, 4585–4596.
72 H. J. Kim and J. T. Hynes, *J. Chem. Phys.*, 1992, **96**, 5088–5110.
73 D. N. LeBard, M. Lilichenko, D. V. Matyushov, Y. A. Berlin and M. A. Ratner, *J. Phys. Chem. B*, 2003, **107**, 14509–14520.
74 H. Wang, E. R. McNellis, S. Kinge, M. Bonn and E. Canovas, *Nano Lett.*, 2013, **13**, 5311–5315.
75 D. M. Adams, L. Brus, C. E. D. Chidsey, S. Creager, C. Creutz, C. R. Kagan, P. V. Kamat, M. Lieberman, S. Lindsay, R. A. Marcus, R. M. Metzger, M. E. Michel-Beyerle, J. R. Miller, M. D. Newton, D. R. Rolison, O. Sankey, K. S. Schanze, J. Yardley and X. Zhu, *J. Phys. Chem. B*, 2003, **107**, 6668–6697.
76 A. B. Ricks, K. E. Brown, M. Wenninger, S. D. Karlen, Y. A. Berlin, D. T. Co and M. R. Wasielewski, *J. Am. Chem. Soc.*, 2012, **134**, 4581–4588.

V. Towards Iron(II) Complexes as Photosensitizers for Dye-Sensitized Solar Cells

V.1 Introduction

A coordination complex consists of a coordination center (*i.e.* transition metal) surrounded by ligands (*i.e.* ions or molecules). For instance, vitamin B_{12} and Chlorophyll are natural coordination complexes that have been noticed by modern chemistry since the 1800s. For the d shell metal, the octahedral organization of six ligands around the coordination center was first proposed and proven by an Alsatian chemist Alfred Werner in 1893, which brought him a Noble Prize in 1913.[131]

According to the ligand field theory, the electric field created by the ligands surrounding the coordination center lifts the degeneracy of the five *d* orbitals of the metal. In a perfect octahedral geometry, six ligands are symmetrically arranged along x, y and z-axes. Thus its corresponding electric field splits the *d* orbitals into a subset of three orbitals, namely d_{xy}, d_{yz} and d_{zx}, and a subset of two orbitals, namely d_z^2 and d_{x2-y2}, which are called t_{2g} and $e_{g.,}$ orbitals, respectively, in the irreducible representation. The anti-bonding t_{2g} orbitals are lower in energy than the antibonding $e_{g.,}$ orbitals.

The splitting between t_{2g} and e_g orbitals is characterized by the ligand field strength, noted Δ_o. The amplitude of Δ_o depends on the metal center and the ligands. As a general rule, the ligand field strength, Δ_o:

1. increases while increasing the oxidation number of the metal. Indeed, a more oxidized metal is smaller, and thus the distances between the ligands and the metal are reduced giving a larger Δ_o.
2. increases as the number of row transition metal increases, because the expanded shells from 3*d* to 4*d* orbitals have a larger bonding strength.

Coordination complexes have numerous applications due to their high molar extinction coefficient in the visible and long-lived excited state(s): pigments in Nature, photosensitizers, photocatalysts in organic synthesis[132], organic light-emitting diodes (OLED[133]), light-driven hydrogen production[134,135] and Dye-Sensitized Solar Cells (DSSCs) [64].

V.1.1 Ruthenium complexes

Figure V.1 shows the molecular energy diagram of ruthenium (II) surrounded by six ligands in an octahedral geometry, noted, Ru(II)L_6. Four kinds of electronic transitions can occur:

1. Metal-Centered (MC) transitions: transitions involving only the orbitals of the metal, *i.e.* from t_{2g} to e_g;
2. Ligand-Centered (LC) transitions: π-π* transitions from the orbitals of the ligands;
3. Ligand-to-Metal Charge Transfer (LMCT) transitions: new transitions from the ligands π orbital to the metal e_g orbitals;
4. Metal-to-Ligand Charge Transfer (MLCT) transitions: new transitions from the metal t_{2g} orbitals to the ligands π* orbital.

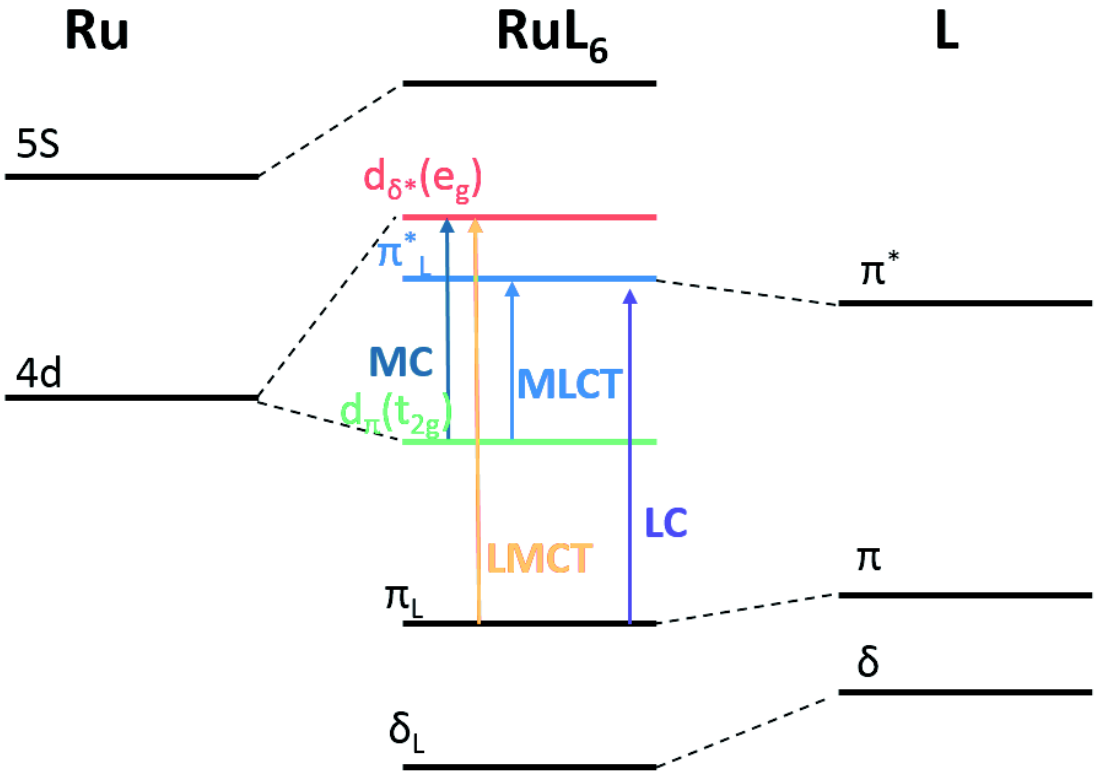

Figure V.1 Molecular energy diagram of a Ru(II)L_6 complex including the relation between orbitals in the complex and the individual Ru part and ligand part. Four transitions are formed: MC transitions, LC transitions, LMCT transitions and MLCT transitions.

The ultrafast spectroscopy studies on coordination complexes started recently. In 1997, the first reported femtosecond transient absorption experiment shows the ultrafast evolution of the excited state of the ubiquitous coordination complex: tris(2,2'-bipyridine)ruthenium(II) ($[Ru(bpy)_3]^{2+}$, (bpy=2,2'-bipyridine))[136].After optical excitation in the visible of $[Ru(bpy)_3]^{2+}$, its first excited state is a singlet MLCT (^{1}MLCT). The spin is converted from singlet to triplet (^{3}MLCT) within 100fs through an ultrafast intersystem crossing (ISC)[136]. The relaxation from ^{3}MLCT state to the ground state takes 1100 ns at room temperature.[137]

This long-lived ^{3}MLCT state makes the Ru(II) complex a good sensitizer to collect photons for many applications, such as catalysis and solar cells. Especially since 1991, Grätzel invented the Dye-Sensitized Solar Cells (DSSCs, described more precisely in § II), called Grätzel cells, by grafting Ru complexes on wide-band-gap nanocrystalline titanium dioxide (TiO_2) semiconductors.[64] Until now, the best power conversion efficiency (PCE) based on Ru(II) complex could reach 11.5%.[138]

To achieve optimum PCE of DSSCs, a long-lived excited state is a key parameter and an additional crucial parameter is the injection efficiency into TiO_2. Figure V.2 illustrates the energy levels and characteristic lifetimes of a well-studied Ru(II) complex (N719) grafted on a standard electrolyte.[78 81] From the steady-state absorption and emission spectra, the ^{1}MLCT and ^{3}MLCT state energies were estimated to be ~1.95 and ~1.6 eV, respectively. The electron injection into TiO_2 potentially involves both ^{1}MLCT and ^{3}MLCT states since their energy levels are higher than the bottom of the TiO_2 conduction band. The total injection efficiency depends on the ratio between injection process and relaxation decay (ISC for ^{1}MLCT state and phosphorescence for the ^{3}MLCT state). According to the ref. 79, multiple electron injection processes are observed in N3-TiO_2 film and the dominant electron injection is from ^{1}MLCT state but recent works on N719 show that the situation could be different and that electron injection from ^{3}MLCT state dominates. Therefore, the key parameter to achieve an efficient electron injection is to get a long-lived ^{3}MLCT state.

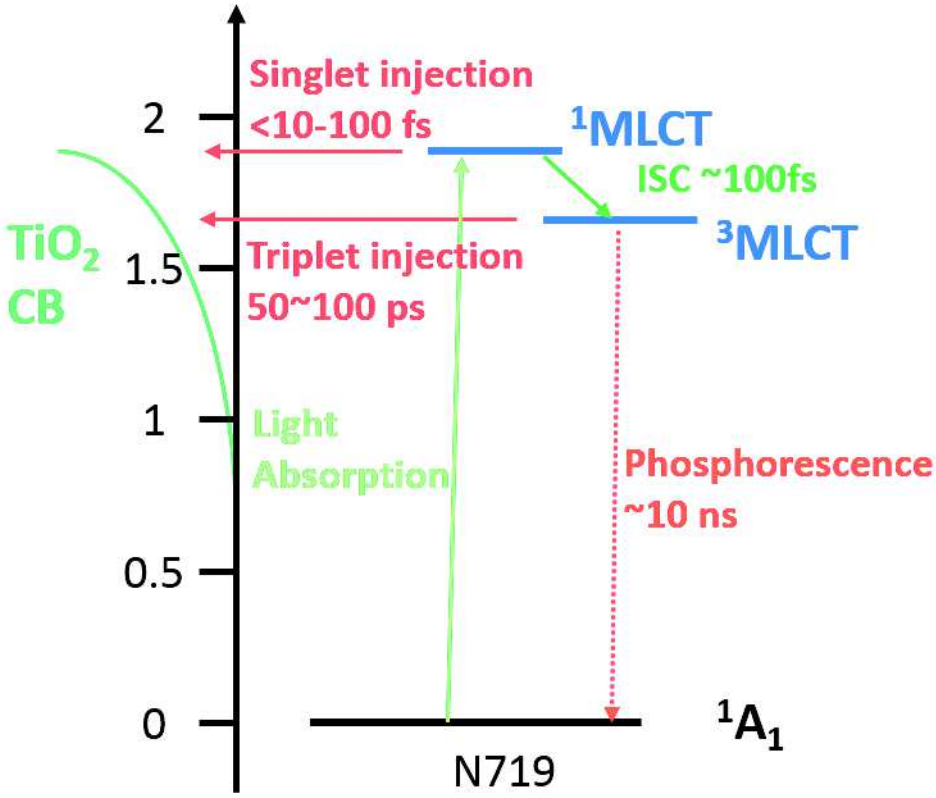

Figure V.2 Energy levels and characteristics lifetimes of N719 in DSSCs, adapted from ref. 78. The electron injection takes place from nonthermalized and thermalized MLCT states within 100 ps.

V.1.2 Iron complex

Even though the ruthenium DSSCs can achieve more than 10% PCE and are commercialized, the price and the rarity of this metal prevent further industrial developments. Figure V.3 gives an overview of the abundance of chemical elements on Earth.[139] It clearly appears how important it is to design new DSSCs with more abundant and cheaper transition metal like copper or iron.

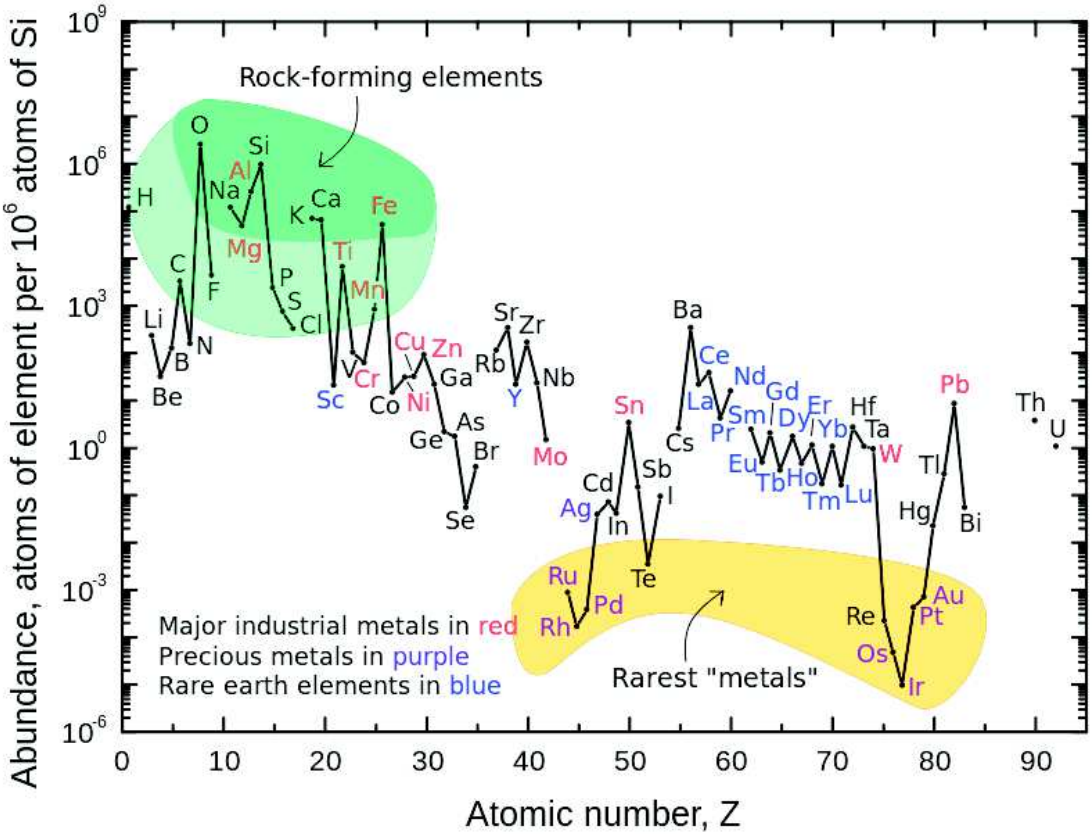

Figure V.3 Abundance (atom fraction) of chemical elements in the Earth's upper continental crust as a function of atomic number. The amount of Fe is 10^8 times more than that of Ru.[139]

From Ru(II)L_6 to Fe(II)L_6, the e_g orbitals become lower in energy than the π^* orbital, as shown in Figure V.4. Indeed, the ligand field strength from the 3*d* shell is weaker than the one from the 4*d* shell (Ru). Thus, the first excited state of Fe(II)L_6 is a MC state and not anymore a MLCT state. Instead of having a long-lived ^{3}MLCT state, the excited state of Fe(II)L_6 relaxes into a high-spin quintet state ($^5T_2$/^{5}MC) in the ultrafast sub-100fs time scale, named as spin crossover modulation (SCO).[140, 141, 142, 143]

The energetic downhill from ^{1,3}MLCT states to $^5T_2$ state takes at least 1 eV. Thus, the electrons located in the MC states can not inject into the TiO_2. Therefore, SCO is a competitive and detrimental process for the DSSCs application.

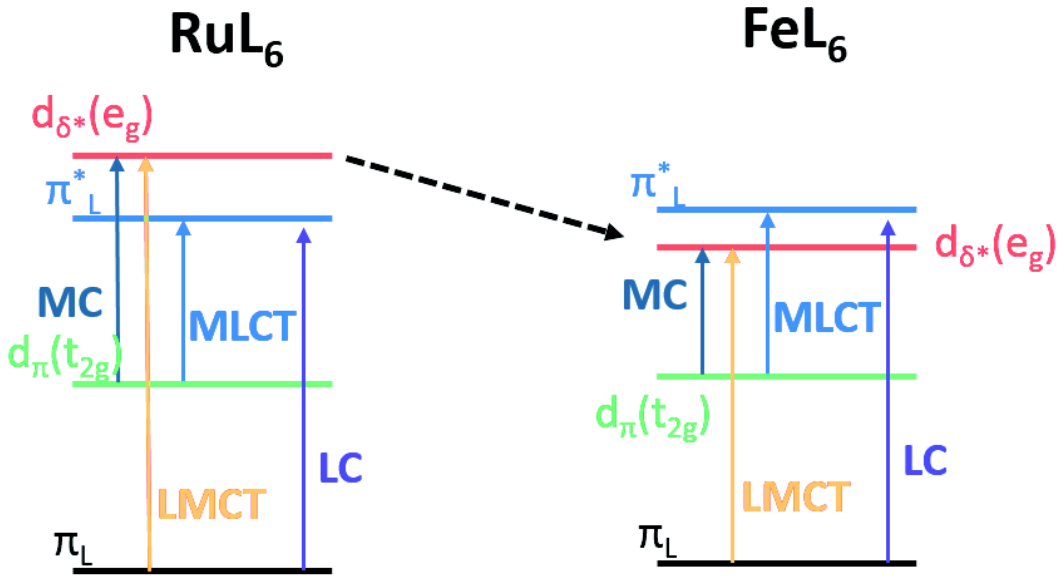

Figure V.4 Electronic diagrams of Ru(II)L_6 and Fe(II)L_6 complexes. Due to the smaller ligand field strength from the 3*d* shell of Fe(II), the energy level of e_g is lower. Therefore, in the typical FeL_6 complex, the energy of MC transient is low-lying compared with MLCT transition.

V.1.2.1 Spin crossover modulation (SCO)

SCO was firstly reported, in 1931, by Cambi when he observed unusual magnetic properties under different conditions. Pauling and co-workers followed it by studying the magnetic properties of various derivatives of Fe(II) and Fe(III). Besides magnetic field, temperature and pressure, this phenomenon is also triggered by irradiation in the visible. McGravery *et al.* discovered that for Fe(II)[144] and Fe(III)[145] polypyridine complexes in solution, the high spin state (HS, $^5T_2$ state) could be populated more efficiently than the low spin (LS, $^1A_1$ state) state by pulsed laser excitation.

Figure V.5 shows a simplified energy diagram of tris(2,2'-bipyridine)iron(II), $[Fe(bpy)_3]^{2+}$ which is a well-known SCO complex. In the literature, there is a discrepancy about the population of the $^5T_2$ state from the ^{3}MLCT state within 100 fs:

- direct mechanism where the ^{3}MLCT state decays directly to the HS quintet excited state ($^5T_2$)[146,147];
- indirect mechanism where the $^5T_2$ state is formed through a triplet excited-state (^3T)[148,142].

Chergui *et al.* have shown by UV-Vis transient absorption spectroscopies that there is a direct formation of $^5T_2$ state from ^{3}MLCT.[143] Whereas the X-ray Kβ fluorescence studies of Gaffney *et al.* support the second mechanism with the following spin relaxation pathway: $^3MLCT \rightarrow {}^3T \rightarrow {}^5T_2$.[142] However, the ^3T lifetime is extremely short (< 100 fs), making its observation challenging. The calculations of Graaf and Sousa indicate that both pathways are energetically feasible with minimal activation barriers.[149,150,151] Due to the complexity of observing SCO experimentally, both mechanisms remain an open question in the community. But, the studies of SCO in complexes, such as $Fe(bpy)_3$ and $Fe(tpy)_2$ give a fundamental understanding about Fe(II) complexes.

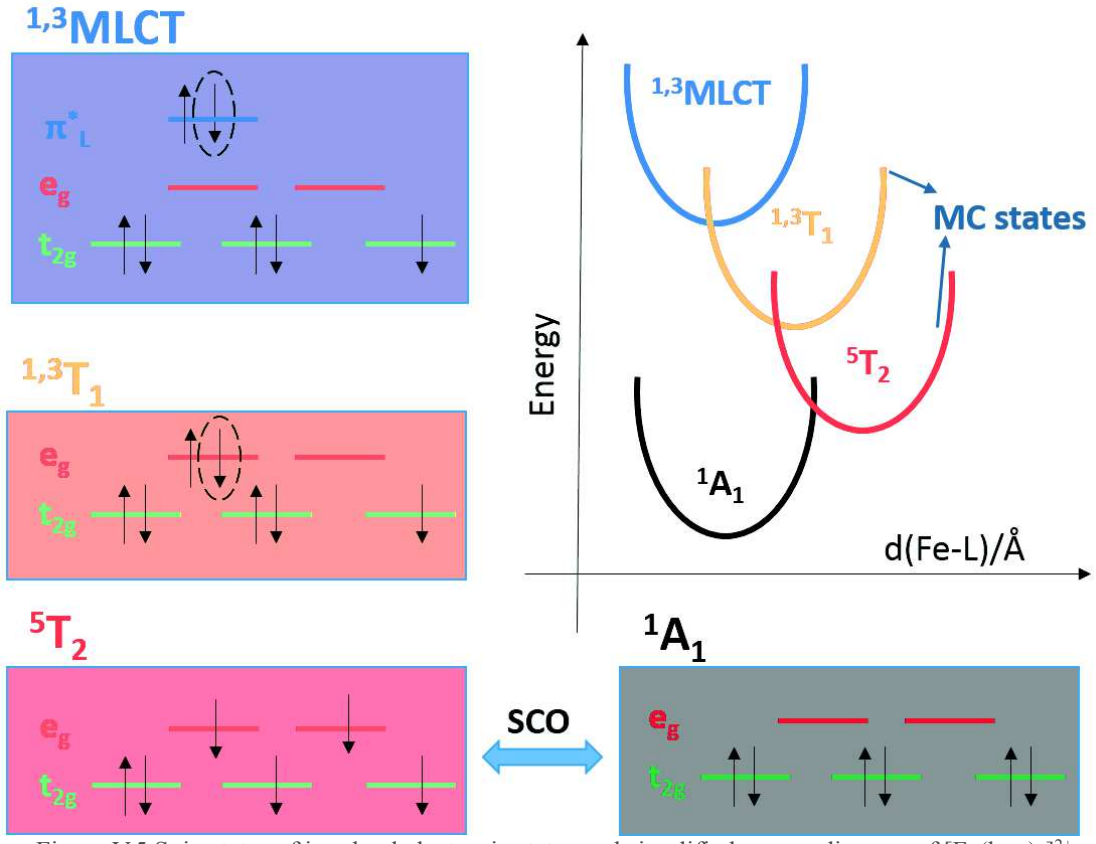

Figure V.5 Spin states of involved electronic states and simplified energy diagram of $[Fe(bpy)_3]^{2+}$ showing electronic states involved. Adapted from ref.152

$Fe(tpyCOOH)_2$ is taken as a reference for the following studies in order to spectroscopically assign the ^{3}MLCT and the $^5T_2$ states. $Fe(tpyCOOH)_2$ is diluted in acetonitrile (MeCN) to achieve an absorbance of 0.45 in 1 mm pathway at the maximum of absorption (~600 µmol*L^{-1}). The solution contained in a 1-mm quartz cuvette was continuously moved at 10 Hz on a louder speaker to avoid photo-degradation. The excitation wavelength is centered at 515 nm, and the sample was pumped with 40nJ/pulse. The relative polarization of the pump and the probe was set at the magic angle (54.7º). Unless mentioned otherwise, all the samples studied in solution were investigated under the same conditions except the excitation wavelength. The 2D plot of transient absorption data set of $Fe(tpyCOOH)_2$ is illustrated in the Figure V.6(A).

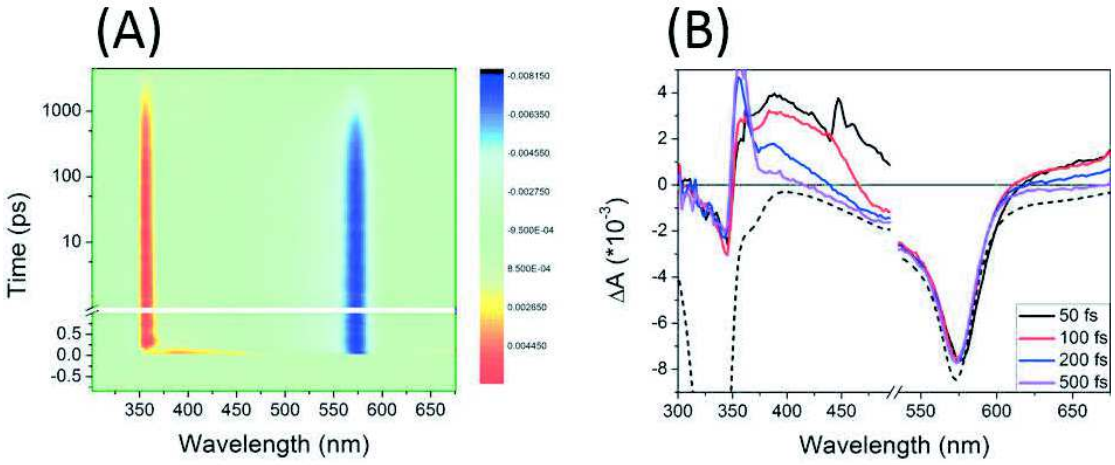

Figure V.6 Transient absorption (A) 2D dataset and (B) spectral evolution within the first 500 fs of $Fe(tpyCOOH)_2$ excited at 515 nm. The ^{3}MLCT state relaxes within first 200 fs and forms the long-lived $^5T_2$ state.

The Figure V.6.(B) highlights the spectral evolution of $Fe(tpyCOOH)_2$ within the first 500 fs. In the first 100 fs, two broad ESA bands are formed: i) 350-500 nm, ii) above 610 nm. After 200 fs, the transient absorption spectra have a sharp PA peak around 355 nm and a quasi-pure GSB band (reversed steady-state absorption spectrum shown as the dotted curve in Figure V.6(B)) and decays without any spectral changes until several nanoseconds. The differential spectrum associated with the 2.2 ns lifetime is similar to the characteristic narrow ESA spectrum of the $^5T_2$ $Fe(bpy)_3$ in H_2O.[153] As pointed out by other authors, UV/Vis transient absorption spectroscopy does not give any indications of short-lived MC states.[141] The transient absorption spectra at early time delay, with two broad ESA bands, indicates the presence of the ^{3}MLCT state.[154]
In conclusion, the photo-induced reaction scenario of $Fe(tpyCOOH)_2$ is:

$$^{1,}MLCT \rightarrow {}^{3}MLCT \rightarrow {}^{5}T_2$$

V.1.2.2 Dye-sensitized Solar Cells

Since the late 1990s, Iron(II) polypyridine complexes are considered as putative candidates for DSSCs[155,156,157,158]. Unfortunately, the PCEs of such devices remain very low (<0.1%), due to the presence of low-lying MC states. Thus, it is crucial to increase the energy level of the e_g orbitals in $Fe(II)L_6$. One solution to achieve this goal is to add strong σ-donating ligands, such as N-heterocyclic carbenes (NHCs). The electron involved in the carbene-iron bond is more energetic than the common N-donors, such as pyridine, the electronegativity of carbon is lower than the one of nitrogen.

NHCs can easily be modified by functionalization of the imidazolium ring, principally at the nitrogen position to play on the electronic and steric properties of such ligands. Thus, they are widely used in applications, in complexes with metals other than Fe: OLEDs[159], biological labeling agents[160], charge transfer reactions in DNA[161], antitumoral agents [162] phosphorescent sensors[163], photocatalyst for CO_2 reduction[164] and photochemical water splitting[165]. It is worth noting that the ruthenium DSCCs with NHCs have successfully achieved higher efficiency than N719.[166] More recently, Wärnmark *et al.* have proposed to use NHC ligands for Fe(II) complexes. The first Fe(II)-HNC complex designed by them displayed an extended ^{3}MLCT state lifetime of 9 ps.[167]

Following the same strategy, *i.e.* the increase of the e_g orbitals energy, our collaborators (Dr. Thibaut Duchanois and Dr. Philippe C. Gros in *SRSMC, Université de Lorraine*) have synthesized a series of Fe(II) complexes with several modified ligands for the DSSCs application (Figure V.7). We will present and discuss in the following how these substitutions affect the ^{3}MLCT lifetime.

V.2 Isolated complexes in the solution

Even though the electron injection only occurs in the film, it is still worth to study the photophysical properties in the solution, especially the energy pathway, and use these results as a reference. In the photoinduced processes, the ^{3}MLCT state is crucial. Its lifetime should be long enough to inject electrons into the semiconductor and its energy should be higher than the conduction band of the semiconductor. Therefore, the ^{3}MLCT state is treated as the indicator. We adopt a "screening" approach based on the solution data: We search for the chemical modifications, which enhance the ^{3}MLCT lifetime. Then, complemented with ab initio quantum chemical calculations from our Nancy partners (A. Monari & X. Assfeld), we aim at rationalizing how the substitutions act on the excited state energies, so as to ultimately outline general rules of the photophysics of these complexes in view of optimum (longest) ^{3}MLCT lifetimes.

V.2.1 Results

C1, the parent compound developed by the Wärnmark group, is chosen as the reference compound to illustrate the characteristic spectral evolution of the Fe(II) family.

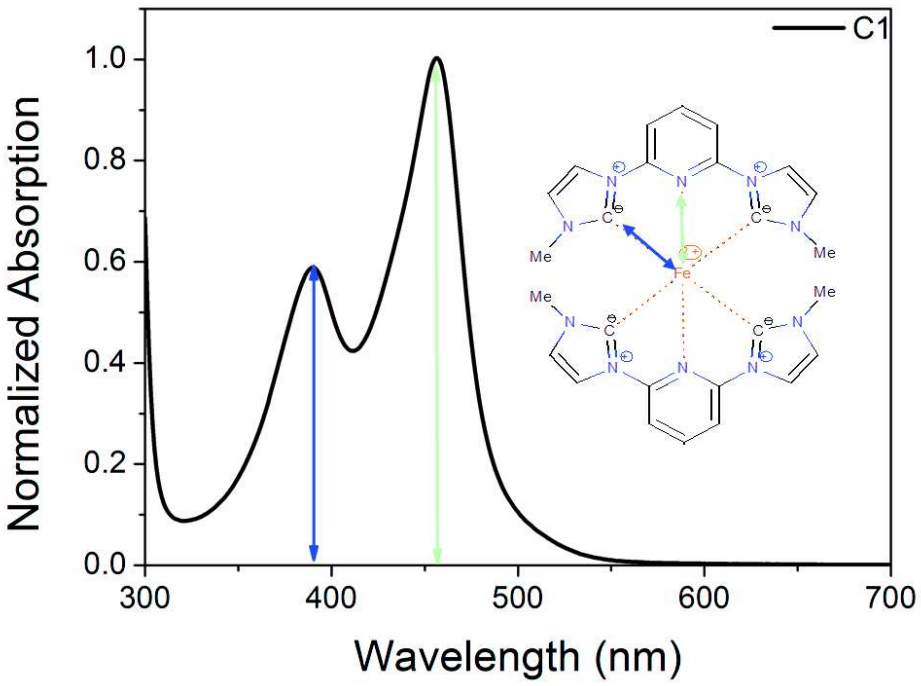

Figure V.7 Normalized steady-state absorption spectrum of **C1** and its chemical structure.

Figure V.7 illustrates the normalized steady-state absorption spectrum of **C1** and its chemical structure. The **C1** contains two bis(imidazolylidene)pyridine tridentate ligands. Thus, two MLCT transitions exist in the visible regime: $t_{2g} \rightarrow \pi^*$(pyridine, Fe-N) and $t_{2g} \rightarrow \pi^*$ (imidazolylidene, Fe-C). Due to the higher energy level of the LUMO of imidazolylidene, the absorption peaks at 390 and 460 nm correspond to the MLCT state of Fe-C and the one of Fe-N, respectively.[168]

The spectral evolution of **C1** after excitation at 480 nm (Figure V.8) is summarized as follow:

- within the first 200 fs, a broad ESA band from 500 to >675 nm is formed with two well separated GSB bands at 380 and 460 nm. An additional weak ESA band is observed below 350 nm.
- after 500 fs, two GSB bands remain, while the ESA band narrows and displays a blue shift of the positive contribution in the range of 500-600 nm.
- On a 20-30 ps timescale, the entire TA spectrum fully decays back to zero without any spectral change.

The early evolution of the induced absorption evidences a sub-100fs relaxation of the initially excited state, as shown by the ESA kinetics plotted in Figure V.8(C). Then, both ESA and GSB traces decay back to zero with the same rate constants.
A global analysis of the data was performed with three components. Since fast components are very close to the instrument response function (IRF=60 fs), the first fitting component is chosen as a Gaussian function and followed by a bi-exponential function. The Decay-Associated differential Spectra (DASs) with their lifetimes are presented in Figure V.8.(D):

- The first DAS shows a decay of the ESA band from 500-600nm, interpreted as an ultrafast intersystem crossing into the vibrational excited ^{3}MLCT state.
- The second 550 fs DAS has a small amplitude in the full spectral range with a broad ESA band centered at 580 nm and two characteristics GSB peaks at 390 and 460 nm. Compared with the 10 ps DAS, the redder ESA band indicates that the 550 fs DAS is associated with a thermalization process.
- Finally, the 10 ps DAS with a narrower ESA band centered at 540 nm means that the vibrationally relaxed ^{3}MLCT state recombines non-radiatively within 10 ps.

According to the above discussion, the reaction scheme could be defined as:

$$^1MLCT^+ \xrightarrow{<IRF} \begin{cases} ^1MLCT \xrightarrow{\tau_{cool}} {}^3MCLT \xrightarrow{\tau\ {}^3MLCT} S_0 \\ ^3MLCT^+ \end{cases}$$

In the present case, τ_{cool} is 550 fs and τ_{3MLCT} is 10 ps.

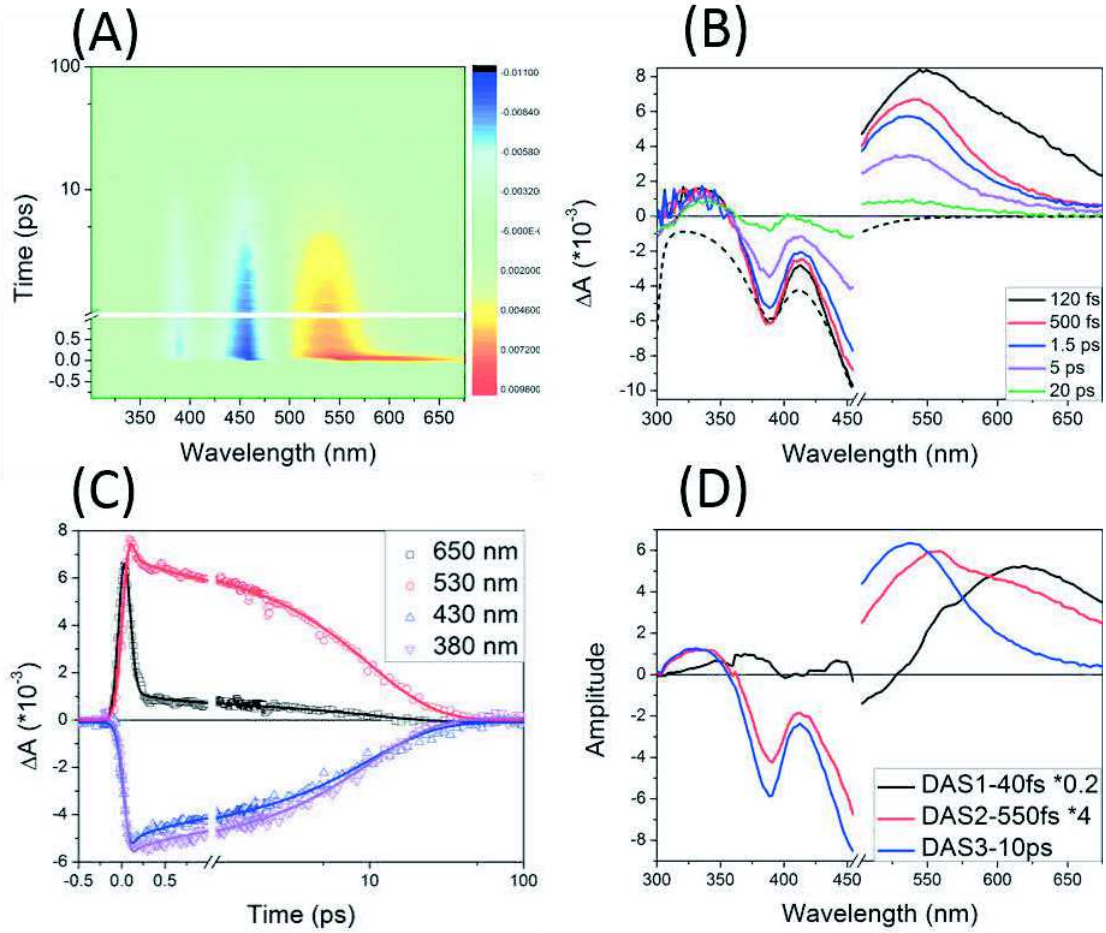

Figure V.8 (A) 2D plot of transient absorption data, (B) spectral evolution (C) kinetic traces and (D) decay-associated differential spectra of **C1** in MeCN after excitation at 480 nm.

The deactivation pathway of **C1** was also investigated theoretically by Fredin *et al.*, through calculated potential energy curves (PECs) and potential energy surfaces (PESs) as illustrated in Figure V.9.[169] ^{5}MC state is ruled out as its geometry needs to extend the Fe-C distance on both ligands. Other states (ground state (GS), MLCT manifold and ^{3}T state) are more likely to be involved in the relaxation process, which for the particular "facile" pathway (green arrows in fig. V.9) would require a bond length change on one ligand only.
The role of the ^{3}MC state as the mediator state for the relaxation of the ^{3}MLCT state. It appears from these calculations that two parameters are critical:

1. the energy difference between the ^{3}MLCT state and ^{3}MC state: if it was possible to have the ^{3}MC state at higher energy level than that of ^{3}MLCT state, the lifetime of the ^{3}MLCT state should significantly increase.
2. the ability of extension along the Fe-C bond: the barriers along this path will prevent the relaxation and extend the ^{3}MLCT state lifetime.

In the following, we will discuss the effect of chemical substitutions of the parent compound **C1** mainly along these lines.

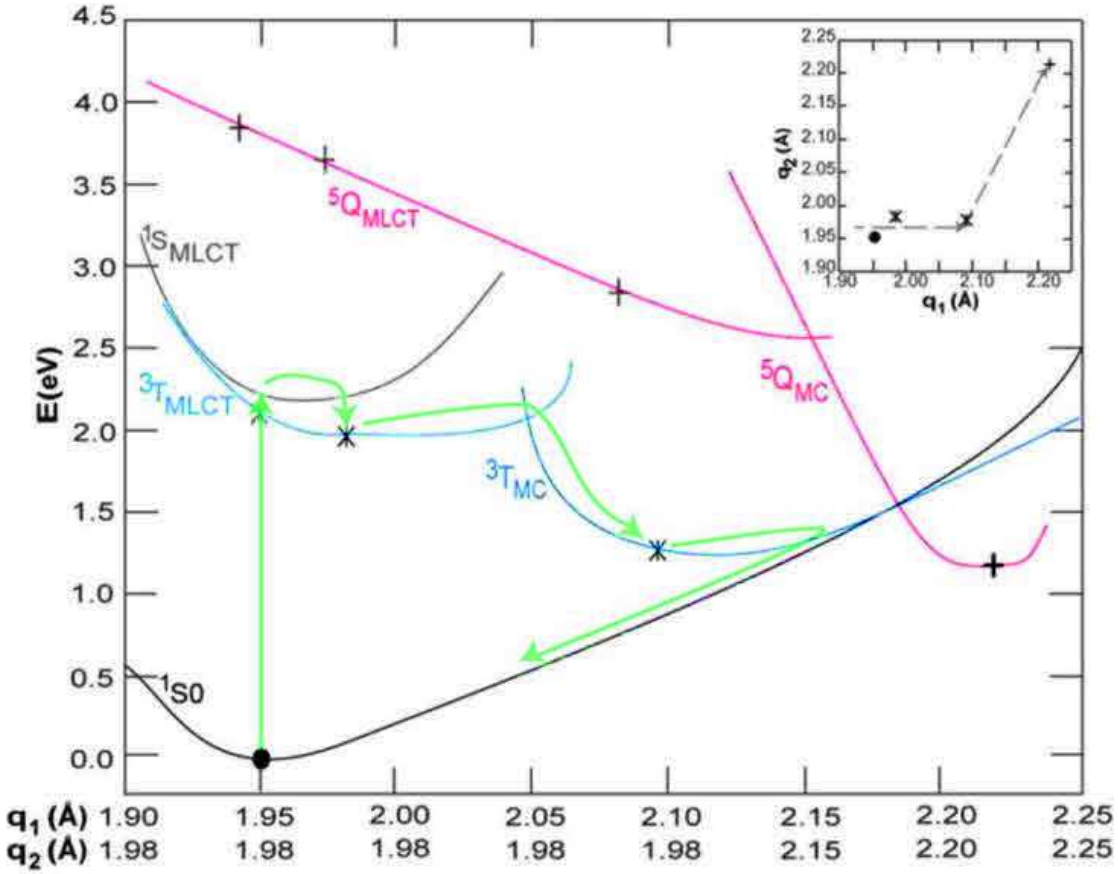

Figure V.9 Schematic excitation and deactivation pathway based on calculated PECs and PESs. q_1 and q_2 are the averages of Fe-C bonds on two ligand side. The relaxation of ^{3}MLCT and ^{3}MC state only involve one ligand, q_1 and the relaxation of ^{5}MC involves both ligand sides. (Figure 4 in the ref.169)

In order to enhance the extended ^{3}MLCT state lifetime of **C1**, several possible strategies with their potential consequences are displayed in Figure V.10.

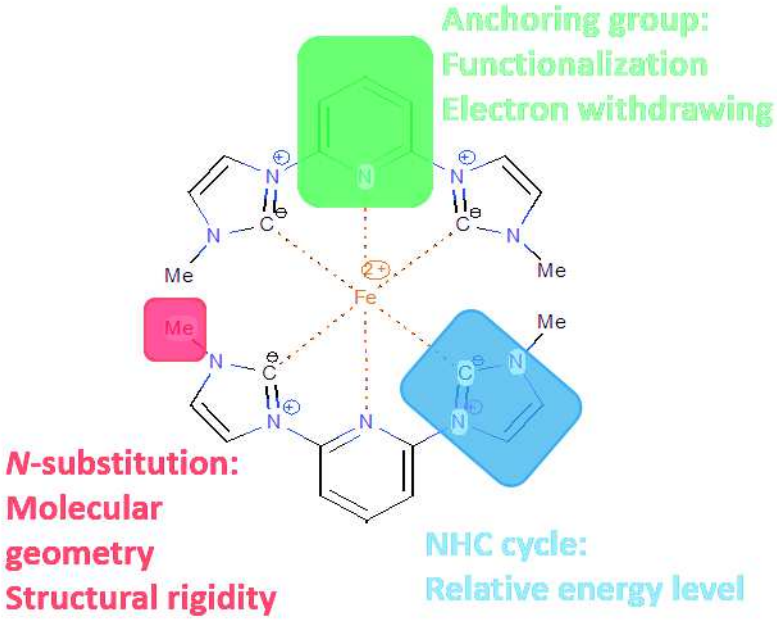

Figure V.10 Possible strategies for extending ^{3}MLCT state lifetime by adding the anchoring group and modifications on the NHC cycle and N-substitution.

- **Adding the anchoring group**: makes the Fe(II) complexes graftable on a TiO_2 surface to achieve efficient electron injection and works as an electron withdrawing substitution reducing optical band gap
- **Modification of the NHC cycle**: increases the electron donating character of NHC to increase the MC state energy level.
- **Modification of *N*-substitution**: introduces the steric rigidity and/or deviations from the octahedral geometry.

Following these ideas, nine Fe(II) complexes have been synthesized and studied in solution (MeCN) to examine:

- the effect of carboxyl groups (complex **C1**, **C2** and **C5**),
- the effect of ligand substitutions (complex **C1**, **C2**, **C3** and **C4**),
- the effect of push-pull (complex **C5**, **C6** and **C7**),
- the effect of rigidity (complex **C1**, **C3**, **C8** and **C9**)

The precise chemical structures are given in the following discussion and in the chart.

To get insight into the interactions between complexes and environment, two types of solvent effects are studied

- the effect of pH (complex **C2** in MeCN, MeCN+hydrochloric acid/HCl and MeCN+sodium hydroxide/NaOH)
- the effect of polarity (complex **C4** in MeCN, MeCN+HCl, ethanol, Dimethyl sulfoxide/DMSO, 2-butanol and Dimethylformamide/DMF).

Under the same experimental conditions as described for $Fe(tpyCOOH)_2$ (§ V.1.2.1), the sample was translated by a loudspeaker to avoid any photo-degradation. For the samples without any carboxyl group (**C1**, **C3**, **C8** and **C9**), **C2** in MeCN-NaOH and **C4** in 2-butanol and DMF, the excitation wavelength was set at 480 nm. For the samples with carboxyl groups (**C2**, **C4**, **C5**, **C6** and **C7**) in MeCN, **C2** in MeCN-HCl and **C4** in MeCN-HCl, ethanol and DMSO, the excitation wavelength was centered at 515 nm.

The 2D map and spectral evolutions of other complexes with similar spectral behaviors are shown in the Appendix. II. Therefore, the following sections only highlight the effects of different electronic structures through dynamic traces with their fittings. The fitting parameters are identical to the ones obtained by global analysis on the whole spectral regime (global analysis is described in details in § III.3.2.)

V.2.1.1 Effect of a carboxyl group on the pyridines

As described previously, the complexes are needed to be grafted onto the TiO_2 surface in order to obtain an efficient electron injection. Thus, **C1** needs at least one acidic group to achieve this goal. The carboxyl group is chosen as a classic anchoring group, offering a carboxylic bond with the oxygens of TiO_2. Due to its electron-attractive character, the carboxyl group has an important effect on the relative energy level of the ^{1}MLCT state: the transition $t_{2g} \rightarrow \pi^*$ (pyridine) has a lower energy level suggesting a down-shift of ^{1}MLCT state, and most probably of ^{3}MLCT state also. Firstly, the homoleptic complex **C2** was synthesized and investigated (Figure V.11). [154] As shown by the ATR-FTIR (attenuated total reflectance Fourier transform infrared) studies on N719-TiO_2, the carboxyl group binds to TiO_2 through a bidentate bridge,[170] resulting in a heteroleptic configuration. Since the transition $t_{2g} \rightarrow \pi^*$ has the lower energy for pyridine-COOH than for pyridine only, it was also interesting to study the heteroleptic complex **C5** in solution and films.

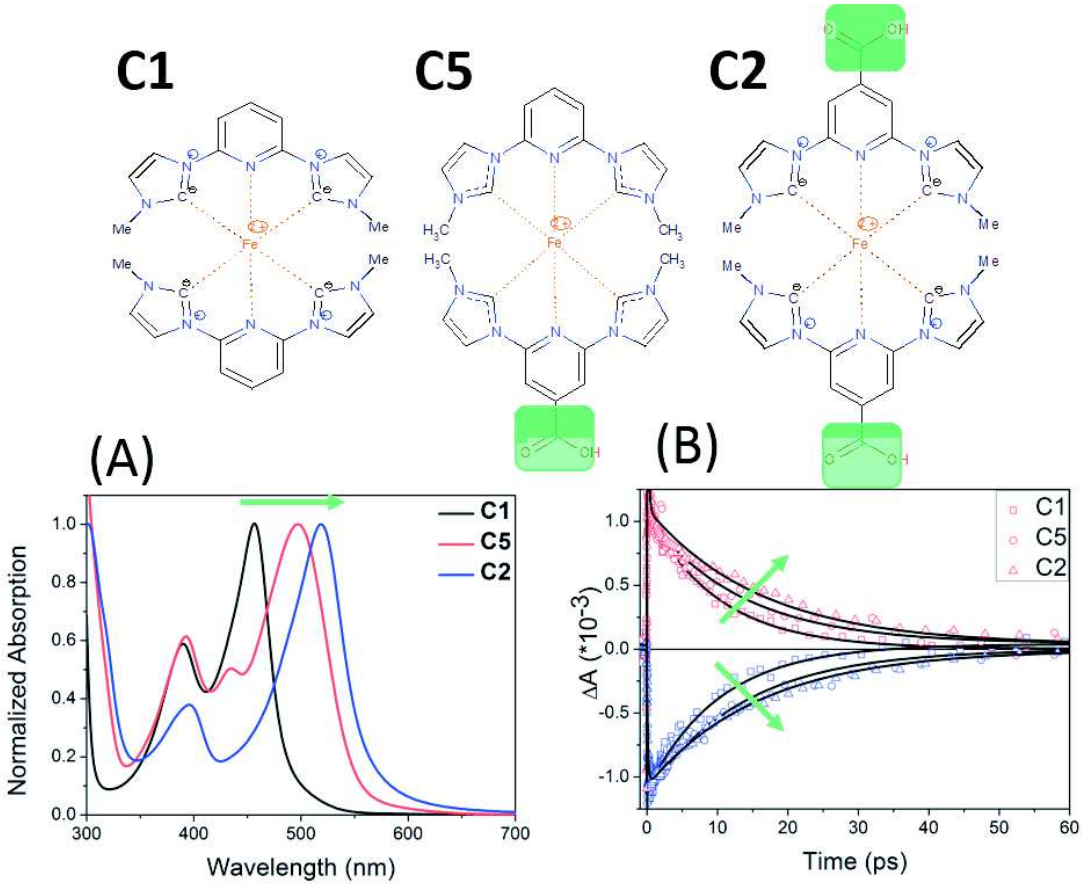

Figure V.11 Bottom: (A) Normalize steady-state absorption spectra of **C1** (black curve), **C5** (red curve) and **C2** (blue curve) in MeCN, showing with more carboxylic group, the absorption spectra have a red-shift. (B) Kinetic traces in the ESA (red symbol curves) and GSB (blue symbol curves) bands normalized at 1 ps of **C1** (square symbol curves), **C5** (circular symbol curves) and **C2** (up-triangle symbol curves) in MeCN with their corresponding fits (solid black curves).Top: Chemical structures of **C1**, **C5** and **C2**

Figure V.11.(A) illustrates the effect of the addition of carboxyl groups on the **C1** complex (**C1**: zero carboxyl group, black curve, **C5**: one carboxyl group, called heteroleptic complex, red curve, and **C2**: two carboxyl groups, called homoleptic complex, blue curve). After addition of two carboxyl groups on both side of the central pyridine part (**C2**), a 60 nm bathochromic shift from 460 nm to 520 nm (ΔE= 310 meV) occurs on the $t_{2g} \rightarrow \pi^*$ (pyridine) transition. The carboxyl groups lower the LUMO energy level by attracting electrons further away from the metal center. In the heteroleptic case **C5**, the $t_{2g} \rightarrow \pi^*$ (pyridine) transition splits into two with a 40 nm bathochromic shift (from 460 nm to 500 nm) and a 25 nm hypochromic shift (from 460 nm to 435 nm). Interestingly, the hypochromic shift results also in a decrease of half of the main absorption peak (resonance splitting, oscillator strength sharing).

Figure V.11(B) shows the kinetic traces normalized at 1 ps of **C1** (square symbol curves), **C5** (circular symbol curves) and **C2** (up-triangle symbol curves) taken in the ESA (red symbol curves) and GSB (blue symbol curves) bands after excitation in the visible (480 nm for **C1** and 515 nm for **C5** and **C2**) with their corresponding fits (solid black curves). For the two complexes with a carboxyl group, the ESA and GSB signals display the same decay kinetics, indicating direct ground state recovery from the excited state, as in **C1**. Furthermore, the spectral features (two broad ESA bands in the visible and UV region, in Appendix II) are very similar to the ones observed in **C1**, indicating that for these two compounds the ESA also comes from ^{3}MLCT, and its decay goes directly (or without a notable signal of any intermediate state) into S_0.

The data were fitted to the sum of a Gaussian and a bi-exponential function by global analysis, resulting in the above-discussed reaction scheme with similar rate constants (Table V.1). As shown in Figure V.11, ^{3}MLCT lifetimes increase as the number of carboxyl group increases. (10 ps for **C1**, 14 ps for **C5** and 16.5 ps for **C2**)
As **C5** is asymmetric, a possible scenario is that two deactivation pathways coexist with slightly different constant rates. The ^{3}MLCT state could be a combination of the ^{3}MLCT state of **C1** and the one of **C2**. On the other hand, it is also possible that the whole complex has just one ^{3}MLCT state. Unfortunately, these two ^{3}MLCT states are spectrally similar and more importantly, too close temporally to be distinguished. A fit with a mono-exponential component for the ^{3}MLCT state was carried out and as well with two components. The fits are of the same quality, within the present experimental accuracy.

A theoretical analysis was carried out for **C2** by density functional theory (DFT) and time-dependent DFT (TD-DFT) calculations to characterize the ground to excited state electronic density redistribution.[171] In the formalism, “Occupied” natural transitions orbitals (oNTO) can be seen as the “hole” orbital, *i.e.* the orbital from which the electron is removed during the transition, while “virtual” NTO (vNTO) is the orbital in which the electron is promoted in the excited state, as shown in Figure V.12. A significant charge transfer of the excited electron into the carboxyl group is observed. The enhanced electron charge transfer character (termed "delocalization" in the following, *i.e.* displacement of electron density away from the Fe center), is held responsible for the enhanced ^{3}MLCT state lifetime. Indeed, according to the Marcus description, we expect the electronic coupling between ^{3}MLCT state and ^{3}MC state to decrease, when the distance between the center of the electron density and the central Fe increases.
The calculations also indicate that the electron delocalization could be helpful for the electron injection since the complexes are grafted onto TiO_2 through the carboxyl group.

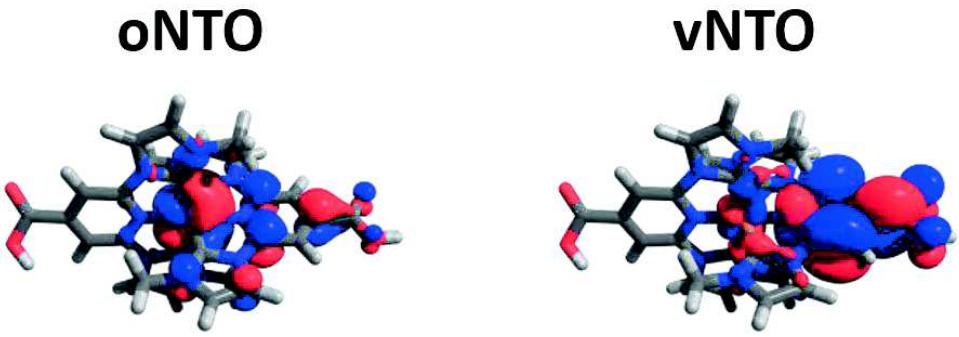

Figure V.12 Calculated NTOs of **C2**. [154] "Occupied" natural transitions orbitals (oNTO) can be seen as the "hole" orbital and "virtual" natural transitions orbitals (vNTO) can be seen as the "electron" orbital. The electron delocalization could be helpful for the electron injection since the complexes are grafted onto TiO_2 through the carboxyl group.

V.2.1.2 Ligand Effect

In order to enhance the electron charge transfer towards the ligands and the NHC effect, the benzimidazolylidene groups were introduced, replacing the imidazolylidene groups on the pyridine ring (**C3**). To graft coordination complexes onto TiO_2, two carboxyl groups were added to **C3** to generate the homoleptic complex **C4**.

As shown in the Figure V.13, a strong absorption peak appears around 310 nm due to the $\pi \rightarrow \pi^*$ transition of benzimidazolylidene. A shoulder at 365 nm attributed to the MLCT state of $t_{2g} \rightarrow \pi^*$ (benzimidazolylidene) replaces the previous absorption peak at 390 nm. The transition of $t_{2g} \rightarrow \pi^*$ (pyridine) has only a 14 nm hypsochromic shift from 460 nm to 446 nm. Two carboxyl groups are added on the central pyridine parts in order to graft on the TiO_2, leading to **C4** (red solid curve). In line with the red shift of $t_{2g} \rightarrow \pi^*$ (pyridine) transition, carboxyl groups lower the MLCT state energy by 270 meV, a 50 nm bathochromic shift from 445 nm to 495 nm.

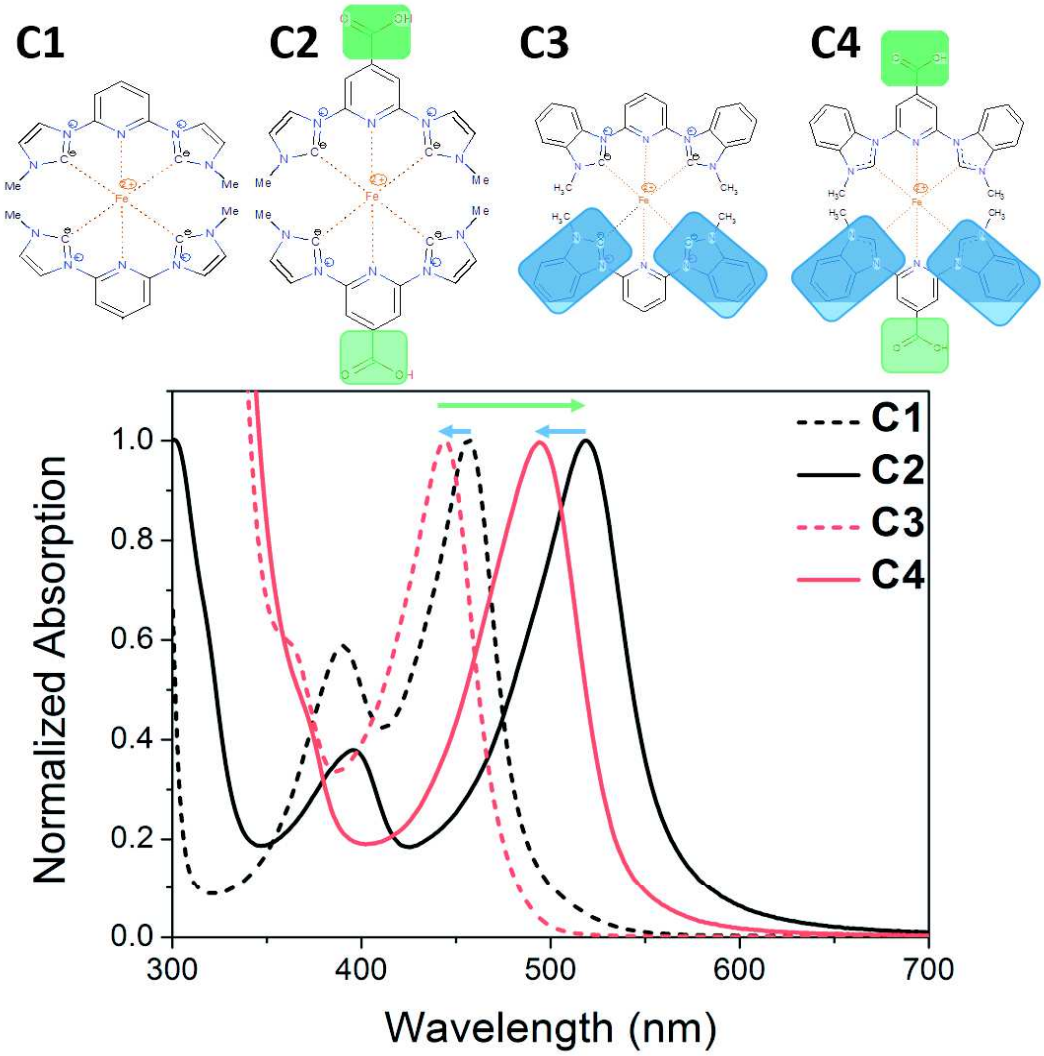

Figure V.13 Bottom: Normalized steady-state absorption spectra of Fe(II) complexes to study the effect of ligand. (**C1** (black dotted curve), **C2** (black solid curve), **C3** (red dotted curve) and **C4** (red solid curve)) and Top: their chemical structures. The replacement of imidazolylidene by benzimidazolylidene induces a slight blue shift and the red shift due to carboxyl group is still available.

The comparison of **C1** and **C3** kinetic traces shows an increase of the ^{3}MLCT state lifetime, as expected by a larger delocalization of electrons (Figure. 14 (A) and (B)). The kinetic traces in the ESA (red symbol curves, square symbols for **C1** and **C2** and up-triangle symbol curves for **C3** and **C4**) and GSB bands (blue symbol curves) with their fits (solid black lines) are normalized at 1 ps. Indeed, after 1 ps, the initial thermalization is finished and thus it is easier to compare the lifetimes of the ^{3}MLCT state. The lifetimes for every complex determined by Global Analysis are given in Table V.1. Apparently, the modification of ligands, with and without carboxyl group, prolongs the ^{3}MLCT state lifetime significantly. The lifetime of the ^{3}MLCT state of **C3** is considerably increased (16.4 ps) compared to one of **C1** (10 ps). The benzimidazolylidene ligand has a clear positive effect. **C4,** benefiting from the carboxylic acid groups, has the longest ^{3}MLCT state lifetime (26 ps).

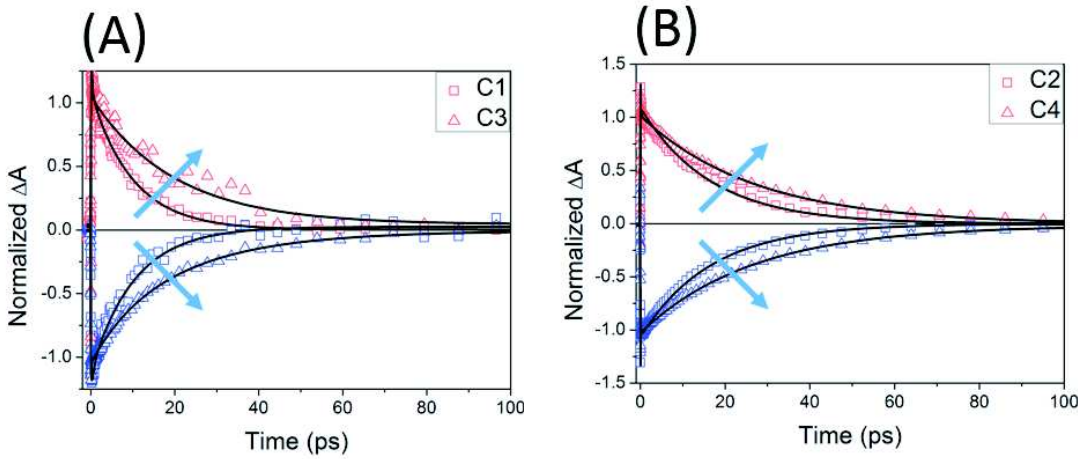

Figure V.14 Kinetic traces in the ESA (red symbol curves) and GSB bands (blue symbol curves) with their fits (solid black lines), normalized at 1 ps for the ligand effect (A) without **C1** and **C3** (B) and with carboxyl groups **C2** and **C4**.

The same theoretical studies, done on **C2**, were carried out on **C4**[172]. As shown in Figure V.14, a significant accumulation of electron density is also observed on the carbonyl unit. In order to rationalize the photophysics, the geometry of the lowest ^{3}MLCT and ^{3}MC states were relaxed at the potential energy minimum for **C2** and **C4**.

In the case of **C2**, the two states are almost degenerate as $\Delta E = E_{3MLCT}-E_{3MC} = -80$ meV. And in **C4**, the ^{3}MLCT state is found at higher energy than the ^{3}MC state, since $\Delta E = 120$ meV. Even though the energy difference is still quite small, both ^{3}MLCT and ^{3}MC states can be thermally populated, this observation may rationalize the longer ^{3}MLCT state lifetime of **C4**. Indeed, according to the picture outlined by Fredin *et al.* (Figure. V.9), the photophysical channel leading to the ^{3}MC state population and the subsequent deactivation now appears energetically less favorable.

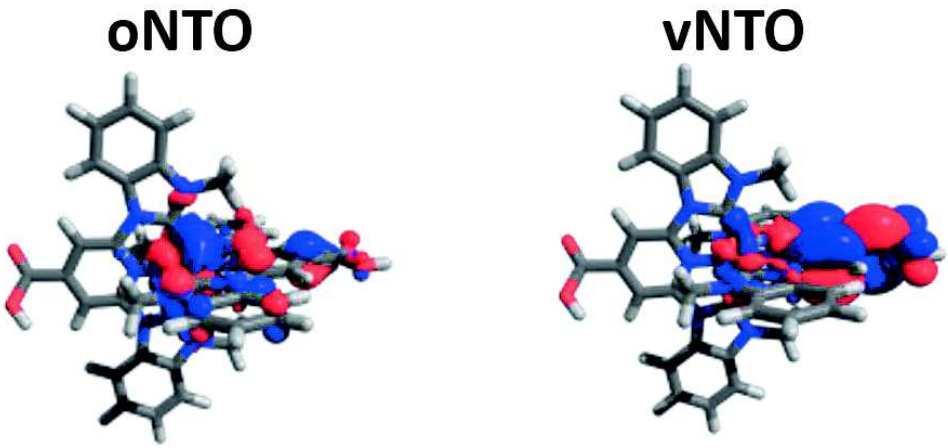

Figure V.15 Calculated NTOs of **C4**.[172]"Occupied" natural transitions orbitals (oNTO) could be seen as the "hole" orbital and "virtual" natural transitions orbitals (vNTO) can be seen as the "electron" orbital.

V.2.1.3 *N*-substitution

Once grafted in TiO_2, in order to avoid charge recombination, the distance between hole and electron should be large. The electron injection is expected to happen through the carboxylic bond, leaving the hole located on the side chains. In addition, the modification of the ligands in the *N*-substitution may allow us to modify the electronic structure of the carbene ring by

increasing the σ-character of the NHC. Therefore, the methyl groups in **C5** are replaced by strong electron-donating conjugated units, such as methoxyphenyl (**C6**) or triphenylamine (**C7**). Furthermore, due to the strong σ-donating character of these groups, a hole created after electron injection is likely to be located on them. As a consequence, the hole is pushed further away from the semiconductor surface than in **C5**.
In a first step, we investigated the effect of these substitutions on the ^{3}MLCT lifetime in solution.

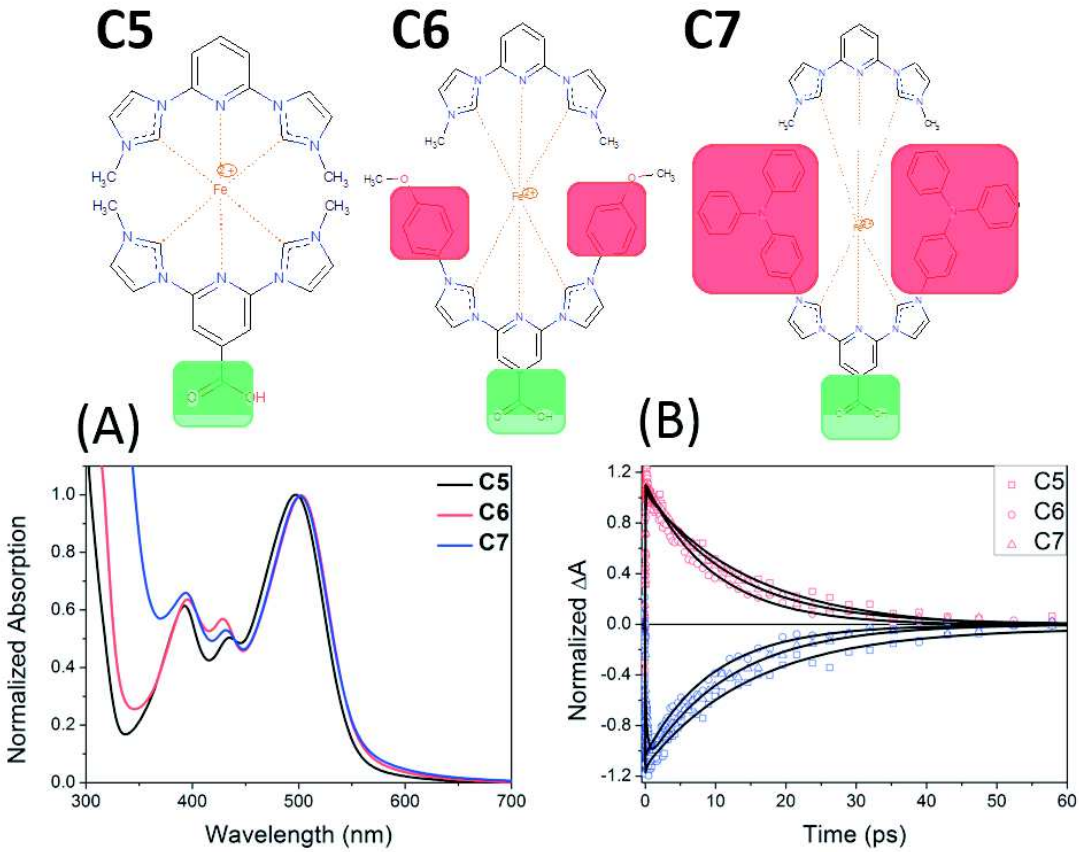

Figure V.16 Bottom: (A) Normalized steady-state absorption spectra of **C5** (black curve), **C6** (red curve) and C7 (red curve) in MeCN to study different *N*-substitutions on Fe(II) complexes (B) Kinetic traces in the ESA (red) and GSB (blue) bands after normalization at 1 ps for the N-substituted complexes: a methyl group for **C5** (square), methoxyphenyl group for **C6** (circle) and triphenylamine for **C7** (triangle) Top: their chemical structures

The *N*-substitution on the imidazolylidene is carried out, with **C5** as the reference compound. The two methyl groups are replaced by two methoxyphenyl groups (**C6**) or two triphenylamine groups (**C7**) on the side of central pyridine carrying the carboxyl group. As shown in the Figure V.16.(A), the normalized absorption spectra of **C6** (red curve) and **C7** (blue curve) increase in 300~360 nm range and have a 4 nm bathochromic shift from 500 nm (**C5**) to 504 nm (**C6** and **C7**), compared to the one of **C5** (black curve). Clearly, the modification of *N*-substitution has a significant influence on LC/$\pi \rightarrow \pi^*$ transition below 350 nm, slightly lowers the $t_{2g} \rightarrow \pi^*$ (pyridine) transition and no impact on the $t_{2g} \rightarrow \pi^*$ (carben) transition as the same amplitude at 390 nm.
The *N*-substitutions have a small effect on the lowest MLCT transition because those substitutions do not interact directly with the central pyridine ring. The ^{3}MLCT state lifetimes of the *N*-substituted complexes are similar: 14, 10 and 12 ps for **C5**, **C6** and **C7**, respectively (Figure V.16(B)).

As discussed above, the ^{3}MLCT lifetime of **C5** is between the ones of **C1** and **C2**. The stabilization of the ^{3}MLCT state by attracting the electron away from the metal center like for **C4,** is not observed for **C6** and **C7**. Clearly, these *N*-substitutions do not extend the ^{3}MLCT state lifetime; they even shorten it slightly for reasons that need to be explored by calculation of the excited state energy structures. Besides, it will be interesting to study its impact on the charge recombination in the Fe(II)-TiO_2 films.

V.2.1.4 Rigidity

Wärnmark and co-workers have suggested that the ^{3}MLCT state of complexes with more rigid ligands could last longer by comparing **C1** (Fe(Carben-Met)$_2$) and Fe(Carben-*t*Bu)$_2$.[167] The steric hindrance increases from a methyl to a *tert*butyl group, decreases the electron donating effect of the coordination center (Fe) and the ligands and enlarges the binding length.
According to those results, we decided to substitute the methyl group to hexyl group, which is a common substitution in organic dyes to increase the rigidity of the ligands.[173] This modification was carried out on two ligands: **C1** and **C3** to become **C8** and **C9**, respectively. The hexyl group has two more benefits: i) protection of the metal center, ii) and solubility increase in apolar solvents.

Since two tridentate ligands are orthogonal, the chains on two sides could have an influence on the steric rigidity. To identify this effect, two methyl groups on the side of imidazolylidene (**C1**, black curve) and benzimidazolylidene (**C3**, red curve) are replaced by two hexylic groups in **C8** (black dotted curve) and **C9** (red dotted curve). The normalized steady-state absorption spectra are illustrated in the Figure V.17. The extra –$(CH_2)_5$-chains have no influence on the $t_{2g} \rightarrow \pi^*$ (pyridine) transition because neither a spectral shift nor an additional shoulder between two MLCT transitions is observed. The mechanism for broadening in **C9** needs further clarification.

Figure V.18 (A) and (B) shows that of the increase of the rigidity of **C1** and **C3** extends the lifetime of the ^{3}MLCT state: from 10 to 14 ps and from 16.4 to 19.5 ps in the case of the imidazolylidene (**C1** to **C8**) and the benzimidazolylidene (**C3** to **C9**) ligands, respectively. According to the calculated PESs and PECs (Figure V.9), the stretching of the binding length Fe-C is needed to deactivate the ^{3}MLCT state. Indeed, the rigidity of the ligand prevents the relaxation and extends the ^{3}MLCT state lifetime. Our assumption requires the ongoing quantum calculations to confirm.

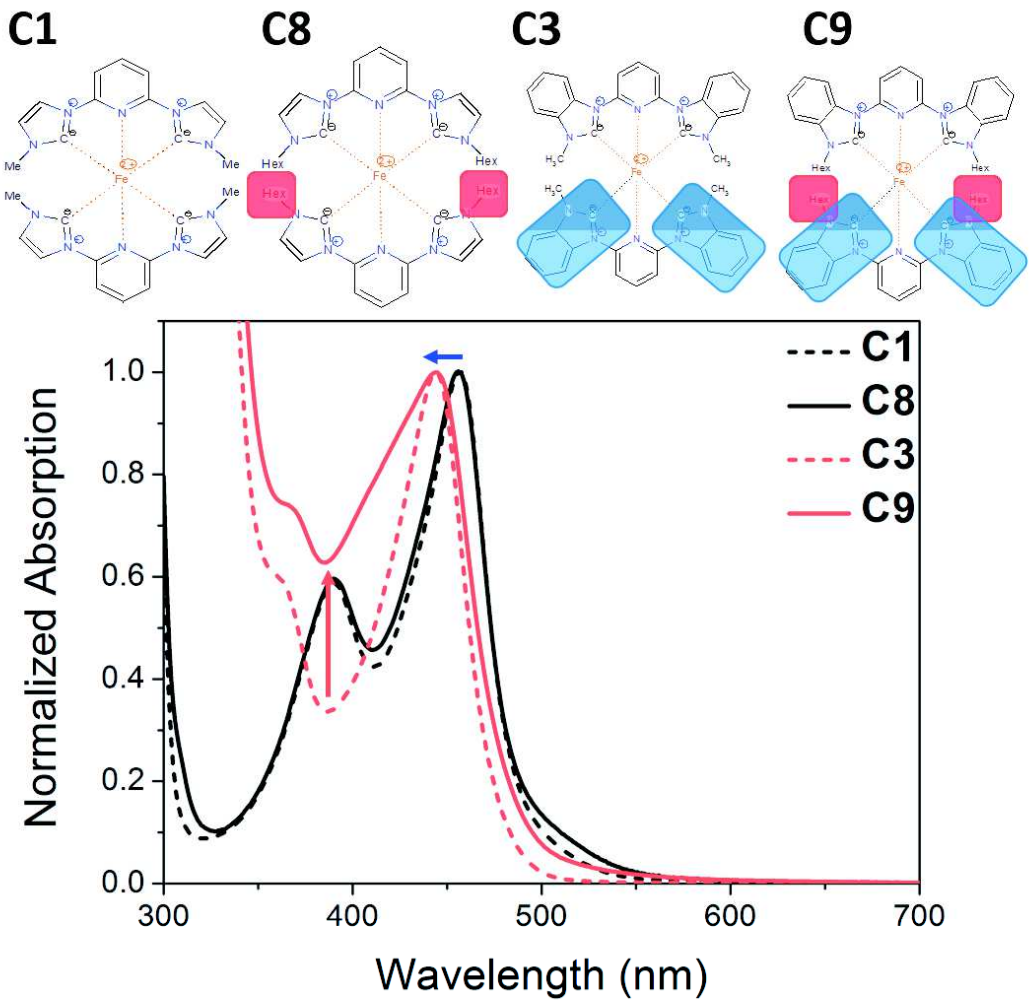

Figure V.17 Bottom: Normalized steady-state absorption spectra of Fe(II) complexes to study the effect of rigidity. (**C1** (black dotted curve), **C8** (black solid curve), **C3** (red dotted curve) and **C9** (red solid curve)) and Top: their chemical structures.

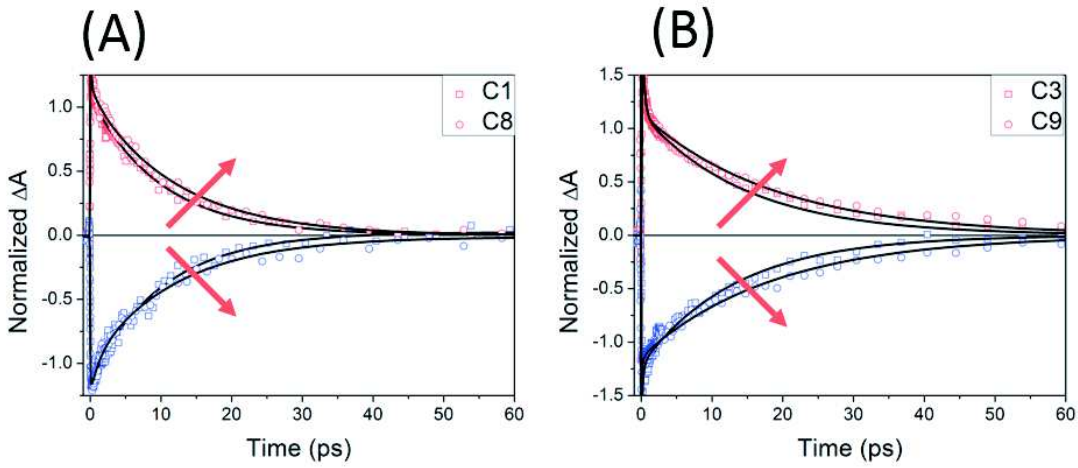

Figure V.18 Kinetic traces in the ESA (blue) and GSB (red) bands with their fits, normalized at 1 ps for the rigidity effect based on (A) imidazolylidene ligand (**C1**:Met and **C8**: Hex) and (B) benzimidazolylidene ligand (**C3**: Met and **C9**: Hex).

V.2.1.5 pH effect

As described previously, the addition of carboxyl group extends the ^{3}MLCT state lifetime of **C2**. This effect might be correlated to an enhancement of the charge transfer character in the complexes. To address this hypothesis more clearly, **C2** was studied at different pH: neutral (MeCN), acidic (MeCN-HCl), and basic (MeCN-NaOH).

In order to vary the pH, the pH of the pure MeCN is adjusted with one drop of 37% HCl or one drop of 2 mol L^{-1} NaOH in H_2O in 50 mL MeCN, named MeCN-HCl and MeCN-NaOH, respectively. **C2** is dissolved at different pH: MeCN-HCl (black curve), MeCN (red curve) and MeCN-NaOH (blue curve). The steady-state absorption spectra are shown in Figure V.19.(A). In the low pH condition (MeCN-HCl and MeCN), **C2** is protonated, with the lowest MLCT state centered at 520 nm. In the basic condition (MeCN-NaOH), **C2** is deprotonated and the carboxyl group is negatively charged. The deprotonated form results in a 40 nm hypsochromic shift of the absorption spectrum. It indicates that the negatively charged carboxyl groups increase the energy of the lowest ^{1}MLCT states.

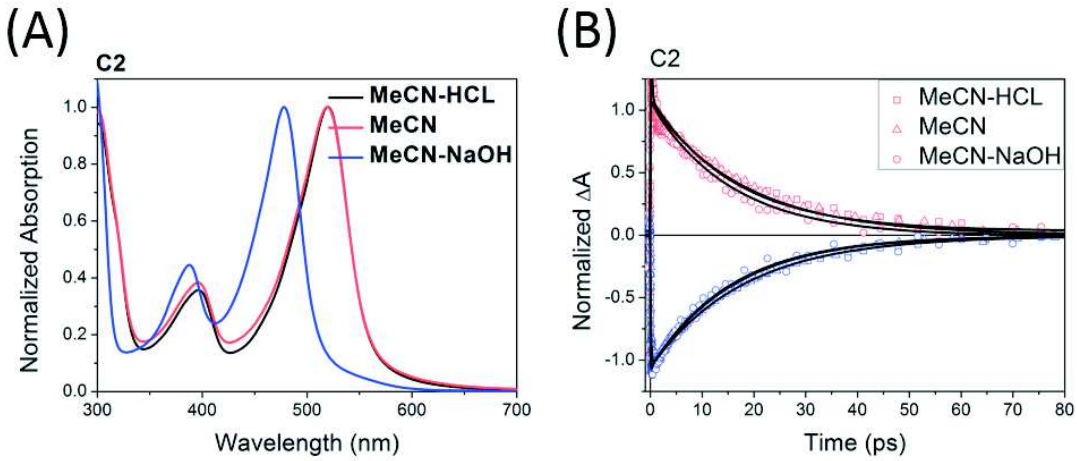

Figure V.19.(A) Normalized steady-state absorption spectra of C2 in solutions of different pH values (complex **C2** in pure MeCN (black curve) , MeCN+HCl (red curve) and MeCN+NaOH (blue curve)) and (B) Kinetic traces of **C2** in the ESA (red) and GSB (blue) bands in MeCN (square), MeCN-HCl (circle) and MeCN-NaOH (triangle) normalized at 1ps with their fits (black curves).

The transient absorption experiments were performed under the same conditions, except that **C2** in MeCN-NaOH was excited at 480 nm instead of 515 nm for **C2** in MeCN and MeCN-HCl.
The dynamics of **C2** in neutral and acidic conditions are identical (the lifetime of the ^{3}MLCT state is 16.5 ps) whereas the ones under basic conditions are slightly faster (14.5 ps). Negatively charging the ligands prevents the charge transfer to the ligands and thus the MLCT states become lower in energy. The theoretical studies have shown that the neutral carboxyl group decreases by 10% the electronic coupling, as the dipole moment $\overrightarrow{\mu_1}$ shown in Figure V.22 which reduces the ^{3}MLCT state lifetime.

V.2.1.6 Solvent Polarity effects

C4 is the complex with the longest ^{3}MLCT lifetime. As charges should be separated to increase the lifetime of the ^{3}MLCT, the effect of the solvent polarity was tested on **C4** in dissolved in six solutions with different dielectric constant (MeCN/MeCN-HCl: 37.5, ethanol: 24.5, DMSO: 46.7, 2-butanol: 17.2 and DMF: 36.7)[117].

For the steady-state absorption spectra are shown in Figure V.20, ~0.3 mg of **C4** is dissolved in 1 ml of several solutions (MeCN, MeCN-HCL, ethanol, DMSO, 2-butanol and DMF). The idea is to test the effect of the dielectric constants on the relative position of MC ad MLCT states (MeCN/MeCN-HCl: 37.5, ethanol: 24.5, DMSO: 46.7, 2-butanol: 17.2 and DMF: 36.7). The absorption spectra are classified into two groups: i) the MLCT state peak is centered at 460 nm in 2-butanol and DMF; ii) The MLCT state peak is lower in energy between 490 and 500 nm in ethanol (490 nm), DMSO (492 nm), MeCN (495 nm) and MeCN-HCl (500 nm). It is worth noticing that the solubility of **C4** in 2-butanol and ethanol (maximal absorbance of 0.06 and 0.09, respectively, in the visible region) is significantly lower than the one for the other solvents (absorbance of 0.3~0.4 in the visible). This classification is surprising because it does not obey the expected trends according to the dielectric constants or the presence of H-bonding.

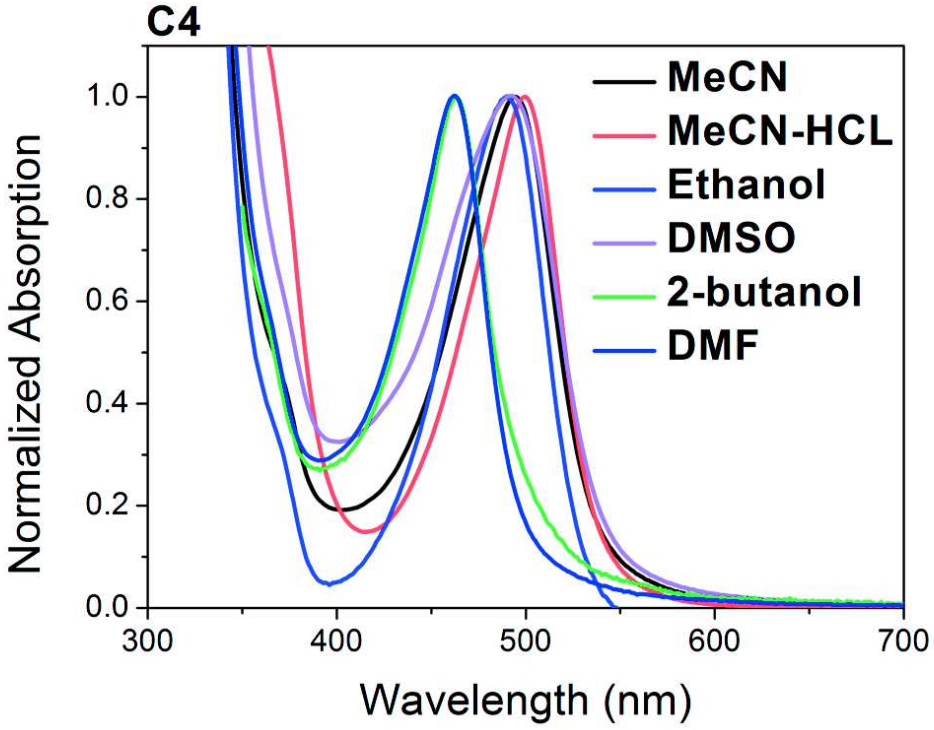

Figure V.20 Normalized steady-state absorption spectra of C4 to study effect of polarity (complex **C4** in pure MeCN (black curve), MeCN+HCl (red curve), ethanol (blue curve), Dimethyl sulfoxide/DMSO (purple curve), 2-butanol (dark green curve) and Dimethylformamide/DMF (dark blue curve))

Regarding the solvent effect on the ^{3}MLCT lifetimes, we expect a lengthening of it in polar solvents since the charge transfer character would be increased and thus the state lowered in energy with respect to the ^{3}MC state. Excited state solvation effects are expected to act fast enough, on a sub-10 ps timescale, for the highest polarity solvents.

The kinetic traces normalized at 1 ps of **C4** in different solvents taken in the ESA and GSB bands are depicted in Figure V.21. Surprisingly, in all cases, the ^{3}MLCT state lifetime is identical (26 ps). A closer inspection suggests the following interpretation: the solvent polarity has an influence on the interaction between metal center and the counter-anion $[PF_6]^-$ ($\overrightarrow{\mu_2}$ in Figure V.22), and solvates the ionic complex in the ground state. The cation-anion dipole is larger than the photo-induced excited state dipole moment due to charge transfer (Figure V.22). Therefore, the solvent configuration is most likely clamped by the former, and solvation and thus stabilisation of the excited state dipole moment can be neglected.

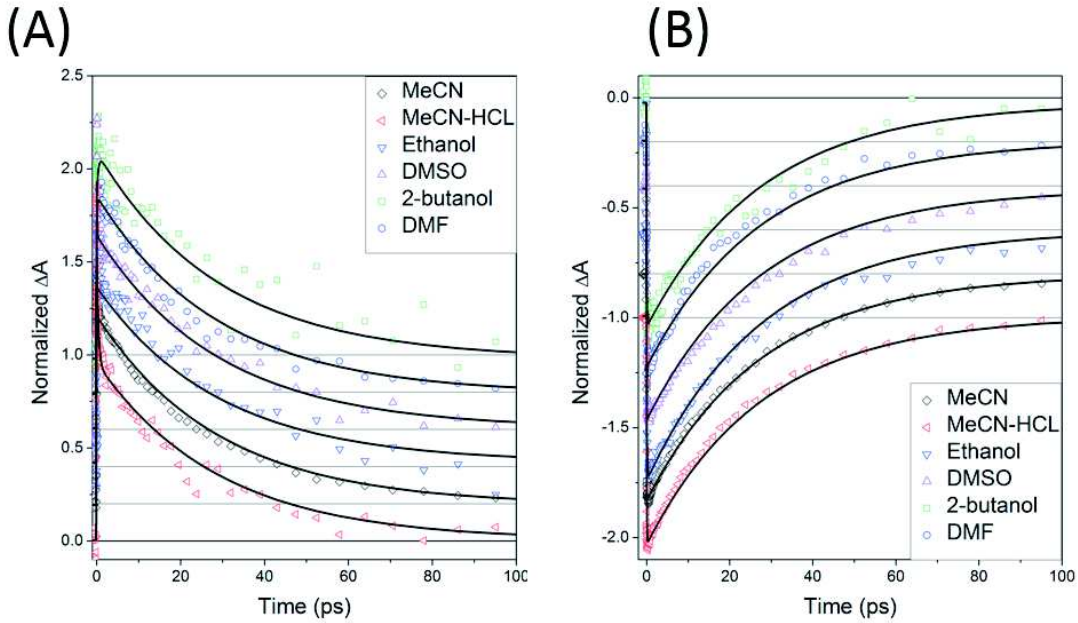

Figure V.21 Kinetic traces of **C4** in MeCN (black symbol), MeCN-HCl (red symbol) and ethanol (blue symbol), DMSO (purple symbol), 2-butanol (green symbol) and DMF (dark blue symbol) normalized at 1ps with their fits taken in the (A) ESA and (B) GSB bands.

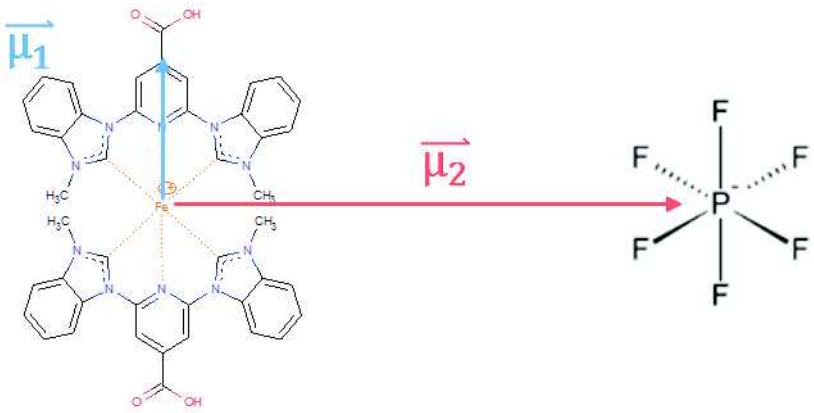

Figure V.22 Schematic sketch of the dipole moments depending on the pH ($\overrightarrow{\mu_1}$) and the solvent ($\overrightarrow{\mu_2}$)

V.2.1.7 Energy level of the ^{3}MLCT state

In order to obtain high PCE of DSSCs, the electron injection has to be most efficient. The two key parameters to achieve this are: i) a long lifetime of the ^{3}MLCT state, ii) the energy level of the ^{3}MLCT state must be higher than the bottom of the TiO_2 conduction band. This second parameter is not trivially measured because only the energies of the ground state and the ^{1}MLCT state can be measured by cyclic voltammetry but not one of the ^{3}MLCT states. However, the energy band gap of the ^{3}MLCT state can be directly determined by time-resolved fluorescence measurements. The time resolution can, in principle, discriminate the low-density ^{3}MLCT state emission from the intense and short-lived ^{1}MLCT state fluorescence. Thus, knowing the ground state energy, the energy level of the ^{3}MLCT state can be estimated.

The time-resolved fluorescence measurements were carried out using a Streak Camera (setup described in details in § III.2.2) with a time resolution of ~10 ps. The photoluminescence (PL) of **C2** excited at 515 nm is shown in Figure V.23. The PL spectrum at 15 ps (maximum PL intensity) presents an intense peak at 550 nm and a broad shoulder from 570 to 750 nm. After 30 ps, the narrow band has almost disappeared. A small blue shift occurs from 575 to 550nm within the first hundred picoseconds. On the 370 ps to 1 ns time scale, the PL spectra do not evolve.

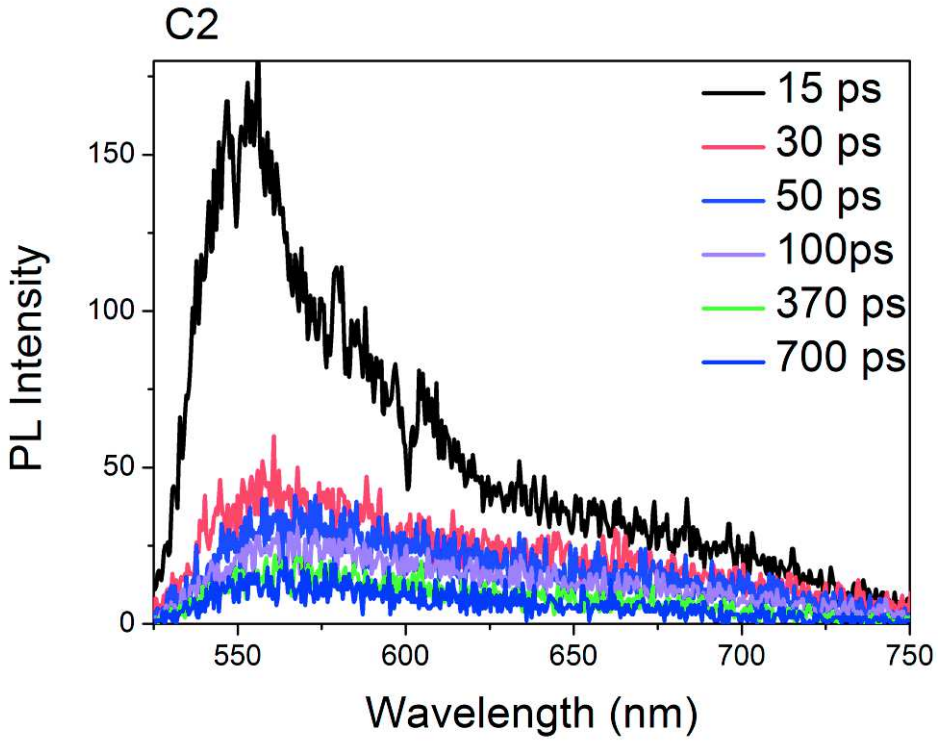

Figure V.23 A selected photoluminescence evolution of **C2** after excitation at 515 nm in MeCN obtained by time-resolved fluorescence experiment.

Figure V.24(A) illustrates normalized PL spectra at 15 ps (black curve) and 30 ps (red curve) after an FFT filter to reduce high-frequency noise to identify which states are involved with a reference curve: normalized steady-state absorption spectrum (blue curve). The 15 ps PL spectrum stands a mirror image of the steady-state absorption spectrum with a 130 meV Stokes shift from 520 to 550 nm. And the 30 ps PL spectrum is much broader in 500-600 nm range and its peak shifts from 550 nm to 575 nm (100 meV). The observations indicate that the 15 ps PL is discriminated by ^{1}MLCT state emission and after 30 ps, the ^{3}MLCT state emission dominates.

The same interpretation is also suggested by the kinetic traces at 555 nm and 625 nm with two Gaussian functions which have a same temporal width as IRF with different amplitudes shown in Figure V.24(B). The intense ^{1}MLCT state emission contributes to the high intensity of the Gaussian function. Furthermore, due to the small amplitude of ^{3}MLCT state, its lifetime (16.5 ps component in transient absorption spectroscopy) is not clearly distinguishable.

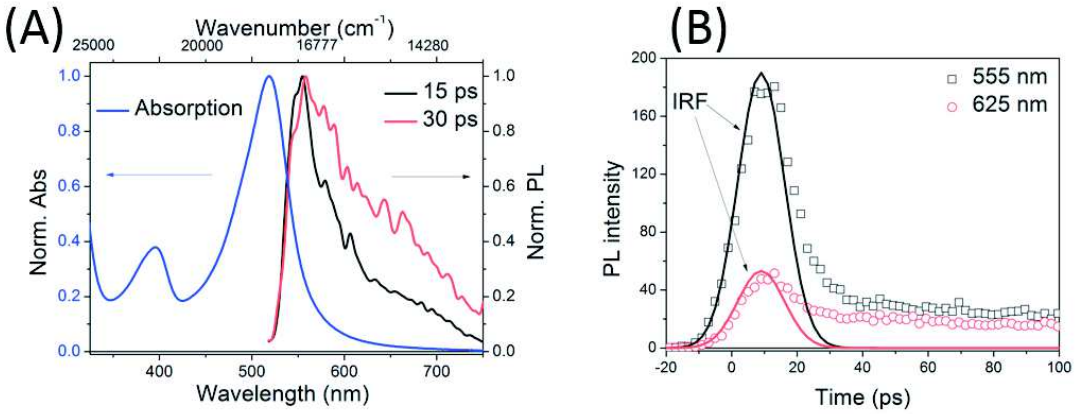

Figure V.24 (A) Normalized PL spectra at 15 ps (black curve) and 30 ps (red curve) after an FFT filter to reduce high frequency noise and normalized steady-state absorption spectrum (blue curve). (B) Kinetic traces (symbol curves) at 555 nm and 625 nm after an average within 1 nm with two Gaussian functions which have a same temporal width as IRF with different amplitudes.

The Streak Camera probes only the excited states lifetimes and has a higher dynamic range than a transient absorption setup. Thus, we think that the slower components, which have a small amplitude are not noticeable in a transient absorption experiment.

It is difficult to disentangle the long-lived species since both their energy and spectral shape are very similar to the ones of the short-lived ^{3}MLCT photoluminescence. One interpretation could be that they represent the same state but from different populations. Indeed, a structural heterogeneity could exist in the ground state.

In conclusion, ^{3}MLCT state energy level is very close to ^{1}MLCT state energy level with a ~130 meV down shift. The energy difference between ^{1}MLCT and ^{3}MLCT states is similar to other Fe(II) complex, *e.g.*, $Fe(bpy)_3$.[174]

V.2.2 Discussion

The photophysics of a series of Fe(II) complexes in solution was investigated by transient absorption and time-resolved fluorescence spectroscopies and, thus, the longest lifetime ever reported of the ^{3}MLCT state in those complexes (26 ps for **C4**).

This systematic study showed that the electronic structure of Fe(II) complex has a strong influence on its excited state lifetime. Their excited state lifetimes are shown in Table V.1. Our experimental results combined with quantum chemical calculations rationalized the effect of the carboxyl group on the MLCT state lifetime, and how the replacement of imidazolylidene by benzimidazolylidene enhances the ^{3}MLCT state lifetime.

Table V.1 Excited state lifetimes of all Fe(II) complexes investigated in MeCN by transient absorption spectroscopy. Those lifetimes as defined in the photo-induced scenario of **C1** were obtained by a global fit with the sum of three components.

Complex	^{1}MLCT (fs)	$(^3MLCT)^+$ (fs)	^{3}MLCT (ps)
C1	50	550	10
C2	20	130	16.5
C3	25	260	16.4
C4	15	65	26
C5	20	300	14
C6	10	---	10
C7	20	400	12
C8	60	1800	14
C9	20	150	19.5

In the DSSCs based on the Ru(II) complex, the electrons inject into TiO_2 semiconductor through two processes: i) an ultrafast efficient injection from the ^{1}MLCT state within 100fs, ii) and a slower injection from the ^{3}MLCT state within 50 ps. Since our Fe(II) complexes have a relative long-lived ^{3}MLCT state, it is worth to study their photovoltaics performances and their photophysical properties in the film. If we assume the same time window for electron injection, as for Ru(II), and if this mechanism is the dominant one, the longer excited state lifetimes should lead to higher PCEs. In the case of **C4**, a PCE value comparable to the N719 complex can be expected.

Table V.2 displays the photovoltaic performances of DSSCs based on our Fe(II) complexes without any specific material/device engineering compared to a standard Ru(II) complex (N719). Solar cells are prepared according to the standard protocol and the PV performances are measured by Thibaut Duchanois[154,175]. Protocol validated by the performances of N719 is acceptable.
The PCEs based on Fe(II) complexes are still low. Especially, the Jsc is at least 30 times less, than for the Ru reference complex. As mentioned in § II.4.2.2, it could be due to the low electron injection efficiency or carrier recombination. Most notably, even if **C4** has the longest ^{3}MLCT state lifetime in solution, its PCE is 10 times lower than the other Fe(II) complexes.

Table V.2 Photovoltaics performances of DSSCs fabricated with Fe complexes compared to reference N719.

Complex	Jsc ($mA*cm^{-2}$)	Voc (mV)	FF	PCE (%)
C2	0.41	457	0.68	0.13
C4	0.016	250	0.5	0.01
C5	0.33	400	0.73	0.10
C6	0.36	440	0.73	0.11
C7	0.36	390	0.71	0.10
N719	13.25	687	0.67	6.1

This suggests that the conditions and molecular mechanisms present in the DSSCs fabricated with the Fe(II)-NHC complexes contradict our above assumptions. The PCE is not simply governed by the ^{3}MLCT lifetimes determined in solution conditions, or cannot be extrapolated from the behavior or injection kinetics of N719 on TiO_2. Note that according to the previous chapter, electron injection has in principle enough driving force from the ^{3}MLCT states of the Fe(II) complexes, as for Ru(II), but structural differences such as the grafting conditions may lead to largely different unfavorable reorganization energies[20]. In addition, other yet unknown mechanisms must be accounted for such as charge recombination. As a matter of fact, a recent theoretical work points to the importance of the latter[175].
Thus, it is worth to investigate the photophysical processes in the Fe(II) complexes attached to TiO_2 to have a better understanding of the DSCCs. The fundamental questions are: i) how many electrons are injected into TiO_2, ii) how many electrons recombine to go back to the ground state instead of diffusing away from the interface, iii) and how the electronic structure of Fe(II) complexes impacts on those photophysical processes.

V.3 Transient Absorption Experiments on Semiconductor Films

The ^{3}MLCT state lifetimes of the new Fe(II) complexes in solution are comparable to the ones of efficient DSSCs based on Ru(II) complexes (larger than 10 ps), but their PCEs performances are still low, and not significantly improved compared to the ones previously reported by Gregg *et al.*[155]. Therefore, it is critical to address the question of the electron injection efficiency from the ^{3}MLCT state in the new Fe(II) complexes.
Recently, Wärnmark and co-workers claimed that **C2** has a close-to-unity electron injection through the ^{3}MLCT state after studying **C2** by electron paramagnetic resonance, transient absorption spectroscopy, transient terahertz spectroscopy and quantum chemical calculations.[176] The high (92%) electron injection efficiency is calculated based on a quantum yield equation:

$$\phi_{inj} = \frac{\tau_{inj}}{\tau_{inj}+\tau_{3MLCT}} \quad \text{Eq. V.1}$$

Such a high electron injection efficiency looks suspicious, because once **C2** is grafted onto a nanoporous TiO_2/Al_2O_3 surface, one carboxyl group is attached to the surface and the complex becomes heteroleptic like **C5**. In a heteroleptic complex, two ^{3}MLCT states are expected with similar energy level: i) the bottom part grafted on TiO_2/Al_2O_3, ii) and the top with a free carboxyl group. Thus, upon excitation, the population of the ^{1}MLCT state is split into those two ^{3}MLCT states with a ratio of almost 50/50%. Then, it looks difficult to reach close-to-unity electron injection efficiency through the ^{3}MLCT state.

To support our hypothesis of a lower electron injection efficiency through the ^{3}MLCT state, transient absorption and time-resolved fluorescence experiments were performed on **C2**, **C4**, **C5** and **C7** in the film.

V.3.1 Results

To approach similar conditions as the ones in DSCCs, the sample was prepared in a sandwich-like structure as shown in Figure V.21(B).
The films were prepared on FTO (Fluorine-doped tin oxide) glass (for TiO_2) or a microscope slide (for Al_2O_3) for the layer of TiO_2 and Al_2O_3 nanoparticles, respectively. The TiO_2 substrate was made following the standard procedure described in ref. 154,175. For the Al_2O_3 substrate, colloidal aluminum oxide (Sigma 13 nm) was diluted with distilled water (50:50) and hydroxypropyl cellulose (2 wt% Sigma 370000 g.mol^{-1}) was added. The paste was stirred for three weeks to allow the polymer to dissolve completely. The Al_2O_3 was doctor bladed on a microscope slide and dried at room temperature and calcined at 400 ºC for 30 mins.

The complexes are grafted on the surfaces by immersion of the films in the solution containing 0.5 mmol L^{-1} of Fe(II) complex solutions for at least 12h at room temperature. They are cleaned by MeCN more than three times to remove the ungrafted complexes and dried under nitrogen just before measurements. The absorption maxima of films in the visible are around 0.1 except for **C2** (~0.2).

A quartz slide is placed in the front of the sample face and two slides are fixed by a paper clip. Between the two slides, the solvent is injected by a syringe. Unless mentioned specially, otherwise, the solvent is acetonitrile. In the case of environment study, the solution could be MeCN-HCl (same recipes as the pH effect study in § V.2.2.5) or the solution is removed and called Air. The liquid environment produces a similar condition as the working DSSCs devices. In general, the solution is refilled every 20 minutes between two transient absorption experiment scans. The sample is also placed on the loudspeaker to avoid the photo-degradation. The incident laser beam comes from the quartz side. The pump wavelength is set at 515 nm.

Compared with other complexes (**C2**, **C4** and **C7**), **C5** is less heteroleptic after being grafted on TiO_2. The fact that **C5** is grafted on TiO_2 is conspicuous in the absorption spectrum in Figure V.25(A). The maximal absorption peak of the **C5**-TiO_2 in the film (black solid curve) is 485 nm with a 15 nm hypochromic shift compared to the one in solution. This blue shift was already observed when one carboxyl group is removed for a complex in solution. (**C2** → **C5**: 20 nm blue shift in Figure V.11(A)) Moreover, the MLCT state band of **C5**-TiO_2 has a 20 nm red shift compared to the one of the homoleptic **C1**-MeCN complex and is broader. It implies that in **C5**-TiO_2 the effect of the carboxyl group on the electronic levels is reduced, but an asymmetric character prevails.

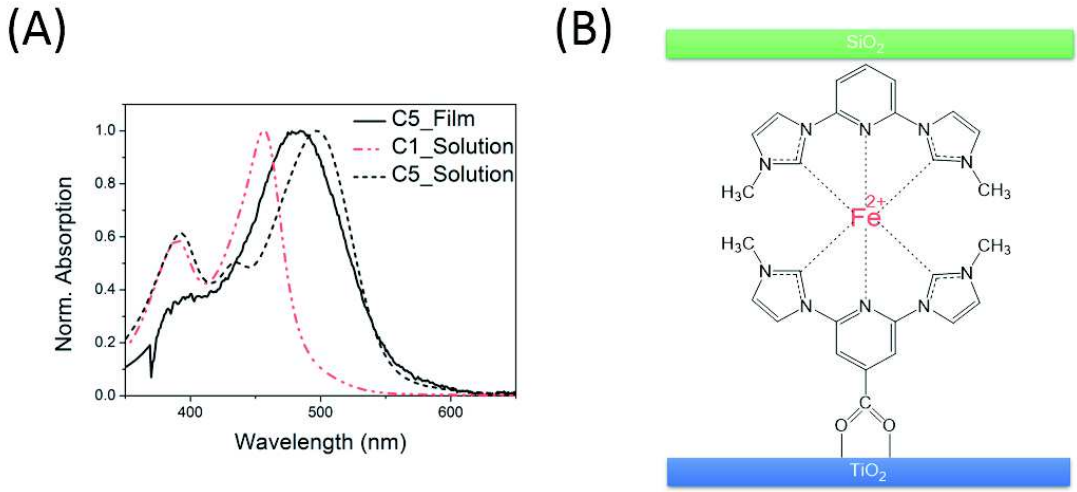

Figure V.25 (A) Normalized absorption spectra of **C5** grafted onto TiO_2 film (black solid curve), **C5** (black dotted curve) and **C1** (red dotted curve) in MeCN solution and (B) a sketch of the sandwich-like sample. The TiO_2 substrate grafted by Fe(II) complexes is covered by a quartz slide. The solvent between the two slides produces a similar condition as in DSSCs

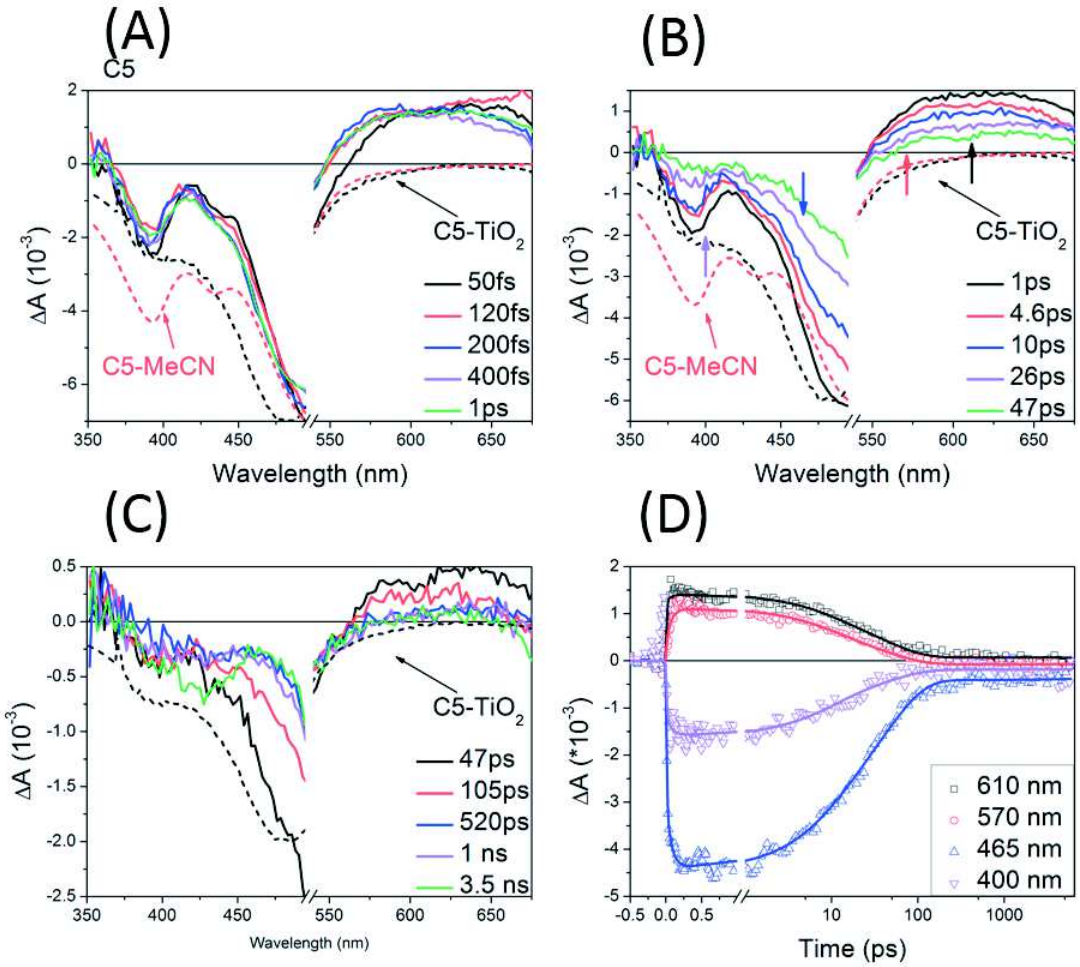

Figure V.26 Selection of transient absorption spectra of **C5**-TiO_2 after excitation at 515 nm, and reversed steady-state absorption spectra of **C5**-TiO_2 (black dotted curve) and **C5**-MeCN (red dotted curve) (A) within the first ps (B) from 1 to 47 ps and (C) until 3.5 ns. (D) Kinetic traces in the ESA (610 nm: black symbol curve and 570 nm: red symbol curve) and the GSB band (465 nm: blue symbol curve and 400 nm: violet symbol curves) with their fits (solid curves with respective colors).

Figure V.26(A)~(C) shows the TA spectra of **C5**-TiO_2 at different delay times after excitation at 515 nm. Those spectra are dominated by two bands: i) an intense negative band in the 360-560 nm region that can be attributed to the GSB, ii) and one broad ESA band above 570 nm. The dynamics of **C5**-TiO_2 evolves in three regimes:

- within the first 1 ps (Figure V.26(A)), the dominant GSB band has a similar spectral shape as **C5** in MeCN solution with a second negative peak at 395 nm. Additionally, the broad ESA band has a slight red shift within the first 200 fs to reach the 600 nm. And the 400 fs TA spectrum is comparable to the one of the ^{3}MLCT state differential spectrum in solution.
- from 5 to 50 ps (Figure V.26(B)), the intensity of the GSB peak centered at 485 nm decreases greatly. And more importantly, the shape of the GSB band evolves in this temporal window. The 5 ps GSB band looks more like the absorption of **C5** in MeCN with two negative peaks, whereas the 50 ps GSB band is similar to the absorption of **C5** grafted to TiO_2 with the flat contribution from 400 to 450 nm.
- at longer time delay (Figure V.26(C)), the ESA band significantly reduces for delay times greater than 500 ps. Then the TA spectra do not evolve until 5 ns. Remarkably a weak ESA signal at >600 nm and a clear GSB remain at long times.

The Figure V.26(D) shows the kinetic evolution of the transient absorption data. To illustrate the spectral changes in the ESA band, two wavelengths are represented: i) 610 nm which is near the central broad ESA band observed in the 47 ps TA spectrum, and ii) 570 nm where it goes back to zero at longer delay time (>500 ps). And the changes of the GSB band are also highlighted by two peaks at 400 and 485 nm which are probed at 400 and 465 nm, respectively. After the ultrafast process within the IRF, all four kinetics decays are fitted to a bi-exponential and a fixed l0 ns-lived plateau function with a small amplitude in the first 10 ps and a large one in the 100 ps time scale.

The TA data were globally fitted to three exponential decays and a Gaussian function (Figure V.27.(A) and Table V.3). To identify which states are involved, Figure V.27 (B) displays two references curves: i) the 14 ps DAS of **C5** in MeCN and the 10 ps DAS of **C1** in MeCN to determine the ^{3}MLCT state TA spectrum.

The assignment of those four lifetimes is:

- the unresolved first SAS (65 and 140 fs, black curve) exhibits a rapid red shift in the ESA band above 570 nm. This ultrafast component is the decay of the ^{1}MLCT state like in solution. The decay involves ISC and possible electron injection into TiO_2.
- the 7 ps SAS can be interpreted in two different ways:
  - electron injection, since ESA decay at >550 nm. This is in agreement with the 3 ps electron injection time in C2-TiO_2.[176]
  - electron-hole recombination since GSB recovers and the ESA band >550 nm could indicate the decay of Fe(III) formed from ^{1}MLCT state

  In the following, we stay as the optimum situation as this 7 ps component is the electron injection.
- the differential spectrum associated to the 45 ps component is very similar to the SAS of **C5** in MeCN with a negative contribution of the GSB band centered at 600 nm and a broad ESA band. Thus the 45 ps species, which is three times longer than that in the isolated compound, is attributed to the relaxation of the ^{3}MLCT state, probably from the top ungrafted part.
- for the longest > 10 ns component, its ESA band is different from the one for the 45 ps SAS and its GSB band is similar to the one from the film with an extremely long-lived lifetime. Thus, it might be associated with the electron-hole recombination.

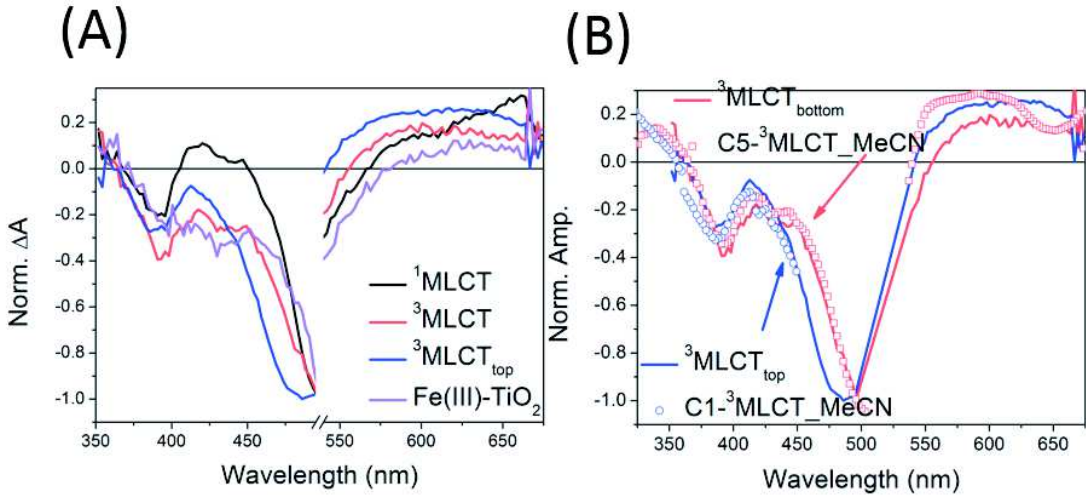

Figure V.27 (A) Decay-Associated Differential Spectra of **C5**-TiO_2 excited at 515nm obtained by global analysis and (B) Spectral identification of putatively involved states

These observations allow us to propose a reaction scheme describing the photoreaction of **C5**

grafted onto TiO_2. After excitation at 515 nm, the initial ^{1}MLCT state is populated. The first step is unresolved and the electrons can evolve through three possible pathways: i) direct electron injection into TiO_2, ii) ISC to ^{3}MLCT state on the bottom anchoring ligand, iii) and ISC to the ^{3}MLCT state on the top ligand. Then, the ^{3}MLCT state localized on the bottom ligand injects its electrons into TiO_2 within 7 ps. And the ^{3}MLCT state localized on the top ligand can not inject an electron to TiO_2 and directly relaxes back to the ground state in 45 ps. The injected electron recombination lifetime is larger than 10 ns. The proposed reaction scheme is summarizing the observations presented in Figure V.28.

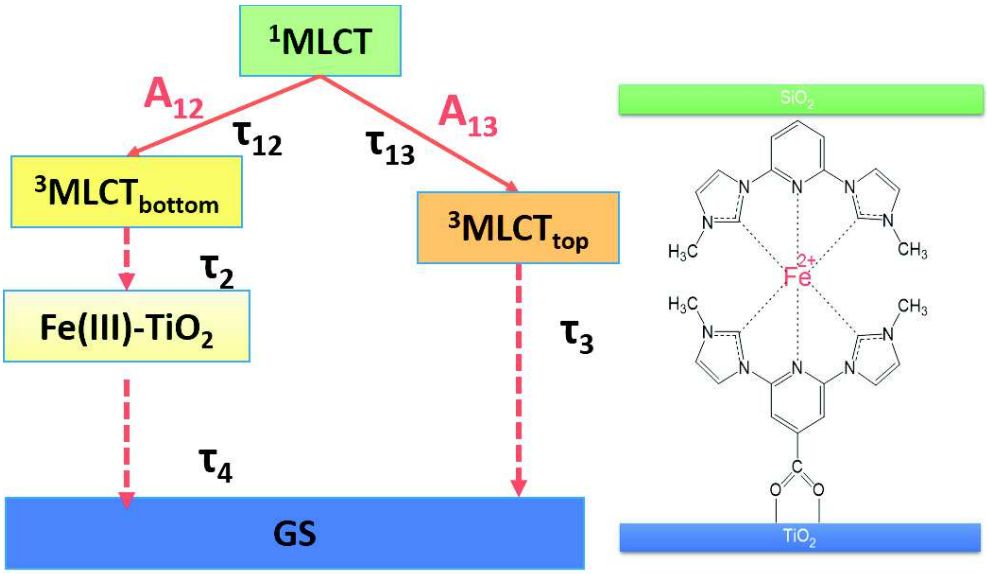

Figure V.28 Reaction scheme of **C5**-TiO_2 excited at 515 nm. After excitation at 515 nm, the initial ^{1}MLCT state is populated. The first step is unresolved and the electrons can evolve through three possible pathways: : i) direct electron injection into TiO_2, ii) ISC to ^{3}MLCT state on the bottom anchoring ligand, iii) and ISC to the ^{3}MLCT state on the top ligand. Then, the ^{3}MLCT state localized on the bottom ligand injects its electrons into TiO_2 within 7 ps. And the ^{3}MLCT state localized on the top ligand can't inject an electron to TiO_2 and directly relaxes back to the ground state in 45 ps. The injected electron recombination lifetime is larger than 10 ns.

Similar dynamics are observed for the other Fe(II)-TiO_2 samples (**C2**-TiO_2, **C4**-TiO_2 and **C7**-TiO_2). However, when the solution conditions were modified (MeCN, MeCN-HCl and air), the ESA band presented a red shift (Air → MeCN → MeCN-HCl) from 600 to 650 nm at 1 ps time delay and the kinetics were shortened (Table V.3). More details are given in the Appendix.II.

As mentioned by Wärnmark *et al.*[176], in the Ru(II) case, the multi-exponential recombination is also very common, and the two last DAS are akin to a dominant GSB band and a broad ESA band. However, with our above interpretation, 3 fold of the ^{3}MLCT state relaxation lifetime is surprising. We need a solid evidence for proving the relaxation of the ^{3}MLCT state population.

To confirm our assumption, time-resolved fluorescence measurements were performed on Fe(II) complexes grafted onto two types of substrates: TiO_2 and Al_2O_3 where the electron injection can occur and cannot occur, respectively. Indeed, Al_2O_3 has a large optical band gap, and thus its conduction band is much higher than the ^{1,3}MLCT states of Fe(II) complexes. The protocol of the Al_2O_3 substrate preparation is described above.

Four samples were studied by TR fluorescence measurements: **C2**-TiO_2, **C2**-Al_2O_3, **C4**-TiO_2 and **C4**-Al_2O_3. We focus on the **C4**-TiO_2 and **C4**-Al_2O_3 as a model compound. The transient absorption spectroscopy data for **C4-TiO$_2$** are in Appendix II.
No spectral shift is observed in the first ns time range. In order to increase the signal-to-noise

ratio, the average dynamic traces are taken from 560 to 700 nm and are normalized at their maxima, as displayed in Figure V.29.

The averaged kinetic trace of **C4**-Al_2O_3 was fitted to a bi-exponential function, 38 and 319 ps and the one of **C4**-TiO_2 needed an extra Gaussian function contribution (6 ps < IRF) before the bi-exponential part (31 and 319 ps). For the **C4**-Al_2O_3, the major fluorescence decays correspond to the 38 ps lifetime component. This fast component is probably the ^{3}MLCT state relaxation as measured by transient absorption spectroscopy.[176] Once **C4** complexes are grafted on TiO_2, this component is divided into two parts: the sub-10ps unresolved contribution and the 31 ps contribution.

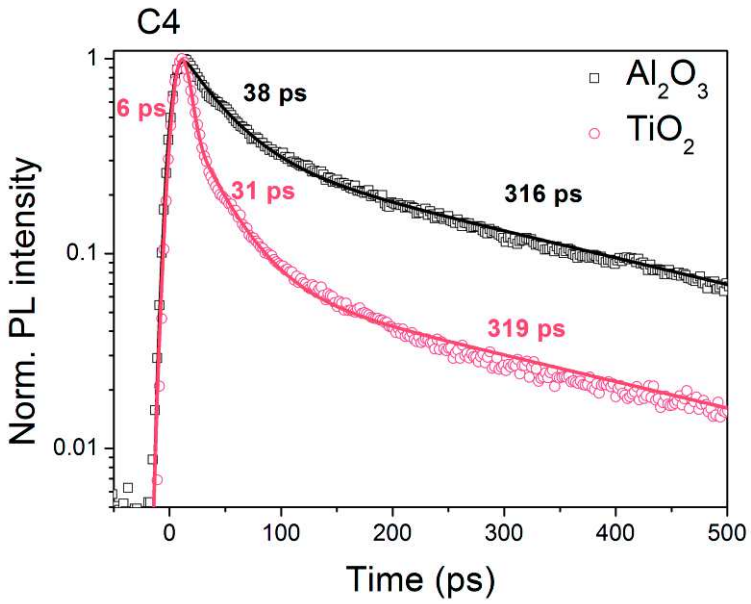

Figure V.29 Normalized TR fluorescence kinetic traces of **C4**-Al_2O_3 (black symbol curve) and **C4**-TiO_2 (red symbol curves) with their fits (solid curves).

The shorter lifetime of the ^{3}MLCT state in TiO_2 compared with in Al_2O_3 indicates the existence of electron injection. However, the unresolved sub-10 ps component makes the quantitative determination of the electron injection efficiency impossible. Thus, fs time-resolved fluorescence experiments will be useful to resolve this issue.

V.3.2 Discussion

The lifetimes of the Fe(II)-TiO_2 films studied by transient absorption spectroscopy and analyzed globally are summarized in Table V.3. All those compounds present similar spectral and dynamic behaviors (Appendix II for more details). Those results support our initial hypothesis where the electrons from the ^{3}MLCT state can take two different pathways: i) injection onto TiO_2 (τ_2) ii) and relaxation to the ground state (τ_3).

The heteroleptic complexes (**C5** and **C7**) show a faster electron injection and the *N*-substitution accelerates the electron injection within 1 ps. In the sandwich structure, the environment also has an effect on the electron injection. Thus, the pH may play a role on the PCE, and it is worth to improve the DSSCs based on Fe(II) by engineering those.

We assess the electron injection efficiencies by taking the ratio between the amplitude of

electron injection and the one of the ^{3}MLCT state relaxation. The differential absorption spectrum is proportional to the molar absorption, concentration and path length. Assuming these two processes have similar molar absorption and pass same path length, different amplitudes in the GSB represent different concentrations involved. Those amplitudes are determined from the GSB contribution of each DAS (τ_2 and τ_3). Instead of close-to-unity electron injection, we estimated electron injection efficiencies around 60 ~ 70 %.

Table V.3 Lifetime of Fe(II)-TiO_2 films obtained by global analysis of transient absorption spectroscopy data

	τ_{12} (fs)	τ_{13} (fs)	τ_2 (ps)	τ_3 (ps)	τ_4 (ns)	$k_{12}/(k_{13}+k_{12})$
C5	65	140	7	45	> 10 ns	0.68
C2	30	70	12	54	> 10 ns	0.70
C4	42	74	3.3	82	> 10 ns	0.64
C7	40	75	0.4	27	> 10 ns	0.65
C2-Air	25	42	5.8	46	> 10 ns	0.63
C2-MeCN-HCl	35	63	1.3	49	> 10 ns	0.64

* the relevant factor to adjust GSB of DAS(τ_3) to the same amplitude as GSB of DAS(τ_2). Noting that the ratio $A_{12}/(A_{13}+A_{12})$ is robustly calculated, it could get a quantitative estimation of the electron injection efficiency. More accurate results should take account on the extinction coefficient of the two steady-state absorptions.

V.4 Conclusion

This work on Fe(II) complexes has been performed in collaboration with our Nancy partners (Synthesis: T. Duchanois, M. Beley and P. C. Gros; Calculation: T. Etienne, M. Pastore, A. Monari and A. Assfeld) providing us the Fe(II) complexes, the PCE performances and the quantum chemistry calculations. With their help, we have investigated a series of Fe(II) complexes in solution and film.

We characterized the ^{3}MLCT state lifetimes of Fe(II) complexes in solution through transient absorption spectroscopy. Those results combined with their corresponding theoretical results allow us to understand how the electronic structure of the complexes affects the energy levels, and then their photophysical properties. With this strategy, the complex with the longest ^{3}MLCT state lifetime was achieved. The *N*-substitution could further contribute to extending the ^{3}MLCT state lifetime of those complexes.

The most surprising result was that increasing the ^{3}MLCT state lifetime over 10 ps did not directly improve the power conversion efficiency of the devices. This result could take its origin in two phenomena: 1) poor electron injection efficiency from the ^{1,3}MLCT states or/and 2) fast electron-hole recombination at the interface. Wärnmark *et al.* proposed that the electron injection efficiency is close-to-unity.[176]

In our option, a more accurate way to estimate the electron injection efficiency relies on the amplitude of the two pathways from the ^{3}MLCT state: electron injection and relaxation to the ground state. After ISC from the ^{1}MLCT state, the electron in the ^{3}MLCT state could be localized on both top and bottom sides of the complex. When the ^{3}MLCT state is located on the top, the electron injection is forbidden due to the geometry. The electron injection can occur only from the electron in the ^{3}MLCT state grafted to TiO_2. Thus, the estimation of the electron injection efficiency based on lifetimes is doubtful.

By transient absorption spectroscopy and time-resolved fluorescence measurements, we spectrally distinguished the ^{3}MLCT state and electron injection. We proposed that the electron injection efficiency can be determined more precisely by calculating the contribution of each pathway. Besides the evidence of the GSB, it is also interesting to directly observe the ESA differences between the electron injection (as the ESA band of Fe(III)) and the ^{3}MLCT state relaxation in the near-IR regime.

For the outlook, besides the material engineering on the PCEs performance, more chemical design can be imagined: 1) more heteroleptic complexes: adding the push-pull effect on the two parts of ligands, make the ISC to the top part more difficult, 2) change the anchoring group position: make both two ligand parts grafted into TiO_2.

Three articles of the study of Fe(II) complexes in solution are published.

1. The effect of the carboxyl group (§V.2.1.1, **C1** and **C2**):
   T. Duchanois, T. Etienne, C. Cebrián, **L. Liu**, A. Monari, M. Beley, X. Assfeld, S. Haacke and P. C. Gros ‘‘An Iron-based Photosensitizer with Extended Excited State Lifetime: Photophysical and Photovoltaic Properties’’*Eur. J. Inorg. Chem.* **2015**, *14*, 2469

2. The effect of ligand (§V.2.1.2, **C1** ~ **C4**):
   L. Liu, T. Duchanois, T. Etienne, A. Monari, M. Beley, X. Assfeld, S. Haacke and P. C. Gros ‘‘A new record excited state ^{3}MLCT lifetime for metalorganic iron(II) complexes’’ *Phys. Chem. Chem. Phys., 2016, 18, 12550*

3. The effect of *N*-substitution (§V.2.1.3, **C2, C4** and **C5** ~ **C7**):
   M. Pastore, T. Duchanois, **L. Liu**, A. Monari, X. Assfeld, S. Haacke, P. C. Gros “Interfacial charge separation and photovoltaic efficiency in Fe(II)-carbene sensitized solar cells” 2016 *Phys. Chem. Chem. Phys., 2016, 18, 28069*

Job/Unit: I50142 /KAP1 Date: 13-04-15 15:25:18 Pages: 10

EurJIC European Journal of Inorganic Chemistry

ChemPubSoc Europe

FULL PAPER

DOI:10.1002/ejic.201500142

An Iron-Based Photosensitizer with Extended Excited-State Lifetime: Photophysical and Photovoltaic Properties

Thibaut Duchanois,[a,b] Thibaud Etienne,[a,b,c] Cristina Cebrián,[a,b] Li Liu,[d] Antonio Monari,[a,b] Marc Beley,[a,b] Xavier Assfeld,[a,b] Stefan Haacke,[d] and Philippe C. Gros*[a,b]

Keywords: Photophysics / Solar cells / Sensitizers / Dyes/Pigments / Charge transfer / Iron / Carbene ligands

Herein, we report a homoleptic iron complex bearing tridentate bis-carbene (C^N^C) ligands designed for sensitization of TiO_2 photoanodes. Its excited state has been characterized by ultra-fast transient spectroscopy and time-dependent density functional theory (TD-DFT) computations, which reveal a record triplet metal-to-ligand charge-transfer (^{3}MLCT) excited-state lifetime (16 ps). The new dye was efficiently chemisorbed on TiO_2 and promoted electron injection and photocurrent generation in a dye-sensitized solar cell upon solar irradiation.

Introduction

Despite the success of ruthenium(II) dyes in dye-sensitized solar cells (DSSCs),[1] the price and rarity of ruthenium limit its use in energy-conversion devices. In contrast with ruthenium, iron, which belongs to the same group of the periodic table but in the first row of metals, is naturally abundant, of low cost, and low toxicity and thus appears as an ideal substitute. Moreover, it was shown that iron–terpyridine complexes exhibit a notably redshifted absorption band in the visible region compared with its ruthenium counterpart. This would improve sunlight harvesting and, subsequently, the DSSC efficiency.

However, while the injection of electrons into the semiconductor from ruthenium complexes can be easily performed (Figure 1, a), this is not the case for the hitherto reported iron complexes, which makes them largely incompatible with energy-conversion processes.[2] As a consequence, photophysical applications of iron(II)–polypyridyl complexes for solar energy conversion are virtually absent from the literature, although quite recently some important papers were published dealing with the spin crossover of iron complexes and DSSC functionalization.[3] The major feature held responsible for the low performances of Fe complexes in DSSCs[4] is a low-lying metal-centered (MC) state that deactivates metal-to-ligand charge-transfer ^{1,3}MLCT states from which the excited electron is normally transferred into the semiconductor (Figure 1, b). These MC states were identified as either a triplet or a high-spin quintuplet $^5T_2$ state.[5] The deactivation is very fast, occurring within the 100 fs regime and thus, short-cutting the injection process operating on similar or longer timescales.[6–8]

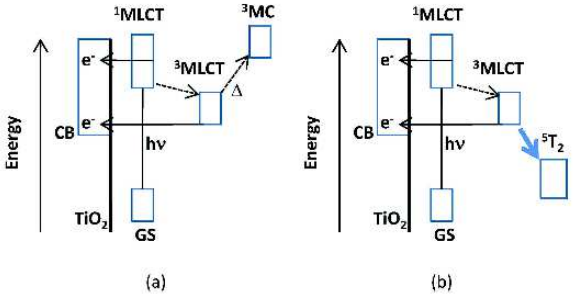

Figure 1. Energy-level diagrams of the most relevant electronic states in (a) $[Ru(tpy)_2]^{2+}$ and (b) $[Fe(tpy)_2]^{2+}$.

The main challenge to further develop Fe^{II}–polypyridine complexes for DSSCs is to be able to tune the relative energy of the low-energy triplet-states manifold so as to achieve an energy-level diagram resembling that of Ru^{II} (Figure 1, a). Synthetic modification of different organometallic compounds to extend excited-state lifetimes has been reported in the past.[9] Two strategies can be envisaged to slow down or impede the deactivation process. The MC state can be shifted to higher energies, ideally above the ^{3}MLCT state. Alternatively, the deactivation process can be slowed down or impeded when the relaxation into the MC

[a] Université de Lorraine, Photosens, SRSMC,
Boulevard des Aiguillettes, 54506 Vandoeuvre-Lès-Nancy, France
E-mail: philippe.gros@univ-lorraine.fr
http://www.srsmc.univ-lorraine.fr
[b] CNRS, Photosens, SRSMC,
Boulevard des Aiguillettes, 54506 Vandoeuvre-Lès-Nancy, France
http://www.srsmc.univ-lorraine.fr
[c] UCPTS, Université de Namur,
Rue de Bruxelles 61, 5000 Namur, Belgium
[d] IPCMS & Labex NIE, Université de Strasbourg & CNRS, 67034 Strasbourg Cedex, France
Supporting information for this article is available on the WWW under http://dx.doi.org/10.1002/ejic.201500142.

Job/Unit: I50142 /KAP1 Date: 13-04-15 15:25:18 Pages: 10

states requires a large structural rearrangement of the organic ligands.[10] Ferrere and Cregg reported the [Fe(dcbpy)$_2$(CN)$_2$] sensitizer bearing the attracting 4,4′-dicarboxy-2,2′-bipyridine (dcbpy) ligands. Although this dye led to very poor efficiency (<0.1%), it definitely opened the way to possible application of iron complexes in DSSCs.[11] However, the synthesis of the complex involved the use of a large excess amount of highly toxic cyanide salts, which is fully incompatible with future development of ecofriendly solar cells on a large scale.

In recent works by Wärnmark et al.,[12] the use of N-heterocyclic carbenes (NHC) as ligands for iron(II) (see **1**, Figure 2), promoted a remarkable increase of the ^{3}MLCT lifetime (9 ps) followed by a complete return to the molecular ground state (GS) in the corresponding homoleptic complexes. This was rationalized by recent quantum chemistry calculations showing that relaxation into the $^5T_2$ states requires an unfavorable and simultaneous increase of the Fe–C bond lengths in both ligands.[10] This work was very recently followed up by the synthesis and complete investigation of the electronic structure of a heteroleptic bis-dentate Fe^{II} complex, featuring mesoionic triazolylidene ligands and a ^{3}MLCT lifetime as long as 14 ps.[3c]

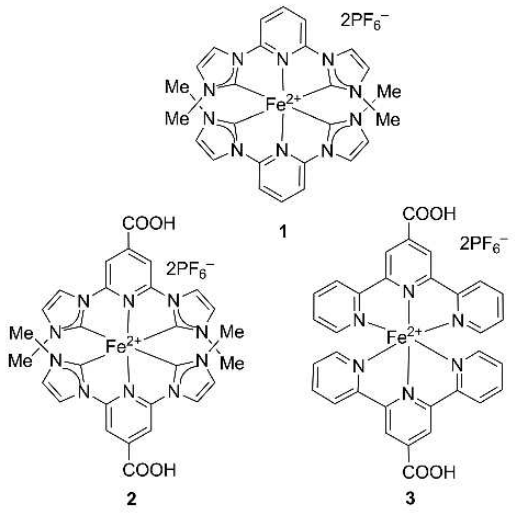

Figure 2. Iron complexes studied in this work.

In addition, recent works by the Jakubikova group, based on density functional theory (DFT) and quantum dynamics calculations suggest the crucial role of cyclometalation in ensuring electron injection from iron-based complexes.[2b] Recent works by the Jakubikova group, based on DFT and quantum dynamics calculations suggest the crucial role of cyclometalation in ensuring electron injection from iron-based complexes.[3d] Nevertheless, despite these promising results, there was no evidence of the ability of such complexes to efficiently sensitize TiO_2 for current generation.

We report here on a new carbene-based iron(II) complex (see **2** in Figure 2) that, to the best of our knowledge, has the longest ^{3}MLCT excited-state lifetime ever reported for a photostable iron(II) compound, and a first successful application of such a complex in a DSSC device delivering a nonetheless modest photocurrent of 0.41 mA cm^{-2}.

Results and Discussion

Dye **2** (Figure 2) was designed to bear carboxylic groups to enable efficient grafting on the semiconductor surface, namely TiO_2, which is clearly a prerequisite for injection into its conduction band. Tuning of the complex electronic properties was also expected from the introduction of such an electron-withdrawing group.[13]

Dye **2** was prepared (Scheme 1) from ligand **4**,[14] which was previously obtained by reaction of 4-carboxy-2,6-dibromopyridine with *N*-methylimidazole. To improve its solubility in organic solvents, we decided to turn the bis-imidazolium dibromide into its PF_6 salt. The final coordination of **2** with $FeCl_2$ was accomplished in DMF in the presence of *t*BuOK as deprotonating agent to afford the targeted complex in 56% yield (Scheme 1).

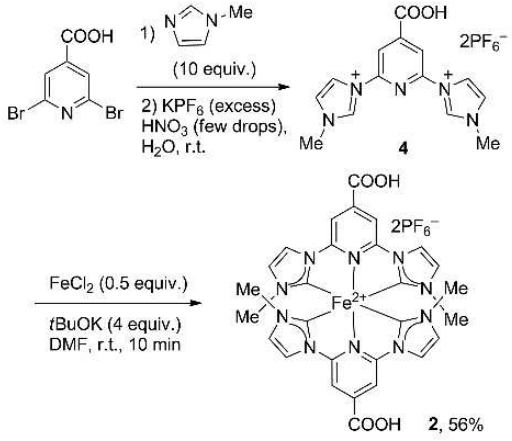

Scheme 1. Synthesis of dye **2**.

For comparison, complexes **1** and **3** were also prepared. Complex **1** was prepared according to the literature,[10] while **3**, which bears terpyridine ligands, was synthesized in 83% yield from 4′-(2-furyl)-2,2′:6′,2′′-terpyridine **5**[15] (Scheme 2).

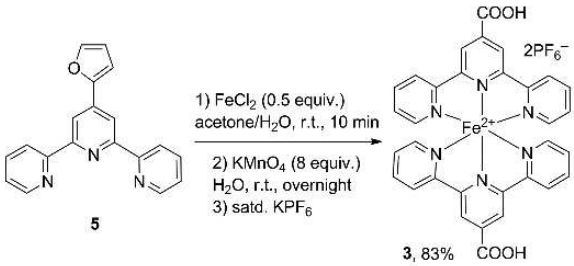

Scheme 2. Synthesis of dye **3**.

The complexes have been characterized by UV/Vis spectroscopy (Figure 3) and electrochemistry (Table 1).

Job/Unit: I50142 /KAP1 Date: 13-04-15 15:25:18 Pages: 10

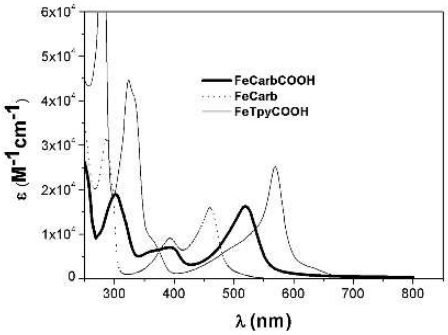

Figure 3. Absorption spectra of iron complexes in acetonitrile. Carbene coordination of Fe leads to a blueshift of the lowest MLCT transition, which is partially compensated by conjugation with the COOH group. See text for assignment of the bands.

Table 1. Photophysical and electrochemical properties of complexes.

	$\lambda_{abs\text{-}max}$ [nm] (ε [10^3 M^{-1} cm^{-1}])[a]	$E_{ox}(Fe^{III}/Fe^{II})$ [V] (SCE)[b]	E_{red1} [V] (SCE)	ΔE [eV][c]
1	287 (31.4) 393 (9.0) 460 (15.9)	0.80 (rev)	–1.95 (irrev.)	2.75
2	302 (19.0) 394 (7.0) 520 (16.2)	0.85 (rev)	–1.35 (irrev.)	2.20
3	276 (71.4) 324 (44.6) 569 (25.1)	1.21 (rev)	–1.05 (rev.)	2.26

[a] Measured in CH_3CN at 25 °C. [b] First oxidation potential. Potentials are quoted versus SCE. Under these conditions, $E_{1/2(Fc+/Fc)}$ = 0.39 V (SCE). Recorded in CH_3CN using Bu_4NPF_6 (0.1 M) as supporting electrolyte at 100 mV s^{-1}. [c] Electrochemical bandgap ($\Delta E = E_{ox} - E_{red1}$).

For all three complexes, the absorption spectra are composed of three main bands representing individual electronic transitions of different nature. The intense band near 300–320 nm corresponds to π–π* transitions in the ligands. At longer wavelengths, a band centered at 360–380 nm is observed that is little affected by the nature of the organic ligand. The longer wavelength bands, in the 450–600 nm range, are subjected to significant shifts and change in shape. In particular, for the carbene-coordinating ligands, the functionalization of the central pyridine nucleus with a carboxylic group promotes a dramatic redshift of this band from 460 to 520 nm, that is, from **1** to **2**, respectively.

Thus, it appears that the iron center affords two MLCT transitions in the visible region: one involving the carbene units whose energy remained unchanged whatever substitution (380 nm), the other at lower energies involving the central pyridine ring sensitive to electronic tuning on this ring. Compared with **3** (λ_{max} MLCT = 560 nm), the complexes containing the carbenes show blueshifted MLCT transitions. Nevertheless, the visible region is efficiently covered by **2** especially in the 380–500 nm range, with $\varepsilon > 5 \times 10^3$ M^{-1} cm^{-1}, where **3** is almost transparent. Therefore, the absorption spectrum of **2** in solution reflects promising optical properties for satisfactory light harvesting in DSSCs.

The cyclic voltammogram of **2** (see the Supporting Information, Figure S1) shows a reversible oxidation wave of the Fe^{2+}/Fe^{3+} couple. This is an important characteristic for ground-state regeneration of the oxidized dye in the DSSC. Moreover the oxidation potential of this couple is found at 0.85 V (SCE), which indicates highly favorable thermodynamics for dye regeneration by the commonly used redox mediators such as the I_2/I^- couple [0.2 V (SCE)]. The reduction potential of the ligand is found to be irreversible at –1.35 V (SCE), which suggests that the dye exhibits sufficient energy by far to allow the electron injection into the conduction band of TiO_2, the bottom of which is estimated to lie at about –0.7 V (SCE)[16] (Figure 4). For comparison, the oxidation potential of **3** (see the Supporting Information, Figure S2) was found at 1.21 V (SCE) in perfect agreement with the lower σ-donor character of the carboxyterpyridine ligand. The reduction potential [–1.05 V (SCE), reversible] was also found at a higher value than that for **2** as expected for carbene-based π* orbitals. Another important feature was the notable decrease of the electrochemical bandgap on going from **1** to **2**, which indicates that a lower energy is required to operate the metal-to-ligand charge transfer in **2**. This decrease of the bandgap is in perfect agreement with the redshift of the absorption band in the visible region shifting from 460 to 520 nm on going from for **1** to **2**.

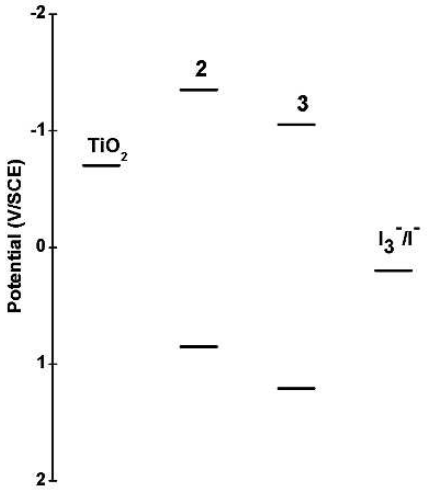

Figure 4. Electrochemical potential diagrams of **2**, **3**, TiO_2, and the I_3^-/I^- couple.

To shed light on its electronic structure, the new dye was analyzed by means of DFT and time-dependent DFT (TD-DFT) calculations. Computed absorption spectra (see the Supporting Information, Figure S12), obtained as a convolution of vertical transitions from the ground-state equilibrium geometry showed a good agreement with the experimental results, especially for the low-energy band. To characterize the ground- to excited-state electronic density redis-

Job/Unit: I50142 /KAP1 Date: 13-04-15 15:25:18 Pages: 10

tribution we used natural transition orbitals (NTO)[17] calculated for the most relevant transitions (Table 2). For the reader's convenience we remind them that NTOs are obtained by singular value decomposition (SVD) of the transition density matrix and thus can be considered as optimal orbitals to describe an electronic transition in the TD-DFT formalism. In contrast to the Kohn–Sham molecular orbitals basis, with which many occupied–virtual orbital couples are required to describe an electronic transition, the NTO basis generally provides only one (or at maximum two) couples of orbitals to entirely represent all the physics underlying the transition.

Table 2. NTOs isodensity surface in **2**.

λ [nm]	f[a]	s*s[b]	oNTO	vNTO
		0.467		
543	0.27			
		0.424		
473	0.22	0.865		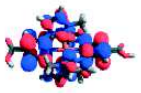

[a] Oscillator strength (a.u.). [b] Weight of the NTOs couples.

In this formalism, the "occupied" NTO (oNTO) can be seen as the "hole" orbital, that is, the orbital from which the electron is removed during transition, whereas the "virtual" NTO (vNTO) is the orbital in which the electron is promoted in the excited state.

In the case of **2**, the two major UV/Vis transitions are of ^{1}MLCT type since the oNTO is located at the metal center whereas the vNTO extends onto the pyridine ring of the ligand. Energy differences below 0.15 eV were found when comparing the lowest-energy transition with the experimental ones, further confirming the suitability of the computational protocol.

A significant delocalization of the excited electron into the carboxylic moieties is required for electron injection into the semiconductor upon photoexcitation, as it was extensively studied and proved in the case of ruthenium complexes.[18] Indeed, the efficiency of the injection is expected to depend on the location of vNTO on the carbene ligands bearing the carboxylic group bound to the TiO_2 surface. According to Table 1, the best injection efficiency would be expected for the lowest-energy transition, which incidentally corresponds to the most intense transition in the recorded spectra. Overall the excited-states topology of **2** seems extremely favorable to electron injection.

To get further insight into the behavior of our new dye, and with the aim of rationalizing differences in photocurrent generation, the ultrafast photophysics of **1**, **2**, and **3** in acetonitrile were investigated by using transient absorption spectroscopy (TA) with 80 fs time resolution (Figures 5 and 6). Molecules were excited with 60 fs pulses close to the maximum of their lowest-energy absorption bands (515 nm for **2**), and the differential absorption (ΔA) was probed in the 300–700 nm window with white-light pulses generated in CaF_2. Figures 4 (A and B) display the ΔA spectra of **2** and **3**, respectively, for selected delay times as indicated. Complex **3** shows the well-known behavior of an ultrafast transition from the ^{1,3}MLCT states into the $^5T_2$ quintuplet on a 100–200 fs time scale, as highlighted by the disappearance of ^{1,3}MLCT excited-state absorption (ESA) in the 380–460 nm range and above 600 nm.[5b,5c] The $^5T_2$ state is characterized by the sharp induced absorption at 355 nm, the prominent bleach features peaking at 574 and 342 nm, and a long lifetime of 2.2 ns. In addition to the latter, our assignment is based on the spectral similarity with the $^5T_2$ state of $[Fe(bpy)_3]^{2+}$ in H_2O.[5d] As pointed out by other authors, UV/Vis pump–probe spectroscopy does not give indications for short-lived MC states, which were predicted to lie energetically in between the ^{3}MLCT and $^5T_2$ states.[19]

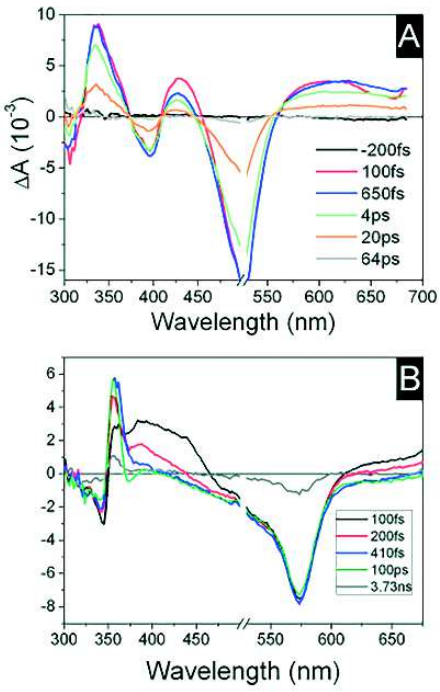

Figure 5. Photoinduced differential absorption spectra of (A) **2** and (B) **3** in acetonitrile. The dominant negative features are due to ground-state bleach. While the 355 nm peak for **3** is due to population of the high-spin $^5T_2$ state, the strikingly different excited-state absorption of **2** is assigned to a 16.5 ps lifetime population of the ^{3}MLCT state. A 20–30 nm region around the excitation wavelength is disregarded due to excessive pump light scattering.

The ΔA spectra of **2**, in contrast (Figure 5, A), is dominated by broad positive ESA bands in the near-UV (320–

Job/Unit: I50142 /KAP1 Date: 13-04-15 15:25:18 Pages: 10

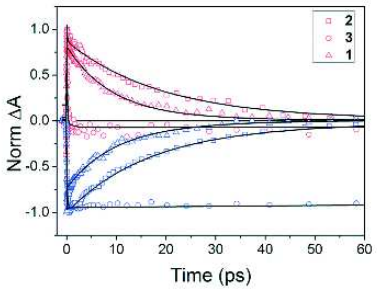

Figure 6. Kinetic traces monitoring the excited-state decay (red) and ground-state recovery (blue), together with multiexponential fits (solid lines), for the three different Fe complexes investigated (cf. legend). The exact probe wavelengths are sample dependent: excited state decay was probed in the long-wavelength ESA bands, and $^1A_1$ recovery close to the wavelength of maximum bleach. The ^{3}MLCT state of **2** displays a record 16.5 ps lifetime. See SI for details.

360 nm), the blue (420–450), and in the red part of the spectrum (>580 nm). Promoting electrons into the excited state induces a transient bleach of the ground-state transitions (GSB) peaking at 400 and 505 nm. The ESA bands differ significantly from those of $^5T_2$ in **3** (Figure 5, B), but they show a strong similarity with the ^{3}MLCT state ESA reported for **1**[12] and with those of **3** in the first 200 fs, even though modified by the spectrally shifted GSB transitions. Indeed, these three ESA bands are characteristic of the ^{3}MLCT state in Fe^{II} complexes as argued by Y. Liu and coworkers.[3c] Moreover, spectral changes observed on a sub-200 fs timescale are indicative of the ^{1}MLCT→^{3}MLCT excited-state relaxation in **2** (Figure S10 in the Supporting Information).

Note that the ^{3}MLCT decay converts the molecules entirely back into the ground state $^1A_1$ since the GSB decays fully on exactly the same timescale as the ESA decay (Figure 5, A).

The characteristic lifetimes of the ^{3}MLCT state and how they evolve as a function of the chemical structure of the Fe complexes (Table 3) can be read from Figure 5. The positive ESA and negative GSB traces are almost mirror images of each other for **1** and **2**, but clearly not for **3** owing to the population of $^5T_2$ in this compound only. Multiexponential fits accounting for the above ^{1}MLCT→^{3}MLCT→($^5T_2$)→$^1A_1$ relaxation scheme yields the lifetimes summarized in Table 2. Note that due to the limited temporal resolution, the initial sub-200 fs MLCT relaxation phase is difficult to decipher (interstate relaxation vs. intrastate thermalization). In **1**, a small (<10%) amplitude ESA decay component of 20 ps is found in addition to the already reported 9 ps majority decay of the ^{3}MLCT state.

Two remarkable features highlight how the carbene bonds modify the excited-state relaxation scheme with respect to Fe polypyridine complexes and induce a significant stabilization of the ^{3}MLCT state. First, the ^{3}MLCT decays entirely back into the ground state $^1A_1$ (Figure 6). As pointed out by Wärnmark for **1**,[10,12] this indicates that $^5T_2$ is not populated at all, because this state would delay

Table 3. Summary of excited-state lifetimes of the three Fe complexes investigated.[a]

	t_1 [fs]	t_2 [ps] ^{3}MLCT lifetime	t_3 [ns] $^5T_2$ lifetime
3	unresolved	<0.1	2.20±0.05
1	<100	9.5 ± 1.0	–[b]
2	180 ± 30	16.5 ± 1.0	–[b]

[a] The ^{3}MLCT lifetime is significantly enhanced in the carbene-containing complexes. Addition of COOH increases it by almost a factor of two. [b] The $^5T_2$ state is not populated in the cases of **1** and **2**.

the ground-state bleach (GSB) into the nanosecond range, as it does for the terpyridine-based complex **3** (Figure 5).

Second, the excited-state lifetime is nearly twice as large as in **1**, the ESA and GSB signals of ^{3}MLCT being perfectly fitted by exponential decays of 16–17 ps.

As suggested by the TD-DFT calculations, the electron-accepting character of the COOH groups displaces the excited-state electron density to the periphery of the organic ligands (Table 2), so as to reduce the electronic coupling with the Fe center, thereby leading to slower ^{3}MLCT–$^1A_1$ relaxation times.

Along the conclusions drawn from quantum chemistry calculations,[10] the suppression of the ^{3}MLCT–$^5T_2$ relaxation is most probably due to the large geometry difference between both electronic states. The longer lifetime in **2** relative to **1** can be tentatively assigned to the presence of a small barrier along the ^{3}MLCT–^{3}MC pathway.

Calculations of the triplet lowest energy spectrum (see Table T3 in the Supporting Information) were carried out for **1**, **2**, and **3** and triplet states were identified in terms of spin-density distribution. Excited-state modeling helped to rationalize the observed extended MLCT lifetime. The energy levels of the first ^{3}MLCT and ^{3}MC state calculated at the Franck Condon region, that is, at the equilibrium geometry of the singlet ground state are reported in Table 4. Since at the Franck–Condon region we are not allowing geometry relaxation, the MLCT state is always the lowest in energy. Nonetheless, significant differences can be underlined. Indeed, the MLCT and MC states for **3** are extremely close, with an energy difference of only 0.2 eV. This quasi-degeneracy is in agreement with observations, as it implies that, upon geometry relaxation, the MC states would easily cross the MLCT, ultimately resulting in the inversion of the order of the two triplets, population of the MC state, and consequent deactivation. In contrast, the more electron-donating carbene ligand strongly destabilizes the first MC state, giving rise to a more than double energy difference. Population of the ^{3}MC becomes therefore more difficult and hence, the ^{3}MLCT lifetime is longer. When the carbene-based ligand is functionalized with a carboxylic group, we may still notice a strong destabilization of the MC state, but the electron-withdrawing COOH moiety is now selectively stabilizing the MLCT state, in agreement with the observed spectral redshift (Figure 3). Because of these combined effects, in the case of **2** the energy difference between MC and MLCT becomes close to 1 eV.

Job/Unit: I50142 /KAP1 Date: 13-04-15 15:25:18 Pages: 10

Table 4. Triplet-state energy levels for the three complexes calculated at the TD-DFT level and in the Franck–Condon region.

	MLCT [eV]	MC [eV]	ΔE [eV]
1	1.88	2.31	0.43
2	1.48	2.30	0.82
3	1.39	1.59	0.20

Computations of the excited-states equilibrium geometries of ^{3}MC and ^{3}MLCT states for both carbene complexes (Table 5) show that the ^{3}MC state is more stable than the ^{3}MLCT one for **1** (ΔE = 0.73 eV), but for **2**, the two states are almost degenerate (ΔE = 0.08 eV).

Table 5. Energies of the ^{3}MLCT and ^{3}MC states of **1** and **2**[a] and the relative energies between the two states.

	^{3}MLCT [eV]	^{3}MC [eV]	ΔE [eV]
1	2.02	1.29	0.73
2	1.24	1.16	0.08

[a] Computed at respective optimized geometries with respect to the respective S_0 equilibrium energy at its equilibrium geometry.

From the energetic point of view one can see that the ^{3}MC state of **1** should be populated. This partly explains the quite short lifetime of the ^{3}MLCT state for this complex.[12] The energetic barrier between the two states will consequently govern the photophysical behavior. For complex **2**, because of the ^{3}MC–^{3}MLCT degeneracy, both states can be populated.

One can anticipate that, after structural relaxation departing from the calculated FC region, the barrier separating ^{3}MLCT and ^{3}MC will be higher for **2** than for **1** owing to the relative stabilization of the ^{3}MLCT state. The important role of the carboxylic group in enhancing the ^{3}MLCT lifetime can therefore be better ascertained. Indeed, while the carbene inclusion destabilizes both the ^{3}MLCT and ^{3}MC, COOH strongly stabilizes the ^{3}MLCT leaving the ^{3}MC almost unaltered. This effect can be understood by looking at the NTOs results (Table 2): since the electron in the MLCT accumulates in the ligand, the presence of an electron-withdrawing COOH group would certainly stabilize this electron distribution. In contrast, little influence would be expected to occur on the ^{3}MC state whose electron-density reorganization is centered on the metal, that is, far away from the carboxylic acid. These considerations explain why the lifetime of the ^{3}MLCT state of **2** is longer than that of **1**. Lowering the energy of the ^{3}MLCT state by grafting a more electron-withdrawing group on the ligand could lead to the inversion of energy levels of the two states as is the case in ruthenium-based complexes.

The promising photophysical properties of **2** prompted us to assemble a DSSC employing the new dye. The sensitization of a TiO_2 photoanode via **2** was first monitored by UV/Vis spectroscopy and compared with those operated with **3** (Figure S3 in the Supporting Information). As observed in solution for the carbene-based dye, the electrode exhibited high extinction, dominated by the absorbance of sensitizer **2**. Sunlight was collected over a wide window from 400 to 600 nm in contrast with **3**, which displayed only a narrow absorption near 580 nm.

The subsequent DSSC assembled using **2** was subjected to incident photon-to-current efficiency (IPCE) measurements [Figure 7 (solid line)].

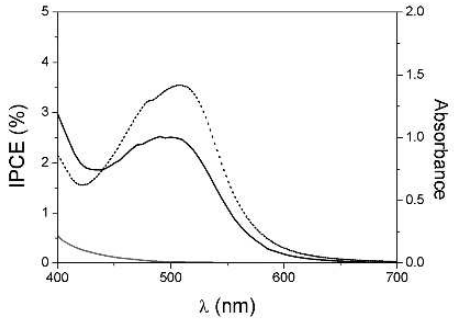

Figure 7. IPCE curves for DSSCs sensitized with **2** (solid line) and **3** (gray line) using I_2/I^- as mediator. Diffusive absorption spectrum (dotted line) of **2** on a TiO_2 electrode.

The experiments were performed using the I_3^-/I^- couple and chenodeoxycholic acid (CDA) as coadsorbate.[20] Comparison of the IPCE curve with the absorption spectrum of the chemisorbed dye [Figure 7 (dotted line)] revealed that the injection into the TiO_2 conduction band occurs indeed from the iron–pyridine MLCT state of the dye as clearly evidenced by the large band centered at 500 nm.

In particular, a 2.5% IPCE value was measured at these wavelengths. Whereas the grafted dye shows extinction due to absorbance and light scattering over the entire spectrum from 400 to 600 nm, the IPCE graph showed a dip in the 420–430 nm range in agreement with a reduced absorbance of **2** (Figure 3). The full IPCE action spectrum is in good agreement with the absorbance of the pure dye. By comparison, a DSSC sensitized with complex **3** did not show any electron injection [Figure 7 (gray line)] under the same conditions clearly underlining the effect of the carbene-based ligands. To the best of our knowledge this is the first example of the transfer of a significant amount of excited electrons into TiO_2 from an iron–carbene complex.

The current density (J)/voltage (V) curves obtained on a 0.36 cm^2 irradiated surface area under AM1.5 G (100 mW cm^{-2}) are reported in Figure 8 and the associated data are collected in Table 6.

Under these conditions, with dye **2** a good 0.68 fill factor (FF) was obtained along with an overall efficiency of 0.13%, a 0.41 mA cm^{-2} short-circuit photocurrent density (J_{SC}), and a reasonable open-circuit voltage (V_{OC}) of 457 mV. In agreement with the IPCE measurement, expectedly, **3** [see Figure 8 (gray line)] did not produce any photocurrent. This was also observed for a DSSC made of unsensitized TiO_2 (Table 6).

Under the same conditions, the well-known Ru dye N719 [*cis*-di(thiocyanato)bis(2,2′-bipyridyl-4,4′′-dicarboxylate)-ruthenium(II)][21] led to a 6.1% efficiency with similar fill factor. Such values, in full agreement with those generally obtained in the literature validate our DSSC fabrication

Job/Unit: I50142 /KAP1 Date: 13-04-15 15:25:18 Pages: 10

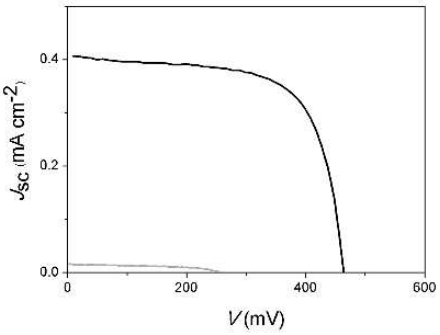

Figure 8. *J*/*V* curve and performance data of DSSC sensitized with **2** and **3** (gray line).

Table 6. Photovoltaic performance of DSSCs based on **2**, **3**, and N719.[a]

Dye	J_{SC} [mA cm^{-2}]	V_{oc} [mV]	*FF*	η/%	Dye load [μmol cm^{-2}][b]
2	0.41	457	0.68	0.13	0.09
3	0.016	250	0.50	0.01	0.05
N719	13.25	687	0.67	6.1	0.08
TiO_2	0.01	364	0.51	0.01	

[a] Measurements performed under AM 1.5 G irradiation (100 mW cm^{-2}), irradiated area: 0.36 cm^2 on TiO_2 layers (10–11 μm). Values obtained from at least three DSSCs for each dye. [b] Dye load calculated from absorbance data of the sensitized electrode. Values confirmed by desorption of dyes from TiO_2 under basic conditions.

process. Since the efficiency of the dye uptake by TiO_2 upon the impregnation process could also dramatically affect the performance, the dye load (Table 5), as well as the optimal impregnation time (see the Supporting Information) were determined from the absorption data of sensitized electrodes according to reported procedures.[22,23] As shown in Table 5, a similar dye load was obtained for both **2** and N719 (0.09 and 0.08 μmol cm^{-2}, respectively), which indicate the efficiency of the iron complex chemisorption at the semiconductor surface.

Despite an unexpectedly small short-circuit current density, the DSSC sensitized with **2** showed without any ambiguity that the novel complex **2** can inject electrons into the semiconductor conduction band. Its ground state can be readily regenerated by the I_2/I^- redox mediator, thus fully completing the normal electronic circuit of a DSSC.

Conclusion

In summary, we have prepared a novel iron(II) complex bearing two tridentate bis-carbene pyridine (C^N^C) ligands. The stabilization of its ^{3}MLCT state, clearly demonstrated by means of ultrafast photophysics, together with a concomitant destabilization of the MC state, entail the longest ^{3}MLCT state ever reported for an iron(II) complex. We have shown that the iron complex can sensitize the TiO_2 semiconductor in a laboratory DSSC, which leads to measurable photocurrent and power conversion efficiency. Beyond this proof of concept, work is in progress to investigate the origin of the weak injection efficiency by means of femtosecond transient spectroscopy on sensitized TiO_2 photoanodes and electrochemical impedance experiments to determine the electronic processes at play in the DSSC.

Experimental Section

Materials: Solvents and commercially available reagents were used as received. Thin-layer chromatography (TLC) was performed by using silica gel 60 F-254 (Merck) plates and visualized under UV light. Chromatographic purification was performed by using silica gel 60 (0.063–0.2 mm/70–230 mesh).

Instrumentation: ^{1}H and ^{13}C NMR spectra were recorded on DRX400 Bruker spectrometers at ambient temperature. The chemical shifts (δ) were calibrated by using either tetramethylsilane (TMS) or signals from the residual protons of the deuterated solvents and are reported in parts per million (ppm) from low to high field. High-resolution mass spectrometry (HRMS) data was obtained by using a Bruker micrOTOF-Q spectrometer. UV/Vis spectra were recorded in a 1 cm path-length quartz cell on a LAMBDA 1050 (Perkin Elmer) spectrophotometer. Cyclic voltammetry was performed on a Radiometer PST006 potentiostat using a conventional three-electrode cell. The saturated calomel electrode (SCE) was separated from the test compartment using a bridge tube. The solutions of studied complexes (0.2 mM) were purged with argon before each measurement. The test solution was acetonitrile containing 0.1 M Bu_4NPF_6 as supporting electrolyte. The working electrode was a vitreous carbon rod (1 cm^2) wire and the counter electrode was a 1 cm^2 Pt disc. After the measurement, ferrocene was added as the internal reference for calibration. All potentials were quoted versus a SCE. Under these conditions the redox potential of the couple Fc^+/Fc was found at 0.39 V. In all the experiments the scan rate was 100 mV s^{-1}.

{[2,6-Bis(3-methylimidazolium-1-yl)pyridine-4-carboxylic Acid]} Bishexafluorophosphate (4): This compound was prepared by modification of a reported procedure.[13] 2,6-Dibromopyridine-4-carboxylic acid (0.35 g, 1.24 mmol) and 1-methylimidazole (1 mL, 12.4 mmol) were heated at 150 °C without solvent overnight. After cooling, Et_2O (5 mL) was added and the resultant precipitate was filtered. The crude product was dissolved in a minimum amount of water and a saturated solution of KPF_6 in water (10 mL) was added. The solution was acidified to pH = 2 using diluted HNO_3. The solid was collected by filtration to afford **2** as a brownish solid (0.46 g, 65%). ^{1}H NMR (200 MHz, CD_3CN): δ = 9.52 (s, 2 H), 8.42 (s, 2 H), 8.30 (s, 2 H), 7.66 (s, 2 H), 4.04 (s, 6 H) ppm. ^{13}C NMR (50 MHz, CD_3CN): δ = 162.5, 146.4, 146.0, 135.3, 124.9, 119.3, 114.3, 36.5 ppm.

Synthesis of 2: KO*t*Bu (195 mg, 1.5 mmol) was added to a solution of ligand **4** (200 mg, 0.35 mmol) and $FeCl_2$ (22 mg, 0.175 mmol) in dry DMF. The reaction mixture was stirred at room temperature for 10 min and treated with diluted HNO_3 until pH = 2. The dark orange solution became pink-red. A saturated solution of aqueous KPF_6 was then added and a dark red solid precipitated. The solid was filtered, washed with water and diethyl ether, and dried under vacuum yielding **2** (89 mg, 56%). ^{1}H NMR (400Mz, CD_3CN): δ = 8.30 (s, 4 H), 8.16 (d, J = 2.3 Hz, 4 H), 7.01 (d, J = 2.3 Hz, 4 H), 2.5 (s, 12 H) ppm. ^{13}C NMR (100 MHz, CD_3CN): δ = 199.8, 165.2, 155.3, 140.7, 127.8, 105.8, 35.6 ppm. HRMS (ESI): calcd. for $C_{28}H_{26}FeN_{10}O_4P_2F_{12}$ [M − 2 PF_6]$^{2+}$ 311.0752; found 311.0738.

Job/Unit: I50142 /KAP1 Date: 13-04-15 15:25:18 Pages: 10

Synthesis of 3: $FeCl_2$ (106 mg, 0.84 mmol) in water (50 mL) was added to a solution of 4′-(2-furyl)-2,2′:6′,2″-terpyridine (**5**)[15] (0.5 g, 1.67 mmol) in acetone (50 mL). The reaction mixture was stirred for 10 min until a clear dark purple solution was obtained. $KMnO_4$ (2 g, 13 mmol) was then added and the reaction was stirred overnight at room temperature. The formed MnO_2 precipitate was removed by filtration. A saturated aqueous KPF_6 solution (10 mL) was added and the solution was acidified until pH = 2 by adding diluted HNO_3. The dark purple solid was finally collected by filtration, washed with water, and dried under vacuum yielding FeTpyCOOH (0.625 g, 83%). ^{1}H NMR (400 MHz, CD_3CN): δ = 9.40 (s, 4 H), 8.68 (d, J = 8.1 Hz, 4 H), 7.90 (dt, J = 8.1, 4.6 Hz, 4 H), 7.08 (2×d, J = 4.6 Hz, 8 H) ppm. ^{13}C NMR (100 MHz, CD_3CN): δ = 165.6, 162.0, 158.3, 154.0, 140.2, 128.8, 125.8, 123.9 ppm. HRMS (ESI) calcd. for $C_{32}H_{22}FeN_6O_4P_2F_{12}$ [M – 2 PF_6]$^{2+}$ 305.0521; found 305.0520.

DSSC Fabrication and Photovoltaic Measurements: The fluorine-doped tin oxide (FTO) glass plates (TEC Glass-TEC 8, solar 2.3 mm thickness), TiO_2 paste, electrolyte (AN50), and Pt paste (Platisol T/SP) were purchased from Salaronix. FTO glass plates were cleaned in a detergent solution using an ultrasonic bath for 30 min and then rinsed with water and ethanol. Next, the plates were immersed into a 40 mM aqueous $TiCl_4$ at 70 °C for 30 min in a chamber. After being washed with deionized water and fully rinsed with ethanol, a transparent nanocrystalline layer was prepared on the FTO glass plates by using a screen-printing technique. TiO_2 paste was dried for 5 min at 150 °C. The TiO_2 electrodes were finally heated under an air atmosphere at 450 °C for 30 min. The TiO_2 electrodes were treated again with $TiCl_4$ at 70 °C for 30 min and sintered at 450 °C for 30 min. A TiO_2 film comprising a 10–11 μm-thick transparent layer was obtained as checked using a profilometer. The prepared TiO_2 film on the FTO electrode was immersed in 0.5 mM acetonitrile dye solution containing chenodeoxycholic acid (0.1 mM) at room temperature overnight and finally quickly rinsed with acetonitrile before assembly. FTO plates for the counter electrodes were cleaned in an ultrasonic bath in acetone. The counter electrodes were prepared by screen-printing of Platisol onto the FTO-coated glass substrate and then heated at 450 °C for 30 min under air atmosphere. The platinum counter electrodes and the dye-adsorbed TiO_2 electrodes were assembled into a sealed sandwich-type cell by heating at 80 °C using a hot-melt film (30 μm spacer Surlyn) between the electrodes. A drop of AN50 solution was placed in the drilled hole of the counter electrode. Finally, the hole was sealed using additional Surlyn and a cover glass (0.1 mm thickness). The photovoltaic characterization of the Fe–carbene-sensitized TiO_2 cells was obtained using two complementary techniques. The irradiated surface was 0.36 cm^2. The spectral response was determined by measuring the wavelength dependence of the incident photon-to-current conversion efficiency (IPCE) using light from an Osram 300 W xenon lamp coupled to a Newport monochromator (Oriel Cornerstone 260). Photocurrents were measured under short-circuit conditions (DC mode) using a Newport 1936R optical power meter. Incident irradiance was measured with a 1 cm^2 calibrated silicon photodiode. For J/V measurements we used the same lamp (Osram 300 W xenon) with an AM 1.5 G filter solar spectrum in the 350–900 nm domain and a power of 100 mW cm^{-2}. Incident irradiance was measured with a ISO-Tech ISM410 instrument. The current–voltage characteristics were determined by applying an external potential bias to the cell using a radiometer potentiostat (PGP 201) sweeping the potential with a scan rate of 10 mV s^{-1}.

Photophysics: In our setup, the 800 nm output of a 5 kHz regenerative Ti:sapphire amplifier (Amplitude Technologies) was used to generate excitation pulses by a pumping commercial collinear optical parametric amplifier (TOPAS, Light Conversion) followed by frequency doubling to produce approximately 60 fs pulses at 515 nm. Broadband white-light probe pulses were obtained by focusing the approximately 30 fs 800 nm pulses onto a 2 mm-thick CaF_2 crystal. The 300–700 nm region was measured in two separate sets of data with a Peltier-cooled high-speed charge-coupled device (CCD) mounted at the output of a 25 cm focal-length spectrometer (resolution 3 nm). The pump and probe pulses were focused on 80×80 μm^2 and 40×40 μm^2, respectively. The pump–pulse intensity was carefully reduced so as to work in a regime of linear signal response. The relative linear polarizations of pump and probe were set at the magic angle (54.7°). The concentration of the complexes dissolved in MeCN was adjusted to an absorbance of 0.45 mm^{-1} at the peak of the S0–S1 transition. The 1 mm path-length quartz cell containing the solution was placed on a loud speaker with orthogonal vibration at 10 Hz to avoid degradation (see Figure S3 in the Supporting Information) and make sure that the sample remains intact during the experiment. All transient absorption data presented in this paper are processed following the procedure described in the literature[24] to compensate for group velocity dispersion and define time zero within +/–20 fs over the entire spectral range. The Raman response from the solvent and cross-phase modulation artifacts were measured in an MeCN-only containing flow cell. In order to retain only the solute differential transient absorption in the raw data, the solvent response is reduced by an appropriate weighting coefficient accounting for the solute absorption and subtracted. Quantitative analysis methods are described in the Supporting Information. Kinetic traces in Figure 5 were fitted by Equation (1), which represents the sequential model ^{1}MLCT $\overset{\tau_1}{\rightarrow}$ ^{3}MLCT $\overset{\tau_2}{\rightarrow}$ ^{1}A$_1$ for complexes **1** and **2** and ^{1}MLCT $\overset{\tau_1}{\rightarrow}$ ^{3}MLCT $\rightarrow$ ^{5}T$_2$ $\overset{\tau_3}{\rightarrow}$ ^{1}A$_1$ for **3**

$$F(t) = \left|\sum_{2,3} a_i e^{-t/\tau_i}\right| \otimes IRF(t) \quad (1)$$

The multiexponential is convoluted by the temporal instrument response function (IRF), assumed to be a Gaussian, centered at t = 0, with 60 fs full width at half-maximum (FWHM). Individual fits are shown in Figure 5 and in the Supporting Information for **3**.

Computations: All quantum chemistry calculations were performed by using the Gaussian09 suite of programs. The ground-state geometry was optimized at the DFT level by using the B3LYP exchange correlation functional. The LANL2DZ basis set was used for the iron atom, whereas carbon, hydrogen, and nitrogen were described by using the 6-31+G(d,p) basis set. Excited states were obtained as vertical transitions from the equilibrium geometry using TD-DFT to assess the excited-state energy. In this case we used the HCTCH exchange correlation functional, and all the atoms were represented by using the 6-31+G(d,p) basis set. Note that these conditions have been chosen as the ones that better reproduce the lowest energy part of the absorption spectrum relative to the experimental one. For TD-DFT we computed 30 excited states and vertical transition spectra were convoluted with Gaussian functions of fixed-width at a half length of 0.3 eV to simulate the vibrational structure and better compare them to the experimental results. In all the calculations solvent effects were taken into account by using the polarizable continuum model (PCM); more specifically, acetonitrile was considered throughout. The density reorganization in the excited states was analyzed in terms of NTOs[16] by using a locally produced and free downloadable code NancyEX (see www.nancyex.sourceforge.net/).

Job/Unit: I50142 /KAP1 Date: 13-04-15 15:25:18 Pages: 10

Acknowledgments

Support from the Université de Lorraine and the Centre National de la Recherche Scientifique (CNRS) is gratefully acknowledged. IS2-SAS is also thanked for grants to T. D. and T. E. The authors thank S. Parant for absorption spectroscopy and photovoltaic measurements. A. M. thanks the CNRS for the funding of the "Chaire d'excellence" program.

[1] a) M. K. Nazeeruddin, A. Kay, L. Rodicio, R. Humphry-Baker, E. Muller, P. Liska, N. Vlachopoulos, M. Grätzel, *J. Am. Chem. Soc.* **1993**, *115*, 6382–6390; b) M. K. Nazeeruddin, P. Pechy, T. Renouard, S. M. Zakeeruddin, R. Humphry-Baker, P. Comte, P. Liska, L. Cevey, E. Costa, V. Shklover, L. Spiccia, G. B. Deacon, C. A. Bignozzi, M. Grätzel, *J. Am. Chem. Soc.* **2001**, *123*, 1613–1624.

[2] T. J. Meyer, *Pure Appl. Chem.* **1986**, *58*, 1193–1206.

[3] a) I. M. Dixon, F. Alary, M. Boggio-Pasqua, J. L. Heully, *Inorg. Chem.* **2013**, *52*, 13369–13374; b) I. M. Dixon, S. Khan, F. Alary, M. Boggio-Pasqua, J.-L. Heully, *Dalton Trans.* **2014**, *43*, 15898–15905; c) S. E. Canton, X. Zhang, M. L. Lawson Daku, Y. Liu, J. Zhang, S. Alvarez, *J. Phys. Chem. C* **2015**, *119*, 3322–3330; d) S. Mukherjee, D. N. Bowman, E. Jakubikova, *Inorg. Chem.* **2015**, *54*, 560–569; e) Y. Liu, K. S. Kjærl, L. A. Fredin, P. Chábera, T. Harlang, S. E. Canton, S. Lidin, J. Zhang, R. Lomoth, K.-E. Bergquist, P. Persson, K. Wärnmark, V. Sundström, *Chem. Eur. J.* **2015**, *21*, 3628–3639.

[4] B. O'Regan, M. Grätzel, *Nature* **1991**, *353*, 737–740.

[5] a) A. Hauser, *Top. Curr. Chem.* **2004**, *234*, 155–198; b) J. E. Monat, J. K. McCusker, *J. Am. Chem. Soc.* **2000**, *122*, 4092–4097; c) W. Gawelda, A. Cannizzo, V.-T. Pham, F. van Mourik, Ch. Bressler, M. Chergui, *J. Am. Chem. Soc.* **2007**, *129*, 8199–8206; d) C. Consani, M. Prémont-Schwarz, A. El-Nahhas, Ch. Bressler, F. van Mourik, A. Cannizzo, M. Chergui, *Angew. Chem. Int. Ed.* **2009**, *48*, 7184–7187; *Angew. Chem.* **2009**, *121*, 7320.

[6] a) J. B. Asbury, R. J. Ellingson, H. N. Ghosh, S. Ferrere, A. J. Nozik, T. Q. Lian, *J. Phys. Chem. B* **1999**, *103*, 3110–3119; b) G. Ramakrishna, D. A. Jose, D. K. Kumar, A. Das, D. K. Palit, H. N. Ghosh, *J. Phys. Chem. B* **2005**, *109*, 15445–15453; c) G. Benko, J. Kallioinen, J. E. I. Korppi-Tommola, A. P. Yartsev, V. Sundstrom, *J. Am. Chem. Soc.* **2002**, *124*, 489–493; d) D. Kuang, S. Ito, B. Wenger, C. Klein, J.-E. Moser, R. Humphry-Baker, S. M. Zakeeruddin, M. Grätzel, *J. Am. Chem. Soc.* **2006**, *128*, 4146–4154.

[7] D. Bowman, J. H. Blew, T. Tsuchiya, E. Jakubikova, *Inorg. Chem.* **2013**, *52*, 8621–8628.

[8] W. Zhang, R. Alonso-Mori, U. Bergmann, Ch. Bressler, M. Chollet, A. Galler, W. Gawelda, R. G. Radt, R. W. Hartsock, T. Kroll, K. S. Kjær, K. Kubiček, H. T. Lemke, H. W. Liang, D. A. Meyer, M. M. Nielsen, C. Purser, J. S. Robinson, E. I. Solomon, Z. Sun, D. Sokaras, T. B. van Driel, G. Vankó, T.-C. Weng, D. Zhu, K. J. Gaffney, *Nature* **2014**, *509*, 345–348.

[9] a) M. S. Lowry, S. Bernhard, *Chem. Eur. J.* **2006**, *12*, 7970–7977; b) D. V. Scaltrito, D. W. Thompson, J. A. O'Challagan, G. J. Meyer, *Coord. Chem. Rev.* **2000**, *208*, 243–266; c) W. Wu, J. Sun, S. Ji, W. Wu, J. Zhao, H. Guo, *Dalton Trans.* **2011**, *40*, 11550–11561; d) A. Breinvogel, M. Meister, C. Förster, F. Laquai, K. Heinze, *Chem. Eur. J.* **2013**, *19*, 3745–13760.

[10] L. A. Fredin, M. Pápai, E. Rozsályi, G. Vankó, K. Wärnmark, V. Sundström, P. Persson, *J. Phys. Chem. Lett.* **2014**, *5*, 2066–2071.

[11] a) S. Ferrere, B. A. Cregg, *J. Am. Chem. Soc.* **1998**, *120*, 843–844; b) S. Ferrere, *Chem. Mater.* **2000**, *12*, 1083–1089.

[12] a) Y. Liu, T. Harlang, S. Canton, S. Chabera, K. Suarez Alcantara, A. Fleckhaus, E. Göransson, E. Corani, A. Lomoth, R. Sundström, V. K. Wärnmark, *Chem. Commun.* **2013**, *49*, 6412–6414.

[13] T. Duchanois, T. Etienne, M. Beley, X. Assfeld, E. A. Perpète, A. Monari, P. C. Gros, *Eur. J. Inorg. Chem.* **2014**, *23*, 3747–3753.

[14] H.-J. Park, K. H. Kim, S. Y. Choi, H.-M. Kim, W. I. Lee, Y. K. Kang, Y. K. Chung, *Inorg. Chem.* **2010**, *49*, 7340–7352.

[15] a) M. Beley, J. Husson, G. Kirsch, *Tetrahedron Lett.* **2003**, *44*, 1767–1770; b) C. P. Berlinguette, D. G. Brown, N. Sanguantrakun, U. S. Schubert, B. Schulze, *J. Am. Chem. Soc.* **2012**, *134*, 12354–12357.

[16] a) M. Graetzel, *Inorg. Chem.* **2005**, *44*, 6841–6851; b) Z. Zhang, F. Liu, Q. L. Huang, G. Zhou, Z. S. Wang, *J. Phys. Chem. C* **2011**, *115*, 12665–12672.

[17] a) J.-D. Chai, M. Head-Gordon, *Phys. Chem. Chem. Phys.* **2008**, *10*, 6615–6620; b) A. Monari, T. Very, J.-L. Rivail, X. Assfeld, *Comput. Theor. Chem.* **2012**, *990*, 119–125; c) T. Etienne, X. Assfeld, A. Monari, *J. Chem. Theory Comput.* **2014**, *10*, 3895–3905; d) T. Etienne, X. Assfeld, A. Monari, *J. Chem. Theory Comput.* **2014**, *10*, 3906–3914; e) T. Etienne, *J. Chem. Theory Comput.* **2015**, DOI: 10.1021/ct501163b.

[18] a) F. Gao, Y. Wang, D. Shi, J. Zhang, M. Wang, X. Jing, R. Humprey-Baker, P. Wang, S. M. Zakeeruddin, M. Grätzel, *J. Am. Chem. Soc.* **2008**, *130*, 10720–10728; b) Y. Cao, Y. Bai, Q. Yu, Y. Cheng, S. Liu, D. Shi, F. Gao, P. Wang, *J. Phys. Chem. C* **2009**, 6290–6297; c) A. Monari, X. Assfeld, M. Beley, P. C. Gros, *J. Phys. Chem. A* **2011**, *115*, 3596–3603.

[19] A. Cannizzo, C. J. Milne, C. Consani, W. Gawelda, Ch. Bressler, F. van Mourik, M. Chergui, *Coord. Chem. Rev.* **2010**, *254*, 2677–2686.

[20] X. Ren, Q. Feng, G. Zhou, C.-H. Huang, Z.-S. Wang, *J. Phys. Chem. C* **2010**, *114*, 7190–7195.

[21] M. K. Nazeeruddin, A. Kay, L. Rodicio, R. Humphry-Baker, E. Muller, P. Liska, N. Vlachopoulos, M. Grätzel, *J. Am. Chem. Soc.* **1993**, *115*, 6382–6390.

[22] E. Dell'Orto, L. Raimondo, A. Sassella, A. Abbotto, *J. Mater. Chem.* **2012**, *22*, 11364–11369.

[23] D. P. Hagberg, T. Marinado, K. M. Karlsson, K. Nonomura, P. Qin, G. Boschloo, T. Brinck, A. Hagfeldt, L. Sun, *J. Org. Chem.* **2007**, *72*, 9550–9556.

[24] J. Briand, J. Réhault, O. Bräm, J. Léonard, J. Helbing, A. Cannizzo, V. Zanirato, M. Chergui, M. Olivucci, S. Haacke, *Phys. Chem. Chem. Phys.* **2010**, *12*, 3178–3187.

Received: February 10, 2015
Published Online: ■

PCCP

PAPER

View Article Online
View Journal | View Issue

Cite this: *Phys. Chem. Chem. Phys.*, 2016, **18**, 12550

A new record excited state ^{3}MLCT lifetime for metalorganic iron(II) complexes†

Li Liu,[a] Thibaut Duchanois,[b] Thibaud Etienne,‡[c] Antonio Monari,[c] Marc Beley,[b] Xavier Assfeld,[c] Stefan Haacke*[a] and Philippe C. Gros*[b]

Received 1st March 2016,
Accepted 5th April 2016

DOI: 10.1039/c6cp01418f

www.rsc.org/pccp

Herein we report the synthesis and time-resolved spectroscopic characterization of a homoleptic Fe(II) complex exhibiting a record ^{3}MLCT lifetime of 26 ps promoted by benzimidazolylidene-based ligands. Time dependent density functional molecular modeling of the triplet excited state manifold clearly reveals that, at equilibrium geometries, the lowest ^{3}MC state lies higher in energy than the lowest ^{3}MLCT one. This unprecedented energetic reversal in a series of iron complexes, with the stabilization of the charge-transfer state, opens up new perspectives towards iron-made excitonic and photonic devices, hampering the deactivation of the excitation *via* metal centered channels.

1. Introduction

The exploitation of the photophysical and photochemical properties of transition metal complexes (Pt, Ir, Ru) have been the focus of much attention due to the ability of these compounds to promote energy transfer from their electronic excited states.[1] Platinoid metal complexes have been the most used due to their ideal photophysical properties spurring their implementation in OLED[2] or DSSC[3] devices with high efficiency and stability. However these strategic metals are expensive, scarce and can exhibit some degree of toxicity. As a consequence, the development of light-responsive compounds from cheap and environmentally benign metal-complexes is critical to preserve natural resources and reduce the environmental impact of this potential branch of chemical industry. In this context iron-based complexes can be considered as promising candidates for such a transition.

However, the replacement of ruthenium by iron is extremely challenging. Due to a smaller ligand field splitting, Fe–pyridine complexes are rather known as photoinduced spin-transition materials,[4] and are used as such in the research area of molecular magnetism.[5,6] The low-to-high spin transition is due to an ultrafast non-radiative deactivation of the ^{1,3}MLCT states into the low-energy metal-centered quintuplet $^5T_2$,[7] cutting short on applications of Fe–pyridine requiring higher free energies.

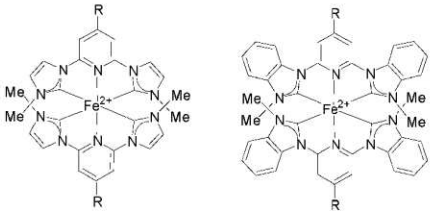

Fig. 1 Chemical structures of iron complexes, the counter anion is PF_6^-.

Recently it has been reported that the use of N-heterocyclic carbene (NHC) ligands in complex **C1** (Fig. 1) can prolong the ^{3}MLCT lifetime (9 ps).[8] This was rationalized by quantum chemical calculations showing that in these compounds the ^{3}MC and $^5T_2$ states are up-shifted in energy, but still below the ^{3}MLCT. The introduction of σ-donating carbene ligands coordinating Fe is held responsible for these significant changes in the electronic structure. A heteroleptic Fe(II) complex featuring mesoionic triazolylidene bidentate ligands and a ^{3}MLCT lifetime as long as 13 ps while also promoting the red-shift of the absorption band was also reported.[9] However the coordination by both bis-carbene ligands resulted in an extremely low oxidation potential for the Fe^{II}/Fe^{III} couple (−0.35 V *vs.* Fc/Fc^+) prohibiting the possible ground state regeneration by usual redox mediators (−0.2 V) in a photoelectrochemical application.

Our group recently improved the ^{3}MLCT lifetime up to a record value of 16.5 ps from a homoleptic carbene-based complex

[a] *IPCMS & Labex NIE, Université de Strasbourg & CNRS, Rue du Loess, 67034 Strasbourg Cedex, France. E-mail: stefan.haacke@ipcms.unistra.fr*
[b] *Université de Lorraine–Nancy & CNRS, HecRIn, SRSMC, Boulevard des Aiguillettes, 54506 Vandoeuvre-Lès-Nancy, France. E-mail: philippe.gros@univ-lorraine.fr*
[c] *Université de Lorraine–Nancy & CNRS, TMS, SRSMC, Boulevard des Aiguillettes, 54506 Vandoeuvre-Lès-Nancy, France*

† Electronic supplementary information (ESI) available: Compound characterization, computational methods, photophysics details and additional data. See DOI: 10.1039/c6cp01418f

‡ Current address: Computational Laboratory for Hybrid/Organic Photovoltaics (CLHYO), CNR-ISTM, via Elce di Sotto, I-06123, Perugia, Italy.

C2 bearing carboxylic groups (Fig. 1).[10] In addition, the photocurrent generation in a dye-sensitized solar cell (DSSC) fabricated from this sensitizer was demonstrated for the first time, albeit with a low power conversion efficiency. Very recently, the Wärnmark group working on the same complex[11] published an important additive to this work by demonstrating that injection into the TiO_2 semiconductor can occur efficiently from the ^{3}MLCT state.

Thus the improvement of ^{3}MLCT lifetime in iron complexes is a topic of high interest for their further development as photosensitizers applicable in photochemical energy conversion processes, and organic electronics at large.

Starting from the idea that an increase of the delocalization of the MLCT frontier orbitals towards the periphery of the organic ligand should contribute to better stabilization of the ^{3}MLCT state, the new complexes **C3** and **C4** have been designed (Fig. 1) where iron was coordinated by benzimidazolylidene-based ligands. Herein we report the synthesis and characterization of these new complexes and a new record ^{3}MLCT lifetime of 26 ps.

2. Results and discussion

2.1. Synthesis

The synthesis of complexes **C3** and **C4** required the preparation of, respectively, imidazolium salts **3** and **4** that were obtained by controlled methylation of compounds **1**[14] and **2**.[15] The coordination was accomplished by the reaction of the appropriate imidazolium salt with $FeCl_2$ in DMF in the presence of *t*-BuOK as a deprotonating agent affording the targeted complexes **C3** and **C4** (Scheme 1). Complexes **C1**[8] and **C2**[10] were also prepared for comparison purposes.

2.2. Electronic and electrochemical properties

The complexes were characterized by UV-vis spectroscopy (Fig. 2) and electrochemistry (Table 1).

For all the complexes, the absorption spectra are composed of three bands comprising individual electronic transitions of different nature. The intense band near 300–350 nm corresponds to π–π^* transitions in the ligands. These bands are expectedly particularly intense in cases of **C3** and **C4** due to the phenyl rings of benzimidazolylidene (BIm) moieties.

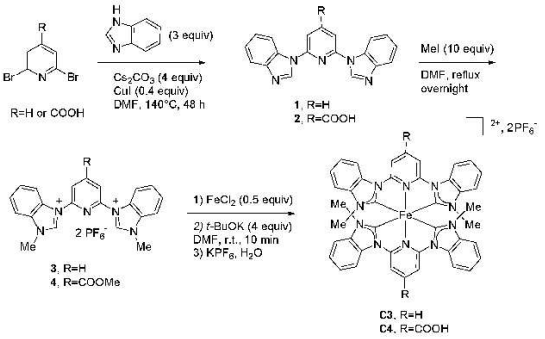

Scheme 1 Synthesis of complexes **C3** and **C4**.

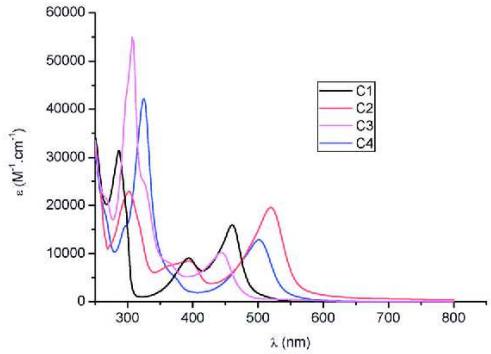

Fig. 2 Absorption spectra of complexes in acetonitrile.

Table 1 Photophysical and electrochemical properties of complexes

	$\lambda_{abs\text{-}max}$[a] (nm) (ε(M^{-1} cm^{-1}))	E_{ox} (Fe^{III}/Fe^{II})[b] (V/SCE)	E_{red1} (V/SCE)	ΔE[c] (eV)
C1	287 (31 400) 393 (9000) 460 (15 900)	0.80 (rev.)	−1.95 (irrev.)	2.75
C2	302 (19 000) 394 (7000) 520 (16 200)	0.85 (rev.)	−1.35 (irrev.)	2.20
C3	310 (55 000) 360 (9000) 440 (12 500)	1.04 (rev.)	−1.80 (irrev.)	2.84
C4	325 (42 200) 370 (5000) 501 (12 800)	1.13 (rev.)	−1.23 (irrev.)	2.36

[a] Measured in CH_3CN at 25 °C. [b] First oxidation potential. Potentials are quoted *vs.* SCE. Under these conditions, $E_{1/2(Fc+/Fc)}$ = 0.39 V/SCE. Recorded in CH_3CN using $Bu_4N^+PF_6^-$ (0.1 M) as a supporting electrolyte at 100 mV s^{-1}. [c] Electrochemical band gap ($\Delta E = E_{ox} - E_{red1}$).

At longer wavelengths, the complexes exhibit two distinct band families corresponding to MLCT transitions that are subjected to significant shifts and a change in the shape as a function of the ligands. The bands in the 360–390 nm range are related to the carbene–Fe MLCT transition[10] that is strongly affected in energy by switching from imidazolylidene (Im) to benzimidazolylidene (BIm). Indeed the absorption maxima for complexes **C3** and **C4** are blue-shifted by 20 nm compared with those of **C1** and **C2**.

The same observation can be made for the MLCT bands at lower energy in the 450–600 nm range involving the central pyridine ring that are blue-shifted by 60 nm in BIm containing complexes. This blue shift is clearly in agreement with the electron-accepting effect of the phenyl ring in BIm and in line with cyclic voltammetry measurements (Table 1) showing an increase of the Fe^{II}/Fe^{III} oxidation potential going from **C1** (0.8 V) and **C2** (0.85 V) complexes to **C3** (1.04 V) and **C4** (1.13 V).

Finally, as already observed for the Im-based complex **C2**,[10] the functionalization of the central pyridine nucleus with the carboxylic groups promotes a notable red-shift of the band at the lowest energy in BIm-based complexes moving from 440 to 500 nm, *i.e.* from **C3** to **C4** respectively.

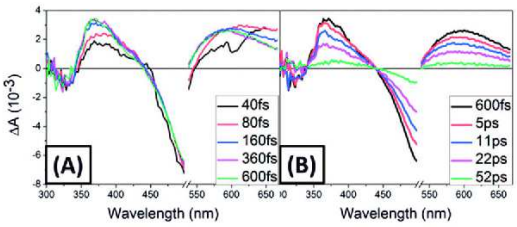

Fig. 3 Selected transient differential spectra of **C4** in MeCN excited at 515 nm. (A) Time delays <600 fs and (B) time range <52 ps. After the initial blue-shift in the first 200–300 fs, the ESA bands do not evolve spectrally, but decay until 100 ps. A 30 nm region around the excitation wavelength is disregarded due to pump scattering.

2.3. Photophysics

In order to get further insights into the impact of the BIm ligand on the photophysical properties of the complexes, ultrafast photophysics of **C1**–**C4** were investigated in acetonitrile using transient absorption spectroscopy (TA).

The TA data reveal that the excited state processes happen to follow the same scheme for all iron complexes (data not shown). As an example, Fig. 3 shows a selection of transient differential spectra of **C4** in acetonitrile after excitation at 515 nm within the first 600 fs (Fig. 3A) and up to 52 ps (Fig. 3B).

The intense negative signals in the 450–520 nm range and at $\lambda < 350$ nm are due to ground state bleaching (GSB). In the visible domain, the GSB band coincides perfectly with the ground state absorption maximum (Fig. 2). The positive bands in the 350–450 nm region and above 550 nm reveal two excited state absorptions (ESA). Within the first 200 fs, both ESA bands display a 20–50 nm blue-shift, and their shapes change significantly between spectra until 160 fs. After 600 fs, the differential spectra decay until 100 ps without a noticeable spectral shift.

The long-lived spectral feature with two ESA bands is very similar to the ones reported for the ^{3}MLCT states of **C1**[8] and **C2**[10] in MeCN. The spectra reported in Fig. 3B are different from the characteristic ESA of the $^5T_2$ quintuplet state observed, for example in Fe(tpy)$_2$, featuring a 10 nm narrow ESA in the near-UV region and zero absorption in the red part of the spectrum.[8]

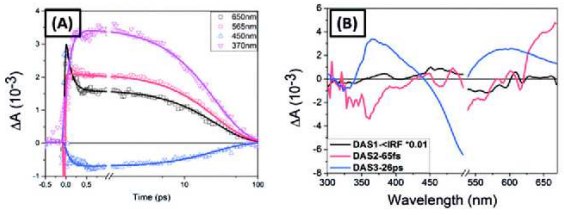

Fig. 4 (A) Kinetic traces (open symbol) of **C4** with their fits (solid lines) at characteristic wavelengths and (B) decay-associated difference spectra generated by global analysis using one Gaussian and two exponential functions. ^{3}MLCT relaxes to S_0 with 27 ps lifetime as shown by the simultaneous recovery of ESA and GSB. At <500 fs, the fast component with 65 fs lifetime is attributed to the relaxation of ^{1}MLCT to ^{3}MLCT and the thermalization of ^{3}MCLT.

Fig. 4A shows kinetic traces at characteristic wavelengths (651 nm black, 556 nm red, 449 nm blue and 371 nm pink) with their fits (solid lines). The spectral blue-shift is characterized by a fast initial decay at 650 nm and a slow rise at 556 nm and 449 nm in the first 0.5 ps.

Note that both ESA and GSB traces decay with the same time constant, *i.e.* the excited state decay directly fills the ground state, as already reported for other imidazole-based iron complexes.[8,10]

After correction of chirp and solvent contributions, we apply singular value decomposition (SVD) of data in order to filter the spectral and temporal components that are above the noise level. These N components, $N = 5$ in our case, are retained for global analysis (GA). All N traces are fitted simultaneously by a function with same time constants (see ESI† for details).

Since fast components are very close to the instrument response function (IRF, 60 fs), the first fitting component is chosen as Gaussian and followed by a bi-exponential function. The decay-associated differential spectra (DADS) with their lifetimes are shown in Fig. 4B. DADS3 shows the spectral feature of ^{3}MLCT with two ESA bands, as identified in the raw data. The fit gives a 26 ps lifetime for the ^{3}MLCT state.

In addition, the fitting suggests two sub-100 fs components. The DADS related to the IRF-related Gaussian function is most likely related to spurious, non-corrected solvent response. The 65 fs-DADS is an approximation to the above described spectral blue-shift of ESA observed within the first 200 fs.

The above-discussed spectral and temporal features combined with the lifetime determination by GA allow defining the following excited state reaction scheme for **C4**:

$$^1\text{MLCT}^+ \xrightarrow{<\text{IRF}} \begin{cases} ^1\text{MLCT} \\ ^3\text{MLCT}^+ \end{cases} \xrightarrow{65\text{ fs}} {}^3\text{MLCT} \xrightarrow{26\text{ ps}} S_0$$

The reaction starts with a "hot" ^{1}MLCT$^+$ state since the transition is excited with excess energy, above the 0–0 energy of the GS–^{1}MLCT transition. It relaxes on time scales faster than 50 fs (instrument response function, IRF) on the ^{1}MLCT surface and undergoes an ultrafast intersystem crossing into the vibrationally excited manifold in ^{3}MLCT.[7d] An effective lifetime of 65–100 fs is associated with this thermalization process (see below). The vibrationally relaxed ^{3}MLCT state recombines non-radiatively within 26 ps in **C4**.

The three other complexes were studied by TA spectroscopy under identical conditions (low excitation density, similar GSB levels). The spectral evolution is very similar to the one shown in Fig. 4, with a double ESA structure, characteristic of the ^{3}MLCT states[10] dominating the differential absorption for delay times >500 fs. The SVD traces are well described by the same kinetic fit function as **C4**, but with variations in the lifetimes.

Kinetic traces clearly showed a notable ^{3}MLCT lifetime improvement switching from Im to BIm-based ligands without and with the acid group, respectively, in Fig. 5A and B. The ESA and GSB kinetic traces have been normalized at 1 ps, after the initial thermalization period, to facilitate a comparison with the slower ^{3}MLCT decay (solid black lines).

Table 2 presents the excited state lifetimes obtained by the GA as described above for all the complexes. As shown, **C3** has a

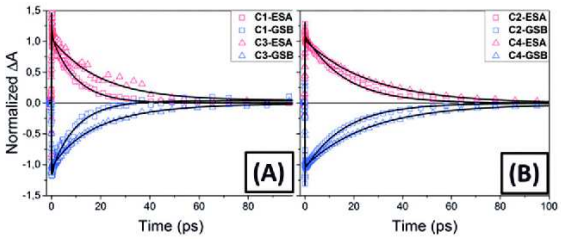

Fig. 5 Kinetic traces of ESA decay (red) and GSB (blue) with their fits (solid black lines), normalized at 1 ps for (A) **C1** and **C3** and (B) **C2** and **C4**. The BIm-ligand extends the ^{3}MLCT lifetime with and without the –COOH group.

Table 2 Excited state lifetimes for all iron complexes investigated by global analysis

Complex	^{1}MLCT (fs)	$(^3\text{MLCT})^*$ (fs)	^{3}MLCT (ps)
C1	50 ± 1	550 ± 50	10 ± 0.2
C2	20 < IRF	130 ± 40	16.5 ± 0.7
C3	25 < IRF	260 ± 8	16.4 ± 0.4
C4	15 < IRF	65 ± 10	26 ± 1

considerably increased ^{3}MLCT lifetime (16.4 ps) compared with **C1** (10 ps) clearly evidencing the positive effect of the BIm ligand, and **C4** benefiting from the carboxylic acid groups has the longest ^{3}MLCT lifetime (26 ps) ever reported for a FeNHC complex in solution. As a general trend, the BIm ligand prolonged the ^{3}MLCT lifetimes by more than 60%.

2.4. Computational studies

The new dyes have been analyzed by means of density functional theory (DFT) and time-dependent DFT (TD-DFT) calculations. Solvent (acetonitrile) effects have been taken into account using a polarizable continuum method. Firstly, the most relevant singlet excited states responsible for the absorption spectrum have been characterized by means of natural transition orbitals (NTO),[12] **C4**'s NTOs are presented in Table 3, while the ones of **C2** dye can be found in our previous work.[10]

For the reader's convenience we remind that NTOs can be considered as the optimal orbitals to describe an electronic transition in the TD-DFT formalism. In contrast to the Kohn–Sham molecular orbital basis, with which many occupied-virtual orbital couples are required to describe an electronic transition, the NTO basis generally provides only one (or at maximum two) couple of orbitals to entirely represent all the physics underlying the transition.

As it was the case for the **C2** dye[10] the low energy portion of the spectrum of **C4** is dominated by MLCT transitions. In particular for the lowest transition the density is displaced from the iron atom to both the ligands and particularly in the pyridyl moiety. A significant density accumulation on the carbonyl unit is also observed; hence charge injection into a semiconductor like TiO_2 should in principle be possible, since the molecules are grafted onto it through the carbonyl end. Remarkably and because of the

Table 3 NTO isodensity surface in **C4**[a]

λ (nm) (state number)	f[b]	s*s[c]	oNTO	vNTO
532 (#5)	0.3	0.570		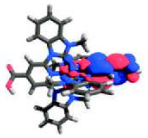
		0.413	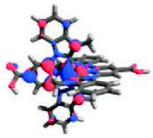	
433 (#9)	0.09	0.818		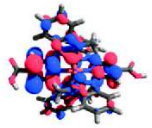

[a] Level of theory: The HCTCH exchange correlation functional and the 6-31+G(d,p) basis set for all the atoms were used. [b] Oscillator strength (a.u.). [c] Weight of the NTO couples.

Table 4 Adiabatic energy difference between the ^{3}MLCT and ^{3}MC states of **C2** and **C4** in eV

Complex	$E^{^3\text{MLCT}} - E^{^3\text{MC}}$ (eV)
C2	−0.08
C4	0.12

symmetry of the complex the charge is almost equally transferred on both ligands.

In order to rationalize the photophysics of the most relevant dyes, we relaxed the geometry of the lowest ^{3}MLCT and ^{3}MC states for **C2** and **C4** dyes (Table 4). This means that we let the molecule evolve structurally into the respective potential energy minimum.

As shown in Table 4, while the two states are almost degenerate (ΔE = −0.08 eV) in the case of **C2**, the ^{3}MLCT state is found better stabilized than the ^{3}MC state in **C4** (ΔE = 0.12 eV). This is the first example of such energetic reversal for an iron complex.[13] Although the energy difference is still quite low, such that both ^{3}MLCT and ^{3}MC states can be thermally populated, this observation may rationalize the longer lifetime of the **C4** complex. Indeed the photophysical channel leading to the ^{3}MC population and the subsequent deactivation now appear energetically less favorable. Furthermore, the energetic inversion between the two states is most probably coupled with a higher barrier on the potential energy surface connecting the two states, adding a further kinetic blockage.

In our previous paper,[10] we argued that the increased ^{3}MLCT lifetime of **C2** as compared to **C1** was due to an enhanced charge-transfer character induced by the COOH group. This argument is further supported by the effect of deprotonation that leads to a reduced (14 ps, unpublished result) lifetime due to the negatively charged COO termination (see ESI† for details). Is a similar

effect at work for the lifetime increase observed going from Im to BIm-complexes? To assess this problem we have analyzed the charge-transfer *versus* the local nature of the excited states. Indeed, the more local a state will be the more favoured will be its recombination within the MC states. Although many factors may affect the excited state lifetime,[14] some of them, like the excited state electronic structure, should be seen as more crucial in dictating the photophysics. Locality of the excited states has been calculated, thanks to the ϕ_S index recently developed by some of us.[15] The former index is based on the overlap between ground and excited state electronic densities and is normalized by construction. Values close to 1.0 are characteristic of local transitions while values close to 0.0 indicate extensive charge transfer. Both **C2** and **C4** show MLCT states with relatively high ϕ_S values of 0.68 and 0.72, respectively. Such values are indicative of a poor charge-separation and with **C4** displaying a slightly more localized excited state than **C2** (about 6%), indicating that the electronic coupling argument does not explain the longer ^{3}MLCT lifetime of **C4**.

3. Conclusion

In summary, a new homoleptic NHC–Fe(II) complex was synthesized, featuring 4 BIm and two pyridine Fe-coordinating ligands. When the pyridines are substituted with COOH groups, a record excited state lifetime of 26 ps is observed for the ^{3}MLCT state. Calculations of the excited state structure of the substituted and the unsubstituted compounds show that in the former the ^{3}MC state lies higher in energy than the ^{3}MLCT, providing a clear explanation for the increased lifetime. The combined experimental and computational study thus opens new prospects for the design of novel NHC–Fe(II) complexes with yet enhanced light-harvesting capabilities: a further increased ^{3}MLCT lifetime and absorption spectra optimized for the red wavelength region may come at hand soon.

4. Methods

4.1. Materials

Solvents and commercially available reagents were used as received. Thin layer chromatography (TLC) was performed by using silica gel 60 F-254 (Merck) plates and visualized under UV light. Chromatographic purification was performed by using silica gel 60 (0.063–0.2 mm/70–230 mesh). Compounds **1**[16] and **2**[17] have been prepared according to reported procedures.

4.2. Instrumentation

^{1}H (400 MHz) and ^{13}C NMR (100 MHz) spectra were recorded on a DRX400 Bruker spectrometer at ambient temperature. The chemical shifts (δ) were calibrated by using either tetramethylsilane (TMS) or signals from the residual protons of the deuterated solvents, and are reported in parts per million (ppm) from low to high field. High-resolution mass spectrometry (HRMS) data were obtained by using a Bruker micrOTOF-Q spectrometer. UV-vis spectra were recorded in a 1 cm path length quartz cell on a LAMBDA 1050 (Perkin Elmer) spectrophotometer. Cyclic voltammetry was performed on a Radiometer PST006 potentiostat using a conventional three-electrode cell. The saturated calomel electrode (SCE) was separated from the test compartment using a bridge tube. The solutions of studied complexes (0.2 mM) were purged with argon before each measurement. The test solution was acetonitrile containing 0.1 M Bu_4NPF_6 as a supporting electrolyte. The working electrode was a vitreous carbon rod (1 cm^2) wire and the counter-electrode was a 1 cm^2 Pt disc. After the measurement, ferrocene was added as the internal reference for calibration. All potentials were quoted *versus* SCE. Under these conditions the redox potential of the Fc^+/Fc couple was found at 0.39 V. In all the experiments the scan rate was 100 mV s^{-1}.

4.3. Synthesis

Synthesis of ligand 3. To a solution of **1**[16] (160 mg, 0.52 mmol) in DMF (5 ml) was added iodomethane (0.32 ml, 5.2 mmol), and the mixture was refluxed overnight. After cooling at room temperature, a saturated solution of KPF_6 was added (10 ml), the precipitate was washed with distilled water and dried under vacuum affording **3** (290 mg, 95%): ^{1}H NMR (200 MHz, CD_3CN): δ = 9.68 (s, 2H), 8.64 (t, J = 9.2 Hz, 1H), 8.38 (dd, J = 6.7 and 2.2 Hz, 2H), 8.15 (d, J = 8.4 Hz, 2H), 8.06 (dd, J = 6.7 and 2.2 Hz, 2H), 7.87 (m, 4H), 4.28 (s, 6H) ppm. ^{13}C NMR (50 MHz, CD_3CN): δ = 146.3, 144.8, 141.1, 132.3, 129.4, 128.2, 127.7, 117.9, 115.0, 113.6, 33.8 ppm. HRMS (ESI) calcd for $C_{21}H_{19}N_5P_2F_{12}$, m/z = 170.5820 [M-2PF_6], found 170.5832.

Synthesis of complex C3. To a solution of **3** (300 mg, 0.48 mmol) in anhydrous DMF (3 ml) was added $FeCl_2$ (30 mg, 0.24 mmol). Then *t*BuOK (170 mg, 1.5 mmol) was added and the mixture was stirred for 10 min at room temperature. A saturated solution of KPF_6 was added (10 ml) and the precipitate was collected by filtration. The solid was purified by column chromatography eluting with a acetone/H_2O/$KNO_{3(sat)}$ = 5 : 3 : 1 mixture. The yellow fraction was collected and treated with a saturated solution of KPF_6 (10 ml). After evaporation of acetone, the solid was filtered, washed with distilled water and dried under vacuum affording **C3** (46 mg, 20%). ^{1}H NMR (400 MHz, CD_3CN): δ = 8.54 (t, J = 8.7, 2H), 8.30 (d, J = 8.2 Hz, 2H), 8.25 (d, J = 7.9 Hz, 4H), 7.53–7.39 (m, 8H) 7.0 (d, J = 7.6 Hz, 4H), 2.74 (s, 12H) ppm. ^{13}C NMR (100 MHz, $CDCl_3$): δ = 211.0, 154.6, 151.8, 140.2, 138.4, 125.0, 124.1, 111.8, 110.6, 107.0, 31.5 ppm. HR MS (ESI) calcd for $C_{42}H_{34}FeN_{10}P_2F_{12}$, m/z = 367.1154 [M-2PF_6], found 367.1189.

Synthesis of ligand 4. **2**[17] (300 mg, 1.17 mmol) was suspended in acetonitrile (10 ml) and iodomethane was added (0.72 ml, 11.7 mmol), the mixture was refluxed overnight. After cooling at room temperature, a saturated solution of KPF_6 was added (10 ml), the precipitate was washed with distilled water and dried under vacuum affording **4** (630 mg, 90%). ^{1}H NMR (200 MHz, CD_3CN): δ = 9.80 (s, 2H), 8.57 (s, 2H), 8.42 (dd, J = 7.5 and 1.9 Hz, 2H), 8.07 (dd, J = 7.5 and 1.9 Hz, 2H), 7.87 (m, 4H), 4.29 (s, 6H), 4.15 (s, 3H) ppm. ^{13}C NMR (50 MHz, $CDCl_3$): δ = 163.1, 147.7, 146.2, 141.9, 132.9, 130.1, 129.0, 128.4, 118.0, 115.7, 114. 5, 54.0, 34.6 ppm. HRMS (ESI) calcd for $C_{23}H_{21}N_5O_2P_2F_{12}$ m/z = 199.5848 $[M - 2PF_6]^{2+}$. Found: 199.5842.

Synthesis of complex C4. To a mixture of **4** (100 mg, 0.25 mmol) and $FeCl_2$ (16 mg, 0.125 mmol) in anhydrous DMF (3 ml) was added *t*BuOK (110 mg, 1 mmol). The mixture was stirred for 10 min at room temperature. Diluted HNO_3 was then added to adjust the pH to 2. A saturated solution of KPF_6 was added (5 ml), and the precipitate was collected by filtration. The solid was purified by column chromatography eluting with a acetone/H_2O/$KNO_{3(sat)}$ = 10 : 3 : 1 mixture. The yellow fraction was collected and treated with diluted HNO_3 until reaching pH = 2 leading to a dark orange solution that was treated with a saturated solution of KPF_6 (10 ml). After evaporation of acetone, the solid was filtered, washed with distilled water and dried under vacuum affording **C4** (14 mg, 10%). ^{1}H NMR (400 MHz, CD_3CN): δ = 8.30 (s, 4H), 8.16 (d, J = 2.3 Hz, 4H), 7.55 (dt, J = 7.8 and 1.1 Hz, 4H), 7.47 (dt, J = 7.9 and 1.0 Hz, 4H), 7.35 (d, J = 8 Hz, 4H), 2.5 (s, 12H) ppm. ^{13}C NMR (100 MHz, CD_3CN): δ = 209.5, 154.7, 138.2, 130.8, 125.0, 124.2, 111.9, 110.5, 105.8, 31.5 ppm. HRMS (ESI) calcd for $C_{44}H_{34}FeN_{10}O_4P_2F_{12}$ m/z = 411.1052 $[M - 2PF_6]^{2+}$. Found: 411.1086.

4.4. Photophysics

In our set-up, the 800 nm output of a 5 kHz regenerative Ti:Sapphire amplifier (Amplitude Technologies) is used to generate excitation pulses using a pumping commercial collinear optical parametric amplifier (TOPAS, Light Conversion) followed by frequency doubling to produce ~60 fs pulses at 515 nm. Broadband white-light probe pulses are obtained by focusing the ~30 fs 800 nm pulses on a 2 mm thick CaF_2 crystal. The 300–700 nm output is measured in two separate sets of data using a Peltier-cooled high-speed charge-coupled device (CCD) mounted at the output of a 25 cm focal length spectrometer (resolution 3 nm). The pump and probe pulses are focused on 80 × 80 μm^2 and 40 × 40 μm^2, respectively. The pump pulse intensity is carefully reduced so as to work in a regime of linear signal response. The relative linear polarizations of pump and probe are set to a magic angle (54.7°). The concentration of the complexes dissolved in MeCN is adjusted to an absorbance of 0.45 mm $^{-1}$ at the peak of the S_0–S_1 transition. The 1 mm path length quartz cell containing the solution is set on a loud-speaker with orthogonal vibration at 10 Hz to avoid degradation which attests that the sample remains intact during the experiment. All transient absorption data presented in this paper are processed following the procedure described in ref. 18 in order to compensate for group velocity dispersion and define time zero within ±20 fs over the entire spectral range. Raman responses from the solvent and cross-phase modulation artefacts are measured in a MeCN only containing flow cell and subtracted after application of an appropriate weighting coefficient.

4.5. Molecular modelling and simulations

All quantum chemical calculations were performed by using the Gaussian09 suite of programs. The ground-state geometry of all the complexes has been optimized at the DFT level by using the B3LYP exchange correlation functional. The double-z LANL2DZ basis set was used for the iron atom, whereas carbon, hydrogen, and nitrogen were described by using the 6-31+G(d,p) basis set. Singlet excited states were firstly obtained as vertical transitions from the equilibrium geometry, following the usual Franck–Condon approach, at the TD-DFT level. In this case the system was described using the HCTCH exchange correlation functional and the 6-31+G(d,p) basis set for all the atoms. Note that these conditions have been chosen as the ones that better reproduce the lowest energy part of the absorption spectrum relative to the experimental one. In all the calculations solvent effects were taken into account by using the polarizable continuum model (PCM); more specifically, acetonitrile was considered throughout. The density reorganization in the excited states was analyzed in terms of NTOs by using a locally produced and free downloadable code NancyEX (see www.nancyex.sourceforge.net/). Once the singlet states were assessed the same level of theory was used to investigate the triplet manifold, triplet nature (MC or MLCT) was easily identified using the NTO analysis. Subsequently, the first ^{3}MLCT and the first ^{3}MC have been optimized, again using TDDFT at the HCTCH/6-31+G(d,p) level of theory, in order to obtain the adiabatic relaxation energies. Finally ϕ_S values have been obtained once again using the NancyEX code from post-processing of the attachment and detachment densities. For the convenience of the reader we recall that f_s is based on the normalized overlap of the detachment and attachment densities, calculated in the direct space. As such values close to 1.0 are indicative of localized transitions, while charge-transfer states are characterized by values close to zero. The lower the value of ϕ_s, the higher is the charge-transfer nature of the state.

Acknowledgements

The Nancy team is grateful to S. Parant for UV spectroscopy and F. Lachaud for mass spectrometry. The Strasbourg team acknowledges insightful discussions with J. Léonard and technical support from O. Crégut.

Notes and references

1 H. Xu, R. Chen, Q. Sun, W. Lai, S. Qianqian, W. Huang and X. Liu, *Chem. Soc. Rev.*, 2014, **43**, 3259.
2 (*a*) J. A. G. Williams, S. Develay, D. L. Rochester and L. Murphy, *Coord. Chem. Rev.*, 2008, **252**, 2596; (*b*) C. Cebrian, M. Mauro, D. Kourkoulos, P. Mercandelli, D. Hertel, K. Meerholz, C. A. Strassert and L. De Cola, *Adv. Mat.*, 2012, **25**(3), 437.
3 (*a*) M. K. Nazeeruddin, A. Kay, L. Rodicio, R. Humphry-Baker, E. Muller, P. Liska, N. Vlachopoulos and M. Grätzel, *J. Am. Chem. Soc.*, 1993, **115**, 6382; (*b*) M. K. Nazeeruddin, P. Pechy, T. Renouard, S. M. Zakeeruddin, R. Humphry-Baker, P. Comte, P. Liska, L. Cevey, E. Costa, V. Shklover, L. Spiccia, G. B. Deacon, C. A. Bignozzi and M. Grätzel, *J. Am. Chem. Soc.*, 2001, **123**, 1613.
4 A. Hauser, *Top. Curr. Chem.*, 2004, **234**, 155.
5 R. A. Layfield, *Organometallics*, 2014, **33**(5), 1084.
6 J. F. Létard, J. A. Real, S. Kawata and S. Kaizaki, *Chem. – Eur. J.*, 2009, **15**, 4165–4171.

7 (*a*) J. E. Monat and J. K. McCusker, *J. Am. Chem. Soc.*, 2000, **122**, 4092; (*b*) W. Gawelda, A. Cannizzo, V.-T. Pham, F. van Mourik, C. Bressler and M. Chergui, *J. Am. Chem. Soc.*, 2007, **129**, 8199; (*c*) C. Consani, M. Prémont-Schwarz, A. ElNahhas, C. Bressler, F. van Mourik, A. Cannizzo and M. Chergui, *Angew. Chem., Int. Ed.*, 2009, **48**, 7184; (*d*) G. Auböck and M. Chergui, *Nat. Chem.*, 2015, **7**, 629–633.

8 (*a*) Y. Liu, T. Harlang, S. Canton, S. Chabera, K. Suarez Alcantara, A. Fleckhaus, E. Göransson, E. Corani, A. Lomoth, R. Sundström and V. K. Wärnmark, *Chem. Comm.*, 2013, 6412; (*b*) L. A. Fredin, M. Pápai, E. Rozsályi, G. Vankó, K. Wärnmark, V. Sundström and P. Persson, *J. Phys. Chem. Lett.*, 2014, **5**, 2066.

9 Y. Liu, K. S. Kjærl, L. A. Fredin, P. Chábera, T. Harlang, S. E. Canton, S. Lidin, J. Zhang, R. Lomoth, K.-E. Bergquist, P. Persson, K. Wärnmark and V. Sundström, *Chem. – Eur. J.*, 2015, **21**, 3628.

10 T. Duchanois, T. Etienne, C. Cebrián, L. Liu, A. Monari, M. Beley, X. Assfeld, S. Haacke and P. C. Gros, *Eur. J. Inorg. Chem.*, 2015, 2469.

11 T. C. B. Harlang, Y. Liu, O. Gordivska, L. A. Fredin, C. S. Ponseca, P. Huang, P. Chabera, K. S. Kjaer, H. Mateo, J. Jens Uhlig, R. Lomoth, R. Wallenberg, S. Styring, P. Persson, V. Sundström and K. Wärnmark, *Nat. Chem.*, 2015, **7**, 883.

12 (*a*) J.-D. Chai and M. Head-Gordon, *Phys. Chem. Chem. Phys.*, 2008, **10**, 6615; (*b*) A. Monari, T. Very, J.-L. Rivail and X. Assfeld, *Comput. Theor. Chem.*, 2012, **990**, 119.

13 Such a reversal has been reported but only for computationally designed virtual cyclometallated complexes see I. M. Dixon, F. Alary, M. Boggio-Pasqua and J.-L. Heully, *Dalton Trans.*, 2015, **44**, 13498.

14 D. Escudero and D. Jacquemin, *Dalton Trans.*, 2015, **44**, 8346.

15 (*a*) T. Etienne, X. Assfeld and A. Monari, *J. Chem. Theory Comp.*, 2014, **10**, 3896; (*b*) T. Etienne, X. Assfeld and A. Monari, *J. Chem. Theory Comp.*, 2014, **10**, 3906; (*c*) T. Etienne, *J. Chem. Theory Comp.*, 2015, **11**, 1692.

16 A. Herbst, C. Bronner, P. Dechambenoit and O. S. Wenger, *Organometallics*, 2013, **32**, 1807–1814.

17 T. Tu, X. Feng, Z. Wang and X. Liu, *Dalton Trans.*, 2010, **39**, 10598.

18 J. Briand, J. Réhault, O. Bräm, J. Léonard, J. Helbing, A. Cannizzo, V. Zanirato, M. Chergui, M. Olivucci and S. Haacke, *Phys. Chem. Chem. Phys.*, 2010, **12**, 3178.

PCCP

PAPER

View Article Online
View Journal | View Issue

Cite this: *Phys. Chem. Chem. Phys.*, 2016, **18**, 28069

Interfacial charge separation and photovoltaic efficiency in Fe(II)–carbene sensitized solar cells†

Mariachiara Pastore,*[a] Thibaut Duchanois,[b] Li Liu,[c] Antonio Monari,[a] Xavier Assfeld,[a] Stefan Haacke[c] and Philippe C. Gros*[b]

Received 9th August 2016,
Accepted 16th September 2016

DOI: 10.1039/c6cp05535d

www.rsc.org/pccp

The first combined theoretical and photovoltaic characterization of both homoleptic and heteroleptic Fe(II)–carbene sensitized photoanodes in working dye sensitized solar cells (DSSCs) has been performed. Three new heteroleptic Fe(II)–NHC dye sensitizers have been synthesized, characterized and tested. Despite an improved interfacial charge separation in comparison to the homoleptic compounds, the heteroleptic complexes did not show boosted photovoltaic performances. The *ab initio* quantitative analysis of the interfacial electron and hole transfers and the measured photovoltaic data clearly evidenced fast recombination reactions for heteroleptics, even associated with un unfavorable directional electron flow, and hence slower injection rates, in the case of homoleptics. Notably, quantum mechanics calculations revealed that deprotonation of the not anchored carboxylic function in the homoleptic complex can effectively accelerate the electron injection rate and completely suppress the electron recombination to the oxidized dye. This result suggests that introduction of strong electron-donating substituents on the not-anchored carbene ligand in heteroleptic complexes, in such a way of mimicking the electronic effects of the carboxylate functionality, should yield markedly improved interfacial charge generation properties. The present results, providing for the first time a detailed understanding of the interfacial electron transfers and photovoltaic characterization in Fe(II)–carbene sensitized solar cells, open the way to a rational molecular engineering of efficient iron-based dyes for photoelectrochemical applications.

1. Introduction

Due to the continuous consumption of fossil fuels and the associated inexorable increase in environmental pollution, exploiting the solar energy to produce electricity,[1] or storing it into H_2 or alternative solar fuels,[2–4] represents one of the most compelling technological challenges. In this context, nanostructured dye-sensitized solar cells (DSSCs)[5–9] offer a valuable solution, at a comparable cost and, in principle, lower environmental impact, to traditional silicon-based photovoltaics. To date ruthenium polypyridyl complexes have been the most extensively studied dye sensitizers with up to 11% conversion efficiency.[10–14] The remarkable success obtained by Ru(II) dyes when employed as photosensitizers or photocatalysts[15,16] can be traced back to their high electron injection quantum yields,[15,17–21] coming from the high values of the electron injection rates compared to the intrinsic long lifetimes (from tens to hundreds of nanoseconds) of metal to ligand charge transfer (MLCT) lowest excited states of isolated complexes. These MLCT states are indeed responsible for the electron injection into the semiconductor conduction band (CB). Electron injection is also favored by an efficient interfacial electron–hole separation and by their peculiar adsorption geometry.[21] The same properties minimize detrimental charge recombination back onto the sensitizer. However, despite its record efficiencies, in the view of large-scale solar energy production, ruthenium suffers from serious drawbacks, which potentially limit its widespread applicability, mainly related to its toxicity and scarcity. This has motivated continuous research efforts to develop valuable alternatives: cheap and easily tunable fully organic sensitizers on one side,[22,23] and earth-abundant, less expensive and environmentally friendly d-block metal (for example iron and copper) complexes on the other side.[24–33] Despite an intense MLCT absorption, however, conventional Fe(II)-polypyridyl complexes are, unfortunately, characterized by an ultrafast (*ca.* 100 fs) deactivation to low-lying metal centered (MC) states, proceeding *via* the triplet ^{3}MC and ultimately populating the quintuplet $^5T_2$ state,[34–39] which impedes electron injection into the sensitized semiconductor.[40,41] One of the most successful strategies employed to delay the deactivation of ^{1,3}MLCT to MC states

[a] *Université de Lorraine & CNRS, SRSMC, TMS, Boulevard des Aiguillettes, 54506 Vandoeuvre-lès-Nancy, France. E-mail: mariachiara.pastore@univ-lorraine.fr*
[b] *Université de Lorraine & CNRS, SRSMC, HecRIn, Boulevard des Aiguillettes, 54506 Vandoeuvre-lès-Nancy, France. E-mail: philippe.gros@univ-lorraine.fr*
[c] *Université de Strasbourg & CNRS, IPCMS & Labex NIE, Rue du Loess, 67034 Strasbourg Cedex, France*

† Electronic supplementary information (ESI) available. See DOI: 10.1039/c6cp05535d

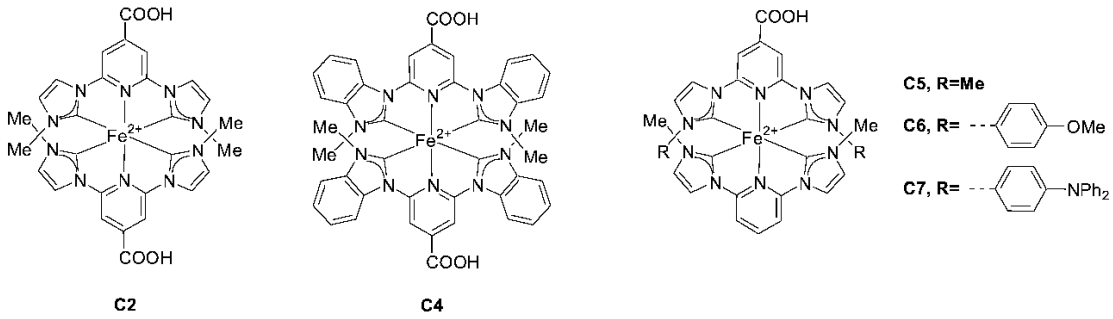

Fig. 1 Chemical structures of the investigated iron complexes.

consists of increasing the ligand field strength.[42–55] In particular, significant advances have been recently reported by using N-heterocyclic carbene (NHC),[47,52–54,56] where, as a consequence of the presence of the σ-donating carbene ligands, the metal-centered ^{3}MC and $^5T_2$ states are strongly destabilized, resulting in record ^{3}MLCT lifetimes of 16 and 26 ps,[54] for the **C2**[52] and **C4**[4] complexes (functionalized by carboxylic groups to be covalently grafted onto the TiO_2 surface) shown in Fig. 1.

Besides the improved ^{1,3}MLCT lifetime, constituting the prerequisite for injecting electrons into the semiconductor's CB, the measured overall cell efficiency finally depends on the peculiar molecule/metal oxide interfacial properties (adsorption configuration, electronic coupling, charge generation, charge recombination *etc.*..), which in turn can be reliably characterized by state-of-the-art first principle calculations.[57–60] In the last decade, indeed, quantum mechanical modeling of the isolated cell components[40,44,48,52–54,61–63] as well as of combined dye/semiconductor systems[39,43,51,57,64–68] has been shown to successfully support the experimental research by providing an atomistic understanding of the fundamental chemical and physical processes governing the cell functioning and its performances.

As a matter of fact, the first photovoltaic characterization of the Fe(II)–NHC complex **C2** (Fig. 1) was reported by some of us in ref. 52, with the first realization of a potentially exploitable iron-based DSSC. **C2**-based devices revealed, however, low current generation and photovoltage, finally resulting in a weak power conversion efficiencies. Interestingly, a subsequent work by Wärnmark and co-workers[49] claimed a record injection efficiency, almost unitary, for the same complex, suggesting that the vibrationally relaxed and long-lived ^{3}MLCT might be responsible for this exceptionally high injection yield. Density functional theory (DFT) calculations were also reported by the authors[49] to rationalize the experimental findings, although their computations were limited to the energy level alignment calculated for the isolated dye and TiO_2 anatase slab, that is the electronic structure of the dye/TiO_2 interface was not considered. The reported high injection yield and low photovoltaic performances in working DSSCs, clearly, pose intriguing questions related to the efficiency of the forward and backward interfacial electron transfer processes, whose interplay determines the final cell performance. This issue was partially tackled by a second recent computational contribution put forward by the same authors:[51] here, along with the electronic and excited state properties of isolated Fe(II)–NHC complexes, the structure of the dye/TiO_2 interface was also investigated, at least for a prototypical heteroleptic analogous of the original **C2** complex (**C5** in Fig. 1). Analysis of the projected dye and TiO_2 density of states (PDOS) at the interface revealed that energetics and nature of the highest occupied and lowest unoccupied molecular orbitals (HOMOs and LUMOs) should allow efficient (*ca.* 100 fs) electron injection from both hot and thermally relaxed dye's ^{3}MLCT excited states to the semiconductor conduction band.[51] As pointed out by Galoppini,[69] a number of open issues, however, still remain toward the development of efficient iron-based DSSCs. The peculiar interfacial properties of the homoleptic **C2** complex showing conflicting unitary injection yield[49] and extremely low photovoltaic efficiency have not yet been elucidated, as well as the impact on the solar cell performances of possible structural modifications of the NHC ligand core (**C4** in Fig. 1). Moreover, calculations suggest that the heteroleptic complexes potentially have the desired interfacial energetic and electronic coupling to efficiently sensitize the TiO_2 surface,[51] but their synthesis and applications in working DSSCs have not been reported up to now.

Thus, with the aim of providing an unified and fundamental understanding of the interfacial charge generation and sensitization properties of Fe(II)–carbene complexes in working DSSCs, we report a quantitative analysis based on high-level DFT calculations on realistic models of the relevant interfacial electron transfers as well as, to the best of our knowledge, the first photovoltaic application of new homoleptic (**C4** in Fig. 1) and heteroleptic (**C5**, **C6** and **C7** Fig. 1) Fe(II)–NHC complexes.

Our findings definitely show that for the homoleptic complexes, although electron injection from the lowest energy MLCT dye's excited state is energetically favored, in the surface-grafted sensitizer the topology of the lowest-energy MLCT state does not allow electronic coupling with the surface and hence an efficient electron injection mechanism. Operational conditions favoring deprotonation of the not-coordinated carboxylic group might however invert the stability of the two lowest MLCT states and allow, to a certain extent, electron injection into the semiconductor. On the other hand, heteroleptic sensitizers, despite being characterized by the desired charge flow toward the TiO_2 surface in the lowest MLCT state, still present lower injection

rates when compared to the best performing Ru(II)–polypyridyl and, as a matter of fact, do not yield improved photovoltaic performances. Besides the design of Fe(II) complexes endowed with long-lived ^{3}MLCT states strongly coupled with the semiconductor CB states, the present results, in line with the fast hole/electron recombination reactions observed by Wärnmark and co-workers,[49] indicate that the main obstacle to the development of efficient Fe(II)-based dye sensitizers is represented by the high favored recombination pathways with both the oxidized dye and the redox mediator.

2. Methods and models

2.1 Synthesis of dyes

C2 and **C4** have been prepared according to ref. 52 and 54 respectively. The preparation of heteroleptic complexes **C5**, **C6** and **C7** is described in the ESI.†

2.2 DSSC fabrication and photovoltaic measurements

The fluorine-doped tin oxide (FTO) glass plates (TEC Glass-TEC 8, solar 2.3 mm thickness), TiO_2 paste, electrolyte (AN50) and Pt-paste (Platisol T/SP) were purchased from Solaronix. FTO glass plates were cleaned in a detergent solution using an ultrasonic bath for 30 min and then rinsed with water and ethanol. Next, the plates were immersed into a 40 mM aqueous $TiCl_4$ at 70 °C for 30 min in a chamber. After being washed with deionized water and fully rinsed with ethanol, a transparent nanocrystalline layer was prepared on the FTO glass plates by using a screen-printing technique. TiO_2 paste was dried for 5 min at 150 °C. The TiO_2 electrodes were finally heated under an air atmosphere at 450 °C for 30 min. The TiO_2 electrodes were treated again with $TiCl_4$ at 70 °C for 30 min and sintered at 450 °C for 30 min. A TiO_2 film comprising a 10–11 μm-thick transparent layer was obtained as checked using a profilometer. The prepared TiO_2 film on the FTO electrode was immersed in the 0.5 mM acetonitrile dye solution containing chenodeoxycholic acid (0.1 mM) at room temperature overnight and finally quickly rinsed with acetonitrile before assembly. FTO plates for the counter electrodes were cleaned in an ultrasonic bath in acetone. The counter electrodes were prepared by screen-printing of Platisol onto the FTO coated glass substrate and then heated at 450 °C for 30 min under an air atmosphere. The platinum counter electrodes and the dye-adsorbed TiO_2 electrodes were assembled into a sealed sandwich-type cell by heating at 80 °C using a hot-melt film (30 μm spacer Surlyn) between the electrodes. A drop of AN50 solution was placed in the drilled hole of the counter electrode. Finally, the hole was sealed using additional Surlyn and a cover glass (0.1 mm thickness). The photovoltaic characterization of the Fe-carbene-sensitized TiO_2 cells was obtained using two complementary techniques. The irradiated surface was 0.36 cm^2. The spectral response was determined by measuring the wavelength dependence of the incident photon-to-current conversion efficiency (IPCE) using light from an Osram 300 W xenon lamp coupled to a Newport monochromator (Oriel Cornerstone 260). Photocurrents were measured under short circuit conditions (DC mode) using a Newport 1936R optical power meter. The incident irradiance was measured using a 1 cm^2 calibrated silicon photodiode. For J/V measurements we used the same lamp (Osram 300 W xenon) with an AM 1.5G filter solar spectrum in the 350–900 nm domain and a power of 100 mW cm^{-2}. The incident irradiance was measured using a ISO-Tech ISM410. The current–voltage characteristics were determined by applying an external potential bias to the cell using a Radiometer potentiostat (PGP 201) sweeping the potential with a scan rate of 10 mV s^{-1}.

2.3 Computations

The semiconductor surface was modeled by a neutral stoichiometric $(TiO_2)_{82}$ cluster of *ca.* 2 × 2 nm side, obtained by "cutting" an anatase slab exposing the majority (101) surface.[70,71] This cluster model provides energy levels in close agreement with experimental band edges of anatase TiO_2,[62,72] when global hybrid functionals and implicit solvation models are employed. Ground state equilibrium geometry of the dye@TiO_2 assemblies was optimized in the gas phase using the ADF program package,[73] using the Becke-Perdew exchange–correlation functional[74,75] and a DZP (C,H,O,N)/TZP (Fe,Ti) basis set. The interfacial electronic structure was determined by single point DFT calculations in acetonitrile solution (ε = 37.5) carried out on the optimized dye@TiO_2 complexes using the hybrid B3LYP functional, a 6-31G* basis set and a polarizable continuum model of solvation (C-PCM)[76,77] as implemented in the Gaussian09 package.[78]

In a simple Newns–Anderson picture, the broadening of the dye's lowest unoccupied molecular orbital (LUMO) projected density of states (PDOS) over the semiconductor CB states can be used to calculate the injection time.[79–84] As recently shown,[85] however, this approach, based on the Mulliken population analysis for the determination of the PDOS, is significantly sensitive to the basis set quality. A more quantitative calculation of the coupling between the dye's donor states and the CB states can be obtained in a diabatic-like scheme, proposed by Thoss and co-workers[86,87] and detailed in the following.

To estimate the efficiency of the electron/hole injection from the dye to the semiconductor, we resorted to a Fermi golden rule framework, where the injection rate k_{inj} (whose inverse is the injection time τ) is defined as:

$$k_{inj} = \frac{2\pi}{\hbar}\sum_k |V_{dk}|^2 \rho(\varepsilon_k) \quad (1)$$

where k represents the manifold of TiO_2 acceptor (conduction or valence band) states of interest and d is the dye donor state (LUMO in the case of injection and HOMO in the case of recombination). The product between the square of the electronic coupling elements, $|V_{dk}|^2$, and the semiconductor density of states (DOS), $\rho(\varepsilon_k)$, defines the electron transfer probability distribution $\Gamma(\varepsilon_k)$. The diabatic donor (dye) and acceptor (TiO_2) states were obtained by localization of the molecular orbitals of the entire complex on the donor and acceptor species. This results in a block Fock matrix of the interacting dye@TiO_2

system, where the diagonal elements represent the energies of the localized states, while the off-diagonal blocks contain the coupling elements V_{dk}. Finally injection times can be calculated as $\tau\ (\mathrm{fs}) = \frac{658}{\Gamma\ (\mathrm{meV})}$.

3. Results and discussion

3.1 Photovoltaic characterization of homoleptic Fe(II)–NHC complexes

The photovoltaic properties of **C2** based DSSCs have been reported by some of us in ref. 52, while for the **C4** complex, featuring benzimidazolylidene(BIm)-based ligands and showing a record ^{3}MLCT lifetime efficiency of 26 ps, solely the synthesis and photophysical characterization have been published up to now.[54] Since **C4** presents a longer excited state lifetime, and thus a larger time window for carrier injection than **C2**, and comparable optical and structural properties, one might expect similar or even better photovoltaic performances in working DSSCs.

Fig. 2 displays the UV-Vis absorption spectra of the complexes in acetonitrile (A) and sensitized TiO_2 films (B) as well as the IPCE (C) and *J*/*V* (D) curves for the cells fabricated with **C2** and **C4**, while the photovoltaic and surface loading data are listed in Table 1. In acetonitrile solution, **C2** presents an absorption peak, associated with the singlet MLCT states, at 520 nm (2.38 eV) with the extinction absorption coefficient of 16 200 M^{-1} cm^{-1}, while the lowest-energy absorption band of **C4** appears slightly blue-shifted (501 nm/2.48 eV) and with an absorbance lower by about 20% (12 800 M^{-1} cm^{-1}, Table S1 in the ESI†). Regarding the optical UV-Vis absorption spectra of the sensitized anatase films (Fig. 2B), the **C4**@TiO_2 absorbance appears to be almost half of that recorded for **C2**@TiO_2, clearly suggesting a less efficient surface coverage. The estimated dye loads are indeed 0.09 and 0.06 μmol cm^{-2} for **C2** and **C4**, respectively, to be compared with the value of 0.08 μmol cm^{-2} recorded under the same conditions for **N719**. Since there are in principle no reasons to hypothesize a different adsorption mode for **C4** with respect to **C2**, the lower coverage seems to be ascribable to the presence of the bulky BIm substituents, which almost double the dye volume.

IPCE plots (Fig. 2C) recorded for devices employing the I_3^-/I^- redox couple and CDCA, to suppress dye aggregation, show that while an appreciable, even if modest, IPCE was recorded (about 2.3% at 500 nm) for **C2**, for the cell fabricated with **C4** basically only negligible electron injection into the semiconductor was detected (about 0.2% at 500 nm). The measured photocurrent density for the **C4**-sensitized solar cell is more than three times lower than that measured for **C2** (0.12 *vs.* 0.41 mA cm^{-2}) and a 20% reduction in V_{oc} is also observed. Both the poor

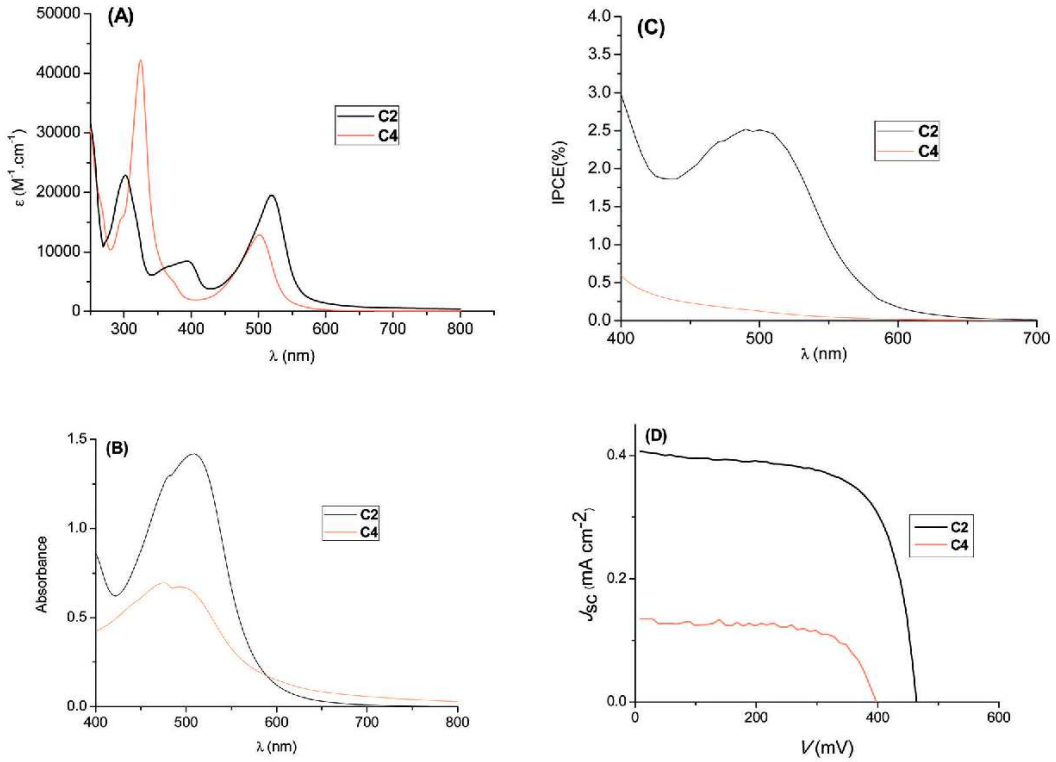

Fig. 2 UV-Vis absorption in acetonitrile (A). UV-Vis absorption spectra of the sensitized TiO_2 film (B), IPCE (C) and *J*/*V* (D) curves for DSSCs based on **C2** and **C4**.

Table 1 Photovoltaic performances of DSSCs fabricated with the **C2** and **C4** dyes and the reference **N719** dye[a]

Dye	J_{sc} (mA cm^{-2})	V_{oc} (mV)	FF	η (%)	Dye load[b] (μmol cm^{-2})
C2	0.41	457	0.68	0.13	0.09
C4	0.12	368	0.71	0.03	0.06
N719	13.25	687	0.67	6.1	0.08

[a] Measurements performed under AM 1.5 G irradiation (100 mW cm^{-2}), irradiated area: 0.36 cm^2 on TiO_2 layers (10–11 μm). Values obtained from at least three DSSCs per dye. [b] Dye load calculated from absorbance data of the sensitized electrode. Values confirmed by desorption of dyes from TiO_2 under basic conditions.

performance of the **C4** complex, and the extremely low photocurrents measured for **C2**, despite its good optical and photophysical properties and the reported 92% injection yield,[49] seem to indicate an inefficient interfacial charge separation process, possibly associated with fast recombination reactions, observed to take place in the picosecond and nanosecond time scale.[49] Importantly, as shown in Table 1, the surface dye load value for **C2** is even larger then that of the **N719** reference dye, allowing us to leave out any problem related to an inefficient TiO_2 sensitization.

3.2 Structural and electronic properties of the Fe(II)–NHC interfaces

To shed light on the efficiency of the interfacial hole and electron transfer processes, here we shall characterize, by means of DFT calculations, the structural and charge separation properties of the sensitized-TiO_2 interfaces.

The ground state optimized structures of the **C2** and **C4** complexes adsorbed on the $(TiO_2)_{82}$ cluster are shown in Fig. S1 in the ESI.† Here we consider the bidentate anchoring of the carboxylate to the undercoordinated Ti atoms of the (101) anatase surface, which is well-known to be the energetically favored one.[61] A first comment concerns the geometrical arrangement of the molecules on the surface. In both cases the complexes appear to be markedly tilted on the semiconductor surface, forming an angle of approximately 45 degrees with the TiO_2 plane. This is consistent with the coordination geometry recently reported for the analogous heteroleptic complex of C2 on an anatase-$(TiO_2)_{92}$ slab.[51] The strong tilt towards the surface also yields a slight elongation of the O–Ti distance, which increases from the typical 2.05–2.10 Å value, calculated for adsorbed carboxylate groups, to an average value of 2.20–2.25 Å.

The electronic structure and energy level alignment of the dye-sensitized TiO_2 interface can be analyzed by inspection of the Projected Density of States (PDOS) and frontier molecular orbitals (MOs), as depicted in Fig. 3 for **C2** (top) and **C4** (bottom), where the % contribution of localization on the dye of the relevant frontier MOs is also indicated. From the energetic point of view, the Fe(II)–carbene/TiO_2 interfaces resemble the typical alignment of Ru(II)–polypyridyl/TiO_2 interfaces, with the highest occupied MOs lying above the semiconductor valence band (VB) and the lowest unoccupied MO above the semiconductor CB edge, that here we calculate at −3.46/−3.47 eV for **C2**@TiO_2/**C4**@TiO_2. As is apparent, both **C2** and **C4** have HOMOs delocalized over the whole molecular skeleton and presenting a sizeable mixing with the TiO_2 VB states (around 30–50%), manifested by the tail of the TiO_2 VB PDOS extending through the dye's HOMO PDOS. Going from **C2** to **C4** the calculated dye's HOMO shifts from −5.70 to −5.96 eV, with a stabilization of 0.26 eV, which, within the simplest Koopman's approximation, almost quantitatively compares with that experimentally measured shift (0.28 eV) in the Fe^{III}/Fe^{II} oxidation potentials (Table S1 in the ESI†).

However, a deeper analysis of the topology and alignment of the unoccupied states may deliver us more precise information on the interfacial charge separation and electron injection capability.

For both **C2** and **C4** we find that the dye's LUMO, calculated at −2.63/−2.71 eV, respectively, is essentially not coupled with the semiconductor CB states: it is, in fact, almost completely localized on the dye (93% and 97% for **C2** and **C4** respectively) and, above all, it extends over the ligand not anchored to the TiO_2 surface (see isodensity plots in Fig. 3). On the other hand, the LUMO+1 distribution is markedly broadened and strongly coupled with the CB states (see the appreciable electronic density on the TiO_2 slab appearing in the isodensity plots in Fig. 3). A 100% dye's LUMO+1 population is, in fact, obtained summing over 190 and 150 dye–TiO_2 mixed states in the case of **C2** and **C4**, respectively. As is apparent from the plots of the isodensity surfaces in Fig. 3, the lower energy tail is dominated by contributions mainly localized on the anchoring moiety with strong delocalization toward the CB TiO_2 states, while at higher energies still large density contributions on the not anchored ligand appear, above all for **C2**. Thus, even if the interfacial energetics would allow electron injection, as discussed in ref. 49, the primary charge transfer character for the lowest MLCT state appears to be in the opposite direction to the one necessary to inject into the TiO_2 CB. This fact is the direct result of the adsorption of the dye onto the TiO_2 surface: the near-degeneracy between the two lowest unoccupied orbitals localized on the two ligands[52] in the isolated complexes is removed upon COOH deprotonation and subsequent binding to the Ti atoms. As TiO_2 is a weaker electron acceptor than the opposite H^+, the orbital localized on the anchored ligand turns out to be destabilized with respect to the one bearing the free COOH group. A structural distortion in the anchored dye can also contribute to the relative stabilization/destabilization of the LUMO and LUMO+1. In particular, since the LUMO (LUMO+1) is considerably delocalized on the COOH unit one can expect a sizeable destabilization upon deprotonation and, indeed, considering the isolated **C2** complex in acetonitrile solution, we calculated (B3LYP/6-31G*) an upshift of about 0.8 eV of the Kohn–Sham eigenvalue of the associated unoccupied MO. Coordination to the anatase surface clearly reduces this energy penalty, even if a LUMO–LUMO+1 energy difference of about 0.4 eV still remains.

With this information in mind, it is interesting to do a step backward and notice the marked broadening and weak, but still appreciable, splitting in the absorption spectra maxima of the **C2**- and **C4**-sensitized TiO_2 films (Fig. 2B). It is worthwhile to stress, however, that the extent of the energy separation between these two MLCT states crucially depends on the cell

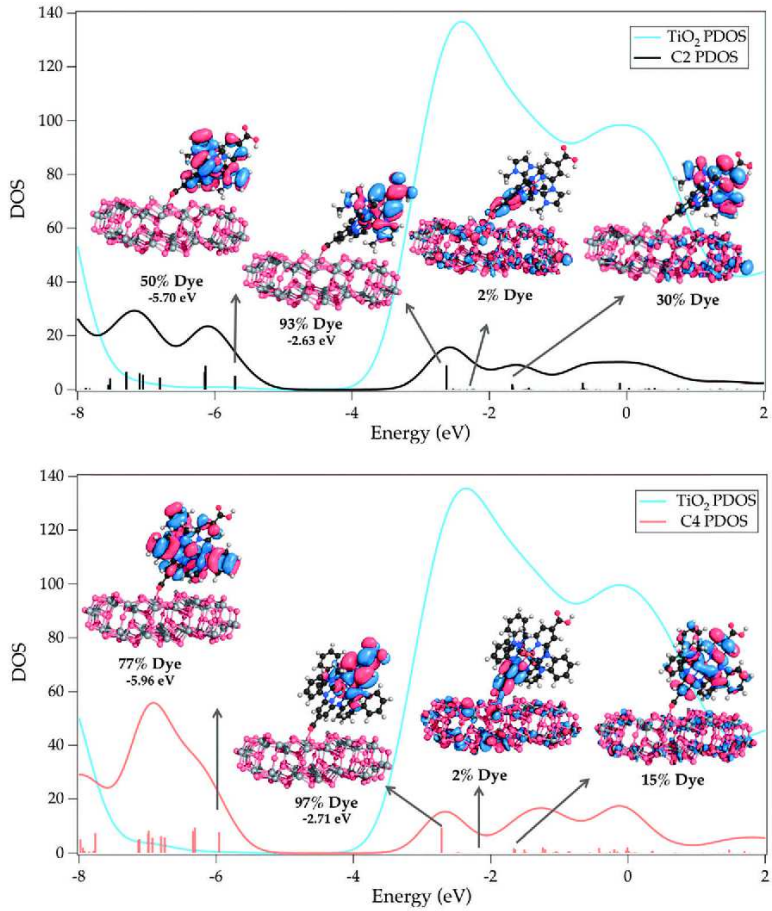

Fig. 3 Projected DOS (PDOS) and main dye's MOs isodensity plots for the **C2** (top) and **C4** (bottom) complexes adsorbed onto the $(TiO_2)_{82}$ cluster. For the depicted MOs the % contribution of population localized on the dye is also indicated. The gaussian broadening used to reproduce the PDOS is equal to 0.3 eV. Vertical sticks represent the Kohn–Sham eigenvalues and their intensity the % dye's population.

preparation and working conditions. The use of ionic additives in the electrolyte, acidic treatment of the TiO_2 substrate, pH conditions and coexistence of multiple anchoring modes can interplay in restoring/removing their near degeneracy. In fact, as shown by the PDOS in Fig. 4, the deprotonation of the not-coordinated COOH group in **C2** is sufficient to invert the LUMO/LUMO+1 nature and to redirect the charge flow of the lowest energy MLCT state toward the surface, guaranteeing a strong coupling with the TiO_2 CB states. In line with what is discussed above for the LUMO+1 population, we notice that the LUMO distribution also contains significant contributions on the not-anchored ligand (a MO with about 67% of population on the dye is found at −1.78 eV). Another beneficial effect of deprotonation seems to be the change in the nature of the highest occupied MO. The HOMO is in fact upshifted at −5.19 eV and it turns out to be strictly localized far from the surface, with no coupling (99% on the dye) with the TiO_2 states and thus less prone to give recombination with injected electrons. However, operating in a strong basic environment in order to maintain the not-coordinated carboxylic group in its deprotonated form and thus inverting the direction of the lowest excited state charge flow, is not possible in practice without desorbing the grafted dyes from the substrate. Thus, omitting one of the carboxylic groups and moving to heteroleptic complexes appear to be the only feasible ways to prevent the deactivation pathway by promoting a unidirectional electron channel toward the semiconductor CB. We report in the bottom panel of Fig. 4 the calculated PDOS and plots of the frontier MOs for the heteroleptic analogous of **C2** (termed **C5** in Fig. 1). The results confirm the desired charge transfer nature of the lowest energy dye level and overall agree with the electronic structure reported in ref. 51 for the same complex adsorbed on a $(TiO_2)_{92}$ slab and calculated at the PBE0 level of theory.

3.3 Photovoltaic characterization of heteroleptic Fe(II)–NHC complexes

On the basis of the electronic structure of the **C5**@TiO_2 complex discussed above, heteroleptic compounds should be able to

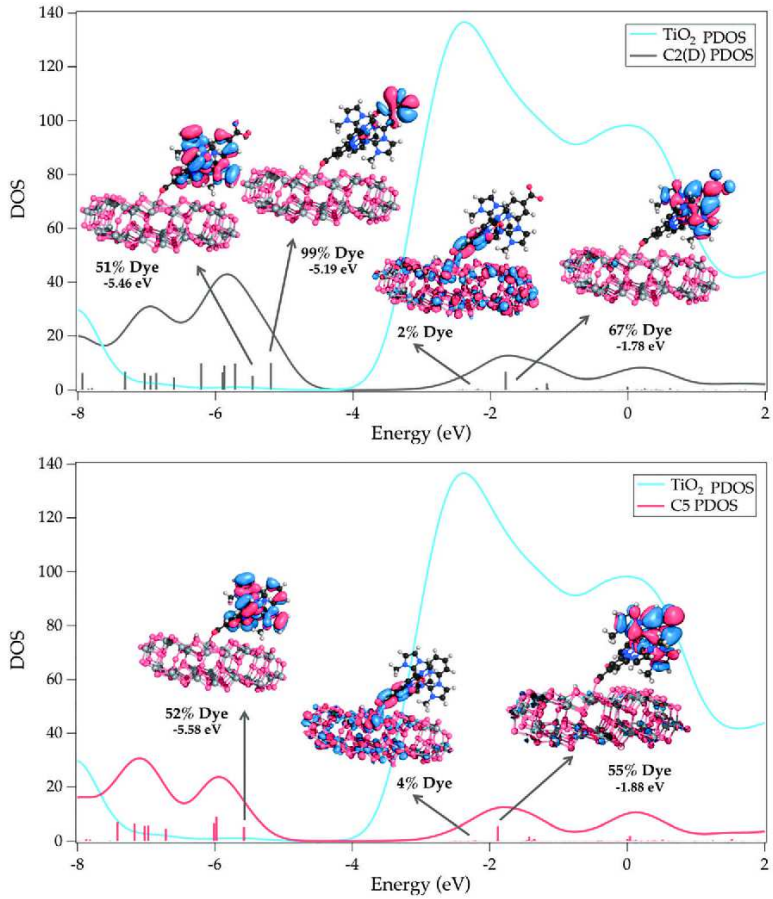

Fig. 4 Projected DOS (PDOS) and main dye's MOs isodensity plots for the deprotonated **C2(D)** (top) and heteroleptic **C5** (bottom) complexes adsorbed onto the $(TiO_2)_{82}$ cluster. For the depicted MOs the % contribution of population localized on the dye is also indicated. The gaussian broadening used to reproduce the PDOS is equal to 0.3 eV. Vertical sticks represent the Kohn–Sham eigenvalues and their intensity the % dye's population.

effectively inject electrons into the semiconductor CB. We therefore prepared the three heteroleptic Fe(II)–carbene complexes **C5**, **C6** and **C7** (see Fig. 1 and the ESI† for preparation) and investigated their electronic and photovoltaic properties (Fig. 5 and Table 2). Besides **C5**, the heteroleptic analogous of **C2**, we also investigated the effect of electron-donating substituents such as anisyl and triphenyl amine on the NHC ligands **C6** and **C7** with the idea of (i) increasing the polarization of the dye and thus enhancing the electron transfer; (ii) maintaining the photo-generated hole far from the semiconductor surface to possibly limit the recapture of injected electrons.

The recorded UV-Vis spectra in acetonitrile (A), on the TiO_2 film (B), the IPCE (C) and J/V (D) curves for all the heteroleptic complexes along with those of the reference **C2** homoleptic complex are reported in Fig. 5, whereas Table 2 compiles the associated photovoltaic data. The UV-Vis absorption maxima in solution and on TiO_2 as well as the redox properties of the complexes are collected in Table S1 in the ESI.†

The absorption spectra of the complexes in acetonitrile (Fig. 5A) clearly show the effect of the dissymmetric structure of the heteroleptic complexes. Indeed, while the homoleptic complex **C2** exhibits two MLCT transitions in the visible domain at 394 nm (metal–carbene MLCT) and 520 nm (metal–pyridine MLCT), an additional MLCT band was observed for the heteroleptics at 430 nm.

In the visible region, complexes **C5**, **C6** and **C7** have a similar three-band spectrum with variations in the ε values, the anisyl substituent in complex **C6** promoting a significant increase of the absorption. In the UV region compound **C7** featured the characteristic intense band (296 nm, ε = 40 600 M^{-1} cm^{-1}) of the π–π^* transition on the triphenylamine moiety.

The removal of one carboxylic acid going from **C2** to the heteroleptic complexes induced a significant blue shift of the lowest energy transition band from 520 nm to *ca.* 509 nm, while the band at 394 nm corresponding to the metal–carbene transition[52,54] remained unchanged. Thus the band at 430 nm in heteroleptic complexes can be attributed to the MLCT transition between the iron center and the ligand with the unsubstituted pyridine. Interestingly, the band at 509 nm appears to be much more intense than the others for every complex indicating that a

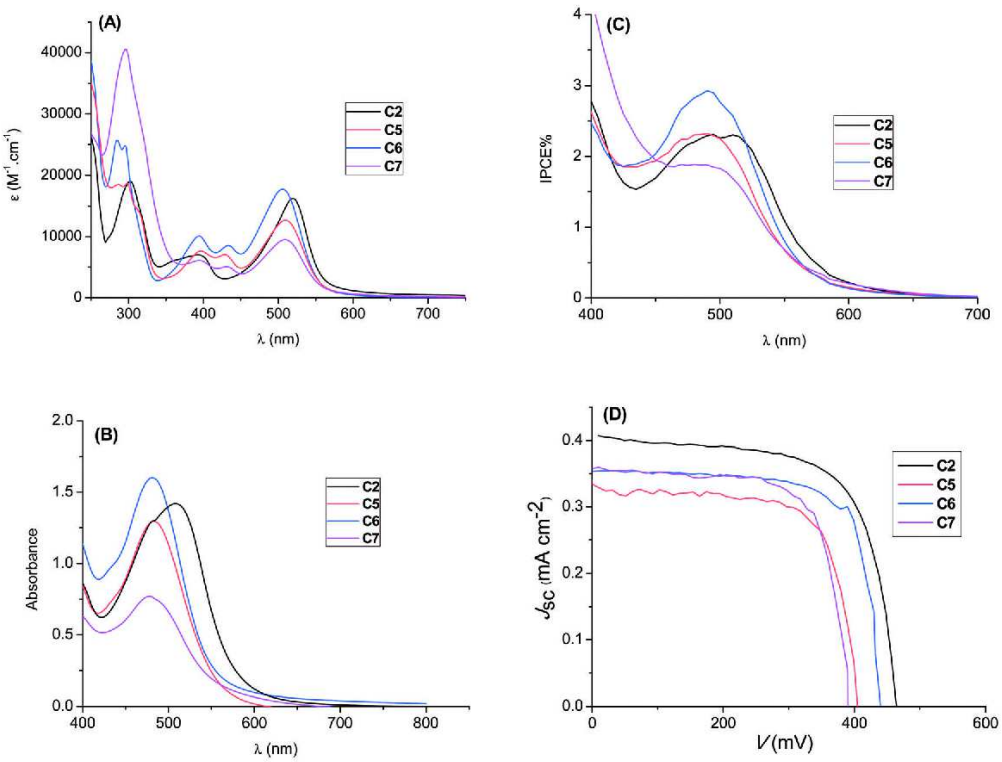

Fig. 5 UV-Vis absorption in acetonitrile (A). UV-Vis absorption spectra of the sensitized TiO_2 film (B), IPCE (C) and *J*/*V* (D) curves for DSSCs based on **C2**, **C5**, **C6** and **C7**.

Table 2 Photovoltaic performances of DSSCs fabricated with the heteroleptic **C5**, **C6** and **C7** dyes compared to the reference homoleptic **C2** and **N719** dyes[a]

Dye	J_{sc} (mA cm^{-2})	V_{oc} (mV)	FF	η (%)	Dye load[b] (μmol cm^{-2})
C5	0.33	400	0.73	0.10	0.10
C6	0.36	440	0.73	0.11	0.12
C7	0.36	390	0.71	0.10	0.07
C2	0.41	457	0.68	0.13	0.09
N719	13.25	687	0.67	6.1	0.08

[a] Measurements performed under AM 1.5 G irradiation (100 mW cm^{-2}), irradiated area: 0.36 cm^2 on TiO_2 layers (10–11 μm). Values obtained from at least three DSSCs per dye. [b] Dye load calculated from absorbance data of the sensitized electrode. Values confirmed by desorption of dyes from TiO_2 under basic conditions.

higher amount of light energy was absorbed by the MLCT transition involving iron and the carboxypyridine. This augmented absorbance should in principle translate into higher IPCE values in DSSCs.

The absorption spectra of the sensitized electrodes (Fig. 5B) perfectly mimicked the solution spectra with the blue-shift of the MLCT band in heteroleptics compared with **C2** and the best absorbance measured for complex **C6**. IPCE curves (Fig. 5C) showed that the dyes were able to harvest light and produce carriers along a wide absorption window. As a consequence of its better absorbance, complex **C6** permitted to reach a 3% IPCE *vs.* 2.5% for **C5** and the homoleptic **C2**.

As is apparent, however, from the *J*/*V* curves (Fig. 5D) and PV data in Table 2, despite possessing the desired interfacial charge separation characteristics the photovoltaic performances of the cells fabricated with all the heteroleptic derivatives did not show any improvement compared to the efficiency obtained with the homoleptic **C2** complex (Table 1). The overall efficiencies of the cells fabricated with the heteroleptic complexes are around 0.1%, with photocurrent values of 0.33 (**C5**) and 0.36 (**C6** and **C7**) mA cm^{-2}. Comparable and even larger surface coverage values are also obtained, with the only exception of **C7**, bearing the bulkier triphenylamine substituents, thus comparable light harvesting capabilities for the sensitized-TiO_2 films can be hypothesized. As a matter of fact, very low V_{oc} values were also obtained, being in all cases around 400 mV, whereas the V_{oc} measured for the **N719** Ru(II) complex under the same operating conditions is around 690 mV (Table 2). These extremely low photovoltage and photocurrent values clearly suggest an unfavorable balance between the interfacial electron injection and recombination (with both oxidized dye and electrolyte)[88] pathways. Concerning the recombination with the electrolyte, it is interesting to notice that such low V_{oc} values resemble those reported in the literature for phthalocyanine[89] and other purely organic and metal centred dyes[90] in combination with the I^-/I_3^- redox couple.[91] These results are usually attributed to the possible formation of stable complexes[92] between the aromatic ligands

and/or particular functional groups and the electrolyte species. The formation of these adducts results in an increased concentration of iodine in proximity of the TiO_2 surface, boosting the recombination probability. We also notice that the highly delocalized nature of the HOMO (hole in the oxidized dye), appearing in Fig. 3 and 4, and the markedly bent adsorption configuration (Fig. S1 in the ESI†) of these Fe(II)–NHC complexes might further favor the approach of the electrolyte to the semiconductor surface in the regeneration process.

3.4 Interfacial electron injection and recombination

On the basis of electronic structure calculations of the Fe(II)–NHC@TiO_2 complexes discussed above and upon localization of the MOs on the dye and TiO_2 fragments, we can quantitatively estimate the rates for both the electron injection from the dye's LUMO (or LUMO+1) into the CB states and hole injection from the dye's HOMO to the CB states (*i.e.* recombination to the oxidized dye). The results are depicted in Fig. 6 in terms of probability distribution $\Gamma(k)$ and diabatic density of acceptor TiO_2 states (see eqn (1)) along with the relevant dye energy levels, while Table 3 summarizes the calculated injection probabilities extracted at the energy of the donor states (LUMO/LUMO+1 and HOMO for electron injection and recombination, respectively). Since **C5**, **C6** and **C7** exhibited similar electronic properties we focused on **C5** for a better comparison with its homoleptic counterpart **C2**. The energies of the corresponding diabatic levels, shown by vertical sticks in Fig. 6, are given in the ESI† (Table S2).

A first comment concerns the homoleptic complexes (**C2** and **C4**). In agreement with the electronic structure reported in Fig. 3 and discussed above, the plots in the top panel of Fig. 6 and the related data in Table 3 show that the electronic coupling between the dye's LUMO and the semiconductor CB states is negligible. The calculated Γ values extracted at the energy of the dye's donor state (LUMO) are of the order of 10^{-4} eV, resulting in calculated injection rates of about 10^{12} s^{-1}. In other words, the electron injection is predicted to take place in the ps timescale, which is exactly the timescale for the deactivation of the ^{3}MLCT state (16 ps and 26 ps, for **C2**[52] and **C4**,[54] respectively). Notably our calculations are also able to provide a quantitative difference between **C2** and **C4**, predicting for the latter a lower injection probability (Γ), over the whole manifold of CB states, possibly due to the higher delocalized character of the MOs induced by the presence of BIm substituents. As expected, on the other hand, the typical ultrafast injection mechanism characteristic of the Ru(II)–polypyridyl complexes is envisaged for LUMO+1, with Γ values of the order of 10^{-1} eV and injection rates of 10^{15} s^{-1} (fs timescale). Also in this case, for **C4** a slower injection rate is calculated at the LUMO+1 energy level and the Γ curve is always lower than that calculated for **C2** (see Fig. S2 in the ESI†). As deprotonation of the not-coordinated COOH group inverts the energetic order between the LUMO and LUMO+1 levels, restoring the desired interfacial charge separation, $\Gamma(\varepsilon_{LUMO})$, for **C2(D)** is in the same order of magnitude of $\Gamma(\varepsilon_{LUMO+1})$ calculated for the protonated **C2** (0.162 *vs.* 0.158 eV) and an injection

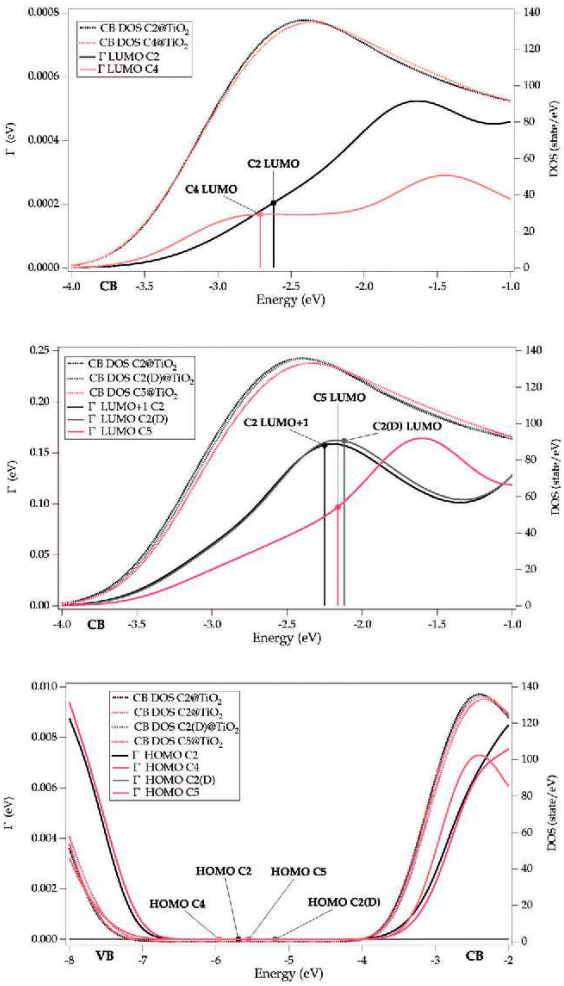

Fig. 6 Probability distribution $\Gamma(\varepsilon_k)$, left scale, solid line, (eV); and diabatic density of states (DOS, right scale, dashed lines eV^{-1}) for electron injection from the **C2**/**C4** LUMO (top), **C2** LUMO+1 and **C2(D)**/**C5** LUMO (middle) to the TiO_2 CB, and hole injection from the **C2**/**C2(D)**/**C4**/**C5** HOMO to the TiO_2 VB (bottom). The relevant dye energy levels are also reported as vertical sticks.

rate in the fs timescale is predicted. It is worthwhile to notice in the middle panel of Fig. 6, that almost coincident Γ curves are obtained for the LUMO+1 of **C2** (black) and LUMO of **C2(D)** (grey), confirming the identical nature of the diabatic states in the two systems. On the other hand, the injection probability distributions of the heteroleptic **C5** complex (red curve in the middle panel of Fig. 6) indicates an appreciable change in the electronic structure, *i.e.* in the diabatic LUMO nature, delivering lower electronic coupling with the low-energy TiO_2 CB states (where the LUMO is energetically located) and larger coupling with higher-energy states (around −1.5 eV). The electronic coupling elements calculated for the LUMO/LUMO+1 of **C5**/**C2** and the TiO_2 CB states are reported in Fig. S3 in the ESI.† Thus the calculated $\Gamma(\varepsilon_{LUMO})$ for **C5** is more than one order of magnitude lower than that calculated for the deprotonated

Table 3 Probability distributions, Γ (eV), DOS (number of states/eV) calculated at the diabatic HOMO, LUMO and LUMO+1 energies, and associated injection rates, k_{inj} (s^{-1})

Electron injection						
System	$\Gamma(\varepsilon_{LUMO})$	$DOS(\varepsilon_{LUMO})$	k_{inj}	$\Gamma(\varepsilon_{LUMO+1})$	$DOS(\varepsilon_{LUMO+1})$	k_{inj}
C2@TiO_2	2.03×10^{-4}	129	1.9×10^{12}	0.158	133	1.5×10^{15}
C4@TiO_2	1.67×10^{-4}	120	1.6×10^{12}	0.120	136	1.1×10^{15}
C2(D)@TiO_2	0.162	129	1.5×10^{15}	1.1×10^{-3}	114	1.0×10^{13}
C5@TiO_2	0.010	130	9.5×10^{13}	1.2×10^{-3}	120	1.1×10^{13}
Recombination to the oxidized dye						
	$\Gamma(\varepsilon_{HOMO})$		$DOS(\varepsilon_{HOMO})$		k_{inj}	
C2@TiO_2	1.0×10^{-11}		1×10^{-8}		9.5×10^{4}	
C4@TiO_2	5.0×10^{-10}		3×10^{-6}		4.8×10^{7}	
C2(D)@TiO_2	1.8×10^{-15}		6×10^{-8}		17	
C5@TiO_2	3.0×10^{-12}		6×10^{-9}		2.6×10^{4}	

complex (0.010 *vs.* 0.162 eV), resulting in a longer injection time, lying in the range of several ps in the same time scale of the ^{3}MLCT lifetimes of the heteroleptic complexes, measured at 14, 10 and 12 ps for **C5**, **C6** and **C7** respectively (see Fig. S6 and Table S3 in the ESI†).

Interesting insights also come from the hole injection Γ curves describing the recombination processes from the dye's HOMO to the TiO_2 CB states (bottom panel of Fig. 6). In line with the typical measured ms time scales for Ru(II)–polypyridyl sensitizers, in our diabatic-like framework recombination to the oxidized dye is calculated to be extremely slow, as a consequence of the negligible energetic overlap between the dye HOMO and the TiO_2 CB states. We however note that for **C2**, **C5** and **C4** (even if at a lower extent) the Γ plots (black, red and orange lines, respectively) and V values (eqn (1)) plotted in Fig. S4 and S5 in the ESI† indicate a sizeable electronic coupling with both the VB and CB states due to the above discussed high delocalization of the HOMO favoring electronic conjugation with the TiO_2 MOs. This inefficient interfacial hole/charge separation suggests that in the complexity of the dye-sensitized TiO_2 interface, where heterogeneous binding modes and supramolecular interactions alter the energetic alignment calculated here, the actual recombination rate to the oxidized dye might be higher, occurring in the nanosecond and even picosecond timescale, as reported in ref. 49. The hole injection (recombination) rate of **C4** is however predicted to be three orders of magnitude faster than of those of **C2** and **C5** (10^7 s^{-1} to be compared to 10^4 s^{-1}), as a consequence of the higher TiO_2 DOS (see the number of states listed in Table 3). Then, as expected, the coupling for the HOMO of the deprotonated **C2(D)** is, instead, almost zero (see the solid grey curve in the bottom panel of Fig. 6), with a practically suppressed recombination rate, predicted to occur in the second timescale.

4. Summary and conclusions

Here we have reported for the first time a combined theoretical and experimental (photovoltaic) characterization of Fe(II)–carbene sensitized photoelectrodes in working solar cells. In addition to the already developed homoleptic Fe(II)–NHC **C2**[52] and **C4**[54] complexes (Fig. 1), the synthesis, characterization and photovoltaic application of three new heteroleptic Fe(II)–NHC dye sensitizers (**C5**, **C6** and **C7**, Fig. 1) has been carried out. Despite an improved interfacial charge separation, the heteroleptic compounds did not show boosted photovoltaic performances compared to the homoleptic ones: photocurrent values of about 0.3–0.4 mA cm^{-2}, V_{oc} of *ca.* 400 mV and overall efficiency of 0.1% are obtained for all the investigated sensitizers. The quantitative analysis of the interfacial electron and hole transfers extracted from our quantum mechanical calculations, along with the measured photovoltaic data, clearly evidence the main problems associated with the poor device efficiencies and the main challenges that have to be faced to develop efficient iron-based sensitizers: (i) fast recombination reactions with both the oxidized dye and I^-/I_3^- electrolyte appear as the main barrier to efficient Fe(II)–NHC dyes; (ii) homoleptic complexes do not present the desired directional electron flow toward the TiO_2 surface in their lowest MLCT state; (iii) heteroleptic complex, although possessing the appropriate interfacial charge separation, are predicted to have lower electron injection rates when compared to the reference Ru(II)–polypyridyl complexes, yielding improved photocurrent and photovoltage values in working devices. Importantly, the calculations revealed that the deprotonation of the not anchored carboxylic function in the homoleptic **C2** complex (**C2(D)**) promoted a notable speeding up of the electron injection (from the ps for **C2** to the fs time scale for **C2(D)**) while suppressing the electron recombination. In this case, the interfacial hole/electron charge separation nicely resembles that of the reference **N719** Ru(II) sensitizer. This result clearly indicates that the introduction of electron-donating substituents (as it is the case for the carboxylate function) on the not-anchored NHC ligand of heteroleptic complexes should be the route of choice to improve the overall interfacial charge generation and make iron-based dyes applicable for photoelectrochemical devices. Work is now in progress towards this direction.

Acknowledgements

Support from Université de Lorraine and CNRS is gratefully acknowledged. MP also thanks the contribution of the

"Perspect H_2O" COST action CM1202. The authors thank S. Parant for setting up the photovoltaic measurements and F. Lachaud for ESI mass spectrometry.

References

1 M. Grätzel, *Acc. Chem. Res.*, 2009, **42**, 1788–1798.
2 K. J. Young, L. A. Martini, R. L. Milot, R. C. Snoeberger III, V. S. Batista, C. A. Schmuttenmaer, R. H. Crabtree and G. W. Brudvig, *Coord. Chem. Rev.*, 2012, **256**, 2503–2520.
3 T. W. Hamann, *Nat. Mater.*, 2014, **13**, 3–4.
4 J. J. Concepcion, R. L. House, J. M. Papanikolas and T. J. Meyer, *Proc. Natl. Acad. Sci. U. S. A.*, 2012, **109**, 15560–15564.
5 B. O'Regan, M. Grätzel and D. Fitzmaurice, *J. Phys. Chem.*, 1991, **95**, 10525–10528.
6 A. Hagfeldt, G. Boschloo, L. Sun, L. Kloo and H. Pettersson, *Chem. Rev.*, 2010, **110**, 6595–6663.
7 H. J. Snaith and L. Schmidt-Mende, *Adv. Mater.*, 2007, **19**, 3187–3200.
8 H. S. Jung and J.-K. Lee, *J. Phys. Chem. Lett.*, 2013, **4**, 1682–1693.
9 B. E. Hardin, H. J. Snaith and M. D. McGehee, *Nat. Photonics*, 2012, **6**, 162.
10 M. K. Nazeeruddin, F. De Angelis, S. Fantacci, A. Selloni, G. Viscardi, P. Liska, S. Ito, B. Takeru and M. Grätzel, *J. Am. Chem. Soc.*, 2005, **127**, 16835–16847.
11 A. Hagfeldt and L. Peter, *Dye-sensitized Solar Cells*, EPFL Press, Lausanne, 2010, p. 323–403.
12 L. Han, A. Islam, H. Chen, C. Malapaka, B. Chiranjeevi, S. Zhang, X. Yang and M. Yanagida, *Energy Environ. Sci.*, 2012, **5**, 6057–6060.
13 M. Pastore, F. De Angelis and C. Angeli, *Theor. Chem. Acc.*, 2016, **135**, 1–11.
14 S. Fantacci, F. De Angelis and A. Selloni, *J. Am. Chem. Soc.*, 2003, **125**, 4381–4387.
15 S. Ardo and G. J. Meyer, *Chem. Soc. Rev.*, 2009, **38**, 115–164.
16 D. L. Ashford, M. K. Gish, A. K. Vannucci, M. K. Brennaman, J. L. Templeton, J. M. Papanikolas and T. J. Meyer, *Chem. Rev.*, 2015, **115**, 13006–13049.
17 A. Listorti, C. Creager, P. Sommeling, J. Kroon, E. Palomares, A. Fornelli, B. Breen, P. R. F. Barnes, J. R. Durrant, C. Law and B. O'Regan, *Energy Environ. Sci.*, 2011, **4**, 3494–3501.
18 A. Listorti, B. O'Regan and J. R. Durrant, *Chem. Mater.*, 2011, **23**, 3381–3399.
19 N. A. Anderson and T. Lian, *Annu. Rev. Phys. Chem.*, 2004, **56**, 491–519.
20 M. G. Lobello, S. Fantacci and F. De Angelis, *J. Phys. Chem. C*, 2011, **115**, 18863–18872.
21 S. E. Koops, P. R. F. Barnes, B. C. O'Regan and J. R. Durrant, *J. Phys. Chem. C*, 2010, **114**, 8054–8061.
22 Z. Yao, M. Zhang, H. Wu, L. Yang, R. Li and P. Wang, *J. Am. Chem. Soc.*, 2015, **137**, 3799–3802.
23 K. Kakiage, Y. Aoyama, T. Yano, K. Oya, J.-I. Fujisawa and M. Hanaya, *Chem. Commun.*, 2015, **51**, 15894–15897.
24 S. Ferrere and B. A. Gregg, *J. Am. Chem. Soc.*, 1998, **120**, 843–844.
25 S. Ferrere, *Chem. Mater.*, 2000, **12**, 1083–1089.
26 S. Ferrere, *Inorg. Chim. Acta*, 2002, **329**, 79–92.
27 M. Yang, D. W. Thompson and G. J. Meyer, *Inorg. Chem.*, 2000, **39**, 3738–3739.
28 M. Yang, D. W. Thompson and G. J. Meyer, *Inorg. Chem.*, 2002, **41**, 1254–1262.
29 I. M. Dixon, S. Khan, F. Alary, M. Boggio-Pasqua and J. L. Heully, *Dalton Trans.*, 2014, **43**, 15898–15905.
30 I. M. Dixon, F. Alary, M. Boggio-Pasqua and J.-L. Heully, *Dalton Trans.*, 2015, **44**, 13498–13503.
31 T. Bessho, E. C. Constable, M. Graetzel, A. Hernandez Redondo, C. E. Housecroft, W. Kylberg, M. K. Nazeeruddin, M. Neuburger and S. Schaffner, *Chem. Commun.*, 2008, 3717–3719.
32 C. E. Housecroft and E. C. Constable, *Chem. Soc. Rev.*, 2015, **44**, 8386–8398.
33 B. Bozic-Weber, E. C. Constable and C. E. Housecroft, *Coord. Chem. Rev.*, 2013, **257**, 3089–3106.
34 J. K. McCusker, K. N. Walda, R. C. Dunn, J. D. Simon, D. Magde and D. N. Hendrickson, *J. Am. Chem. Soc.*, 1993, **115**, 298–307.
35 J. E. Monat and J. K. McCusker, *J. Am. Chem. Soc.*, 2000, **122**, 4092–4097.
36 W. Zhang, R. Alonso-Mori, U. Bergmann, C. Bressler, M. Chollet, A. Galler, W. Gawelda, R. G. Hadt, R. W. Hartsock, T. Kroll, K. S. Kjaer, K. Kubicek, H. T. Lemke, H. W. Liang, D. A. Meyer, M. M. Nielsen, C. Purser, J. S. Robinson, E. I. Solomon, Z. Sun, D. Sokaras, T. B. van Driel, G. Vanko, T.-C. Weng, D. Zhu and K. J. Gaffney, *Nature*, 2014, **509**, 345–348.
37 M. Cammarata, R. Bertoni, M. Lorenc, H. Cailleau, S. Di Matteo, C. Mauriac, S. F. Matar, H. Lemke, M. Chollet, S. Ravy, C. Laulhé, J.-F. Létard and E. Collet, *Phys. Rev. Lett.*, 2014, **113**, 227402.
38 G. Auböck and M. Chergui, *Nat. Chem.*, 2015, **7**, 629–633.
39 E. Jakubikova and D. N. Bowman, *Acc. Chem. Res.*, 2015, **48**, 1441–1449.
40 G. Vankó, A. Bordage, M. Pápai, K. Haldrup, P. Glatzel, A. M. March, G. Doumy, A. Britz, A. Galler, T. Assefa, D. Cabaret, A. Juhin, T. B. van Driel, K. S. Kjær, A. Dohn, K. B. Møller, H. T. Lemke, E. Gallo, M. Rovezzi, Z. Németh, E. Rozsályi, T. Rozgonyi, J. Uhlig, V. Sundström, M. M. Nielsen, L. Young, S. H. Southworth, C. Bressler and W. Gawelda, *J. Phys. Chem. C*, 2015, **119**, 5888–5902.
41 B. E. Van Kuiken, H. Cho, K. Hong, M. Khalil, R. W. Schoenlein, T. K. Kim and N. Huse, *J. Phys. Chem. Lett.*, 2016, **7**, 465–470.
42 I. M. Dixon, F. Alary, M. Boggio-Pasqua and J.-L. Heully, *Inorg. Chem.*, 2013, **52**, 13369–13374.
43 S. Mukherjee, D. N. Bowman and E. Jakubikova, *Inorg. Chem.*, 2015, **54**, 560–569.
44 I. M. Dixon, G. Boissard, H. Whyte, F. Alary and J.-L. Heully, *Inorg. Chem.*, 2016, **55**, 5089–5091.
45 L. L. Jamula, A. M. Brown, D. Guo and J. K. McCusker, *Inorg. Chem.*, 2014, **53**, 15–17.

46 A. K. C. Mengel, C. Förster, A. Breivogel, K. Mack, J. R. Ochsmann, F. Laquai, V. Ksenofontov and K. Heinze, *Chem. – Eur. J.*, 2015, **21**, 704–714.

47 Y. Liu, T. Harlang, S. E. Canton, P. Chabera, K. Suarez-Alcantara, A. Fleckhaus, D. A. Vithanage, E. Goransson, A. Corani, R. Lomoth, V. Sundstrom and K. Warnmark, *Chem. Commun.*, 2013, **49**, 6412–6414.

48 L. A. Fredin, M. Pápai, E. Rozsályi, G. Vankó, K. Wärnmark, V. Sundström and P. Persson, *J. Phys. Chem. Lett.*, 2014, **5**, 2066–2071.

49 T. C. B. Harlang, Y. Liu, O. Gordivska, L. A. Fredin, C. S. Ponseca Jr, P. Huang, P. Chábera, K. S. Kjaer, H. Mateos, J. Uhlig, R. Lomoth, R. Wallenberg, S. Styring, P. Persson, V. Sundström and K. Wärnmark, *Nat. Chem.*, 2015, **7**, 883–889.

50 Y. Liu, K. S. Kjær, L. A. Fredin, P. Chábera, T. Harlang, S. E. Canton, S. Lidin, J. Zhang, R. Lomoth, K.-E. Bergquist, P. Persson, K. Wärnmark and V. Sundström, *Chem. – Eur. J.*, 2015, **21**, 3628–3639.

51 L. A. Fredin, K. Wärnmark, V. Sundström and P. Persson, *ChemSusChem*, 2016, **9**, 652.

52 T. Duchanois, T. Etienne, C. Cebrián, L. Liu, A. Monari, M. Beley, X. Assfeld, S. Haacke and P. C. Gros, *Eur. J. Inorg. Chem.*, 2015, 2469–2477.

53 T. Duchanois, T. Etienne, M. Beley, X. Assfeld, E. A. Perpète, A. Monari and P. C. Gros, *Eur. J. Inorg. Chem.*, 2014, 3747–3753.

54 L. Liu, T. Duchanois, T. Etienne, A. Monari, M. Beley, X. Assfeld, S. Haacke and P. C. Gros, *Phys. Chem. Chem. Phys.*, 2016, **18**, 12550–12556.

55 S. G. Shepard, S. M. Fatur, A. K. Rappé and N. H. Damrauer, *J. Am. Chem. Soc.*, 2016, **138**, 2949–2952.

56 Y. Liu, P. Persson, V. Sundström and K. Wärnmark, *Acc. Chem. Res.*, 2016, 1477–1485.

57 M. Pastore and F. De Angelis, *J. Am. Chem. Soc.*, 2015, **137**, 5798–5809.

58 I. Kondov, M. Čížek, C. Benesch, H. Wang and M. Thoss, *J. Phys. Chem. C*, 2007, **111**, 11970–11981.

59 D. Sulzer, S. Iuchi and K. Yasuda, *J. Chem. Theory Comput.*, 2016, 3074–3086.

60 J. Jiang, J. R. Swierk, S. Hedstrom, A. J. Matula, R. H. Crabtree, V. S. Batista, C. A. Schmuttenmaer and G. W. Brudvig, *Phys. Chem. Chem. Phys.*, 2016, **18**, 18678–18682.

61 M. Pastore and F. Angelis, *Modeling Materials and Processes in Dye-Sensitized Solar Cells: Understanding the Mechanism, Improving the Efficiency*, Top. Curr. Chem., Springer, Berlin Heidelberg, 2014, pp. 1–86.

62 M. Pastore, A. Selloni, S. Fantacci and F. De Angelis, *Electronic and Optical Properties of Dye-Sensitized TiO2 Interfaces*, Top. Curr. Chem., Springer, Berlin Heidelberg, 2014, pp. 1–45.

63 M. Pápai, G. Vankó, T. Rozgonyi and T. J. Penfold, *J. Phys. Chem. Lett.*, 2016, **7**, 2009–2014.

64 D. H. Lee, M. J. Lee, H. M. Song, B. J. Song, K. D. Seo, M. Pastore, C. Anselmi, S. Fantacci, F. De Angelis, M. K. Nazeeruddin, M. Gräetzel and H. K. Kim, *Dyes Pigm.*, 2011, **91**, 192–198.

65 E. Jakubikova, R. C. Snoeberger III, V. S. Batista, R. L. Martin and E. R. Batista, *J. Phys. Chem. A*, 2009, **113**, 12532–12540.

66 P. Salvatori, A. Amat, M. Pastore, G. Vitillaro, K. Sudhakar, L. Giribabu, Y. Soujanya and F. De Angelis, *Comput. Theor. Chem.*, 2014, **1030**, 59–66.

67 S. Agrawal, T. Leijtens, E. Ronca, M. Pastore, H. Snaith and F. De Angelis, *J. Mater. Chem. A*, 2013, **1**, 14675–14685.

68 P. Umari, L. Giacomazzi, F. De Angelis, M. Pastore and S. Baroni, *J. Chem. Phys.*, 2013, **139**, 014709.

69 E. Galoppini, *Nat. Chem.*, 2015, **7**, 861–862.

70 A. Vittadini, A. Selloni, F. P. Rotzinger and M. Grätzel, *Phys. Rev. Lett.*, 1998, **81**, 2954–2957.

71 M. J. Lundqvist, M. Nilsing, P. Persson and S. Lunel, *Int. J. Quantum Chem.*, 2006, **106**, 3214–3234.

72 F. De Angelis, S. Fantacci, E. Mosconi, M. K. Nazeeruddin and M. Grätzel, *J. Phys. Chem. C*, 2011, **115**, 8825–8831.

73 G. te Velde, F. M. Bickelhaupt, E. J. Baerends, C. Fonseca Guerra, S. J. A. van Gisbergen, J. G. Snijders and T. Ziegler, *J. Comput. Chem.*, 2001, **22**, 931–967.

74 A. D. Becke, *Phys. Rev. A: At., Mol., Opt. Phys.*, 1988, **38**, 3098–3100.

75 J. P. Perdew, *Phys. Rev. B: Condens. Matter Mater. Phys.*, 1986, **33**, 8822–8824.

76 M. Cossi, N. Rega, G. Scalmani and V. Barone, *J. Comput. Chem.*, 2003, **24**, 669–681.

77 V. Barone and M. Cossi, *J. Phys. Chem. A*, 1998, **102**, 1995–2001.

78 M. J. Frisch, G. W. Trucks, H. B. Schlegel, G. E. Scuseria, M. A. Robb, J. R. Cheeseman, G. Scalmani, V. Barone, B. Mennucci, G. A. Petersson, H. Nakatsuji, M. Caricato, X. Li, H. P. Hratchian, A. F. Izmaylov, J. Bloino, G. Zheng, J. L. Sonnenberg, M. Hada, M. Ehara, K. Toyota, R. Fukuda, J. Hasegawa, M. Ishida, T. Nakajima, Y. Honda, O. Kitao, H. Nakai, T. Vreven, J. A. Montgomery Jr., J. E. Peralta, F. Ogliaro, M. Bearpark, J. J. Heyd, E. Brothers, K. N. Kudin, V. N. Staroverov, R. Kobayashi, J. Normand, K. Raghavachari, A. Rendell, J. C. Burant, S. S. Iyengar, J. Tomasi, M. Cossi, N. Rega, N. J. Millam, M. Klene, J. E. Knox, J. B. Cross, V. Bakken, C. Adamo, J. Jaramillo, R. Gomperts, R. E. Stratmann, O. Yazyev, A. J. Austin, R. Cammi, C. Pomelli, J. W. Ochterski, R. L. Martin, K. Morokuma, V. G. Zakrzewski, G. A. Voth, P. Salvador, J. J. Dannenberg, S. Dapprich, A. D. Daniels, Ö. Farkas, J. B. Foresman, J. V. Ortiz, J. Cioslowski and D. J. Fox, *Gaussian 09, Revision A.1*, Gaussian, Inc., Wallingford CT, 2009.

79 J. P. Muscat and D. M. Newns, *Prog. Surf. Sci.*, 1978, **9**, 1–43.

80 C. Cohen-Tannoudji, B. Diu and F. Laloe, *Quantum Mechanics*, Wiley, 1977, vol. 2, p. 1524.

81 P. Persson, M. J. Lundqvist, R. Ernstorfer, W. A. Goddard and F. Willig, *J. Chem. Theory Comput.*, 2006, **2**, 441–451.

82 M. J. Lundqvist, M. Nilsing, S. Lunell, B. Åkermark and P. Persson, *J. Phys. Chem. B*, 2006, **110**, 20513–20525.

83 P. Persson and M. J. Lundqvist, *J. Phys. Chem. B*, 2005, **109**, 11918–11924.

84 P. Persson, S. Lunell and L. Ojamäe, *Int. J. Quantum Chem.*, 2002, **89**, 172–180.

85 E. Ronca, G. Marotta, M. Pastore and F. De Angelis, *J. Phys. Chem. C*, 2014, **118**, 16927–16940.
86 I. Kondov, M. Čížek, C. Benesch, H. Wang and M. Thoss, *J. Phys. Chem. C*, 2007, **111**, 11970–11981.
87 J. Li, H. Wang, P. Persson and M. Thoss, *J. Chem. Phys.*, 2012, **137**, 22A529.
88 E. M. Barea and J. Bisquert, *Langmuir*, 2013, **29**, 8773–8781.
89 B. C. O'Regan, I. López-Duarte, M. V. Martínez-Díaz, A. Forneli, J. Albero, A. Morandeira, E. Palomares, T. Torres and J. R. Durrant, *J. Am. Chem. Soc.*, 2008, **130**, 2906–2907.
90 S. Altobello, R. Argazzi, S. Caramori, C. Contado, S. Da Fré, P. Rubino, C. Choné, G. Larramona and C. A. Bignozzi, *J. Am. Chem. Soc.*, 2005, **127**, 15342–15343.
91 J. Wu, Z. Lan, J. Lin, M. Huang, Y. Huang, L. Fan and G. Luo, *Chem. Rev.*, 2015, **115**, 2136–2173.
92 M. Pastore, T. Etienne and F. De Angelis, *J. Mater. Chem. C*, 2016, **4**, 4346–4373.

VI. General Conclusion

The understanding of the photo-induced free carrier formation and recombination dynamics is critical to improve the PV performance of solar cells. Since these processes occur in the ps-ns timescale, time-resolved spectroscopies are versatile experimental methods to access to such ultrafast spectro-temporal dynamics. As shown by many groups and in numerous publications, the spectro-temporal information allows, in principle, to 1) identify the photo-induced species (excited states, excitons, CT states, polarons, etc. and how they are related to each other by a reaction scheme, and 2) to decipher the transition rates or lifetimes of these species, as well as the quantum yields of the corresponding transitions.

In this work, femtosecond broadband transient absorption spectroscopy has been used with a spectral region from 300 to 950 nm, a long delay time range (up to 6 ns) and with sub-60 fs time resolution. However, the temporal and spectral superposition of different contributions renders challenging the interpretation of photoinduced reactions. Thus, time-resolved fluorescence measurements were carried out to investigate the dynamics of the excited state and its quenching processes. The identification of newly formed species, such as the charged species needs the combination of transient spectroscopies with other techniques, such as spectro-electro-chemistry and THz spectroscopy (not used in this work) to determine their spectral signature and to characterize their dynamics, respectively.

However, the classic time-resolved spectroscopies have their limitations: 1) narrow spectral detection and 2) lack of spatial information. To observe and determine the species involved in the photo-induced processes, the spectral detection has to be in their characteristic features range, *e.g.* it will be helpful to identify the electron injection in the mid-IR range. Furthermore, the morphology contributes significantly to the studies of their active layer. The typical probe size (100 μm diameter) allows only a global resolution averaged over several crystalline domains. Even though, the morphology of the films was probed by other techniques, such as TEM and electron diffraction, the heterogeneity of the molecular conformations, as discussed for the D-A oligomer system, complicate the understanding of the whole photo-induced scenario.

The study of D-A oligomer in the solution shows a clear impact on the intramolecular interactions. The different spacers (δ or δ_+) changes the mechanism to form the charge transfer state (through FRET or not, respectively) and its rate constant. Furthermore, the chemical design on the terminal anime (δ_-) extends the charge transfer state recombination lifetime (2~3 times). Supremely, by reducing the solvent polarity, the charge transfer state recombination is down up to one order of magnitude, indicating the environment has a stronger influence.
In films, the prediction of the dominant interaction of molecule and environment is observed. Despite the modification of D moiety, the similar ns-lived photo-product states are formed. Even through direct experiment evidence are needed to identify which state it is, the most plausible possibility is the polaron pair which is a long-lived and non-radiative state.

For the perspective, the key point is to determine the photoproduct state in films. Since the external electric field can only affect the polaron pair not excimer, the charge modulation spectroscopy is another possible alternative to study the effect of an applied bias on the OSCs and observe the charged species spectra. Additional investigations of spatial information are in particular interesting, by combining the classic time-resolved spectroscopy with microscopy, such as ref 177.

It's essential to mention that the best PCE based on OSCs (11.5% in Figure II.1) is still much lower than that based on inorganic solar cells (46%, not shown) and will probably be hard to reach the record in the future. Furthermore, the relative shorter device lifetime of OSCs also limits its applications in some long term and hard to replace projects, such as the solar panels for satellites or float chambers to study the marine. However, due to its facile fabrication on the

flexible large area, low weight and low price, the OSCs still can find its own market share.
The work of Fe(II) complexes results in the record ^{3}MLCT state lifetime at room temperature in the solution by transient absorption spectroscopy.[172] The insight understanding of their photophysical properties is pointed out with the combination of quantum chemical calculation. Through the effect of electronic structure, the ^{3}MC state has a higher energy level than ^{3}MLCT state. The *N*-substitution could further contribute to extend the ^{3}MLCT state lifetime of those complexes.

Even though 26 ps ^{3}MLCT state lifetime is achieved in the solution, the PCE of the corresponding device[154,175] does not have significant improvement compared with other classic Fe(II) complexes. [155] Thus, two possibilities could lead to this effect 1) poor electron injection efficiency from the ^{1,3}MLCT states or/and 2) fast electron-hole recombination at the interface. Wärnmark *et al.* proposed that the electron injection efficiency is close-to-unity. [176] In our option, two-part ligands (the bottom part is grafted on TiO_2 and the top part is free) have similar electronic levels. Once the ^{3}MLCT state is located on the top, the electron injection is forbidden due to the geometry, and relaxation to the ground state occurs. Therefore, the electron injection competes with relaxation to the ground state. Thus, the estimation of the electron injection efficiency based on lifetimes is doubtful.

In the term of the outlook, direct evidence is needed to prove our hypothesis. Besides the time-resolved fluorescence spectroscopy and THz spectroscopy, the time-resolved X-ray spectroscopy could provide more evidence of the electron injection and interfacial recombination. As a cheap photosensitizer, besides the DSSCs, Fe(II) complexes with further modifications, such as adding spacer or secondary complex unit also can be used, not only for DSSCs, but also for other applications, such as water splitting.

This thesis could be achieved thanks to fruitful collaborations with : i) Pierre-Olivier Schwartz and Stéphane Méry (D-A synthesis, IPCMS), Nicolas Leclerc (D-A synthesis, ICPEES), Pierre Eisenbrandt, Matthias Polkehn, Irene Burghardt (D-A quantum calculation, Goethe University Frankfurt) Adrian Ruff, Kirsten Bruchlos, Sabine Ludwigs (Spectro-electro-chemistry, IPOC) within the French ANR PICASSO project and joint DFG/ANR MolNanoMat project, ii) and Thibaut Duchanois, Marc Beley and Philippe. C. Gros (Fe(II) synthesis, Université de Lorraine), Thibaud Etienne, Mariachiara Pastore, Antonio Monari and Xavier Assfeld (Fe(II) quantum chemistry calculation, Université de Lorraine) within the French ANR PhotIron project.

During the last past four years, I was actively involved in two other projects: 1) Ir-Pt complexes for water splitting with Dong Ryeol Whang, Soo Young Park (Ir-Pt synthesis, Seoul National University) and Sandra Mosquera Vazquez, Bernhard Lang, Éric Vauthey (ns-TA measurements, University of Geneva), 2) and organic-inorganic hybrid perovskites for solar cells with Yu-Che Hsiao, Ting Wu, Bin Hu (University of Tennessee).

Additional peer-reviewed articles published during the doctoral study.

1. D.-R. Whang, **L. Liu**, S. Mosquera Vazquez, A. Ruff, S. Ludwigs, B. Lang, É. Vauthey, S. Haacke, and S.-Y. Park ‘‘Highly efficient visible light-driven hydrogen production from water with an Ir(III)-Pt(II) supramolecular device: Beyond molecules’’ *in preparation*
2. P.-Y. Lin, T. Wu, M. Ahmadi, **L. Liu**, S. Haacke, T.-F. Guo, B. Hu Simultaneously Enhancing Dissociation and Suppressing Recombination in Perovskite Solar Cells by Using NiOx Transport Interlayer *Nano energy* **2017** 36 95
3. Q. Liu, Y.-C. Hsiao, M. Ahmadi, T. Wu, **L. Liu**, S. Haacke, H. Wang, B. Hu ‘‘N and p-type properties in organo-metal halide perovskites studied by Seebeck effects’’ *Organic Electronics* **2016**, *35*, 216
4. T. Roland, E. Heyer, **L. Liu**, A. Ruff, S. Ludwigs, R. Ziessel and S. Haacke ‘‘A Detailed Analysis of Multiple Photoreactions in a Light-Harvesting Molecular Triad with Overlapping Spectra by Ultrafast Spectroscopy’’ *J. Phys. Chem. C*, **2014**, *118*, 24290

Appendix I. Donor-Acceptor molecules for organic photovoltaics

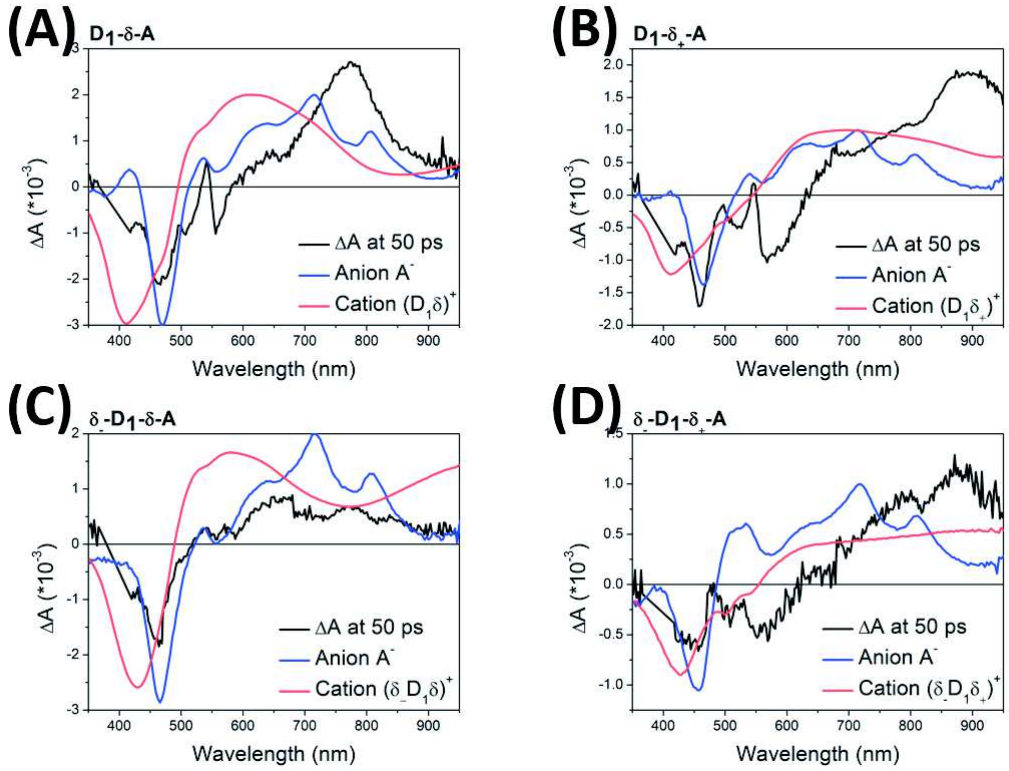

Figure A.I.1 Comparisons of differential absorption spectrum at 50 ps obtained by pump-probe (black curve) and differential absorption spectrum of anion (blue curve) and cation (red curve) obtained by spectro-electro-chemistry. No direct spectral evidence shows the existence of CT state.

Appendix II. Iron complexes

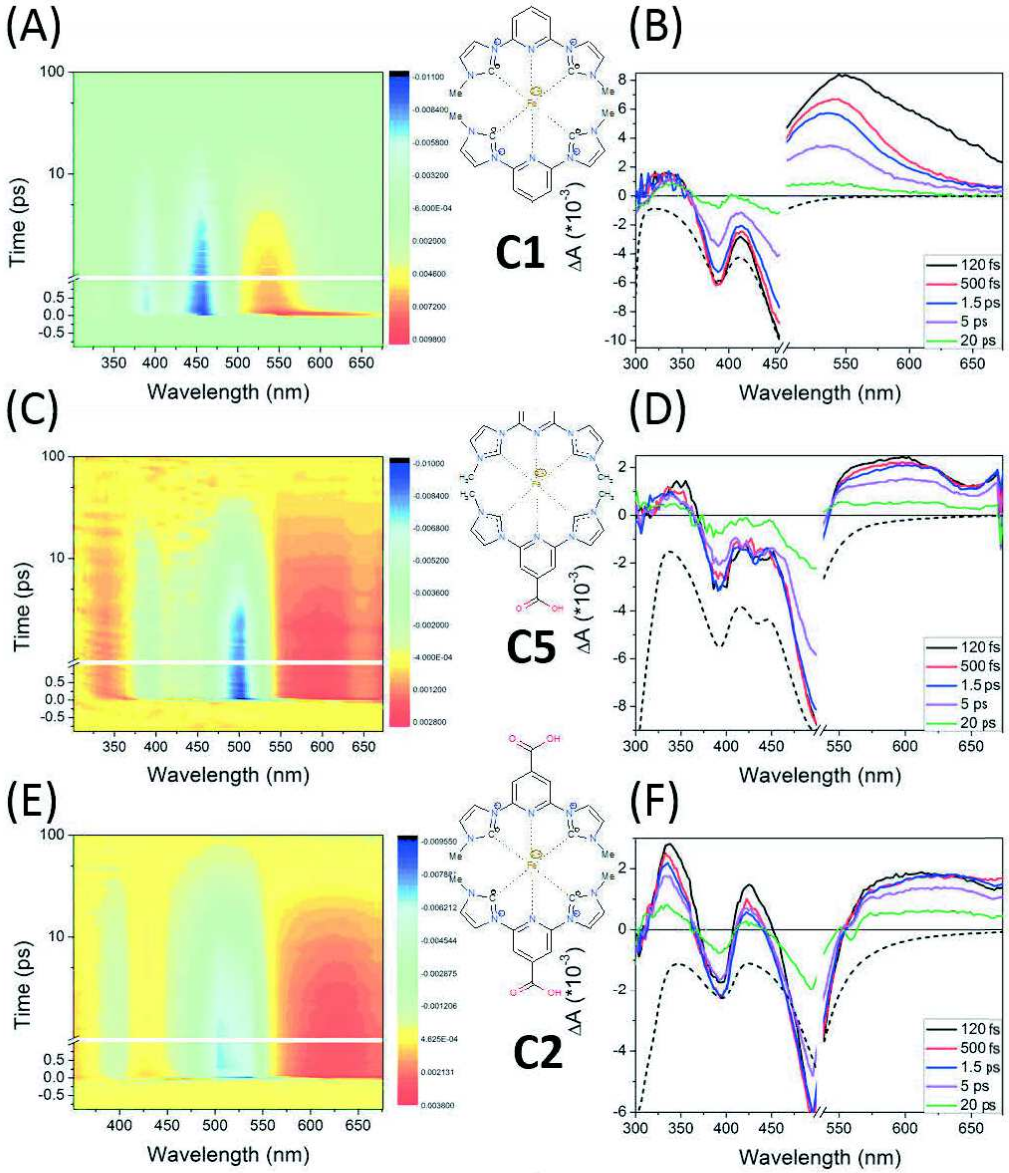

Figure A.II.1 Transient absorption datasets to study the carboxyl group effect of **C1** ((A) and (B)), **C5** ((C) and (D)) and **C2** ((E) and (F)) in MeCN

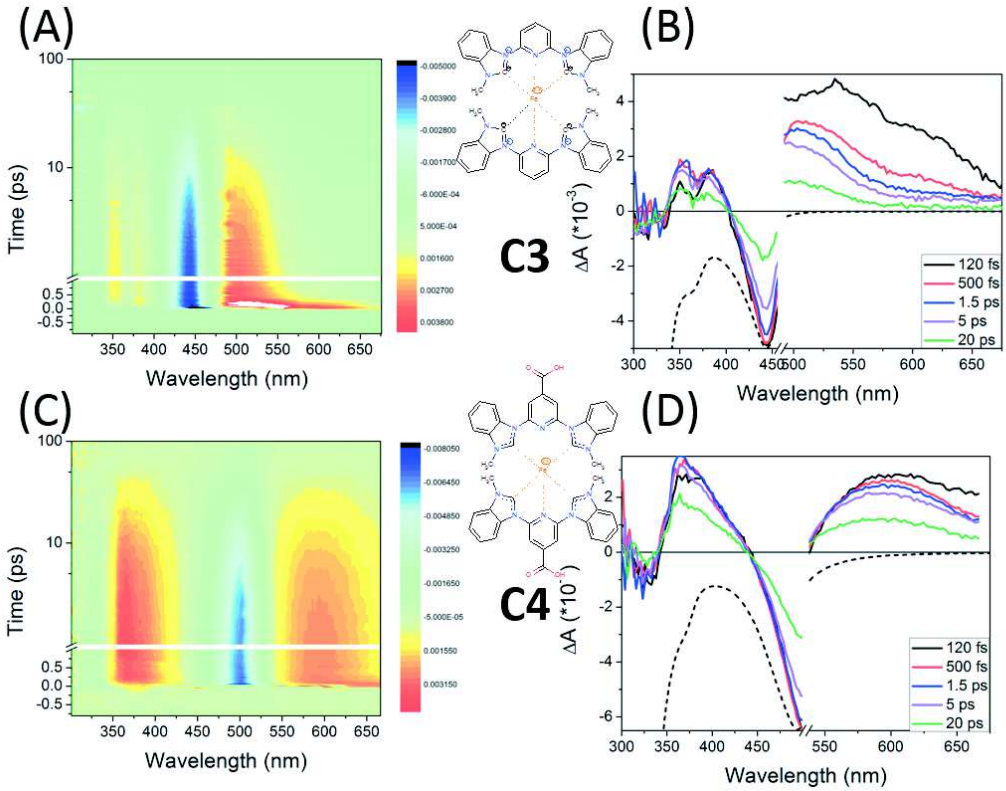

Figure A.II.2 Transient absorption datasets to study the ligand effect of **C2** ((A) and (B)) and **C4** ((C) and (D)) in MeCN

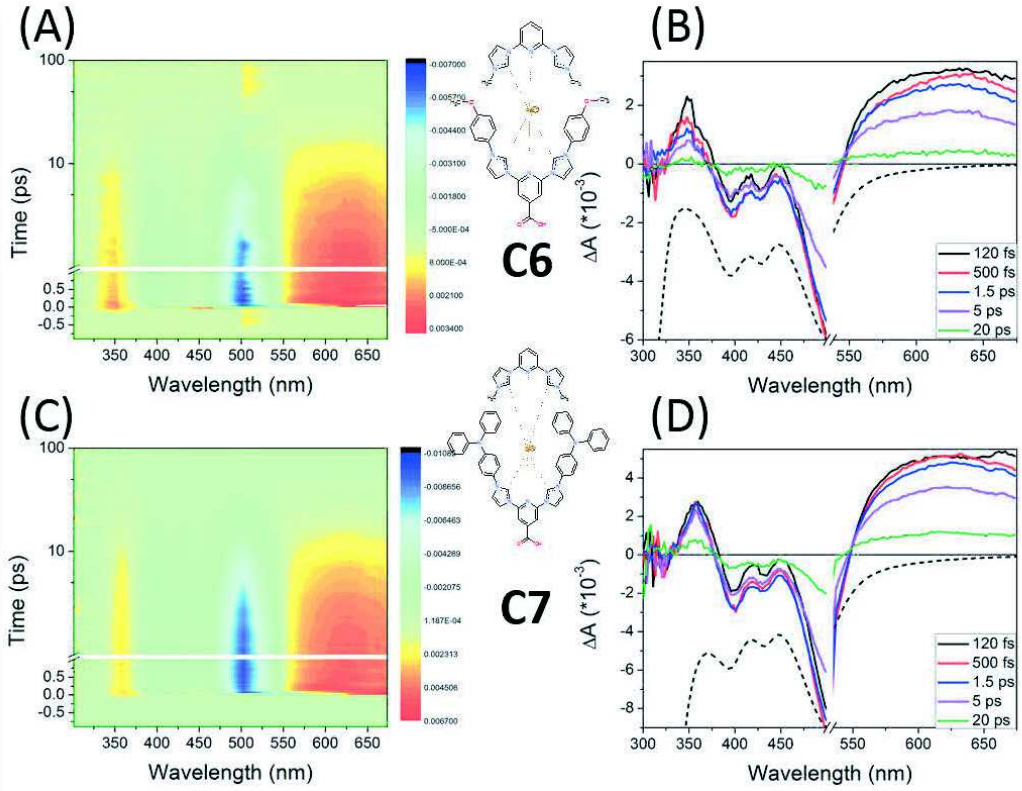

Figure A.II.3 Transient absorption datasets to study the N-substitution effect of **C6** ((A) and (B)) and **C7** ((C) and (D)) in MeCN

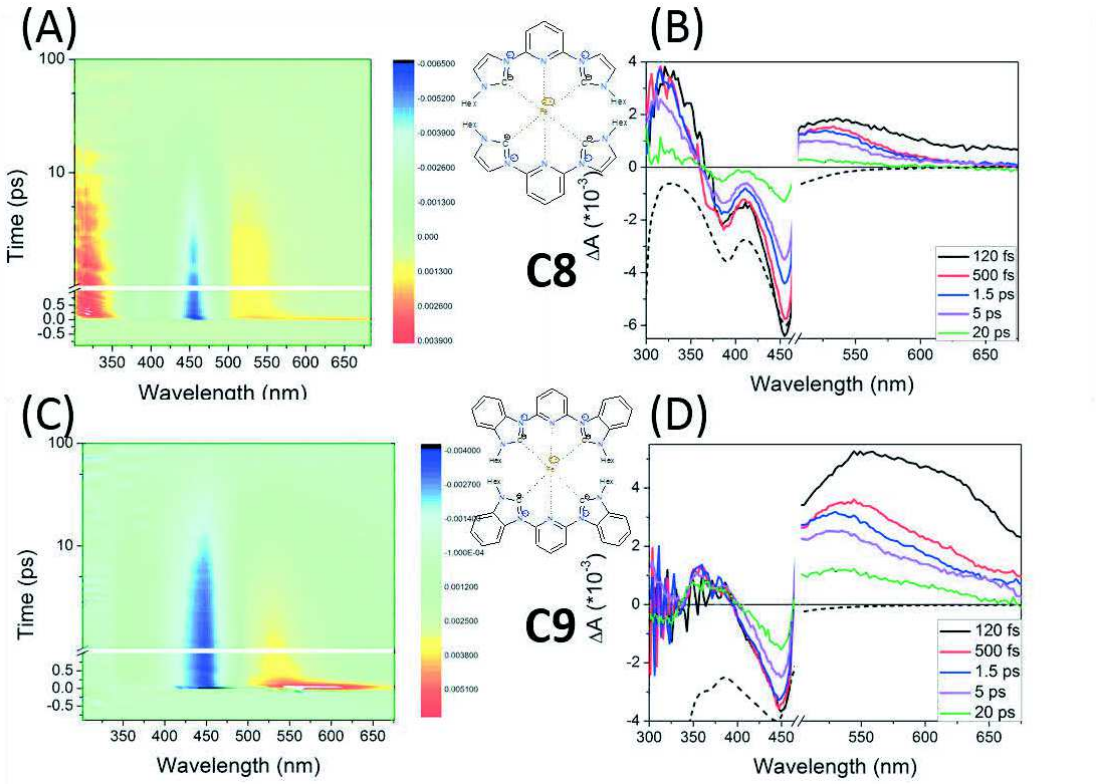

Figure A.II.4 Transient absorption datasets to study the rigidity of **C8** ((A) and (B)) and **C9** ((C) and (D)) in MeCN

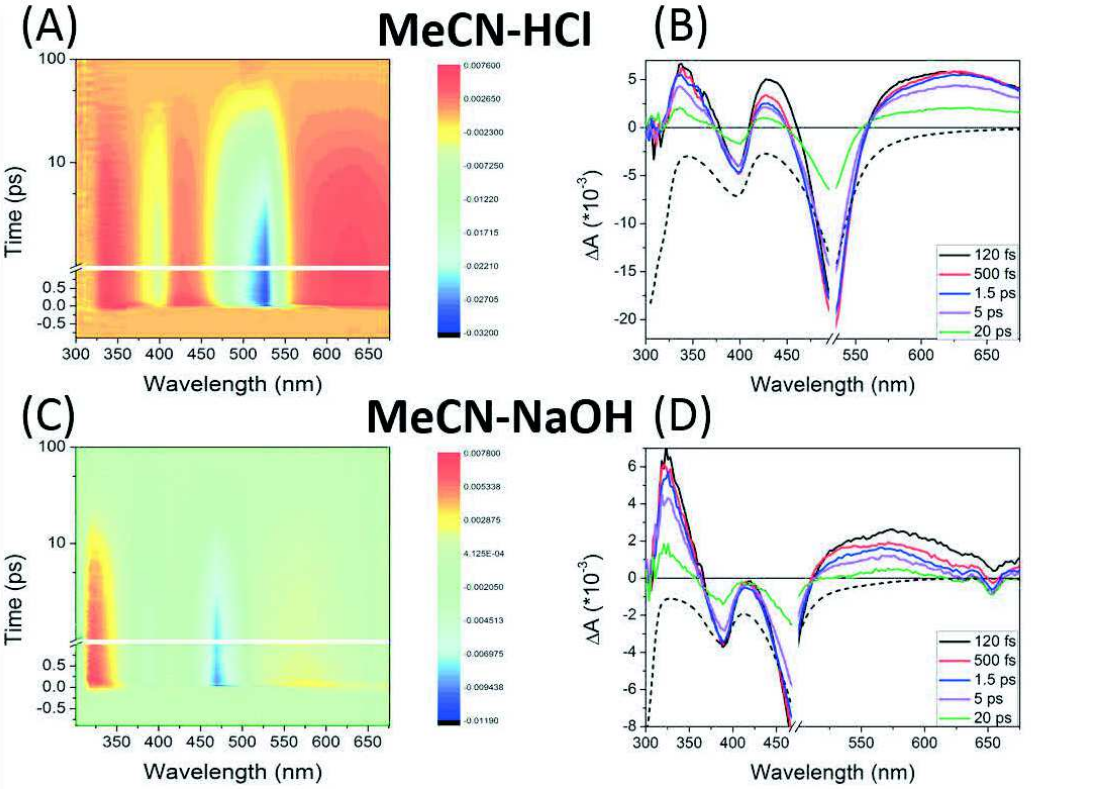

Figure A.II.5 Transient absorption datasets to study the pH effect of **C2-HCl** ((A) and (B)) and **C2-NaOH** ((C) and (D)) in MeCN

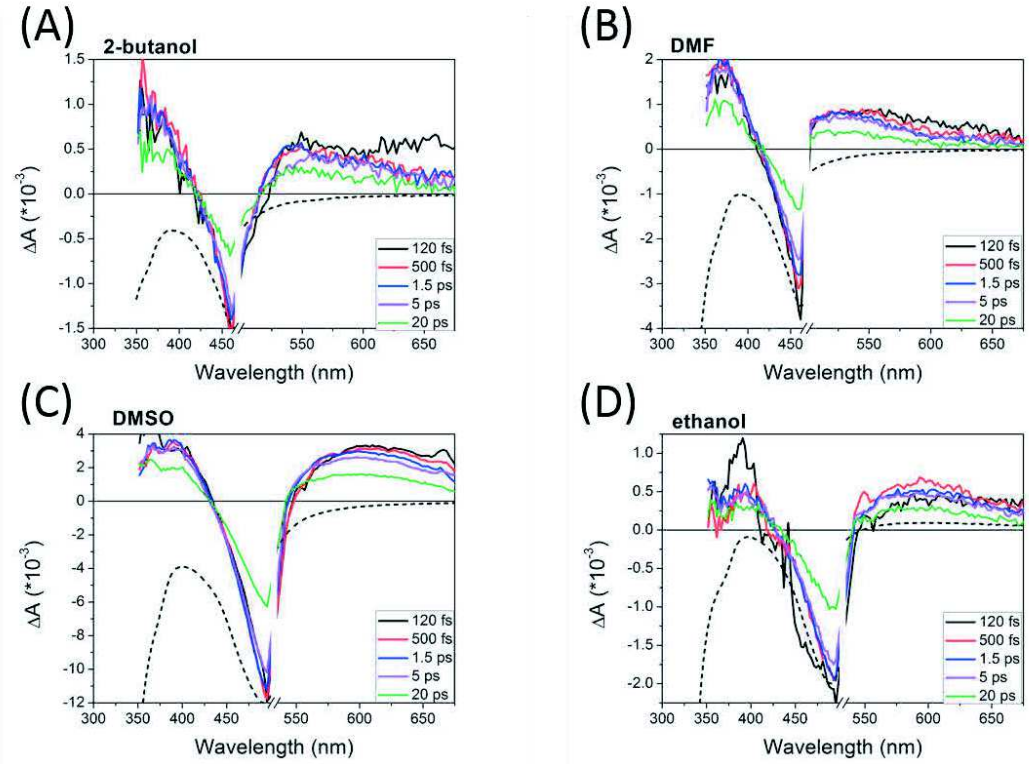

Figure A.II.6 Transient absorption datasets to study the solvent effect of **C2** in (A) 2-butanol (B) DMF (C) DMSO and (D) ethanol.

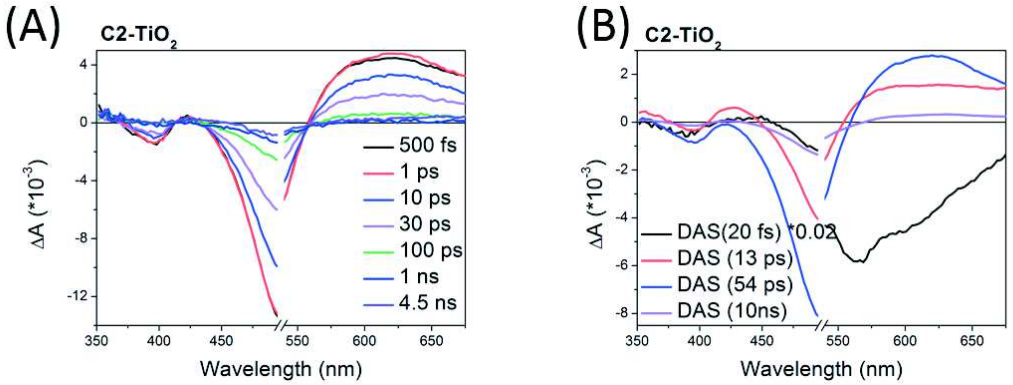

Figure A.II.7 (A) Spectral evolution and (B) Decay-Associated differential Spectra of **C2**-TiO_2

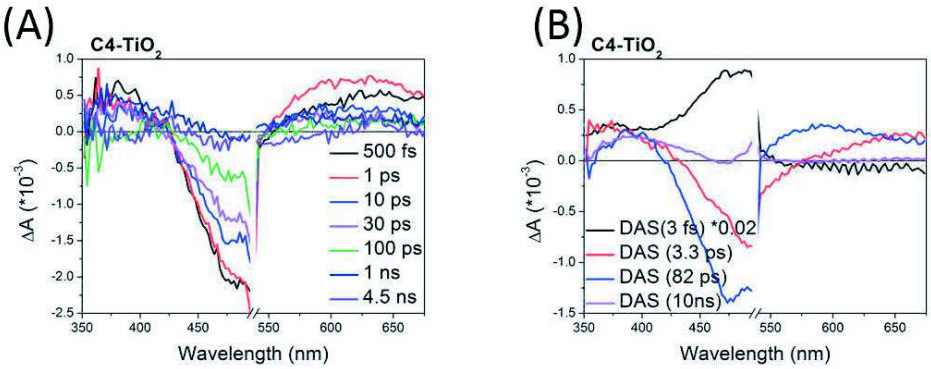

Figure A.II.8 (A) Spectral evolution and (B) Decay-Associated differential Spectra of **C4**-TiO_2

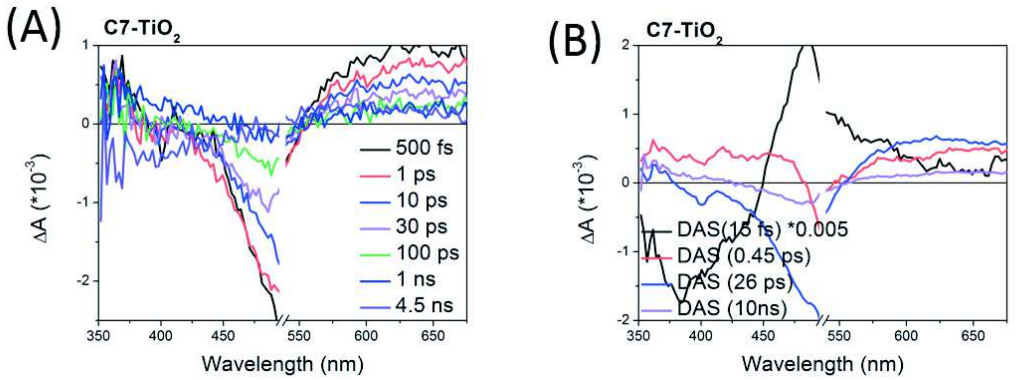

Figure A.II.9 (A) Spectral evolution and (B) Decay-Associated differential Spectra of **C7**-TiO_2

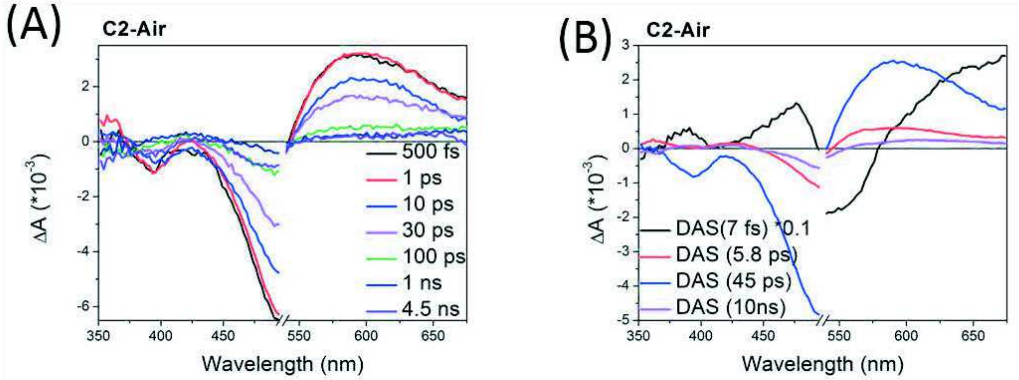

Figure A.II.10 (A) Spectral evolution and (B) Decay-Associated differential Spectra of **C2**-Air

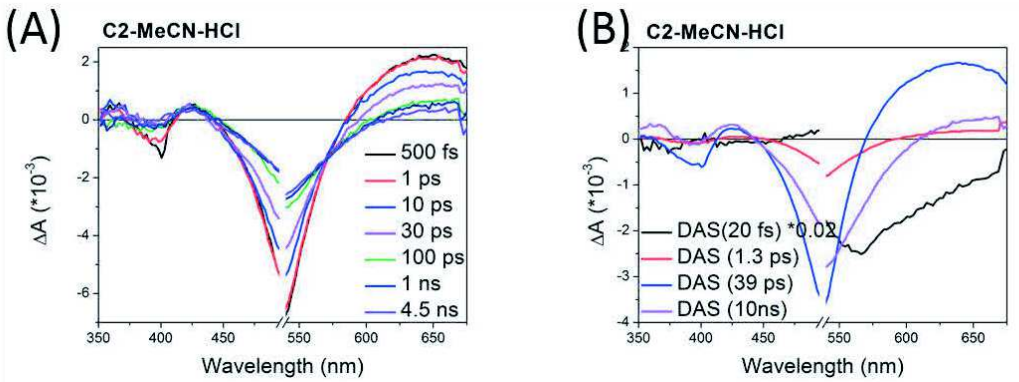

Figure A.II.11 (A) Spectral evolution and (B) Decay-Associated differential Spectra of **C2**-MeCN-HCl

Reference

(1) Solar spectrum. http://klimat.czn.uj.edu.pl/media/archive/11592.jpg.

(2) Spano, F. C. The Spectral Signatures of Frenkel Polarons in H- and J-Aggregates. *Accounts of chemical research* **2010**, *43*, 429-439.

(3) Lanzani, G.: *The Photophysics behind Photovoltaics and Photonics*; Wiley VCH, 2012.

(4) Oelkrag, D.; Egelhaaf, H. J.; Gierschner, J.; Tompert, A. Electronic deactivation in single chains, nano-aggregates and ultrathin films of conjugated oligomers. *Synthetic Metals* **1996**, *76*, 249-253.

(5) Spano, F. C. Excitons in conjugated oligomer aggregates, films, and crystals. *Annual review of physical chemistry* **2006**, *57*, 217-243.

(6) Wurthner, F.; Saha-Moller, C. R.; Fimmel, B.; Ogi, S.; Leowanawat, P.; Schmidt, D. Perylene Bisimide Dye Assemblies as Archetype Functional Supramolecular Materials. *Chemical reviews* **2016**, *116*, 962-1052.

(7) Clark, J.; Silva, C.; Friend, R. H.; Spano, F. C. Role of intermolecular coupling in the photophysics of disordered organic semiconductors: aggregate emission in regioregular polythiophene. *Physical review letters* **2007**, *98*, 206406.

(8) Spano, F. C.; Clark, J.; Silva, C.; Friend, R. H. Determining exciton coherence from the photoluminescence spectral line shape in poly(3-hexylthiophene) thin films. *J Chem Phys* **2009**, *130*, 074904.

(9) Wurthner, F. Perylene bisimide dyes as versatile building blocks for functional supramolecular architectures. *Chemical communications* **2004**, 1564-1579.

(10) Hestand, N. J.; Spano, F. C. Interference between Coulombic and CT-mediated couplings in molecular aggregates: H- to J-aggregate transformation in perylene-based pi-stacks. *J Chem Phys* **2015**, *143*, 244707.

(11) Lower, S. K.; El-Sayed, M. A. The Triplet State and Molecular Electronic Processes in Organic Molecules. *Chemical reviews* **1966**, *66*, 199-241.

(12) El-Sayed, M. A. Triplet state. Its radiative and nonradiative properties. *Accounts of chemical research* **1968**, *1*, 8-16.

(13) Kasha, M. Characterization of electronic transitions in complex molecules. *Discussions of the Faraday Society* **1950**, *9*, 14-19.

(14) Vavilov, S. Die Fluoreszenzausbeute von Farbstof losungen als Funktion der Wellenlange des anregenden Lichtes. *Z. Physik* **1927**, *42*, 9.

(15) Lakowicz, J. R.: *Principles of Fluorescence Spectroscopy*; Springer.

(16) Bastard, G.; Brum, J. A.; Ferreira, R. Electronic States in Semiconductor Heterostructures. *Solid State Physics* **1991**, *44*, 229-415.

(17) Klan, P.; Wirz, J.: *Photochemistry of organic compounds from concepts to practice*; Wiley-Blackwell, 2009.

(18) Pope, M.; Swenberg., C. E.: *Electronic processes in organic crystals and polymers*; Oxford University Press New York, 1999; Vol. 74.

(19) Rehm, D.; Weller, A. Kinetics of Fluorescence Quenching by Electron and H-Atom Transfer. *Israel J. Chem.* **1970**, *8*, 259.

(20) Marcus, R. A.; Sutin, N. Electron transfers in chemistry and biology. *Biochimica et Biophysica Acta (BBA) - Reviews on Bioenergetics* **1985**, *811*, 265-322.

(21) Clarke, T. M.; Durrant, J. R. Charge Photogeneration in Organic Solar Cells. *Chemical reviews* **2010**, *110*, 6736-6767.

(22) Ulstrup, J.; Jortner, J. The effect of intramolecular quantum modes on free energy relationships for electron transfer reactions. *The Journal of chemical physics* **1975**, *63*, 4358-4368.

(23) Miller, J. R.; Calcaterra, L. T.; Closs, G. L. Intramolecular long-distance electron transfer in radical anions. The effects of free energy and solvent on the reaction rates. *Journal of the American Chemical Society* **1984**, *106*, 3047-3049.

(24) Closs, G. L.; Miller, J. R. Intramolecular Long-Distance Electron Transfer in Organic Molecules. *Science* **1988**, *240*, 440.

(25) Mataga, N.; Asahi, T.; Kanda, Y.; Okada, T.; Kakitani, T. The bell-shaped energy gap dependence of the charge recombination reaction of geminate radical ion pairs produced by fluorescence quenching reaction in acetonitrile solution. *Chemical Physics* **1988**, *127*, 249-261.

(26) NREL-Power conversion efficiency. www.nrel.gov/ncpv.

(27) Kippelen, B. Evaluating the power conversion values of organic solar cells. **2009**.

(28) Luque, A.; Hegedus, S.: *Handbook of Photovoltaic Science and Engineering*; Wiley VCH, 2012.

(29) Green, M. A.; Emery, K.; Hishikawa, Y.; Warta, W.; Dunlop, E. D. Solar cell efficiency tables (Version 45). *Progress in Photovoltaics: Research and Applications* **2015**, *23*, 1-9.

(30) Muntwiler, M.; Yang, Q.; Tisdale, W. A.; Zhu, X. Y. Coulomb barrier for charge separation at an organic semiconductor interface. *Physical review letters* **2008**, *101*, 196403.

(31) On the Theory of Oxidation - Reduction Reactions Involving Electron Transfer. I. *The Journal of chemical physics* **1956**, *24*, 966-978.

(32) Onsager, L. Initial Recombination of Ions. *Physical Review* **1938**, *54*, 554-557.

(33) Braun, C. L. Electric field assisted dissociation of charge transfer states as a mechanism of photocarrier production. *The Journal of chemical physics* **1984**, *80*, 4157-4161.

(34) Ohkita, H.; Cook, S.; Astuti, Y.; Duffy, W.; Tierney, S.; Zhang, W.; Heeney, M.;

McCulloch, I.; Nelson, J.; Bradley, D. D. C.; Durrant, J. R. Charge Carrier Formation in Polythiophene/Fullerene Blend Films Studied by Transient Absorption Spectroscopy. *Journal of the American Chemical Society* **2008**, *130*, 3030-3042.

(35) Etzold, F.; Howard, I. A.; Mauer, R.; Meister, M.; Kim, T.-D.; Lee, K.-S.; Baek, N. S.; Laquai, F. Ultrafast Exciton Dissociation Followed by Nongeminate Charge Recombination in PCDTBT:PCBM Photovoltaic Blends. *Journal of the American Chemical Society* **2011**, *133*, 9469-9479.

(36) Bakulin, A. A.; Rao, A.; Pavelyev, V. G.; van Loosdrecht, P. H.; Pshenichnikov, M. S.; Niedzialek, D.; Cornil, J.; Beljonne, D.; Friend, R. H. The role of driving energy and delocalized States for charge separation in organic semiconductors. *Science* **2012**, *335*, 1340-1344.

(37) Grancini, G.; Maiuri, M.; Fazzi, D.; Petrozza, A.; Egelhaaf, H. J.; Brida, D.; Cerullo, G.; Lanzani, G. Hot exciton dissociation in polymer solar cells. *Nature Materials* **2013**, *12*, 29-33.

(38) Jailaubekov, A. E.; Willard, A. P.; Tritsch, J. R.; Chan, W.-L.; Sai, N.; Gearba, R.; Kaake, L. G.; Williams, K. J.; Leung, K.; Rossky, P. J.; Zhu, X. Y. Hot charge-transfer excitons set the time limit for charge separation at donor/acceptor interfaces in organic photovoltaics. *Nature Materials* **2013**, *12*, 66-73.

(39) Gélinas, S.; Rao, A.; Kumar, A.; Smith, S. L.; Chin, A. W.; Clark, J.; van der Poll, T. S.; Bazan, G. C.; Friend, R. H. Ultrafast Long-Range Charge Separation in Organic Semiconductor Photovoltaic Diodes. *Science* **2014**, *343*, 512.

(40) Dimitrov, S. D.; Durrant, J. R. Materials Design Considerations for Charge Generation in Organic Solar Cells. *Chemistry of Materials* **2014**, *26*, 616-630.

(41) De, S.; Pascher, T.; Maiti, M.; Jespersen, K. G.; Kesti, T.; Zhang, F.; Inganäs, O.; Yartsev, A.; Sundström, V. Geminate Charge Recombination in Alternating Polyfluorene Copolymer/Fullerene Blends. *Journal of the American Chemical Society* **2007**, *129*, 8466-8472.

(42) Tang, C. W. Two‐layer organic photovoltaic cell. *Applied Physics Letters* **1986**, *48*, 183-185.

(43) Gulbinas, V.; Mineviciute, I.; Hertel, D.; Wellander, R.; Yartsev, A.; Sundstrom, V. Exciton diffusion and relaxation in methyl-substituted polyparaphenylene polymer films. *The Journal of chemical physics* **2007**, *127*, 144907.

(44)Halls, J. J. M.; Walsh, C. A.; Greenham, N. C.; Marseglia, E. A.; Friend, R. H.; Moratti, S. C.; Holmes, A. B. Efficient photodiodes from interpenetrating polymer networks. *Nature* **1995**, *376*, 498-500.

(45) Yu, G.; Gao, J.; Hummelen, J. C.; Wudl, F.; Heeger, A. J. Polymer Photovoltaic Cells: Enhanced Efficiencies via a Network of Internal Donor-Acceptor Heterojunctions. *Science*

1995, *270*, 1789.

(46) Yu, G.; Heeger, A. J. Charge separation and photovoltaic conversion in polymer composites with internal donor/acceptor heterojunctions. *Journal of Applied Physics* **1995**, *78*, 4510-4515.

(47) Dang, M. T.; Hirsch, L.; Wantz, G. P3HT:PCBM, Best Seller in Polymer Photovoltaic Research. *Advanced Materials* **2011**, *23*, 3597-3602.

(48) Dou, L.; You, J.; Hong, Z.; Xu, Z.; Li, G.; Street, R. A.; Yang, Y. 25th Anniversary Article: A Decade of Organic/Polymeric Photovoltaic Research. *Advanced Materials* **2013**, *25*, 6642-6671.

(49) Lu, L.; Zheng, T.; Wu, Q.; Schneider, A. M.; Zhao, D.; Yu, L. Recent Advances in Bulk Heterojunction Polymer Solar Cells. *Chemical reviews* **2015**, *115*, 12666-12731.

(50) Li, N.; Perea, J. D.; Kassar, T.; Richter, M.; Heumueller, T.; Matt, G. J.; Hou, Y.; Güldal, N. S.; Chen, H.; Chen, S.; Langner, S.; Berlinghof, M.; Unruh, T.; Brabec, C. J. Abnormal strong burn-in degradation of highly efficient polymer solar cells caused by spinodal donor-acceptor demixing. *Nature communications* **2017**, *8*, 14541.

(51) Chen, Z.; Cai, P.; Chen, J.; Liu, X.; Zhang, L.; Lan, L.; Peng, J.; Ma, Y.; Cao, Y. Low Band-Gap Conjugated Polymers with Strong Interchain Aggregation and Very High Hole Mobility Towards Highly Efficient Thick-Film Polymer Solar Cells. *Advanced Materials* **2014**, *26*, 2586-2591.

(52) Zhao, J.; Li, Y.; Yang, G.; Jiang, K.; Lin, H.; Ade, H.; Ma, W.; Yan, H. Efficient organic solar cells processed from hydrocarbon solvents. *Nature Energy* **2016**, *1*, 15027.

(53) Nielsen, C. B.; Holliday, S.; Chen, H. Y.; Cryer, S. J.; McCulloch, I. Non-fullerene electron acceptors for use in organic solar cells. *Accounts of chemical research* **2015**, *48*, 2803-2812.

(54) Bin, H.; Zhang, Z. G.; Gao, L.; Chen, S.; Zhong, L.; Xue, L.; Yang, C.; Li, Y. Non-Fullerene Polymer Solar Cells Based on Alkylthio and Fluorine Substituted 2D-Conjugated Polymers Reach 9.5% Efficiency. *J Am Chem Soc* **2016**, *138*, 4657-4664.

(55) Pivrikas, A.; Neugebauer, H.; Sariciftci, N. S. Influence of processing additives to nano-morphology and efficiency of bulk-heterojunction solar cells: A comparative review. *Solar Energy* **2011**, *85*, 1226-1237.

(56) Schwartz, P. O.; Biniek, L.; Zaborova, E.; Heinrich, B.; Brinkmann, M.; Leclerc, N.; Mery, S. Perylenediimide-based donor-acceptor dyads and triads: impact of molecular architecture on self-assembling properties. *Journal of the American Chemical Society* **2014**, *136*, 5981-5992.

(57) Biniek, L.; Schwartz, P.-O.; Zaborova, E.; Heinrich, B.; Leclerc, N.; Mery, S.; Brinkmann, M. Zipper-like molecular packing of donor-acceptor conjugated co-oligomers based on perylenediimide. *Journal of Materials Chemistry C* **2015**, *3*, 3342-3349.

(58) Loi, M. A.; Toffanin, S.; Muccini, M.; Forster, M.; Scherf, U.; Scharber, M. Charge Transfer Excitons in Bulk Heterojunctions of a Polyfluorene Copolymer and a Fullerene Derivative. *Advanced Functional Materials* **2007**, *17*, 2111-2116.

(59) DSSCs.

(60) Hagfeldt, A.; Boschloo, G.; Sun, L.; Kloo, L.; Pettersson, H. Dye-Sensitized Solar Cells. *Chemical reviews* **2010**, *110*, 6595-6663.

(61) Nazeeruddin, M. K.; Baranoff, E.; Grätzel, M. Dye-sensitized solar cells: A brief overview. *Solar Energy* **2011**, *85*, 1172-1178.

(62) Gerischer, H.; Tributsch, H. *Ber. Bunsen-Ges. Phys. Chem.* **1968**, *72*, 437.

(63) Gerischer, H.; Michel-Beyerle, M. E.; Rebentrost, F.; Tributsch, H. *Electrochim. Acta* **1968**, *13*, 1509.

(64) O'Regan, B.; Grätzel, M. low-cost, high-efficiency solar cell based on dye-sensitized colloidal TiO2 films. *Nature* **1991**, *353*, 737.

(65) Nazeeruddin, M. K.; Kay, A.; Rodicio, I.; Humphry-Baker, R.; Mueller, E.; Liska, P.; Vlachopoulos, N.; Grätzel, M. *J. Am. Chem. Soc.* **1993**, *115*, 6382.

(66) Mathew, S.; Yella, A.; Gao, P.; Humphry-Baker, R.; CurchodBasile, F. E.; Ashari-Astani, N.; Tavernelli, I.; Rothlisberger, U.; NazeeruddinMd, K.; Grätzel, M. Dye-sensitized solar cells with 13% efficiency achieved through the molecular engineering of porphyrin sensitizers. *Nature chemistry* **2014**, *6*, 242-247.

(67) Kuang, D. B.; Klein, C.; Ito, S.; Moser, J. E.; Humphry-Baker, R.; Evans, N.; Duriaux, F.; Grätzel, C.; Zakeeruddin, S. M.; Grätzel, M. *Adv. Mater.* **2007**, *19*, 1133.

(68) Robertson, N. Optimizing Dyes for Dye-Sensitized Solar Cells. *Angew. Chem., Int. Ed.* **2006**, *45*, 2338.

(69) Ito, S.; Miura, H.; Uchida, S.; Takata, M.; Sumioka, K.; Liska, P.; Comte, P.; Pechy, P.; Grätzel, M. High-conversion-efficiency organic dye-sensitized solar cells with a novel indoline dye. *Chem. Commun.* **2008**, 5194.

(70) Freitag, M.; Giordano, F.; Yang, W.; Pazoki, M.; Hao, Y.; Zietz, B.; Grätzel, M.; Hagfeldt, A.; Boschloo, G. Copper Phenanthroline as a Fast and High-Performance Redox Mediator for Dye-Sensitized Solar Cells. *The Journal of Physical Chemistry C* **2016**, *120*, 9595-9603.

(71) Sandroni, M.; Favereau, L.; Planchat, A.; Akdas-Kilig, H.; Szuwarski, N.; Pellegrin, Y.; Blart, E.; Le Bozec, H.; Boujtita, M.; Odobel, F. Heteroleptic copper(i)-polypyridine complexes as efficient sensitizers for dye sensitized solar cells. *Journal of Materials Chemistry A* **2014**, *2*, 9944-9947.

(72) Ikeuchi, T.; Nomoto, H.; Masaki, N.; Griffith, M. J.; Mori, S.; Kimura, M. Molecular engineering of zinc phthalocyanine sensitizers for efficient dye-sensitized solar cells. *Chemical communications* **2014**, *50*, 1941-1943.

(73) Mishra, A.; Fischer, M. K. R.; Bauerle, P. Metal-free organic dyes for dye-sensitized solar cells: from structure: property relationships to design rules. *Angew. Chem., Int. Ed.* **2009**, *48*, 2474.

(74) Jose, R.; Thavasi, V.; Ramakrishna, S. Metal Oxides for Dye-Sensitive Solar Cells. *J. Am. Ceram. Soc.* **2009**, *92*, 289.

(75) Wenger, B.; Grätzel, M.; Moser, J.-E. Rationale for Kinetic Heterogeneity of Ultrafast Light-Induced Electron Transfer from Ru(II) Complex Sensitizers to Nanocrystalline TiO2. *Journal of the American Chemical Society* **2005**, *127*, 12150-12151.

(76) Ardo, S.; Meyer, G. J. Photodriven heterogeneous charge transfer with transition-metal compounds anchored to TiO2 semiconductor surfaces. *Chemical Society reviews* **2009**, *38*, 115-164.

(77) Boschloo, G.; Häggman, L.; Hagfeldt, A. Quantification of the Effect of 4-tert-Butylpyridine Addition to I-/I3- Redox Electrolytes in Dye-Sensitized Nanostructured TiO2 Solar Cells. *J. Phys. Chem. B* **2006**, *110*, 13144.

(78) Koops, S. E.; O'Regan, B. C.; Barnes, P. R. F.; Durrant, J. R. Parameters Influencing the Efficiency of Electron Injection in Dye-Sensitized Solar Cells. *J. Am. Chem. Soc.* **2009**, *131*, 4808.

(79) Benko, G.; Kallioinen, J.; Korppi-Tommola, J. E. I.; Yartsev, A. P.; Sundstrom, V. Photoinduced Ultrafast Dye-to-Semiconductor Electron Injection from Nonthermalized and Thermalized Donor States. *J. Am. Chem. Soc.* **2002**, *124*, 489.

(80) Hannappel, T.; Burfeindt, B.; Storck, W.; Willig, F. Measurement of Ultrafast Photoinduced Electron Transfer from Chemically Anchored Ru-Dye Molecules into Empty Electronic States in a Colloidal Anatase TiO2 Film. *J. Phys. Chem. B* **1997**, *101*, 6799.

(81) Haque, S. A.; Palomares, E.; Cho, B. M.; Green, A. N. M.; Hirata, N.; Klug, D. R.; Durrant, J. R. Charge Separation versus Recombination in Dye-Sensitized Nanocrystalline Solar Cells: the Minization of Kinetic Redundancy. *J. Am. Chem. Soc.* **2005**, *127*, 3456.

(82) Ellingson, R. J.; Asbury, J. B.; Ferrere, S.; Ghosh, H. N.; Sprague, J. R.; Lian, T.; Nozik, A. J. Dynamics of Electron Injection in Nanocrystalline Titanium Dioxide Films Sensitized with [Ru(4,4'-dicarboxy-2,2'-bipyridine)2(NCS)2] by Infrared Transient Absorption. *The Journal of Physical Chemistry B* **1998**, *102*, 6455-6458.

(83) Miyaji, H.; Kim, H.-K.; Sim, E.-K.; Lee, C.-K.; Cho, W.-S.; Sessler, J. L.; Lee, C.-H. Coumarin-Strapped Calix[4]pyrrole: A Fluorogenic Anion Receptor Modulated by Cation and Anion Binding. *Journal of the American Chemical Society* **2005**, *127*, 12510-12512.

(84) Asbury, J. B.; Anderson, N. A.; Hao, E. C.; Ai, X.; Lian, T. Q. Parameters Affecting Electron Injection Dynamics from Ruthenium Dyes to Titanium Dioxide Nanocrystalline Thin Film†. *J. Phys. Chem. B* **2003**, *107*, 7376.

(85) Nillon, J.; Crégut, O.; Bressler, C.; Haacke, S. Two MHz tunable non collinear optical

parametric amplifiers with pulse durations down to 6 fs. *Optics express* **2014**, *22*, 14964-14974.

(86) Streak camera. https://www.hofstragroup.com/product/hamamatsu-c4334-02s-streak-camera-system-for-time-resolved-spectroscopy/.

(87) Cabanillas-Gonzalez, J.; Grancini, G.; Lanzani, G. Pump-probe spectroscopy in organic semiconductors: monitoring fundamental processes of relevance in optoelectronics. *Advanced Materials* **2011**, *23*, 5468-5485.

(88) Lorenc, M.; Ziolek, M.; Naskrecki, R.; Karolczak, J.; Kubicki, J.; Maciejewski, A. Artifacts in femtosecond transient absorption spectroscopy. *Applied Physics B* **2002**, *74*, 19-27.

(89) Günes, S.; Neugebauer, H.; Sariciftci, N. S. Conjugated Polymer-Based Organic Solar Cells. *Chem. Rev.* **2007**, *107*, 1324.

(90) Qu, J.; Gao, B.; Tian, H.; Zhang, X.; Wang, Y.; Xie, Z.; Wang, H.; Geng, Y.; Wang, F. Donor–spacer–acceptor monodisperse conjugated co-oligomers for efficient single-molecule photovoltaic cells based on non-fullerene acceptors. *Journal of Materials Chemistry A* **2014**, *2*, 3632.

(91) Zhong, Y.; Trinh, M. T.; Chen, R.; Wang, W.; Khlyabich, P. P.; Kumar, B.; Xu, Q.; Nam, C.-Y.; Sfeir, M. Y.; Black, C.; Steigerwald, M. L.; Loo, Y.-L.; Xiao, S.; Ng, F.; Zhu, X. Y.; Nuckolls, C. Efficient Organic Solar Cells with Helical Perylene Diimide Electron Acceptors. *Journal of the American Chemical Society* **2014**, *136*, 15215-15221.

(92) Meng, D.; Sun, D.; Zhong, C.; Liu, T.; Fan, B.; Huo, L.; Li, Y.; Jiang, W.; Choi, H.; Kim, T.; Kim, J. Y.; Sun, Y.; Wang, Z.; Heeger, A. J. High-Performance Solution-Processed Non-Fullerene Organic Solar Cells Based on Selenophene-Containing Perylene Bisimide Acceptor. *J Am Chem Soc* **2016**, *138*, 375-380.

(93) Roland, T.; Leonard, J.; Ramirez, G. H.; Mery, S.; Yurchenko, O.; Ludwigs, S.; Haacke, S. Sub-100 fs charge transfer in a novel donor-acceptor-donor triad organized in a smectic film. *Physical chemistry chemical physics : PCCP* **2012**, *14*, 273-279.

(94) Roland, T. Ultrafast Spectroscopy Of New Organic Molecules For Photovoltaic Applications. Université de Strasbourg, 2014.

(95) Wenzel, J.; Dreuw, A.; Burghardt, I. Charge and energy transfer in a bithiophene perylenediimide based donor–acceptor–donor system for use in organic photovoltaics. *Physical chemistry chemical physics : PCCP* **2013**, *15*, 11704.

(96) Stutzmann, N.; Friend, R. H.; Sirringhaus, H. Self-Aligned, Vertical-Channel, Polymer Field-Effect Transistors. *Science* **2003**, *299*, 1881.

(97) Levermore, P. A.; Jin, R.; Wang, X.; de Mello, J. C.; Bradley, D. D. C. Organic Light-Emitting Diodes Based on Poly(9,9-dioctylfluorene-co-bithiophene) (F8T2). *Advanced Functional Materials* **2009**, *19*, 950-957.

(98) Chua, L.-L.; Zaumseil, J.; Chang, J.-F.; Ou, E. C. W.; Ho, P. K. H.; Sirringhaus, H.; Friend, R. H. General observation of n-type field-effect behaviour in organic semiconductors.

Nature **2005**, *434*, 194-199.

(99) Schulz, G. L.; Chen, X.; Holdcroft, S. High band gap poly(9,9-dihexylfluorene-alt-bithiophene) blended with [6,6]-phenyl C61 butyric acid methyl ester for use in efficient photovoltaic devices. *Applied Physics Letters* **2009**, *94*, 023302.

(100) Willy Herbst; Hunger, K.: *Industrial Organic Pigments: Production, Properties, Applications*; Wiley-VCH, 2006.

(101) Weil, T.; Vosch, T.; Hofkens, J.; Peneva, K.; Müllen, K. The Rylene Colorant Family—Tailored Nanoemitters for Photonics Research and Applications. *Angewandte Chemie International Edition* **2010**, *49*, 9068-9093.

(102) Wurthner, F.; Stolte, M. Naphthalene and perylene diimides for organic transistors. *Chemical communications* **2011**, *47*, 5109-5115.

(103) Castellano, F. N. Transition metal complexes meet the rylenes. *Dalton transactions* **2012**, *41*, 8493-8501.

(104) Görl, D.; Zhang, X.; Würthner, F. Molecular Assemblies of Perylene Bisimide Dyes in Water. *Angewandte Chemie International Edition* **2012**, *51*, 6328-6348.

(105) Bu, L.; Guo, X.; Yu, B.; Qu, Y.; Xie, Z.; Yan, D.; Geng, Y.; Wang, F. Monodisperse co-oligomer approach toward nanostructured films with alternating donor-acceptor lamellae. *Journal of the American Chemical Society* **2009**, *131*, 13242-13243.

(106) Langhals, H. Cyclic Carboxylic Imide Structures as Structure Elements of High Stability. Novel Developments in Perylene Dye Chemistry. *Heterocycles* **1995**, *40*, 23.

(107) Ford, W. E.; Kamat, P. V. Photochemistry of 3,4,9,10-perylenetetracarboxylic dianhydride dyes. 3. Singlet and triplet excited-state properties of the bis(2,5-di-tert-butylphenyl)imide derivative. *The Journal of Physical Chemistry* **1987**, *91*, 6373-6380.

(108) Liu, L.; Eisenbrandt, P.; Roland, T.; Polkehn, M.; Schwartz, P. O.; Bruchlos, K.; Omiecienski, B.; Ludwigs, S.; Leclerc, N.; Zaborova, E.; Leonard, J.; Mery, S.; Burghardt, I.; Haacke, S. Controlling charge separation and recombination by chemical design in donor-acceptor dyads. *Phys Chem Chem Phys* **2016**, *18*, 18536-18548.

(109) Jespersen, K. G.; Beenken, W. J.; Zaushitsyn, Y.; Yartsev, A.; Andersson, M.; Pullerits, T.; Sundstrom, V. The electronic states of polyfluorene copolymers with alternating donor-acceptor units. *J Chem Phys* **2004**, *121*, 12613-12617.

(110) Salzner, U.; Köse, M. E. Does the Donor−Acceptor Concept Work for Designing Synthetic Metals? 2. Theoretical Investigation of Copolymers of 4-(Dicyanomethylene)-4H-cyclopenta[2,1-b:3,4-b‘]dithiophene and 3,4-(Ethylenedioxy)thiophene. *The Journal of Physical Chemistry B* **2002**, *106*, 9221-9226.

(111) Veldman, D.; Chopin, S. M. A.; Meskers, S. C. J.; Groeneveld, M. M.; Williams, R. M.; Janssen, R. A. J. Triplet Formation Involving a Polar Transition State in a Well-Defined Intramolecular Perylenediimide Dimeric Aggregate. *The journal of physical chemistry. A* **2008**,

112, 5846-5857.

(112) <Thesis_Roland_Thomas.pdf>.

(113) Gulbinas, V.; Zaushitsyn, Y.; Bässler, H.; Yartsev, A.; Sundström, V. Dynamics of charge pair generation in ladder-type poly(para-phenylene) at different excitation photon energies. *Physical Review B* **2004**, *70*, 035215.

(114) Leonard, J.; Portuondo-Campa, E.; Cannizzo, A.; van Mourik, F.; van der Zwan, G.; Tittor, J.; Haacke, S.; Chergui, M. Functional electric field changes in photoactivated proteins revealed by ultrafast Stark spectroscopy of the Trp residues. *Proceedings of the National Academy of Sciences of the United States of America* **2009**, *106*, 7718-7723.

(115) Scarongella, M.; Paraecattil, A. A.; Buchaca-Domingo, E.; Douglas, J. D.; Beaupre, S.; McCarthy-Ward, T.; Heeney, M.; Moser, J. E.; Leclerc, M.; Frechet, J. M. J.; Stingelin, N.; Banerji, N. The influence of microstructure on charge separation dynamics in organic bulk heterojunction materials for solar cell applications. *Journal of Materials Chemistry A* **2014**, *2*, 6218-6230.

(116) Gorczak, N.; Tarkuc, S.; Renaud, N.; Houtepen, A. J.; Eelkema, R.; Siebbeles, L. D.; Grozema, F. C. Different mechanisms for hole and electron transfer along identical molecular bridges: the importance of the initial state delocalization. *J Phys Chem A* **2014**, *118*, 3891-3898.

(117) Lide, D. R.: *CRC Handbook of Chemistry and Physics*; CRC Press, 1997.

(118) Karsten, B. P.; Bouwer, R. K. M.; Hummelen, J. C.; Williams, R. M.; Janssen, R. A. J. Charge Separation and Recombination in Small Band Gap Oligomer−Fullerene Triads. *The Journal of Physical Chemistry B* **2010**, *114*, 14149-14156.

(119) Copeland, D. A.; Kestner, N. R.; Jortner, J. Excess Electrons in Polar Solvents. *The Journal of chemical physics* **1970**, *53*, 1189-1216.

(120) Kestner, N. R.; Logan, J.; Jortner, J. Thermal electron transfer reactions in polar solvents. *J. Phys. Chem.* **1974**, *78*, 2148.

(121) Moser, C. C.; Keske, J. M.; Warncke, K.; Farid, R. S.; Dutton, P. L. Nature of biological electron transfer. *Nature* **1992**, *355*, 796-802.

(122) Ando, K. Solvation dynamics and electronic structure development of coumarin 120 in methanol: A theoretical modeling study. *The Journal of chemical physics* **1997**, *107*, 4585-4596.

(123) Kim, H. J.; Hynes, J. T. Equilibrium and nonequilibrium solvation and solute electronic structure. III. Quantum theory. *The Journal of chemical physics* **1992**, *96*, 5088-5110.

(124) LeBard, D. N.; Lilichenko, M.; Matyushov, D. V.; Berlin, Y. A.; Ratner, M. A. Solvent Reorganization Energy of Charge Transfer in DNA Hairpins. *The Journal of Physical Chemistry B* **2003**, *107*, 14509-14520.

(125) Wang, H.; McNellis, E. R.; Kinge, S.; Bonn, M.; Cánovas, E. Tuning Electron

Transfer Rates through Molecular Bridges in Quantum Dot Sensitized Oxides. *Nano Letters* **2013**, *13*, 5311-5315.

(126) Leng, W.; Würthner, F.; Kelley, A. M. Resonance Raman Intensity Analysis of Merocyanine Dimers in Solution. *The Journal of Physical Chemistry B* **2004**, *108*, 10284-10294.

(127) Gao, B.-R.; Qu, J.-F.; Wang, Y.; Fu, Y.-Y.; Wang, L.; Chen, Q.-D.; Sun, H.-B.; Geng, Y.-H.; Wang, H.-Y.; Xie, Z.-Y. Femtosecond Spectroscopic Study of Photoinduced Charge Separation and Recombination in the Donor–Acceptor Co-Oligomers for Solar Cells. *The Journal of Physical Chemistry C* **2013**, *117*, 4836-4843.

(128) Lim, J. M.; Kim, P.; Yoon, M.-C.; Sung, J.; Dehm, V.; Chen, Z.; Würthner, F.; Kim, D. Exciton delocalization and dynamics in helical π-stacks of self-assembled perylene bisimides. *Chem. Sci.* **2013**, *4*, 388-397.

(129) Sung, J.; Nowak-Król, A.; Schlosser, F.; Fimmel, B.; Kim, W.; Kim, D.; Würthner, F. Direct Observation of Excimer-Mediated Intramolecular Electron Transfer in a Cofacially-Stacked Perylene Bisimide Pair. *Journal of the American Chemical Society* **2016**, *138*, 9029-9032.

(130) Polkehn, M.; Tamura, H.; Eisenbrandt, P.; Haacke, S.; Méry, S.; Burghardt, I. Molecular Packing Determines Charge Separation in a Liquid Crystalline Bisthiophene–Perylene Diimide Donor–Acceptor Material. *The journal of physical chemistry letters* **2016**, *7*, 1327-1334.

(131) Alfred Werner.

(132) Schultz, D. M.; Yoon, T. P. Solar synthesis: prospects in visible light photocatalysis. *Science* **2014**, *343*, 1239176.

(133) Cebrián, C.; Mauro, M.; Kourkoulos, D.; Mercandelli, P.; Hertel, D.; Meerholz, K.; Strassert, C. A.; De Cola, L. Luminescent Neutral Platinum Complexes Bearing an Asymmetric N^N^N Ligand for High-Performance Solution-Processed OLEDs. *Advanced Materials* **2013**, *25*, 437-442.

(134) Willkomm, J.; Orchard, K. L.; Reynal, A.; Pastor, E.; Durrant, J. R.; Reisner, E. Dye-sensitised semiconductors modified with molecular catalysts for light-driven H2 production. *Chemical Society reviews* **2016**, *45*, 9-23.

(135) Whang, D. R.; Sakai, K.; Park, S. Y. Highly Efficient Photocatalytic Water Reduction with Robust Iridium(III) Photosensitizers Containing Arylsilyl Substituents. *Angewandte Chemie International Edition* **2013**, *52*, 11612-11615.

(136) Damrauer, N. H.; Cerullo, G.; Yeh, A.; Boussie, T. R.; Shank, C. V.; McCusker, J. K. Femtosecond Dynamics of Excited-State Evolution in [Ru(bpy)3]2+. *Science* **1997**, *275*, 54.

(137) Juris, A.; Balzani, V.; Barigelletti, F.; Campagna, S.; Belser, P.; von Zelewsky, A.

Ru(II) polypyridine complexes: photophysics, photochemistry, eletrochemistry, and chemiluminescence. *Coordination Chemistry Reviews* **1988**, *84*, 85-277.

(138) Chen, C.-Y.; Wang, M.; Li, J.-Y.; Pootrakulchote, N.; Alibabaei, L.; Ngoc-le, C.-h.; Decoppet, J.-D.; Tsai, J.-H.; Grätzel, C.; Wu, C.-G.; Zakeeruddin, S. M.; Grätzel, M. Highly Efficient Light-Harvesting Ruthenium Sensitizer for Thin-Film Dye-Sensitized Solar Cells. *ACS Nano* **2009**, *3*, 3103-3109.

(139) chemical elements. https://en.wikipedia.org/wiki/Abundance_of_the_chemical_elements.

(140) Juban, E. A.; Smeigh, A. L.; Monat, J. E.; McCusker, J. K. Ultrafast dynamics of ligand-field excited states. *Coordination Chemistry Reviews* **2006**, *250*, 1783-1791.

(141) Cannizzo, A.; Milne, C. J.; Consani, C.; Gawelda, W.; Bressler, C.; van Mourik, F.; Chergui, M. Light-induced spin crossover in Fe(II)-based complexes: The full photocycle unraveled by ultrafast optical and X-ray spectroscopies. *Coordination Chemistry Reviews* **2010**, *254*, 2677-2686.

(142) Zhang, W.; Alonso-Mori, R.; Bergmann, U.; Bressler, C.; Chollet, M.; Galler, A.; Gawelda, W.; Hadt, R. G.; Hartsock, R. W.; Kroll, T.; Kjaer, K. S.; Kubicek, K.; Lemke, H. T.; Liang, H. W.; Meyer, D. A.; Nielsen, M. M.; Purser, C.; Robinson, J. S.; Solomon, E. I.; Sun, Z.; Sokaras, D.; van Driel, T. B.; Vanko, G.; Weng, T. C.; Zhu, D.; Gaffney, K. J. Tracking excited-state charge and spin dynamics in iron coordination complexes. *Nature* **2014**, *509*, 345-348.

(143) Aubock, G.; Chergui, M. Sub-50-fs photoinduced spin crossover in [Fe(bpy)(3)](2)(+). *Nature chemistry* **2015**, *7*, 629-633.

(144) McGarvey, J. J.; Lawthers, I.; Heremans, K.; Toftlund, H. Spin-state relaxation dynamics in iron(II) complexes: solvent on the activation and reaction and volumes for the 1A [right left harpoons]5T interconversion. *Journal of the Chemical Society, Chemical Communications* **1984**, 1575-1576.

(145) Lawthers, I.; McGarvey, J. J. Spin-state relaxation dynamics in iron(III) complexes: photochemical perturbation of the 2T .dblharw. 6A spin equilibrium by pulsed-laser irradiation in the ligand-to-metal charge-transfer absorption band. *Journal of the American Chemical Society* **1984**, *106*, 4280-4282.

(146) Bressler, C.; Milne, C.; Pham, V. T.; ElNahhas, A.; van der Veen, R. M.; Gawelda, W.; Johnson, S.; Beaud, P.; Grolimund, D.; Kaiser, M.; Borca, C. N.; Ingold, G.; Abela, R.; Chergui, M. Femtosecond XANES Study of the Light-Induced Spin Crossover Dynamics in an Iron(II) Complex. *Science* **2009**, *323*, 489.

(147) Gawelda, W.; Cannizzo, A.; Pham, V.-T.; van Mourik, F.; Bressler, C.; Chergui, M. Ultrafast Nonadiabatic Dynamics of [FeII(bpy)3]2+ in Solution. *Journal of the American Chemical Society* **2007**, *129*, 8199-8206.

(148) Hauser, A. Intersystem crossing dynamics in Fe(II) coordination compounds. *J. Chem. Phys.* **1991**, *94*, 2741.

(149) de Graaf, C.; Sousa, C. Study of the light-induced spin crossover process of the [Fe(II)(bpy)3]2+ complex. *Chemistry* **2010**, *16*, 4550-4556.

(150) Graaf, C. D.; Sousa, C. On the role of the metal-to-ligand charge transfer states in the light-induced spin crossover in FeII (bpy)3. *International Journal of Quantum Chemistry* **2011**, *111*, 3385-3393.

(151) Sousa, C.; de Graaf, C.; Rudavskyi, A.; Broer, R.; Tatchen, J.; Etinski, M.; Marian, C. M. Ultrafast Deactivation Mechanism of the Excited Singlet in the Light-Induced Spin Crossover of [Fe(2,2′-bipyridine)3]2+. *Chemistry – A European Journal* **2013**, *19*, 17541-17551.

(152) Zhang, W.; Gaffney, K. J. Mechanistic Studies of Photoinduced Spin Crossover and Electron Transfer in Inorganic Complexes. *Accounts of chemical research* **2015**, *48*, 1140-1148.

(153) Monat, J. E.; McCusker, J. K. Femtosecond Excited-State Dynamics of an Iron(II) Polypyridyl Solar Cell Sensitizer Model. *Journal of the American Chemical Society* **2000**, *122*, 4092-4097.

(154) Duchanois, T.; Etienne, T.; Cebrián, C.; Liu, L.; Monari, A.; Beley, M.; Assfeld, X.; Haacke, S.; Gros, P. C. An Iron-Based Photosensitizer with Extended Excited-State Lifetime: Photophysical and Photovoltaic Properties. *European Journal of Inorganic Chemistry* **2015**, *2015*, 2469-2477.

(155) Ferrere, S.; Gregg, B. A. Photosensitization of TiO2 by [FeII(2,2'-bipyridine-4,4'-dicarboxylic acid)2(CN)2]: Band Selective Electron Injection from Ultra-Short-Lived Excited States. *J. Am. Chem. Soc.* **1998**, *120*, 843.

(156) Ferrere, S. New Photosensitizers Based upon [Fe(L)2(CN)2] and [Fe(L)3] (L = Substituted 2,2'-Bipyridine): Yields for the Photosensitization of TiO2 and Effects on the Band Selectivity. *Chem. Mater.* **2000**, *12*, 1083.

(157) Ferrere, S. New photosensitizers based upon [FeII(L)2(CN)2] and [FeIIL3], where L is substituted 2,2'-bipyridine. *Inorg. Chim. Acta* **2002**, *329*, 79.

(158) Xia, H.-L.; Ardo, S.; Narducci Sarjeant, A. A.; Huang, S.; Meyer, G. J. Photodriven Spin Change of Fe(II) Benzimidazole Compounds Anchored to Nanocrystalline TiO2 Thin Films. *Langmuir* **2009**, *25*, 13641-13652.

(159) Visbal, R.; Gimeno, M. C. N-heterocyclic carbene metal complexes: photoluminescence and applications. *Chemical Society reviews* **2014**, *43*, 3551-3574.

(160) Lo Kenneth, K.-W.; Zhang Kenneth, Y.; Li Steve, P.-Y.: Design of cyclometalated iridium(III) polypyridine complexes as luminescent biological labels and probes. In *Pure and Applied Chemistry*, 2011; Vol. 83; pp 823.

(161) Kandada, A. R.; Grancini, G.; Petrozza, A.; Perissinotto, S.; Fazzi, D.; Raavi, S. S.; Lanzani, G. Ultrafast energy transfer in ultrathin organic donor/acceptor blend. *Sci Rep* **2013**, *3*, 2073.

(162) Ma, D.-L.; Che, C.-M. A Bifunctional Platinum(II) Complex Capable of Intercalation and Hydrogen-Bonding Interactions with DNA: Binding Studies and Cytotoxicity. *Chemistry – A European Journal* **2003**, *9*, 6133-6144.

(163) You, Y.; Park, S. Y. A Phosphorescent Ir(III) Complex for Selective Fluoride Ion Sensing with a High Signal-to-Noise Ratio. *Advanced Materials* **2008**, *20*, 3820-3826.

(164) Frenking, G.; Koch, W.; Gauss, J.; Cremer, D. Stabilities and nature of the attractive interactions in HeBeO, NeBeO, and ArBeO and a comparison with analogs NGLiF, NGBN, and NGLiH (NG = He, Ar). A theoretical investigation. *Journal of the American Chemical Society* **1988**, *110*, 8007-8016.

(165) Lowry, M. S.; Goldsmith, J. I.; Slinker, J. D.; Rohl, R.; Pascal, R. A.; Malliaras, G. G.; Bernhard, S. Single-Layer Electroluminescent Devices and Photoinduced Hydrogen Production from an Ionic Iridium(III) Complex. *Chemistry of Materials* **2005**, *17*, 5712-5719.

(166) Chang, W. C.; Chen, H. S.; Li, T. Y.; Hsu, N. M.; Tingare, Y. S.; Li, C. Y.; Liu, Y. C.; Su, C.; Li, W. R. Highly efficient N-heterocyclic carbene/pyridine-based ruthenium sensitizers: complexes for dye-sensitized solar cells. *Angewandte Chemie* **2010**, *49*, 8161-8164.

(167) Liu, Y.; Harlang, T.; Canton, S. E.; Chabera, P.; Suarez-Alcantara, K.; Fleckhaus, A.; Vithanage, D. A.; Goransson, E.; Corani, A.; Lomoth, R.; Sundstrom, V.; Warnmark, K. Towards longer-lived metal-to-ligand charge transfer states of iron(II) complexes: an N-heterocyclic carbene approach. *Chemical communications* **2013**, *49*, 6412-6414.

(168) Barbante, G. J.; Francis, P. S.; Hogan, C. F.; Kheradmand, P. R.; Wilson, D. J. D.; Barnard, P. J. Electrochemiluminescent Ruthenium(II) N-Heterocyclic Carbene Complexes: a Combined Experimental and Theoretical Study. *Inorganic chemistry* **2013**, *52*, 7448-7459.

(169) Fredin, L. A.; Papai, M.; Rozsalyi, E.; Vanko, G.; Warnmark, K.; Sundstrom, V.; Persson, P. Exceptional Excited-State Lifetime of an Iron(II)-N-Heterocyclic Carbene Complex Explained. *The journal of physical chemistry letters* **2014**, *5*, 2066-2071.

(170) Lee, K. E.; Gomez, M. A.; Eloutik, S.; Demopoulos, G. P. Further Understanding of the Adsorption Mechanism of N719 Sensitizer on Anatase TiO2 Films for DSSC Applications Using Vibrational Spectroscopy and Confocal Raman Imaging. *Langmuir* **2010**, *26*, 9575.

(171) Monari, A.; Very, T.; Rivail, J.-L.; Assfeld, X. A QM/MM study on the spinach plastocyanin: Redox properties and absorption spectra. *Computational and Theoretical Chemistry* **2012**, *990*, 119-125.

(172) Liu, L.; Duchanois, T.; Etienne, T.; Monari, A.; Beley, M.; Assfeld, X.; Haacke, S.; Gros, P. C. A new record excited state (3)MLCT lifetime for metalorganic iron(ii) complexes.

Phys Chem Chem Phys **2016**, *18*, 12550-12556.

(173) Wang, Z. S.; Koumura, N.; Cui, Y.; Takahashi, M.; Sekiguchi, H.; Mori, A.; Kubo, T.; Furube, A.; Hara, K. Hexylthiophene-Functionalized Carbazole Dyes for Efficient Molecular Photovoltaics: Tuning of Solar-Cell Performance by Structural Modification. *Chem. Mater.* **2008**, *20*, 3993.

(174) Bräm, O.; Messina, F.; El-Zohry, A. M.; Cannizzo, A.; Chergui, M. Polychromatic femtosecond fluorescence studies of metal–polypyridine complexes in solution. *Chemical Physics* **2012**, *393*, 51-57.

(175) Pastore, M.; Duchanois, T.; Liu, L.; Monari, A.; Assfeld, X.; Haacke, S.; Gros, P. C. Interfacial charge separation and photovoltaic efficiency in Fe(ii)-carbene sensitized solar cells. *Phys Chem Chem Phys* **2016**, *18*, 28069-28081.

(176) Harlang, T. C.; Liu, Y.; Gordivska, O.; Fredin, L. A.; Ponseca, C. S., Jr.; Huang, P.; Chabera, P.; Kjaer, K. S.; Mateos, H.; Uhlig, J.; Lomoth, R.; Wallenberg, R.; Styring, S.; Persson, P.; Sundstrom, V.; Warnmark, K. Iron sensitizer converts light to electrons with 92% yield. *Nature chemistry* **2015**, *7*, 883-889.

(177) Schnedermann, C.; Lim, J. M.; Wende, T.; Duarte, A. S.; Ni, L.; Gu, Q.; Sadhanala, A.; Rao, A.; Kukura, P. Sub-10 fs Time-Resolved Vibronic Optical Microscopy. *The journal of physical chemistry letters* **2016**, *7*, 4854-4859.

List of Figures

List of Tables

Abbreviations and chemical compounds

AM 1.5G	1.5 times path length of the air mass
ATR-FTIR	attenuated total reflectance Fourier transform infrared
BBO	beta barium borate
CCD	charge-coupled device
CT	charge transfer
DAS	decay-associated differential spectrum
DCM	dichloromethane
DFG	different frequency generation
DMF	dimethylformamide
DMSO	dimethyl sulfoxide
DSSC	dye-sensitized solar cell
ESA	excited state absorption
ET	energy transfer
FET	field effect transistor
FF	fill-factor
FRET	Förster resonance energy transfer
GSB	ground state bleaching
GVD	group velocity dispersion
HOMO	highest occupied molecular orbital
HR-TEM	high-resolution transmission electron microscope
HS	high spin
IC	internal conversion
ISC	intersystem crossing
IR	infrared
IRF	instrumental response function
IVR	intramolecular vibrational energy redistribution
Jsc	short-circuit current
LC	ligand-centered
LMCT	ligand-to-metal charge transfer
MC	metal-centered
MCP	micro-channel plate
MeCN	acetonitrile
MLCT	metal-to-ligand charge transfer
NHC	N-heterocyclic carbene
NOPA	noncollinear optical parametric amplifier

OLED organic light emitting diode
oNTO "occupied" natural transitions orbital
OSCs organic solar cell
LS low spin
LUMO Lowest Unoccupied Molecular Orbital
OPA optical parametric amplification
PA photoproduct absorption
PCE power conversion efficiency
PDI perylene diimide
PEC potential energy curve
PES potential energy surface
PL photoluminescence
PV photovoltaics
RS Raman scattering
SCO spin crossover
SE stimulated emission
SFG sum-frequency generation
SHG second harmonic generation
SPM self-phase modulation
SVD singular value decomposition
tBP^{+} 4-*tert*-butylpyridine
TA transient absorption
TCE trichloroethylene
UV ultraviolet
VC vibrational cooling
Vis visible
vNTO "virtual" natural transitions orbital
Voc open-circuit voltage
XPM cross-phase modulation